

Cracow University of Technology  
Faculty of Civil Engineering  
Institute for Computational Civil Engineering (L-5)

ADAM WOSATKO

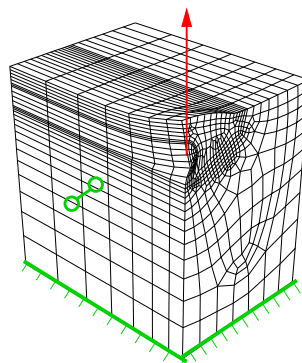
awosatko@L5.pk.edu.pl

---

*Finite-element analysis of cracking in concrete  
using gradient damage-plasticity*

---

supervisor: DR. JERZY PAMIN, PROF. OF CUT



Cracow, April 2008



# PREFACE

*Gloria Patri, et Filio, et Spiritui sancto...*

*To the memory of My Grandfather Stefan and My Father*

This thesis has been worked on starting from project no 7 T07A 020 18 financed by the Polish Committee of Scientific Research. The procedures have been implemented in the FEAP package and then verified by examples using the equipment which was donated by the Alexander von Humboldt Foundation. The research was continued among others during my stay in Glasgow in summer 2006, financed by the Dean of Faculty of Civil Engineering, CUT. The last part of the research on stabilized finite elements for gradient damage was supported by grant no N501 013 32/1520 from the Ministry of Science and Higher Education.

First I would like to thank my wife and my daughter for being with me – always. Usual helpfulness of my both mothers and my sister has been priceless.

I would like to express my sincere gratitude to Prof. Jerzy Pamin, my teacher, supervisor and also adviser in tiny- and large-scale problems. Many discussions and suggestions of Dr. Andrzej Winnicki were very valuable. The cooperation with Dr. Roman Putanowicz concerning the preparation of some visualizations was a useful experience for me. The support of Prof. Maria Anna Polak, Konrad Kukla, Jacek Karolak, Dr. Łukasz Kaczmarczyk, Dr. Aleksander Matuszak and Prof. Nenad Bićanić has also been appreciated.

I acknowledge the helpful tips during the edition of this thesis, provided by Prof. Maria Radwańska who is also my first scientific mentor. Many thanks to my colleagues with whom I neighbour the job rooms, i.e. Dr. Anna Stankiewicz, Dr. Ewa Pabisek, Dr. Magda Jakubek, Wojciech Massalski and Barbara Rodzyńkiewicz, as well as the other colleagues from Institute L-5. Last but not least, I am grateful to our computer administrators – Marcin Klamra and Grzegorz Nowak.

## *Pamięci mojego Dziadka Stefana i mojego Taty*

Niniejsza praca doktorska powstawała zaczynając od grantu KBN nr 7 T07A 020 18. Procedury numeryczne, które były implementowane w pakiecie FEAP, zostały zweryfikowane przykładami obliczanymi na serwerze sfinansowanym przez Fundację Humboldta. Badania były kontynuowane m.in. w czasie pobytu w Glasgow, finansowanego przez Dziekana Wydziału Inżynierii Lądowej PK. Ostatnią część badań dotyczącą stabilizowanych elementów skończonych dla gradientowego modelu mechaniki uszkodzeń wykonano w ramach grantu MNiSW nr N501 013 32/1520.

Najpierw chciałbym podziękować mojej Żonie i mojej Córcie za to, że są ze mną – zawsze. Zwyczajna pomoc obu moich Mam i mojej Siostry pozostaje bezcenną.

Chciałbym złożyć wyrazy wdzięczności Prof. Jerzemu Paminowi, mojemu nauczycielowi, promotorowi oraz doradcy w sprawach małych i dużych. Doceniam też wiele bardzo wartościowych dyskusji i sugestii Dr. Andrzeja Winnickiego. Pożytecznym doświadczeniem dla mnie była współpraca z Dr. Romanem Putanowiczem przy przygotowywaniu niektórych wizualizacji. Przydatna była również pomoc Prof. Marii Anny Polak, Konrada Kukli, Jacka Karolaka, Dr. Łukasza Kaczmarczyka, Dr. Aleksandra Matuszaka i Prof. Nenada Bićanića.

Dziękuję za cenne rady w trakcie edycji tej pracy Prof. Marii Radwańskiej, która jest również moim pierwszym naukowym mentorem. Podziękowania dla moich kolegów i koleżanek z którymi "po sąsiedzku" pracuję, to jest dla Dr Anny Stankiewicz, Dr Ewy Pabisek, Dr Magdy Jakubek, Wojciecha Massalskiego i Barbary Rodzynkiewicz, oraz dla pozostałych pracowników Instytutu L-5. Ponadto jestem wdzięczny naszym administratorom sieci komputerowej - Marcinowi Klamrze i Grzegorzowi Nowakowi.

# NOTATION

In the thesis the Voigt's notation (called also matrix-vector notation) is used. However, when it is necessary, indicial notation is additionally adopted. Despite a transient problem is considered, time  $t$  is usually omitted in the notation. Standard mathematical operations (e.g. matrix transposition) are written in a standard way. The Latin and Greek symbols as well as abbreviations employed are listed below. The page number, optionally preceded by the equation number, in which a symbol is defined the first time, are additionally given to make these lists more helpful.

## LATIN SYMBOLS

$A_r$	cross section for reinforcement, p. 112
$A$	acoustic tensor, Eq. (1.7), p. 5
$B$	width, height, p. 101
$B$	derivatives of shape functions for displacement field, Eq. (3.26), p. 63
$\mathcal{B}$	certain domain, Eq. (1.5), p. 1
$\mathcal{B}^e$	domain of finite element, Eq. (3.100), p. 81
$\partial\mathcal{B}$	boundary (surface) of domain $\mathcal{B}$ , Eq. (3.16), p. 61
$\partial\mathcal{B}_{\text{dis}}$	discontinuity surface (curve), p. 5
$\partial\mathcal{B}_t$	(part of) boundary of domain with given tractions, Eq. (3.16), p. 61
$\partial\mathcal{B}_u$	(part of) boundary of domain with given displacements, Eq. (3.16), p. 61
$E, E_c, E_s$	Young's modulus, Eq. (2.11), p. 15
$E^{\text{tan}}$	tangent stiffness, Eq. (1.9), p. 6
$E$	elastic stiffness operator in matrix form, Eq. (2.5), p. 15
$E_{aa}, E_{ae}$	auxiliary stiffness operators for stabilization, Eq. (3.109), p. 82
$E_{\text{KG}}$	isotropic damage stiffness operator in matrix form, Eq. (2.87), p. 33
$E^{\text{ep}}$	elasto-plastic stiffness operator in matrix form, Eq. (2.34), p. 23
$E^{\text{tan}}$	tangent stiffness operator (general), Eq. (1.4), p. 5
$E_{\text{tan}}$	tangent stiffness operator (crack closing), Eq. (2.83), p. 30
$E_{\text{sec}}$	secant stiffness operator, Eq. (2.51), p. 26
$E^*$	auxiliary stiffness operator (crack closing), Eq. (2.83), p. 30
$\hat{F}$	effective load vector, Eq. (3.85), p. 69
$F_{\text{ext}}$	global vector of external forces, Eq. (3.77), p. 68

$\mathbf{F}_{\text{int}}$	global vector of internal forces, Eq. (3.77), p. 68
$G$	shear (Kirchhoff) modulus, Eq. (2.86), p. 33
$G_f$	fracture energy, Eq. (1.13), p. 8
$\mathbf{G}_a^e$	auxiliary elastic matrix for stabilization, Eq. (3.103), p. 81
$\mathbf{G}_a^{\text{epd}}, \mathbf{G}_e^{\text{epd}}$	auxiliary nonlinear matrices for stabilization, Eq. (3.112), p. 82
$\mathcal{G}$	derivative of damage function in gradient approach, Eq. (3.43), p. 64
$\mathcal{G}_G$	derivative of deviatoric damage function in grad. approach, Eq. (3.66), p. 67
$\mathcal{G}_K$	derivative of volumetric damage function in grad. approach, Eq. (3.66), p. 67
$H$	Heaviside function, Eq. (2.12), p. 16
$\mathbf{H}$	matrix of selection in crack closing model, Eq. (2.57), p. 28
$\mathbf{H}_{\text{Ortiz}}$	matrix of selection according to idea of Ortiz, Eq. (2.65), p. 28
$\mathbf{H}_{\text{SJH}}$	matrix of selection according to idea of Simo-Ju-Hansen, Eq. (2.69), p. 29
$(\ )_I$	indicator of principal direction, Eq. (2.12), p. 16
$I_1^\epsilon$	first invariant of strain tensor, Eq. (2.15), p. 18
$I_1^{\hat{\sigma}}$	first invariant of effective stress tensor, Eq. (2.38), p. 23
$\mathbf{I}$	identity matrix, Eq. (2.89), p. 33
$J_2^\epsilon$	second invariant of strain deviator, Eq. (2.15), p. 18
$J_2^{\hat{\sigma}}$	second invariant of effective stress deviator, Eq. (2.38), p. 23
$K$	bulk modulus, Eq. (2.86), p. 33
$\mathbf{K}$	general tangent operator, Eq. (3.74), p. 68
$\widehat{\mathbf{K}}$	dynamic tangent matrix, Eq. (3.85), p. 69
$\mathbf{K}_{aa}, \mathbf{K}_{ae}$	submatrices of tangent operator from equations of motion, Eq. (3.46), p. 64
$\bar{\mathbf{K}}_{aa}, \bar{\mathbf{K}}_{ae}$	as in previous line, but from first stabilization term, Eq. (3.114), p. 82
$\mathbf{K}_{aa}^{\text{KG}}, \mathbf{K}_{ae}^{\text{KG}}$	submatrices of tangent operator for isotropic damage, Eq. (3.69), p. 67
$\mathbf{K}_{ea}, \mathbf{K}_{ee}$	submatrices of tangent operator from averaging equation, Eq. (3.53), p. 65
$\bar{\mathbf{K}}_{ee}$	submatrix of t. operator from second stabilization term, Eq. (3.131), p. 85
$L$	length, p. 94
$L_{\text{imp}}$	length of weaker zone, p. 94
$\mathbf{L}$	matrix of differential operators, Eq. (2.1), p. 13
$\mathcal{L}$	derivative of damage function in local approach, Eq. (2.48), p. 24
$\mathcal{L}_G$	derivative of deviatoric damage function in local approach, Eq. (2.95), p. 34
$\mathcal{L}_K$	derivative of volumetric damage function in local approach, Eq. (2.95), p. 34
$\mathbf{M}$	general mass matrix, Eq. (3.73), p. 68
$\mathbf{M}_{aa}$	mass matrix from equations of motion, Eq. (3.46), p. 64
$\mathbf{N}$	shape functions for displacement field, Eq. (3.25), p. 63
$\mathcal{N}$	outward normal to boundary (surface) of domain, Eq. (3.17), p. 61
$\mathbf{P}, \mathbf{P}$	load, p. 104
$\mathbf{P}_i$	weighting part of stabilization term, $i = 1, 2$ , Eq. (3.102), p. 81
$\mathbf{P}^+$	projection operator in crack closing model, Eq. (2.52), p. 26

$P_{Ortiz}^+$	projection operator according to idea of Ortiz, Eq. (2.66), p. 28
$P_{SJH}^+$	projection operator according to idea of Simo-Ju-Hansen, Eq. (2.70), p. 29
$Q, Q_0, Q_{dev}$	selection operators for volumetric-deviatoric split, Eq. (2.86), p. 33
$Q^+$	auxiliary tensor in idea of Simo-Ju-Hansen, Eq. (2.67), p. 29
$R, R_i$	considered variational equations, $i = 1, 2$ , Eq. (3.96), p. 80
$R_i^{stab}$	stabilization terms in variational equations, $i = 1, 2$ , Eq. (3.99), p. 81
$\widehat{R}$	residual force vector, Eq. (3.93), p. 69
$R_\sigma$	divergence of stress tensor in Voigt's notation, Eq. (3.105), p. 81
$dS$	elementary surface, Eq. (3.20), p. 62
$dS_{\vec{n}}$	infinitesimal area on section with normal direction $\vec{n}$ , Eq. (1.1), p. 1
$dS_{\vec{n}}^d$	damaged part of this infinitesimal area, Eq. (1.1), p. 1
$dS_{\vec{n}}^u$	undamaged part of this infinitesimal area, Eq. (1.1), p. 1
$T$	thickness, p. 101
$T$	transformation matrix in crack closing model, Eq. (2.57), p. 27
$dV$	elementary volume, Eq. (1.5), p. 5
$a$	arbitrary constant, Eq. (3.125), p. 84
$\mathbf{a}$	nodal displacements, Eq. (3.25), p. 63
$\mathbf{b}$	body force vector, Eq. (2.1), p. 13
$c, c_G, c_K$	coefficients related to internal length squared, Eq. (3.4), p. 59
$c_i$	set of coefficients in Newmark method, $i = 0, \dots, 4$ , Eq. (3.82), p. 69
$c_p$	cohesion function, Eq. (2.36), p. 24
$c_w$	wave velocity, Eq. (1.10), p. 6
$c_\Theta$	cosine of angle between original and principal axes (2D), Eq. (2.62), p. 28
$d$	coefficient related to fourth power of internal length, Eq. (3.4), p. 59
$\mathbf{d}_I$	unit vector along principal direction $I$ , Eq. (2.64), p. 28
$\mathbf{e}$	nodal averaged strains, Eq. (3.25), p. 63
$f_c$	compressive strength, Eq. (2.18), p. 18
$f^d$	damage activation (loading) function, Eq. (2.8), p. 15
$f^p$	yield function, Eq. (2.28), p. 22
$f_t$	tensile strength, Eq. (2.18), p. 18
$\bar{\mathbf{f}}$	right-hand side vector from first stabilization term, Eq. (3.116), p. 82
$\bar{\mathbf{f}}_e$	right-hand side vector from second stabilization term, Eq. (3.132), p. 85
$\mathbf{f}_\epsilon, \mathbf{f}_e$	right-hand side vectors from averaging equation, Eq. (3.53), p. 65
$\mathbf{f}_{ext}$	vector of external forces, Eq. (3.46), p. 64
$\mathbf{f}_{int}$	vector of internal forces, Eq. (3.46), p. 64
$g$	non-local weight function, Eq. (3.1), p. 57
$\bar{g}$	additional gradient field in stabilization term, Eq. (3.123), p. 84
$g^p$	plastic potential function, Eq. (2.26), p. 22
$\mathbf{g}$	derivatives of shape functions for averaged strain field, Eq. (3.26), p. 63

$h$	hardening/softening modulus, Eq. (2.32), p. 23
$h_e$	characteristic length of finite element, Eq. (3.101), p. 81
$\mathbf{h}$	shape functions for averaged strain field, Eq. (3.25), p. 63
$k$	ratio of compressive and tensile strength, Eq. (2.15), p. 18
$k_w$	wave number, Eq. (1.10), p. 6
$l$	internal length scale parameter, Eq. (3.3), p. 94
$\mathbf{m}$	plastic flow direction, Eq. (2.27), p. 22
$\vec{n}$	normal direction, p. 1
$\mathbf{n}$	normal direction to yield function, Eq. (2.31), p. 23
$n_1, n_2$	numerical parameters in alternative exponential law, Eq. (2.22), p. 21
$\hat{p}$	hydrostatic pressure in effective stress space, Eq. (2.36), p. 23
$p$	hydrostatic pressure, Eq. (2.91), p. 33
$\hat{q}$	deviatoric stress measure in effective stress space, Eq. (2.36), p. 23
$\mathbf{q}$	vector of nodal quantities, Eq. (3.75), p. 68
$r$	distance between considered and source points, Eq. (3.2), p. 58
$s_\Theta$	sine of angle between original and principal axes (2D), Eq. (2.62), p. 28
$\mathbf{s}$	derivative of strain measure, Eq. (2.49), p. 24
$\mathbf{s}_G$	derivative of deviatoric strain measure, Eq. (2.104), p. 40
$\mathbf{s}_K$	derivative of dilatancy measure, Eq. (2.104), p. 40
$\mathbf{s}_x$	coordinates of source point for non-local weight function, Eq. (3.1), p. 57
$t$	time, Eq. (1.9), p. 1
$\mathbf{t}$	tractions, Eq. (3.21), p. 62
$\mathbf{t}_e$	vector of twisted form, Eq. (3.125), p. 84
$u$	horizontal displacement, p. 95
$\mathbf{u}$	displacement vector, Eq. (2.1), p. 13
$\bar{\mathbf{u}}$	averaged displacement field, Eq. (3.12), p. 60
$v, \mathbf{v}, w, w_c$	vertical displacement or deflection, p. 115
$v$	axial velocity, Eq. (1.9), p. 6
$w_f$	crack band width, Eq. (1.13), p. 8
$x$	spatial direction, Eq. (1.9), p. 6
$\mathbf{x}$	coordinates of considered material point in $\mathcal{B}$ , Eq. (3.1), p. 57
$\mathbf{x}_e$	all horizontal nodal coordinates in finite element, Eq. (3.125), p. 84
$\mathbf{y}_e$	all vertical nodal coordinates in finite element, Eq. (3.125), p. 84



## GREEK SYMBOLS

$\alpha$	numerical parameter in power and exponential laws, Eq. (2.20), p. 21
$\alpha_p, \beta_p$	functions of internal friction angle, Eq. (2.36), p. 24
$\bar{\alpha}_p$	function of dilatancy angle, Eq. (2.43), p. 24
$\beta$	rate of stress decrease in power law, Eq. (2.20), p. 21
$\beta_N, \gamma_N$	parameters for Newmark method, Eq. (3.80), p. 68
$\gamma$	vectorial operator for stabilization, Eq. (3.125), p. 84
$\epsilon$	smearred crack normal strain or axial strain, Eq. (1.13), p. 9
$\tilde{\epsilon}$	equivalent strain measure, Eq. (2.8), p. 15
$\bar{\epsilon}$	averaged (non-local) strain measure, Eq. (3.1), p. 57
$\epsilon_0$	homogeneous strain, Eq. (1.11), p. 6
$\epsilon^e$	elastic part of strain, p. 98
$\bar{\epsilon}^d$	averaged damage strain measure, Eq. (3.11), p. 60
$\tilde{\epsilon}_{dev}$	equivalent deviatoric strain measure, Eq. (2.99), p. 40
$\bar{\epsilon}_{dev}$	averaged deviatoric strain measure, Eq. (3.60), p. 66
$\epsilon^P$	plastic strain measure, p. 101
$\epsilon$	strain tensor in vector form, Eq. (1.3), p. 5
$\bar{\epsilon}$	averaged strain tensor in vector form, Eq. (3.15), p. 61
$\hat{\epsilon}$	effective strain tensor in vector form, Eq. (2.3), p. 13
$\epsilon^d$	damage strain tensor in vector form, Eq. (3.10), p. 60
$\epsilon_{dev}$	deviatoric strain tensor, Eq. (2.90), p. 33
$\epsilon^e$	elastic strain tensor, Eq. (2.5), p. 15
$\epsilon^{e+}$	tensile part of elastic strain tensor, Eq. (2.52), p. 26
$\epsilon^{e'}$	principal elastic strains, Eq. (2.58), p. 27
$\epsilon^{e+'}$	tensile principal elastic strains, Eq. (2.59), p. 28
$\epsilon^P$	plastic strain tensor, Eq. (2.23), p. 22
$\eta$	material ductility in exponential law, Eq. (2.21), p. 21
$\eta_G$	deviatoric ductility for exponential law, p. 35
$\eta_K$	volumetric ductility for exponential law, p. 35
$\theta$	dilatation, Eq. (2.90), p. 33
$\tilde{\theta}$	equivalent dilatation measure, Eq. (2.98), p. 40
$\bar{\theta}$	averaged dilatation measure, Eq. (3.59), p. 66
$\kappa^d$	damage history parameter, Eq. (2.8), p. 13
$\bar{\kappa}^d$	averaged damage history parameter, Eq. (3.8), p. 60
$\kappa_G^d$	deviatoric damage history parameter, Eq. (2.99), p. 33
$\kappa_K^d$	volumetric damage history parameter, Eq. (2.98), p. 33
$\kappa_o$	initial damage threshold, Eq. (2.9), p. 15
$\kappa^P$	plastic history parameter, Eq. (2.28), p. 22
$\bar{\kappa}^P$	averaged plastic history parameter, Eq. (3.13), p. 60

$\kappa_u$	ultimate parameter for total damage, Eq. (2.19), p. 20
$\kappa_u^G$	ultimate parameter for total deviatoric damage, p. 35
$\kappa_u^K$	ultimate parameter for total volumetric damage, p. 35
$\lambda$	plastic multiplier, Eq. (2.26), p. 22
$\boldsymbol{\mu}$	unit vector connected with direction of jump, Eq. (1.6), p. 5
$\nu$	Poisson's ratio, Eq. (2.15), p. 18
$\nu_\omega$	Poisson's ratio function depending on stiffness degradation, Eq. (2.97), p. 38
$\boldsymbol{\xi}$	deviatoric stress tensor, Eq. (2.91), p. 33
$\rho$	material density, Eq. (1.9), p. 6
$\sigma$	crack normal traction or axial stress, Eq. (1.13), p. 9
$\tilde{\sigma}$	equivalent stress function, Eq. (2.28), p. 22
$\sigma_y$	yield strength, Eq. (2.28), p. 22
$\boldsymbol{\sigma}$	stress tensor in vector form, Eq. (1.3), p. 5
$\hat{\boldsymbol{\sigma}}$	effective stress tensor, Eq. (2.5), p. 13
$\boldsymbol{\sigma}^d$	damage stress tensor, Eq. (2.6), p. 15
$\hat{\boldsymbol{\sigma}}^+$	tensile part of effective stress tensor, Eq. (2.79), p. 30
$\boldsymbol{\sigma}^{d+}$	tensile part of damage stress tensor, Eq. (2.53), p. 27
$\boldsymbol{\tau}$	third-order tensor connected with averaged strain gradients, Eq. (3.15), p. 61
$\boldsymbol{v}$	unit vector normal to discontinuity surface, Eq. (1.6), p. 5
$\varphi$	internal friction angle, Eq. (2.41), p. 24
$\chi$	stabilization scaling factor, Eq. (3.101), p. 81
$\boldsymbol{\chi}_i$	stabilization scaling matrix, $i = 1, 2$ , Eq. (3.101), p. 81
$\psi$	dilatancy angle, Eq. (2.44), p. 24
$\omega$	scalar damage measure, Eq. (2.4), p. 13
$\bar{\omega}$	averaged scalar damage measure, Eq. (3.9), p. 60
$\omega_G$	deviatoric damage measure, Eq. (2.86), p. 33
$\omega_K$	volumetric damage measure, Eq. (2.86), p. 33
$\omega_{\vec{n}}$	damage measure normal to direction $\vec{n}$ , Eq. (1.2), p. 1
$\Theta$	angle between original and principal axes (2D), Eq. (2.62), p. 28
$\Theta_\epsilon$	angle between original and principal strain axes (2D), p. 50
$\Theta_\sigma$	angle between original and principal stress axes (2D), p. 50
$\boldsymbol{\Pi}$	auxiliary Kronecker's vector, Eq. (2.86), p. 33

## ABBREVIATIONS

1D	one dimension, p. 71
2D	two dimensions, p. 5
3D	three dimensions, p. 12
BDP	Burzyński-Drucker-Prager, p. 23
CDM	continuum damage mechanics, p. 2
EER	elastic energy release, p. 15
FE	finite element, p. 8
GLS	Galerkin least-square, p. 81
GGLS	gradient Galerkin least-square, p. 83
FI	full integration, p. 73
FEM	finite element method, p. 26
HMH	Huber-Mises-Hencky, p. 24
IBVP	initial boundary value problem, p. 6
RC	reinforced concrete, p. 12
RI	reduced integration, p. 73
XFEM	extended finite element method, p. 8
dofs	degrees of freedom, p. 68
ips	integration points, p. 71
lin	linear interpolation, p. 71
quad	quadratic interpolation, p. 71
s. eigs	signs of eigenvalues, p. 73



# CONTENTS

<b>1</b>	<b>Introduction</b>	<b>1</b>
1.1	Basis of damage theory . . . . .	1
1.2	Numerical modelling of (reinforced) concrete . . . . .	3
1.2.1	Concrete – quasi-brittle material . . . . .	3
1.2.2	Localization problem – fundamentals . . . . .	4
1.2.3	Review of numerical models . . . . .	7
1.3	Aim and scope . . . . .	11
<b>2</b>	<b>Damage coupled to plasticity</b>	<b>13</b>
2.1	Scalar model . . . . .	13
2.2	Coupling with plasticity . . . . .	22
2.3	Crack closing . . . . .	26
2.4	Isotropic model . . . . .	32
2.4.1	One strain measure . . . . .	33
2.4.2	Two strain measures . . . . .	39
2.5	Willam’s test . . . . .	41
2.5.1	Results for scalar damage . . . . .	43
2.5.2	Results for coupled model . . . . .	46
2.5.3	Results for isotropic damage . . . . .	50
<b>3</b>	<b>Finite elements for gradient damage</b>	<b>57</b>
3.1	Proposals of gradient enhancement for damage . . . . .	57
3.2	Gradient damage with one or two parameters . . . . .	61
3.2.1	Gradient scalar damage with plasticity – dynamics . . . . .	61
3.2.2	Gradient isotropic damage – dynamics . . . . .	66
3.3	Implementation of two-field finite elements . . . . .	67
3.4	Properties of elements and hourglass control . . . . .	72
3.4.1	Four-noded element – spectral analysis . . . . .	73
3.4.2	Stabilized four-noded element . . . . .	80
3.4.3	Other elements – spectral analysis . . . . .	90

<b>4</b>	<b>Testing of finite elements</b>	<b>93</b>
4.1	Bar with imperfection under static tension . . . . .	93
4.1.1	1D simulations . . . . .	94
4.1.2	2D and 3D simulations . . . . .	101
4.2	Two tests for dynamics . . . . .	109
4.2.1	Bar under impact loading . . . . .	109
4.2.2	Dynamic direct tension test . . . . .	111
<b>5</b>	<b>Numerical model applications</b>	<b>115</b>
5.1	Cantilever beam under load reversals . . . . .	115
5.2	Brazilian split test . . . . .	120
5.2.1	Application of scalar damage . . . . .	120
5.2.2	Confrontation with isotropic damage . . . . .	128
5.3	Four-point bending . . . . .	132
5.3.1	Statics – plain concrete . . . . .	133
5.3.2	Statics – reinforced concrete . . . . .	136
5.3.3	Dynamics – reinforced concrete, impact loading . . . . .	139
5.4	Dowel action in 3D . . . . .	141
5.5	RC slab-column connection . . . . .	149
5.5.1	Punching shear in RC slabs – problem description and experiment [1] .	149
5.5.2	Simulation – simplifications and data . . . . .	151
5.5.3	Numerical results and discussion . . . . .	153
<b>6</b>	<b>Conclusions</b>	<b>165</b>
<b>A</b>	<b>Local damage</b>	<b>169</b>
<b>B</b>	<b>Properties of four-noded element – supplement</b>	<b>173</b>
<b>C</b>	<b>Dowel disc test</b>	<b>179</b>
	<b>List of figures</b>	<b>183</b>
	<b>List of tables</b>	<b>189</b>
	<b>Bibliography</b>	<b>191</b>
	<b>Summary</b>	<b>205</b>
	<b>Streszczenie</b>	<b>207</b>

# CHAPTER 1

## INTRODUCTION

### 1.1 BASIS OF DAMAGE THEORY

All materials undergo from partial degradation to total failure. Of course this permanent process is observed also in civil engineering. Different undesirable effects which appear for example in structures originate from defects which can be noticed only at the micro- or even nanoscale. However, larger defects can also be measured at higher levels and during the whole existence of a given structure or its part. The reasonable level of observation firstly depends on the kind of material, associated phenomena, intensity of loading which acts on the structure and hence determines the degree of degradation.

The simplest, but universal representation seems to be the definition of damage firstly introduced by Kachanov [76], but an application to creep of metals under uniaxial load was only performed then. Although this damage concept was proposed for isotropic continuum with one scalar parameter, it can be generalized introducing anisotropy.

A certain domain  $\mathcal{B}$ , occupied by a material body, is considered at time instant  $t$ , see Fig. 1.1. An arbitrary section with normal direction  $\vec{n}$  can be virtually made, dividing this domain into two parts. On this section infinitesimal area  $dS_{\vec{n}}$  is chosen. It consists of damaged part  $dS_{\vec{n}}^d$  and undamaged part  $dS_{\vec{n}}^u$  according to the relation:

$$dS_{\vec{n}} = dS_{\vec{n}}^d + dS_{\vec{n}}^u \quad (1.1)$$

The damaged area includes defects such as cavities, microcracks, voids, etc. The undamaged area constitutes its intact part. The damage in the plane normal to direction  $\vec{n}$  is defined at time  $t$  as:

$$\omega_{\vec{n}} = \frac{dS_{\vec{n}} - dS_{\vec{n}}^u}{dS_{\vec{n}}} = \frac{dS_{\vec{n}}^d}{dS_{\vec{n}}} \quad (1.2)$$

The above definition complies with the interpretation that for a material without any defect (the lack of damage) the parameter  $\omega_{\vec{n}}$  equals 0. For a material with a complete loss of stiffness in direction  $\vec{n}$  (total damage) we obtain  $\omega_{\vec{n}} = 1$ .

If damage directions are distinguished then one scalar parameter is insufficient and an anisotropic model should be adopted. In that case the damage phenomenon should be described using vectors or tensors. For example if the degradation of composites like layered

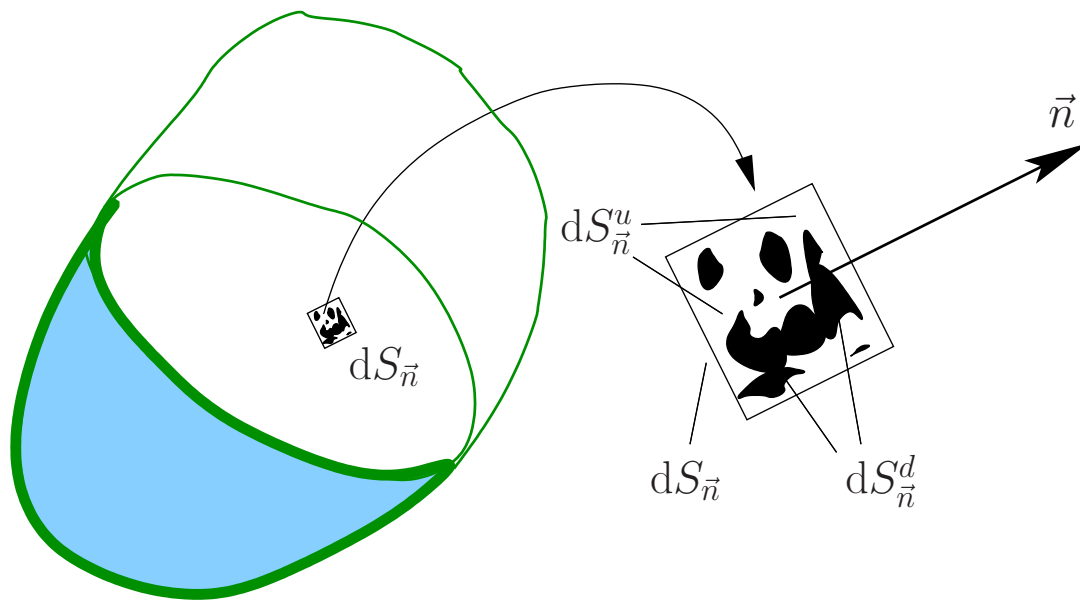


Figure 1.1: Concept of damage.

laminates is modelled then tensors are necessary in mathematical description. In the literature damage vectors [31, 81], second-order damage tensors [14, 95, 109, 164] and fourth-order damage tensors [22, 80, 92] have been introduced and as consequence commonly applied. The theory which bases on the approach presented in Eq. 1.2 is called the continuum damage mechanics CDM [76, 91, 92, 145].

A family of different CDM models can be used for purely mechanical or coupled problems. Among many mechanical features which materials reveals during damage evolution first of all brittle [60, 81] or ductile [44, 91] character of damage can be distinguished. Brittle failure is rather met within composites, while ductile failure - in metals and polymers. The boundary conditions and type of loading also influence the description of the damage phenomenon. Historically creep damage [76, 134, 161] is the oldest where the nucleation and growth of microvoids and microcracks in metal grains was modelled as a permanent effect in time. Another frequently mentioned mechanism is called fatigue damage [90, 92]. This is understood as the degradation of a material under repeated cyclic loading. An interaction between both the observed phenomena is also possible [25]. The problem of creep and/or fatigue damage is quite often formulated if the failure process in metals is described. The details of various mechanical models can be found for example in [92] in Chapter 7. Moreover a wide review of the literature connected with CDM is given for instance in [15, 149].

In coupled problems usually two types of effects are added, namely thermal or chemical. Thermo-mechanical damage is often considered with reference to different materials, see for example [52, 123]. On the other hand, chemical deterioration is usually taken into account for concrete [82, 139].



## 1.2 NUMERICAL MODELLING OF (REINFORCED) CONCRETE

### 1.2.1 CONCRETE – QUASI-BRITTLE MATERIAL

A general classification of materials (cf. for example [69, 168]) which focuses on the progress of degradation inside their structure is similar to the one mentioned in the previous section. The first group is composed of strongly brittle materials like glass, where fracture mechanics with sudden emergence of distinct discontinuities in the domain is adequate. On the other hand ductile materials like some polymers and metals are described using different continuous approaches, for example the plasticity theory. Between brittle and ductile materials there is also place for so-called quasi-brittle materials. There are among others: rocks, polymers and concrete.

In quasi-brittle materials, after the initial state of microdamage, two stages of failure are observed. Firstly, just after the peak load, strains localize in one or several thin zones starting from certain point(s) of the medium. The onset of localization is connected with the origin of rupture [136]. The rest of the domain is subjected to unloading, stiffness degradation and softening of material are observed. At the point which softens increasing strain together with decreasing stress is regarded. This local response projects into the global response of the medium. Here

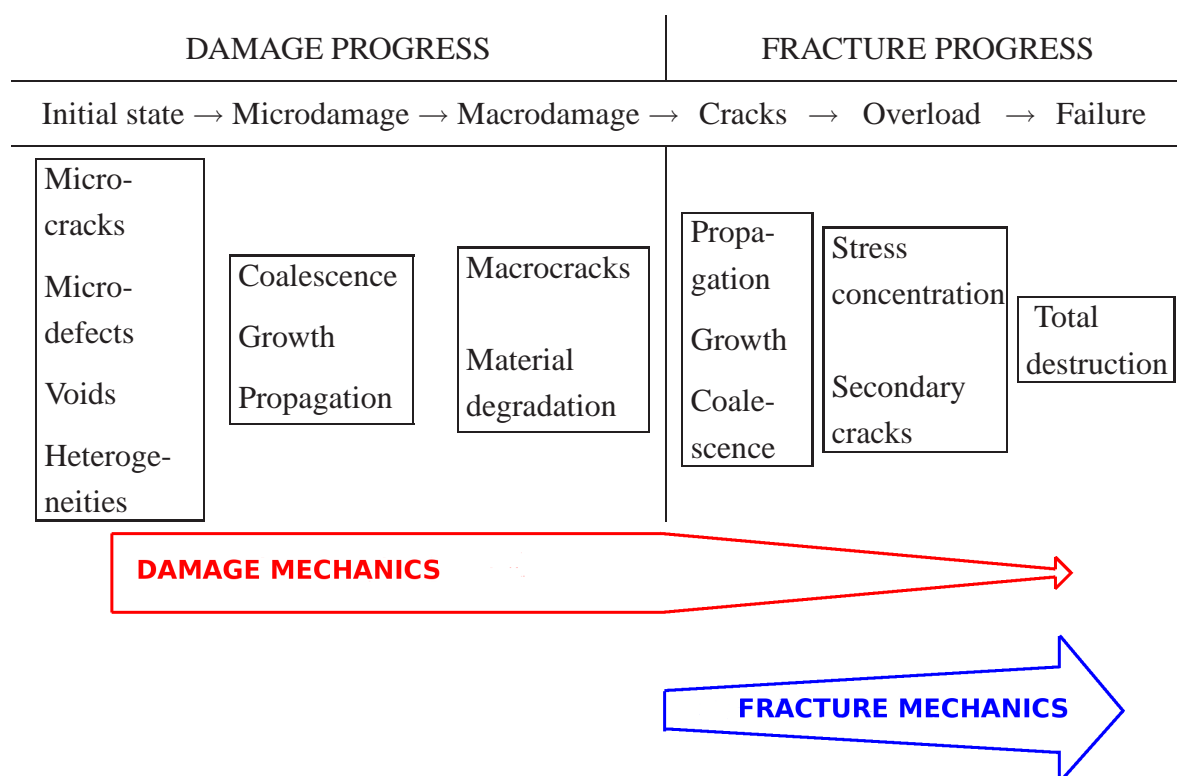


Figure 1.2: Degradation process in quasi-brittle materials. Based on [56].

a continuous description like CDM but with some additional procedures is enough. After that, at an advanced level of degradation process, there are noticeable displacement jumps in the zone of localization. From this moment the role of CDM diminishes in the whole description. Hence discontinuity should be considered, either in an explicit form like in [146, 168] or, simplifying, the continuous approach is still adopted, in which negligible residual stresses and a stiffness close to zero simulate fracture. The latter option is used in this work. The evolution of failure in quasi-brittle materials is depicted in Fig. 1.2.

Concrete is a heterogeneous material which includes aggregate and mortar. The description of its basic features with reference to experiments and different mechanical models can be found for example in [78, 156]. Concrete can be treated as a composite after the hardening process when the carrying capacity achieves a certain assumed (guaranteed) level. During hardening microcracks and microvoids are created due to shrinkage effects at the interface between aggregate and mortar. It should be underlined, that these defects exist before concrete is subjected to any load [135]. It is also possible that microcracks are enclosed within aggregate or mortar. Therefore the weakest link in the whole concrete matrix decides about its behaviour, independently of the kind of other defects. Considering the presence of these ingredients the theory of mixtures can be employed like for example in [115]. An alternative approach is a transition from the micro- and mesoscale to the macroscale, but including effects connected with the lower levels of observation. In quasi-brittle materials like concrete strain localization occurs as a consequence of softening, which is experimentally confirmed [66, 112, 165]. The onset of localization creates so-called weak discontinuity. Eventually, the description of emerging of explicit cracks (strong discontinuity) can be included as described in the previous paragraph.

The observed softening is not a real material property [135], but it is a result of inhomogeneous deformation due to the formation of a macroscopic crack. The growth and coalescence of microdefects lead to visible strain localization and finally to discrete cracking. Hence, the material softening should not be incorporated directly into stress-strain relations of local constitutive theories. Just after the first point in the structure reaches the state of softening, the local continuum theory is not valid. From the mathematical and numerical point of view it provides some complications.

## 1.2.2 LOCALIZATION PROBLEM – FUNDAMENTALS

Firstly, the mathematical rudiments of localization in the classical continuum are recollected, according to the presentation in [37, 116]. Strain localization may occur only if a given material suffers from a loss of stability at a certain level of deformation. Thus a material is called stable [65, 99] if its constitutive relationship satisfies the condition of positive second order work density:

$$\dot{\epsilon}^T \dot{\sigma} > 0 \quad (1.3)$$

In the above inequality  $\dot{\epsilon}$  denotes the strain rate tensor,  $\dot{\sigma}$  is the stress rate tensor (both in the vector form). If incrementally linear constitutive equations are taken into account the relation between stress and strain rates is:

$$\dot{\sigma} = \mathbf{E}^{\text{tan}} \dot{\epsilon} \quad (1.4)$$

with material tangent stiffness operator  $\mathbf{E}^{\text{tan}}$ , which can be treated as general, nonsymmetric and without any reference to the specific model. Substituting Eq. (1.4) into inequality (1.3) it is observed that material stability is held as long as the operator  $\mathbf{E}^{\text{tan}}$  is positive definite. The loss of material stability may occur in the deformation history prior to the limit point and loss of uniqueness related to a diffuse bifurcation, cf. [37]. Concluding, the loss of material stability opens the possibility of structural instability. Structural stability is assured for domain  $\mathcal{B}$  if:

$$\int_{\mathcal{B}} \dot{\epsilon}^T \dot{\sigma} dV > 0 \quad (1.5)$$

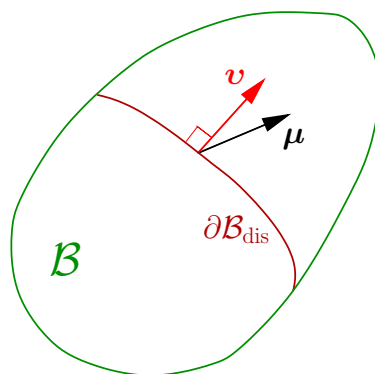


Figure 1.3: Discontinuity surface (curve in 2D). Definition of unit vectors  $\mathbf{v}$  and  $\boldsymbol{\mu}$ .

As a consequence, structural instability causes so-called weak discontinuity (see Fig. 1.3). The weak discontinuity in the structure of a material can appear upon a certain further increment of deformation. Strain jumps across the discontinuity surface (curve)  $\partial\mathcal{B}_{\text{dis}}$  are admitted, but the displacement field remains continuous. From the kinematic compatibility condition for strains and the requirement that tractions across the surface  $\partial\mathcal{B}_{\text{dis}}$  must be continuous (rate jump equals zero) the following relation in the indicial notation is obtained:

$$(v_i E_{ijkl}^{\text{tan}} v_l) \mu_k = 0 \quad (1.6)$$

where  $\mathbf{v}$  is the unit normal to surface  $\partial\mathcal{B}_{\text{dis}}$  and  $\boldsymbol{\mu}$  is the unit vector connected with the direction of the jump. The product within brackets is defined as the acoustic tensor  $\mathbf{A}$  [136, 141]. Here it is written as:

$$A_{jk} = v_i E_{ijkl}^{\text{tan}} v_l \quad (1.7)$$

Eq. (1.6) gives a non-trivial solution if and only if the determinant of the acoustic tensor vanishes:

$$\det \mathbf{A} = 0 \quad (1.8)$$

The singularity of the acoustic tensor  $\mathbf{A}$  implies ill-posedness of the initial boundary value problem. In statics the elliptic character of the boundary value problem changes into hyperbolic. Moreover, in dynamics the hyperbolic character of the initial boundary value problem (further called IBVP) changes into elliptic. The loss of ellipticity for static problems and the loss of hyperbolicity for dynamic problems coincides with the formation of the discontinuity and the onset of strain localization.

For an IBVP of the bar extending along one spatial direction  $x$  the set of governing equations at time  $t$  can be written using the partial differential equation in linearized version (see also [124, 127]):

$$E^{\text{tan}}(\epsilon) \frac{\partial^2 v}{\partial x^2} + \frac{\partial E^{\text{tan}}}{\partial x} \frac{\partial v}{\partial x} = \rho \frac{\partial^2 v}{\partial t^2} \quad (1.9)$$

where  $E^{\text{tan}}$  is the tangent stiffness,  $\epsilon$  is the axial strain,  $v(x, t)$  is the axial velocity and  $\rho$  is the density of the material. If a reference solution with homogeneous strain  $\epsilon_0$  is assumed, the second term on the left disappears. Then a single linear harmonic wave propagating in direction  $x$  along the bar constitutes the solution (cf. [150]):

$$v(x, t) = A e^{i k_w (x - c_w t)} \quad (1.10)$$

Here  $k_w$  denotes the number of wave lengths in the bar over  $2\pi$  and  $c_w$  is the velocity. This solution should satisfy the dispersion relation:

$$k_w^2 (\rho c_w^2 - E^{\text{tan}}(\epsilon_0)) = 0 \quad (1.11)$$

The above equation has the following non-trivial solution:

$$c_w = \sqrt{\frac{E^{\text{tan}}(\epsilon_0)}{\rho}} \quad (1.12)$$

If the tangent stiffness  $E^{\text{tan}}$  is positive the wave velocity  $c_w$  is real. In case of softening  $E^{\text{tan}} < 0$  and the wave velocity becomes imaginary for all wave numbers  $k_w$ . Thus the loading waves cannot propagate and a standing wave appears. Simplyfing, it results in strain localization in dynamics. More details, which concern also the dispersion analysis for different mechanical models, can be found in [56, 59, 117, 150].

The loss of well-posedness of IBVP admits to an infinite number of solutions. In the classical approach during softening the strongest deformation narrows into a discrete form (curve or surface). In finite-element solutions it is simply limited to a band of one-element width, so that the zone of localization is governed by the mesh of finite elements. Standard numerical constitutive models reveal spurious dependency of the results on the density of the mesh and also on the direction of mesh lines. The amount of material which softens is dictated by the numerics and not the physics of the given problem [135]. Thus the lack of objectivity in numerical modelling is noticed.

Mesh sensitivity can easily be shown by the example of a bar subjected to uniaxial tension and discretized with a given different number of elements (see for example [56, 116]). In the constitutive relation linear softening is usually employed. An imperfection is introduced in one element. After elastic loading the material softens and the strains localize in this element (other elements unload). It is clearly shown that the number of elements going to infinity introduces a Dirac delta distribution in the strain field. It means that the mesh refinement determines the solution. For damage this unacceptable fact is presented in Appendix A. When strain localization occurs incorporating an internal length as an additional parameter in the formulation overcomes the problem with spurious sensitivity of the results.

### 1.2.3 REVIEW OF NUMERICAL MODELS

This subsection is devoted to a brief review of computational modelling of cracking in quasi-brittle materials, especially in concrete. Numerical modelling concepts can be divided into discrete methods and methods for continuous media (also those admitting discontinuities).

Discrete methods consider a body composed of suitably small elementary ingredients, see for example [79, 144]. Each entity possesses material properties. The system can be made from lattices, beams, spheres, etc. There are mutually linked and they represent the material microstructure. The links can be cut and this way cracking is simulated.

The methods for continuum models can be distinguished similarly to the classification presented in Subsection 1.2.1. The existence of so-called smeared crack models as a separate group can also be emphasized. Here the total strain is divided into elastic part for the uncracked material and inelastic part related to traction transmitted across the crack (to learn details see [69]). Different variants of the smeared crack approach are analyzed in [140].

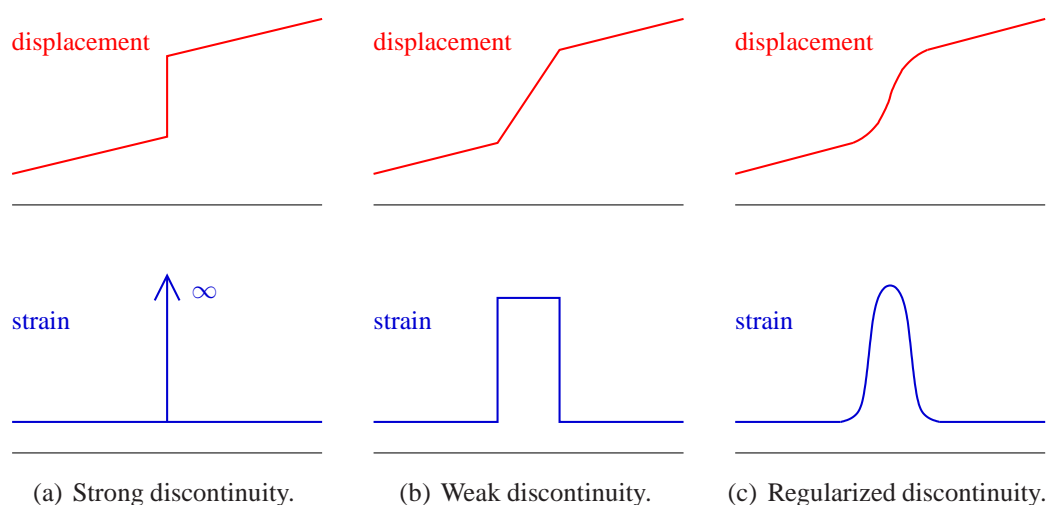


Figure 1.4: Discontinuity – displacement and strain distribution in one dimension.

However, the simplest model seems to be for linear elastic fracture mechanics, where discrete cracks appear suddenly after reaching a certain limit state. The behaviour of such strong discontinuity is shown for the displacement and strain fields in one dimension in Fig. 1.4(a). One of many approaches is to introduce special interface elements with zero thickness into the original finite element (FE) mesh. These elements are placed everywhere inside the mesh between two adjacent original elements. The simulation of cracking using interface elements was performed not only for concrete like in [140, 160], but also for composites [143, 160] or masonry structures [97]. The effect of delamination between material layers [64, 143] can also be simulated. Interface elements can be helpful in the numerical analysis of concrete if bond slip between the reinforcement and the concrete matrix [121, 140, 153] or fracture in concrete observed at the mesolevel [160] are taken into account. Another method is the application of so-called XFEM (extended finite element method) technique according to the theory in [6]. However, standard XFEM seems to be applicable rather to brittle materials like glass (sudden discrete crack) [107] or composites (delamination) [168].

The next group of continuum models contains various regularized methods, also called methods with localization limiters, cf. [12]. The weak discontinuity presented in Fig. 1.4(b) is obviously connected with strain localization. An internal length parameter should be included in the model to get localization, but in a smoothed version like in Fig. 1.4(c) (regularized discontinuity) and, as mentioned in the previous subsection, eventually to prevent spuriously mesh-sensitive results.

The earliest works [9, 128, 140], where mesh-dependence is partly overcome, accept the fact that localization is limited to a band of one-element width, but the size of finite element is related to a certain width  $w_f$  derived from the fracture energy  $G_f$ :

$$G_f = w_f \int \sigma d\epsilon \quad (1.13)$$

$G_f$  is defined as the amount of energy necessary to open a unit crack area. It is depicted in Fig. 1.5 that this energy can correspond to discrete cracking or to smeared cracking over width  $w_f$ . The parameter  $w_f$  is called the crack band width, because it is interpreted as the size of

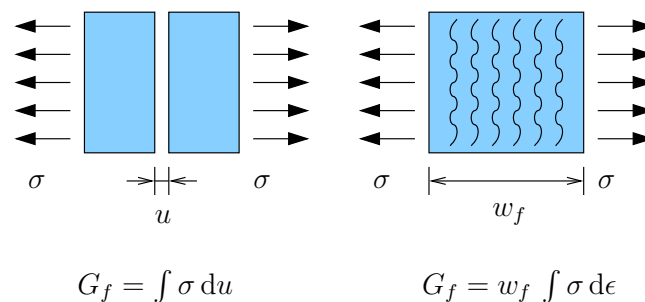


Figure 1.5: Fracture energy for discrete and smeared crack.

the region with smeared microcracks. The crack normal traction  $\sigma$  which depends on strain is under the integral. The integral determines the area under the softening curve in  $\sigma$ - $\epsilon$  diagram. Therefore, fitting the constitutive model to the element size ensures a proper dissipation of energy during the softening stage. Such models are classified as fracture energy-based models.

Regularization is also reached if an additional rate-dependent term like viscosity is enclosed in the constitutive equation. Many authors adopt different versions of rate-dependence to enhance the plasticity theory [59, 96, 110, 150, 172], but a coupled damage-viscoplasticity model [57] can also be applied. It is confirmed in [150] that these models give better effects in dynamics.

The family of higher-order models involves three types of regularization, namely: micropolar (Cosserat) models, non-local (integral) models and gradient-enhanced models.

Apart from standard translations microrotations are considered at a material point in micropolar models. Stress components are augmented with so-called couple-stresses. Couple-stresses are calculated from microcurvatures, whereby an internal length parameter is employed. In application to strain localization, not only in granular materials, the Cosserat continuum theory was presented for instance in [32, 108, 159]. As concluded in [150], a disadvantage of this model is the lack of mesh-objectivity when decohesion (tensile crack) dominates. Regularization is active while strain localization due to slip is analyzed.

Firstly higher-order theories were mentioned in [48, 101] in different contexts of physics (see [117] to read a description of the references). The Laplacian operator was used in order to prevent spurious mesh-sensitive numerical results almost at the same time for the plasticity theory [2] and for the so-called imbricate continuum concept [7]. The damage model is usually enhanced using integral (non-local) or gradient approach.

The framework of integral models, called also non-local, founds on the fact that a given stress component at a material point during the loading history depends on certain state variables at this point, but also at points in its surrounding region. In the numerical analysis this region is defined by means of a membership function with decreasing weights at larger distances from the considered point. Therefore in computations the values of selected state variable are smoothed. The non-local damage theory was proposed in [7, 10, 129]. Many researchers modified this approach, for example to split scalar damage into tensile and compressive actions (cf. [27]). Isotropic damage models with integral averaging are summarized and compared for instance in [68]. An anisotropic nonlocal damage model is derived in [86].

The stress-strain response for pure damage models gives a return to the origin during unloading (cf. Fig. 2.10 in Section 2.2). If an unloading path is considered in a cracking process a coupling of damage and plasticity theories seems to be necessary. During unloading irreversible strains are recovered in such coupled model. The coupling in integral approach is included among others in [17, 61]. Both works introduce a local plastic hardening law and non-locality in the damage function. In [61] a history parameter is non-local, while in [17] – an equivalent strain measure (definitions are present in Section 2.1). Due to the existence of an integral over

the defined region an additional loop over finite elements must be performed in implementation.

Gradient-enhancement regularizes the problem via a certain variable averaged by a gradient operator. That variable is incorporated in the formulation in such a manner that an extra averaging equation appears and additional degrees of freedom must be included in the discretization of finite element. This approach was firstly developed as gradient plasticity, cf. in a sequence [2, 12, 35, 37, 116]. Gradient enhancement in scalar damage was formulated in [125] and then evolved in [55, 124, 126]. Anisotropic gradient damage can be implemented like in [83, 84], but an averaging equation for each component (of strain tensor) demands a number of degrees of freedom in an element and makes computations time-consuming. Combination of gradient plasticity and scalar damage like in [155] or scalar gradient damage and hardening plasticity like in [36, 117] is possible and needs additional computations only at the (integration) point level. The advantages and disadvantages of scalar gradient damage also with coupling to plasticity are presented in this thesis. The use of gradient damage for geometrically non-linear problems [94, 154] is rather relevant for materials such as metals and polymers, not quasi-brittle like concrete.

The most sophisticated methods join continuous and discontinuous modelling. A viscoplastic medium together with discontinuities simulated by means of XFEM is included in [168]. Finite elements with a procedure for non-local damage and embedded displacement discontinuity are formulated and applied in [73]. Gradient damage combined with XFEM is firstly proposed in [146], where also its implementation and verification are shown. Currently a lot of works, published by many authors and not cited here, deals with continuous-discontinuous modelling for different applications.

A general classification of various approaches quoted in this review, in which cracking is modelled not only in quasi-brittle materials, is depicted in Fig. 1.6.

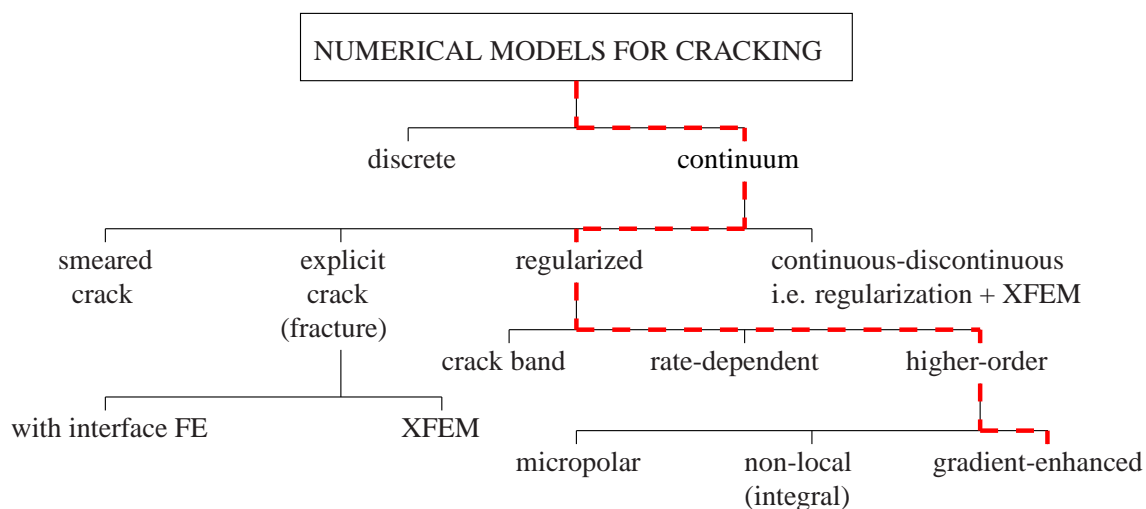


Figure 1.6: Classification of models mentioned in the review.



As mentioned previously correct modelling of concrete structures at the macrolevel requires regularization methods for appropriate simulations of cracking phenomenon in concrete. The interaction between reinforcement and the concrete matrix should be represented if reinforced concrete structures are analyzed. Actually, not only softening of concrete in constitutive equations is considered, not only bond slip between reinforcement bars placed in two orthogonal directions and the concrete matrix is modelled, but also cracking due to dowel action of the reinforcement like in [114] can be reproduced. In this thesis bond slip is omitted as in practical computations, knowing that this aspect of modelling was widely discussed in [117, 121].

### 1.3 AIM AND SCOPE

The thesis of this dissertation is following: if the stress state in plain and reinforced concrete structures is dominated by tension or bending then scalar gradient damage coupled to hardening plasticity gives a possibility to simulate cracking, strain localization and loss of carrying capacity correctly.

The aim is to enhance and verify the scalar gradient damage model for different kinds of cracking simulations. The model is developed for three-dimensional problems. The formulation includes dynamics. The implementation of effective finite elements is tested. This allows one to expand the range of applications of this model in plain and reinforced concrete mechanics.

The main simplifying assumptions and limitations are as follows:

- continuum damage mechanics (CDM) is employed to simulate cracking,
- concrete is treated as a homogeneous material,
- reological effects are omitted,
- linear kinematic relations are satisfied,
- the reinforcement is modelled as elasto-plastic truss elements,
- full bond between the concrete matrix and the reinforcement is assumed.

Chapter 2 deals with the damage model at the level point. Attention is focused on its isotropic version with one or two damage parameters. For the scalar theory (with one parameter) a coupling with the plastic flow theory and crack closing options are included. Isotropic damage is split into volumetric and deviatoric parts. The Willam's test for this model with different components is performed.

The formulation and implementation of the IBVP are discussed in Chapter 3. The gradient enhancement is introduced into the damage model. The algorithm for dynamics without damping is presented. The properties of two-field finite elements for two- and three-dimensional (2D and 3D) problems based on eigenvalue analysis are reported. The possibility of their implementation including hourglass control are explained using the example of four-noded quadrilateral element.

The tests for statics and dynamics are put together in Chapter 4. At the beginning the simplest benchmark, namely a bar with imperfection, is examined. All tests (for example two-dimensional configuration under dynamic direct tension) are analyzed for various parameters to emphasize possibilities of gradient damage model.

The numerical applications given in Chapter 5 are divided into two parts. Firstly two-dimensional problems are computed, in turn: cantilever beam under load reversals, Brazilian split test, four-point bending test for statics and dynamics. Next the cracking phenomenon in three dimensions is simulated. Dowel action in an RC structure and the punching shear in an RC slab-column connection are analyzed. Different components and parameters of the model are employed for its better verification.

Chapter 6 summarizes conclusions and remarks. Further possibilities of the research are also included.

## CHAPTER 2

# DAMAGE COUPLED TO PLASTICITY

### 2.1 SCALAR MODEL

The simplest model of the continuum damage mechanics (CDM) which can describe elastic stiffness degradation in quasi-brittle materials is scalar damage. It means that one damage measure  $\omega$ , which grows monotonically from 0 to 1 [76, 113], is a function of the damage history parameter  $\kappa^d$  and depends on the deformation state in a body.

The system of equations for dynamics (no damping effects) at the material point level consists of: the motion equations, the kinematic equations and the nonlinear constitutive relation.

The equations of motion are written as:

$$\mathbf{L}^T \boldsymbol{\sigma} + \mathbf{b} = \rho \ddot{\mathbf{u}} \quad (2.1)$$

where  $\mathbf{L}$  is a matrix of differential operators,  $\boldsymbol{\sigma}$  is the stress tensor in a vector form,  $\mathbf{b}$  is the body force vector,  $\rho \ddot{\mathbf{u}}$  contains inertia forces with the density  $\rho$  and the acceleration vector  $\ddot{\mathbf{u}}$ . It is also possible to include the inertia forces in  $\mathbf{b}$ , like in [157]. The acceleration vector is calculated from the displacements  $\mathbf{u}$  by double differentiation with respect to time  $t$ . Further the time  $t$  will occur in notation if it is necessary or in the case of special emphasis.

The kinematic equations permit one to obtain strain tensor  $\boldsymbol{\epsilon}$  (similarly in a vector form):

$$\boldsymbol{\epsilon} = \mathbf{L}\mathbf{u} \quad (2.2)$$

Small strains are assumed, i.e. a geometrically linear problem is considered.

During the damage evolution we distinguish fictitious undamaged counterparts of stresses  $\hat{\boldsymbol{\sigma}}$  and strains  $\hat{\boldsymbol{\epsilon}}$ , which are called effective. The strain equivalence has been postulated in [90] (cf. also [145]):

*"the strain associated with a damaged state under the applied stress is equivalent to the strain associated with its undamaged state under the effective stress"*

and hence the following relation is expressed:

$$\boldsymbol{\epsilon} = \hat{\boldsymbol{\epsilon}} \quad (2.3)$$

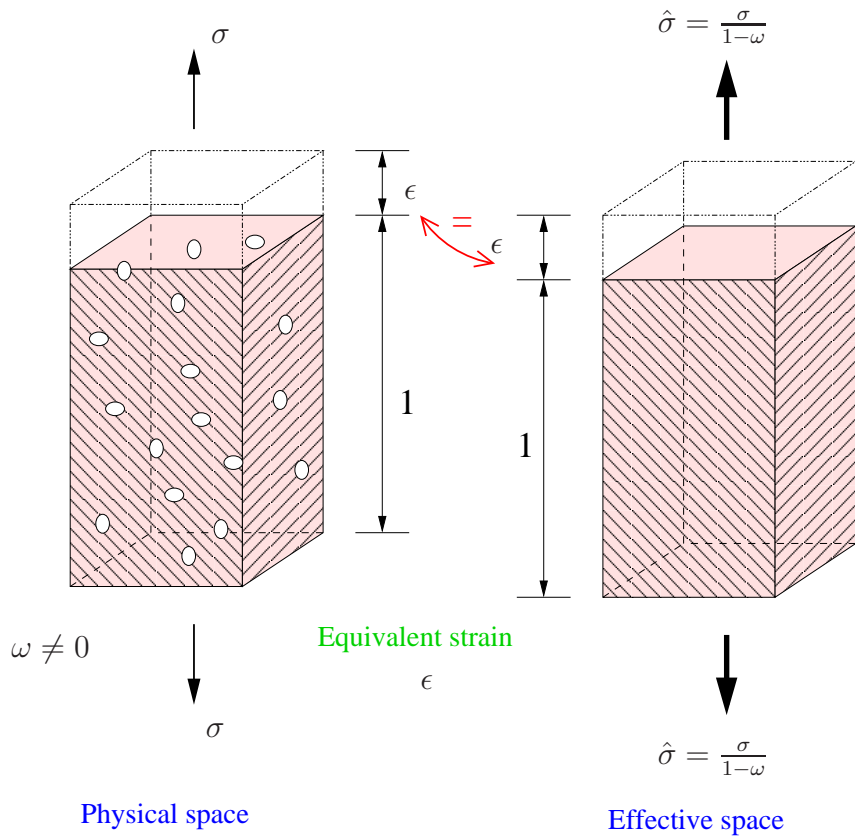


Figure 2.1: Idea of strain equivalence.

The idea is illustrated in Fig. 2.1. The fictitious counterpart represents the undamaged skeleton of the body and the effective stresses  $\hat{\sigma}$  act on it. Indeed, the real stress tensor  $\sigma$  and its effective counterpart  $\hat{\sigma}$  are related by the mentioned above parameter  $\omega$ :

$$\sigma = (1 - \omega) \hat{\sigma} \tag{2.4}$$

where:

$$\hat{\sigma} = E \epsilon^e \tag{2.5}$$

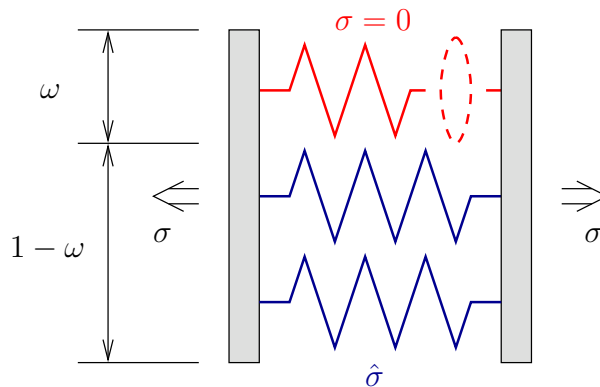


Figure 2.2: Scheme of scalar damage model.

Here  $\mathbf{E}$  is the elastic stiffness operator. The elastic strain tensor  $\boldsymbol{\epsilon}^e$  is equal to the strain tensor  $\boldsymbol{\epsilon}$  when the standard elasto-damage model is considered. The so-called damage stress  $\boldsymbol{\sigma}^d$  which describes the change in the stress state due to damage can be defined:

$$\boldsymbol{\sigma}^d = \omega \mathbf{E} \boldsymbol{\epsilon}^e \quad (2.6)$$

so Eq. (2.4) can be also written as follows:

$$\boldsymbol{\sigma} = \hat{\boldsymbol{\sigma}} - \boldsymbol{\sigma}^d \quad (2.7)$$

This model in one dimension is also visualized in Fig. 2.2, where a single spring can be interpreted as a fibre or tie in the material. Instead of the strain equivalence hypothesis other concepts have been introduced, for example the postulate of elastic energy equivalence [30].

The strain equivalence is related with a loading function  $f^d$  called also a damage activation function defined in the strain space. This function limits the behaviour of the material during the damage process:

$$f^d(\boldsymbol{\epsilon}, \kappa^d) = \tilde{\epsilon}(\boldsymbol{\epsilon}(t)) - \kappa^d(t) = 0 \quad (2.8)$$

An equivalent strain measure  $\tilde{\epsilon}$  will be defined below in details. The parameter  $\kappa^d$  governs the damage evolution:

$$\kappa^d(t) = \max \left\{ \kappa_o, \max_{t_i \in [0, t]} [\tilde{\epsilon}(\boldsymbol{\epsilon}(t_i))] \right\} \quad (2.9)$$

Here  $\max [\tilde{\epsilon}(\boldsymbol{\epsilon}(t_i))]$  denotes the largest value of  $\tilde{\epsilon}$  reached in the loading history at instant  $t_i$ . The elastic state is observed until the initial threshold  $\kappa_o$  is reached by  $\kappa^d$ . The damage process is deactivated if  $f^d < 0$ . The activation of damage follows the loading/unloading conditions written in the Kuhn-Tucker form:

$$f^d \leq 0 \quad \dot{\kappa}^d \geq 0 \quad \dot{\kappa}^d f^d = 0 \quad (2.10)$$

The equivalent strain measure  $\tilde{\epsilon}$  can be described in different ways. In equivalent strain definitions below time  $t$  is omitted in notation. The normalized elastic energy release (EER) rate [74, 92]:

$$\tilde{\epsilon} = \sqrt{\frac{1}{E} \boldsymbol{\epsilon}^T \mathbf{E} \boldsymbol{\epsilon}} \quad (2.11)$$

can be employed for materials which behave in the same manner in tension and compression, for example for metals. Here  $E$  is Young's modulus. It is well-known that the compressive strength of concrete is about 10 times larger than its tensile strength, so this definition is not adequate. However, it will be applied for testing. The shapes of envelopes based on Eq. (2.11) for two- and three-dimensional problems are depicted in Fig. 2.3. Additionally principal directions (positive half-axes) are marked in Figs 2.3(b)–2.3(d) to distinguish the orientation of the surface.

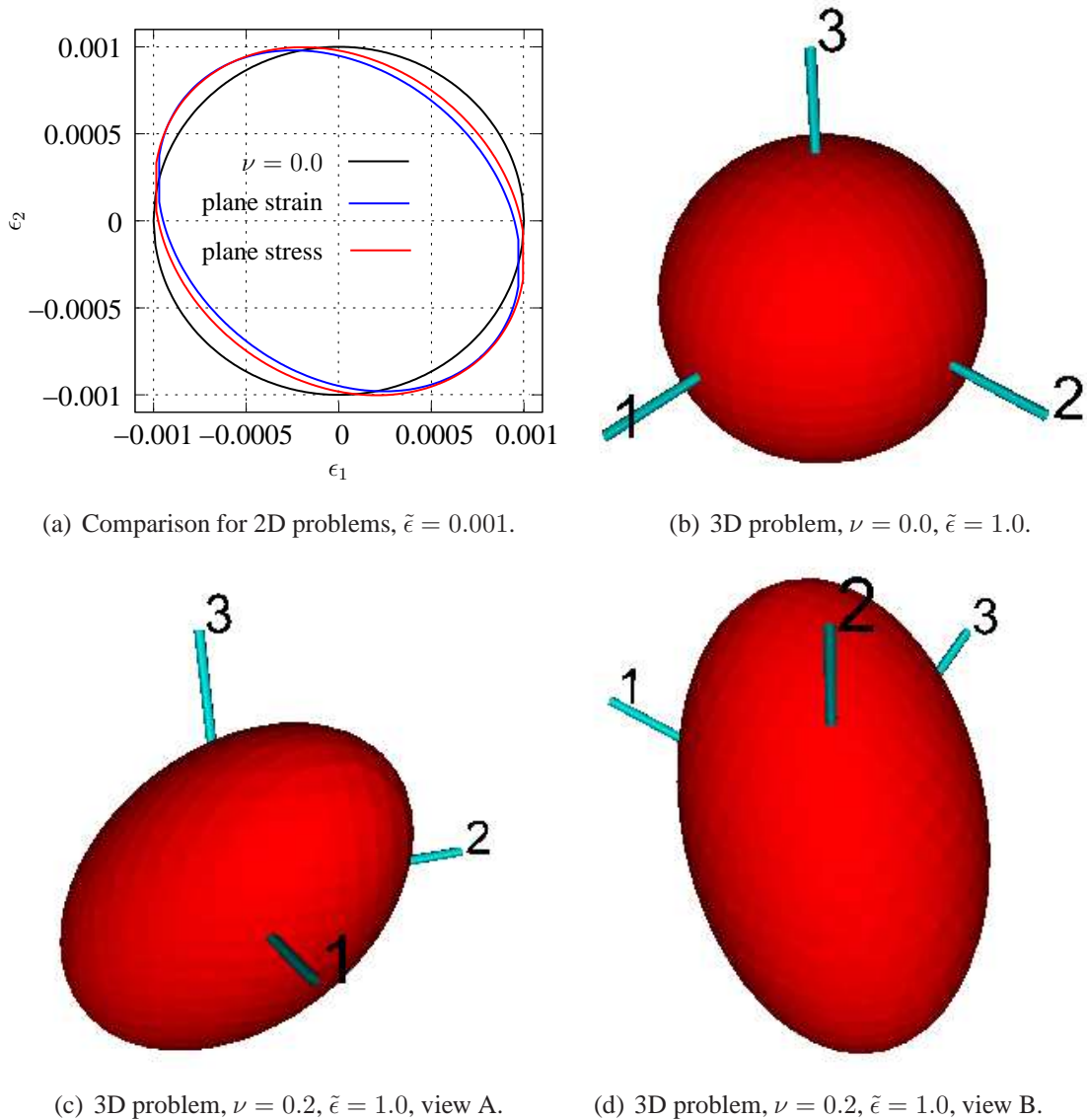
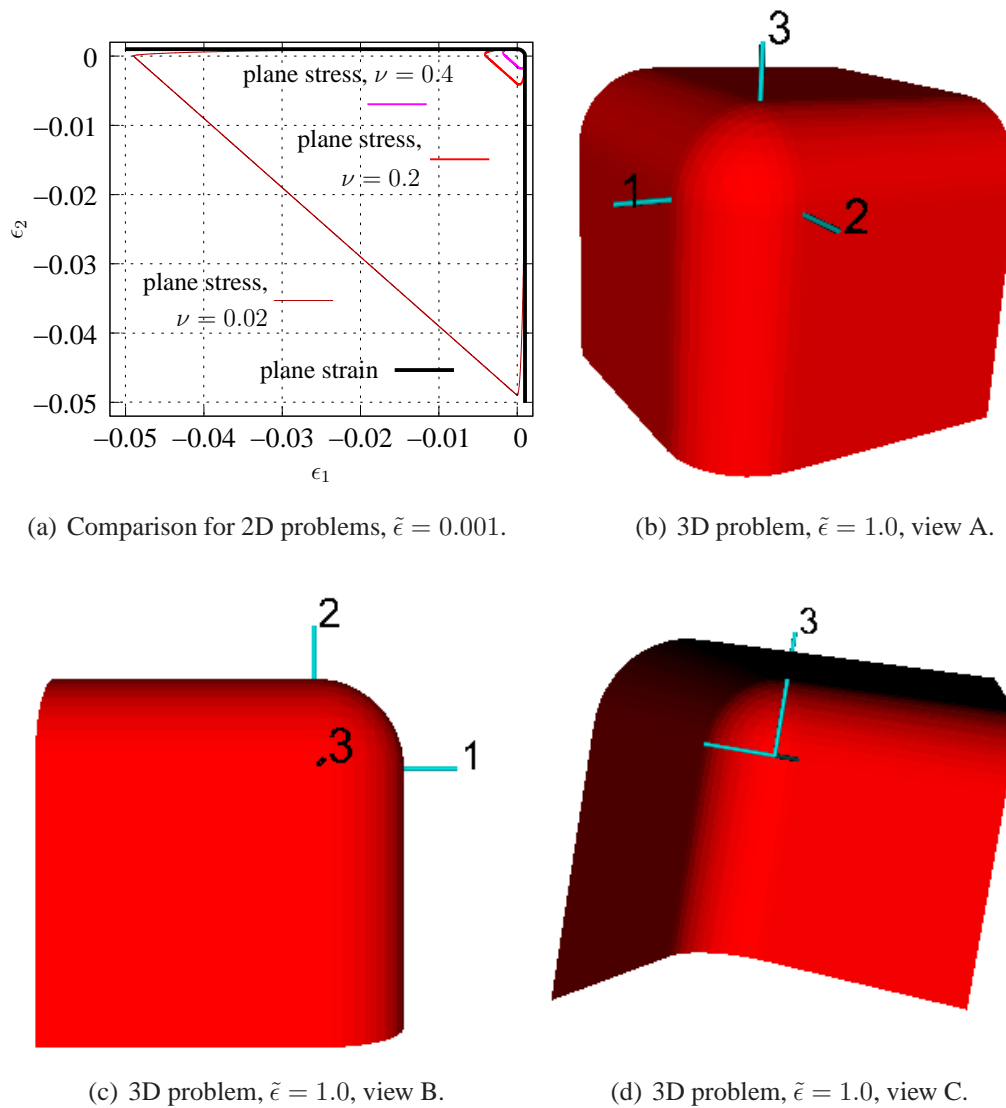


Figure 2.3: EER definition of  $\tilde{\epsilon}$  (2.11) in strain space.

An equivalent strain definition which exhibits different behaviour in tension and compression is the Mazars definition [102, 103]:

$$\tilde{\epsilon} = \sqrt{(H(\epsilon_1)\epsilon_1)^2 + (H(\epsilon_2)\epsilon_2)^2 + (H(\epsilon_3)\epsilon_3)^2} \quad (2.12)$$

The positive principal strains  $\epsilon_I$  ( $I = 1, 2, 3$ ) are chosen using the Heaviside function  $H(\cdot)$ . For this definition the stress conditions have influence on the character of the damage surface for this definition. Like previously this proposal is visualized in Fig. 2.4. For plane strain and three-dimensional problems there are no limits on the compressive side, so as a consequence there is no damage in biaxial compression. For plane stress the loading function depends on the Poisson's ratio like in Fig. 2.4(a). An analogical definition to the Mazars proposal but described

Figure 2.4: Mazars definition of  $\tilde{\epsilon}$  (2.12) in strain space.

in the space of effective stresses  $\hat{\sigma}$  is:

$$\tilde{\epsilon} = \frac{1}{E} \sqrt{(H(\hat{\sigma}_1)\hat{\sigma}_1)^2 + (H(\hat{\sigma}_2)\hat{\sigma}_2)^2 + (H(\hat{\sigma}_3)\hat{\sigma}_3)^2} \quad (2.13)$$

By means of the Heaviside function  $H(\cdot)$  only positive principal effective stresses  $\hat{\sigma}_I$  ( $I = 1, 2, 3$ ) are included. Like in (2.12) a smooth round-off in the tensile region is expected. This definition has been proposed in [71] and then applied also for example in [72]. The following proposal is similar to both the above and the Rankine criterion. The equivalent strain  $\tilde{\epsilon}$  is obtained as the scaled maximum principal effective stress [70]:

$$\tilde{\epsilon} = \frac{1}{E} \max_{I=1,2,3} (H(\hat{\sigma}_I)\hat{\sigma}_I) \quad (2.14)$$

The last definition is depicted and then exploited in computations in [17].

Finally the von Mises definition involving the first and second strain invariants [38] can be adopted:

$$\tilde{\epsilon} = \frac{k-1}{2k(1-2\nu)} I_1^\epsilon + \frac{1}{2k} \sqrt{\left(\frac{k-1}{1-2\nu} I_1^\epsilon\right)^2 + \frac{12k}{(1+\nu)^2} J_2^\epsilon} \quad (2.15)$$

which seems to be a reasonable choice for the description of quasi-brittle materials.  $I_1^\epsilon$  and  $J_2^\epsilon$  are strain invariants:

$$I_1^\epsilon = \epsilon_1 + \epsilon_2 + \epsilon_3 = \text{tr}(\epsilon) \quad (2.16)$$

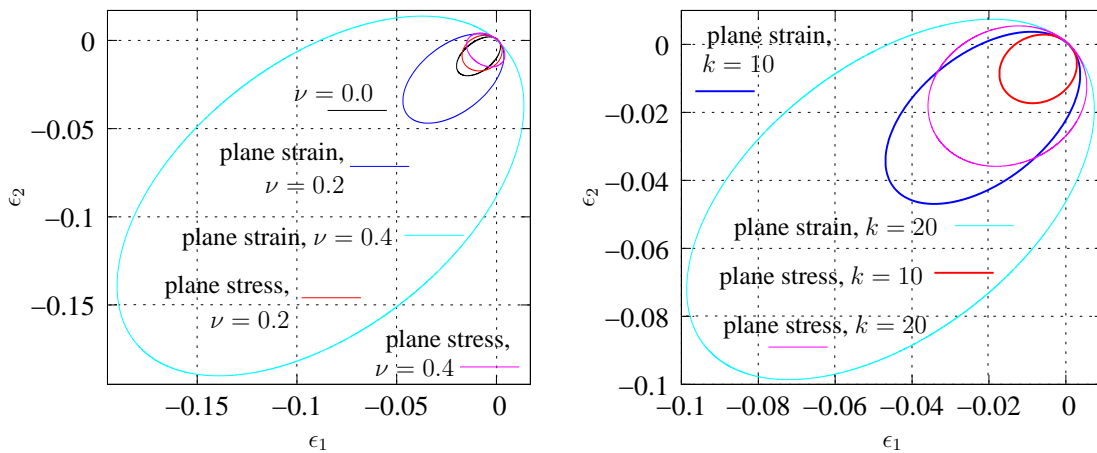
$$J_2^\epsilon = \frac{1}{3} (\epsilon_1^2 + \epsilon_2^2 + \epsilon_3^2 - (\epsilon_1\epsilon_2 + \epsilon_2\epsilon_3 + \epsilon_1\epsilon_3)) \quad (2.17)$$

The loading functions for plane strain and plane stress depending on Poisson's ratio  $\nu$  are put together in Fig. 2.5(a). The parameter  $k$  incorporates the influence of the ratio of compressive and tensile strength:

$$k = \frac{f_c}{f_t} \quad (2.18)$$

In this work the parameter  $k$  is usually set equal to 10 or 20. The size of envelopes for these values is verified in Fig. 2.5(b). Although this proposal looks promising for 2D problems it can be inappropriate for problems in three dimensions. Firstly, as is depicted in Fig. 2.6 the surface has no limits for three-axial compression. Secondly the shape of the surface near the shear region in the strain space  $\epsilon_2 = -\epsilon_1$  expands too widely. Nevertheless, the results for 3D examples (Chapter 5), especially where tension plays an important role, show that the function defined in Eq. (2.15) works quite well.

A comparative analysis respectively for:  $\nu = 0.0$  in Fig. 2.7(a), plane strain in Fig. 2.7(b) and plane stress in Fig. 2.7(c), corresponds to the equivalent strain definitions proposed in Eqs (2.11), (2.12) and (2.15). Similar comparisons for 2D problems can be found in [17].

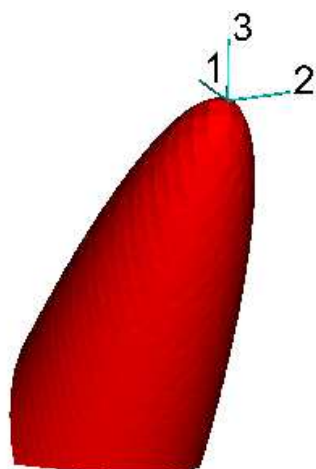


(a) Different Poisson's ratio,  $k = 10$ ,  $\tilde{\epsilon} = 0.001$ .

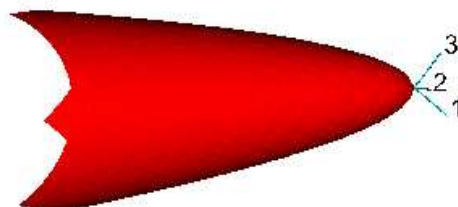
(b) Different parameter  $k$ ,  $\nu = 0.2$ ,  $\tilde{\epsilon} = 0.001$ .

Figure 2.5: Modified von Mises definition of  $\tilde{\epsilon}$  (2.15) in strain space, 2D problems.

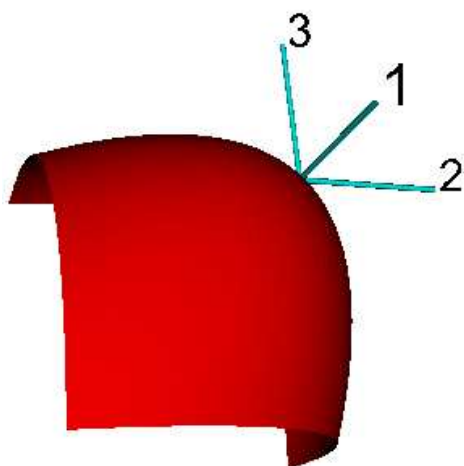




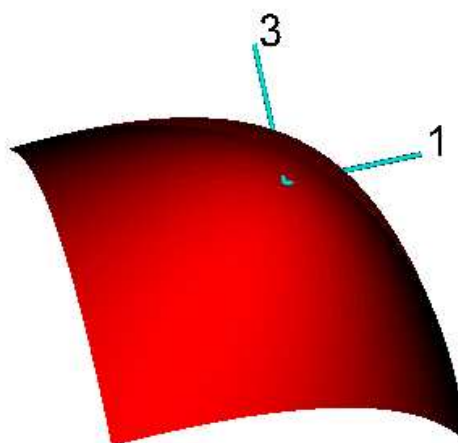
(a) View A.



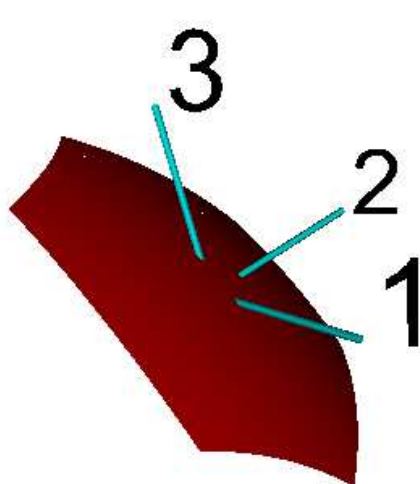
(b) View B.



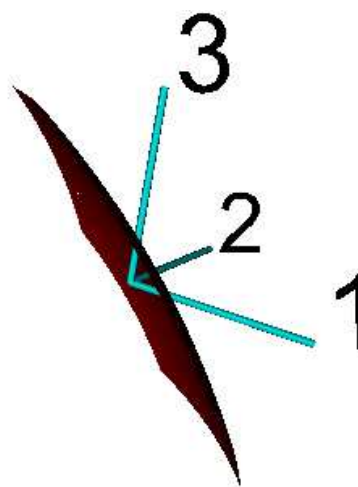
(c) View C, 10 times larger.



(d) View D, 10 times larger.



(e) View E, 100 times larger.



(f) View F, 100 times larger.

Figure 2.6: Modified von Mises definition (2.15) in strain space for 3D problems,  $\tilde{\epsilon} = 1.0$ .

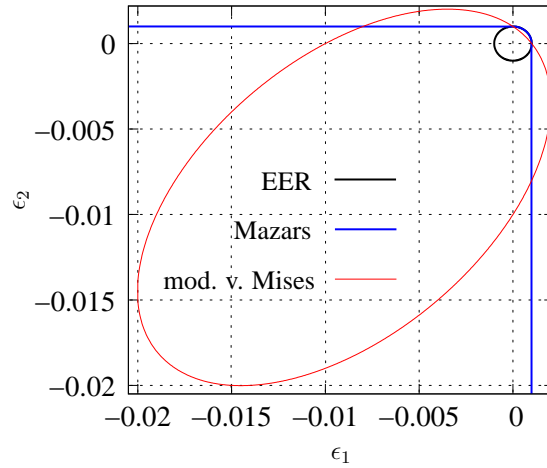
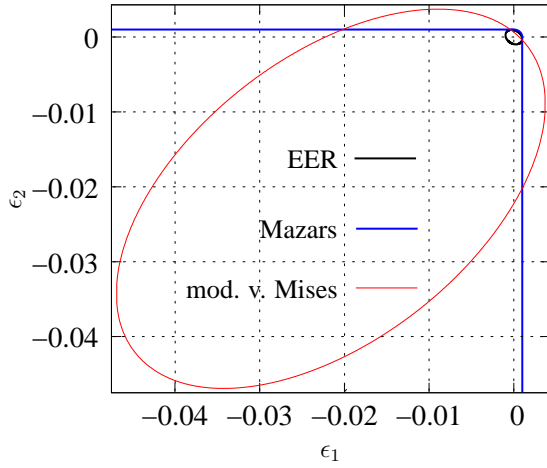
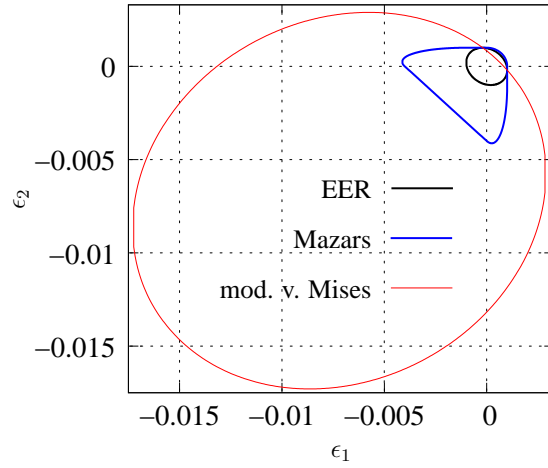
(a) Poisson's ratio  $\nu = 0.0$ ,  $k = 10$ ,  $\tilde{\epsilon} = 0.001$ .(b) Plane strain,  $\nu = 0.2$ ,  $k = 10$ ,  $\tilde{\epsilon} = 0.001$ .(c) Plane stress,  $\nu = 0.2$ ,  $k = 10$ ,  $\tilde{\epsilon} = 0.001$ .

Figure 2.7: Loading functions in 2D strain space.

As it was mentioned at the beginning of this chapter the damage measure  $\omega$  depends on the history parameter  $\kappa^d$ . During the damage evolution  $\kappa^d$  can grow in time in different ways. The laws, by means of which damage is controlled, can be divided into so-called short-range and exponential (see [55]).

In the first group  $\kappa^d$  exceeds from damage threshold  $\kappa_o$  and tends to ultimate value  $\kappa_u$  which corresponds to total damage. For instance, the common function  $\omega(\kappa^d)$  can represent a linear softening stress-strain diagram [125]:

$$\omega(\kappa^d) = \frac{\kappa_u}{\kappa^d(t)} \frac{\kappa^d(t) - \kappa_o}{\kappa_u - \kappa_o} \quad (2.19)$$

The above definition is frequently applied in primary numerical tests. The modified power law is a generalization of Eq. (2.19):

$$\omega(\kappa^d) = 1 - \left( \frac{\kappa_u}{\kappa^d(t)} \right)^\beta \left( \frac{\kappa_u - \kappa^d(t)}{\kappa_u - \kappa_o} \right)^\alpha \quad (2.20)$$

In this equation  $\beta$  and  $\alpha$  are model parameters. The rate of stress decrease depends on both  $\alpha$  and  $\beta$ , but additionally  $\beta$  (if it is less than 1) can change the value of the peak load. In particular, this relation has been used to simulate failure process in fibre reinforced polymers [55].

The second idea assumes that  $\kappa^d$  permanently grows from damage threshold  $\kappa_o$  to infinity so that damage  $\omega$  asymptotically increases but never reaches 1. Now we define the damage growth function according to [103, 126]:

$$\omega(\kappa^d) = 1 - \frac{\kappa_o}{\kappa^d(t)} \left( 1 - \alpha + \alpha e^{-\eta(\kappa^d(t) - \kappa_o)} \right) \quad (2.21)$$

The respective parameters  $\eta$  and  $\alpha$  are responsible for the rate of softening and residual stress which in one dimension tends to  $(1 - \alpha)E\kappa_o$ . The former one is thus connected with material ductility and related to concrete fracture energy  $G_f$ . The latter one prevents the complete loss of material stiffness and residual stresses remain if only  $\alpha < 1$ . As a consequence it leads to a more stable numerical response. The law in Eq. (2.21) is well-suited to reproduce the tensile fracture in concrete, since the experimental uniaxial softening relation is exponential [66]. Alternatively, an exponential relation characterized by three parameters  $n_1$ ,  $n_2$  and  $\eta$  can be used [55]:

$$\omega(\kappa^d) = 1 - \left( 1 - \frac{\kappa_o}{\kappa^d(t)} \right) \left( 0.01 \frac{\kappa_o}{\kappa^d(t)} \right)^{n_1} - \left( \frac{\kappa_o}{\kappa^d(t)} \right)^{n_2} e^{-\eta(\kappa^d(t) - \kappa_o)} \quad (2.22)$$

but Eq. (2.21) is more frequently employed in computations. Some authors also introduced definitions relevant for other materials, for example characterized by hyperbolic softening [129].

Next, one three-dimensional finite element with eight nodes is subjected to static tension in one direction in order to compare the chosen damage growth definitions. The following material data are introduced: Young's modulus  $E = 20000$  MPa, Poisson's ratio  $\nu = 0.20$  and damage threshold  $\kappa_o = 0.0001$ . For linear softening defined in Eq. (2.19) the ultimate value  $\kappa_u = 0.002$

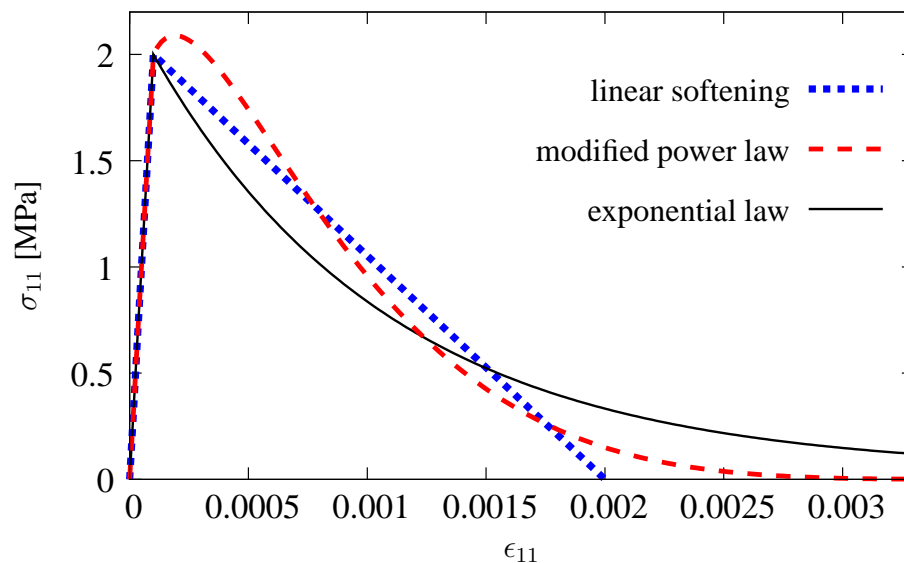


Figure 2.8: Damage growth functions.

is assumed. For Eq. (2.20) with the modified power law the parameters are  $\kappa_u = 0.004$ ,  $\alpha = 5.0$  and  $\beta = 0.75$ . Finally the exponential relation given in Eq. (2.21) with  $\alpha = 0.98$  and  $\eta = 1000$  is verified. The above values of parameters are selected in a such way that the fracture energy for calculated cases is almost equal. In Fig. 2.8 the  $\sigma$ - $\epsilon$  diagrams are presented.

## 2.2 COUPLING WITH PLASTICITY

The coupling of the damage model with plasticity is performed in order to incorporate the physically observed irreversible strains. The damage theory was formulated in the strain space, but the plasticity theory is formulated in the stress space [74, 145]. Both theories have a simple, isotropic format (intrinsic anisotropy is neglected). As before, in this section time  $t$  will be omitted in notation, despite the fact that a transient problem is considered. Hence the damage theory included in previous section is combined with the one described next (see also [36, 119]).

Assuming the standard additive decomposition of the strain tensor into elastic and plastic parts:

$$\boldsymbol{\epsilon} = \boldsymbol{\epsilon}^e + \boldsymbol{\epsilon}^p \quad (2.23)$$

the elastic strain rate can be derived as:

$$\dot{\boldsymbol{\epsilon}}^e = \dot{\boldsymbol{\epsilon}} - \dot{\boldsymbol{\epsilon}}^p \quad (2.24)$$

According to Eq. (2.5) the elastic strain rate is in a one-to-one functional relation with the effective stress rate:

$$\dot{\boldsymbol{\sigma}} = \mathbf{E} \dot{\boldsymbol{\epsilon}}^e \quad (2.25)$$

The plastic strain rate  $\dot{\boldsymbol{\epsilon}}^p$  according to the classical flow rule is governed by the plastic multiplier  $\lambda$ :

$$\dot{\boldsymbol{\epsilon}}^p = \dot{\lambda} \frac{\partial g^p}{\partial \hat{\boldsymbol{\sigma}}} \quad (2.26)$$

where  $g^p$  is a plastic potential. The above derivative is the plastic flow direction  $\mathbf{m}$ :

$$\mathbf{m} = \frac{\partial g^p}{\partial \hat{\boldsymbol{\sigma}}} \quad (2.27)$$

Now the yield condition in the effective stress space is defined:

$$f^p(\hat{\boldsymbol{\sigma}}, \kappa^p) = \tilde{\sigma}(\hat{\boldsymbol{\sigma}}) - \sigma_y(\kappa^p) = 0 \quad (2.28)$$

where  $\tilde{\sigma}$  is an equivalent stress function,  $\sigma_y$  is the yield strength,  $\kappa^p$  is a plastic history parameter. Isotropic hardening is assumed and the loading/unloading Kuhn-Tucker conditions are imposed:

$$f^p \leq 0 \quad \dot{\lambda} \geq 0 \quad \dot{\lambda} f^p = 0 \quad (2.29)$$

The plastic consistency condition  $\dot{f}^p = 0$  constitutes the following partial differential equation:

$$\frac{\partial f^p}{\partial \hat{\boldsymbol{\sigma}}} \dot{\hat{\boldsymbol{\sigma}}} + \frac{\partial f^p}{\partial \kappa^p} \dot{\kappa}^p = 0 \quad (2.30)$$

Next we introduce the definitions of the gradient tensor  $\mathbf{n}$  normal to the yield function:

$$\mathbf{n} = \frac{\partial f^p}{\partial \hat{\boldsymbol{\sigma}}} = \frac{\partial \tilde{\sigma}}{\partial \hat{\boldsymbol{\sigma}}} \quad (2.31)$$

and of the hardening/softening modulus  $h$ :

$$h = -\frac{\dot{\kappa}^p}{\dot{\lambda}} \frac{\partial f^p}{\partial \kappa^p} = -\frac{\dot{\kappa}^p}{\dot{\lambda}} \frac{\partial \sigma_y}{\partial \kappa^p} \quad (2.32)$$

In this theory during the loading history the identity  $\kappa^p = \lambda$  is assumed, but in general inequality of both the variables can be allowed. If  $f^p = g^p$ , then associated plasticity is obtained, however non-associated plastic flow is admitted. From the plastic consistency condition (2.30) the rate of the plastic multiplier  $\dot{\lambda}$  is calculated as:

$$\dot{\lambda} = \frac{1}{h} \mathbf{n}^T \dot{\hat{\boldsymbol{\sigma}}} \quad (2.33)$$

Using relations (2.33), (2.26), (2.27) and Eq. (2.24), the elastic strain rate can be substituted into Eq. (2.25). The Sherman-Morrison formula leads to the tangential relation between the strain and effective stress rates:

$$\dot{\hat{\boldsymbol{\sigma}}} = \mathbf{E}^{ep} \dot{\boldsymbol{\epsilon}} \quad (2.34)$$

with the classical elasto-plastic tensor:

$$\mathbf{E}^{ep} = \mathbf{E} - \frac{\mathbf{E} \mathbf{m} \mathbf{n}^T \mathbf{E}}{h + \mathbf{n}^T \mathbf{E} \mathbf{m}} \quad (2.35)$$

In this work the classical Burzyński-Drucker-Prager (BDP) yield function is applied in computations:

$$f^p(\hat{\boldsymbol{\sigma}}, \kappa^p) = \hat{q} + \alpha_p \hat{p} - \beta_p c_p(\kappa^p) \quad (2.36)$$

where both  $\hat{q}$  – the deviatoric stress measure and  $\hat{p}$  – the hydrostatic pressure are determined in the effective stress space as follows:

$$\hat{q} = \sqrt{3J_2^{\hat{\boldsymbol{\sigma}}}} \quad (2.37)$$

$$\hat{p} = \frac{1}{3} I_1^{\hat{\boldsymbol{\sigma}}} \quad (2.38)$$

The invariants of the effective stress tensor are:

$$I_1^{\hat{\boldsymbol{\sigma}}} = \hat{\sigma}_1 + \hat{\sigma}_2 + \hat{\sigma}_3 = tr(\hat{\boldsymbol{\sigma}}) \quad (2.39)$$

$$J_2^{\hat{\boldsymbol{\sigma}}} = \frac{1}{3} (\hat{\sigma}_1^2 + \hat{\sigma}_2^2 + \hat{\sigma}_3^2 - (\hat{\sigma}_1 \hat{\sigma}_2 + \hat{\sigma}_2 \hat{\sigma}_3 + \hat{\sigma}_1 \hat{\sigma}_3)) \quad (2.40)$$

Coefficients  $\alpha_p$  and  $\beta_p$  are functions of the internal friction angle  $\varphi$ :

$$\alpha_p = \frac{6 \sin \varphi}{3 - \sin \varphi} \quad (2.41)$$

$$\beta_p = \frac{6 \cos \varphi}{3 - \sin \varphi} \quad (2.42)$$

and  $c_p$  is a measure for the cohesion. Further, the plastic potential  $g^p$  has the form:

$$g^p = \hat{q} + \bar{\alpha}_p \hat{p} \quad (2.43)$$

where  $\bar{\alpha}_p$  is a function of the dilatancy angle  $\psi$ , similar to the definition of  $\alpha_p$  in Eq. (2.41):

$$\bar{\alpha}_p = \frac{6 \sin \psi}{3 - \sin \psi} \quad (2.44)$$

If the friction angle  $\varphi$  is equal to the dilatancy angle  $\psi$ , then associated plasticity is ensured. The special case of Huber-Mises-Hencky (HMH) yield function is obtained for  $\sin \varphi = \sin \psi = 0$ .

Now a combination of both models, namely scalar damage and hardening plasticity, can be proposed. The stress rate  $\dot{\sigma}$  can be derived from Eq. (2.4):

$$\dot{\sigma} = (1 - \omega) \dot{\hat{\sigma}} - \dot{\omega} \hat{\sigma} \quad (2.45)$$

where the rate of damage  $\dot{\omega}$  during loading (here  $\kappa^d = \tilde{\epsilon}$ ) is evaluated as:

$$\dot{\omega} = \frac{d\omega}{d\kappa^d} \frac{d\kappa^d}{d\tilde{\epsilon}} \frac{d\tilde{\epsilon}}{d\epsilon} \dot{\epsilon} \quad (2.46)$$

and during unloading  $\dot{\omega} = 0$ . Hence:

$$\frac{d\kappa^d}{d\tilde{\epsilon}} = \begin{cases} 1 & \text{during loading} \\ 0 & \text{for unloading} \end{cases} \quad (2.47)$$

The above derivatives can be denoted in the following way :

$$\mathcal{L} = \frac{d\omega}{d\kappa^d} \frac{d\kappa^d}{d\tilde{\epsilon}} \quad (2.48)$$

and

$$\mathbf{s}^T = \frac{d\tilde{\epsilon}}{d\epsilon} \quad (2.49)$$

Finally taking advantage of the effective stress rate for the plastic process can also be received from Eq. (2.34) and the constitutive relation for the coupled model is obtained:

$$\dot{\sigma} = [(1 - \omega) \mathbf{E}^{ep} - \mathcal{L} \hat{\sigma} \mathbf{s}^T] \dot{\epsilon} \quad (2.50)$$

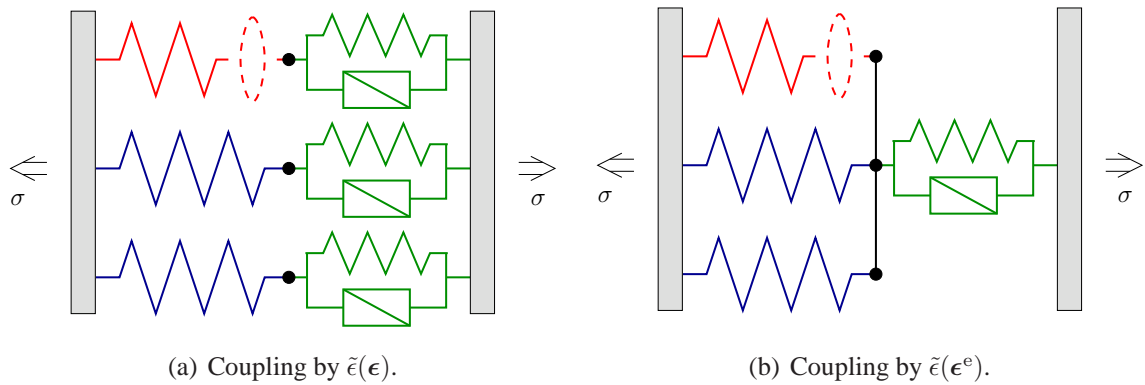


Figure 2.9: Schemes for damage coupled to hardening plasticity.

The equivalent strain  $\tilde{\epsilon}$  can depend on the total strain tensor or its elastic part, which means that the plastic strains either stimulate the damage growth or they do not. If a full coupling exists, for instance for plastically induced damage in metals [47], plastic strains also contribute to  $\tilde{\epsilon}$ . When the second option is chosen, the damage growth is determined by the effective stresses and then the coupling of damage with plasticity is weaker. Here both possibilities are considered, so that the equivalent strain measure is either  $\tilde{\epsilon}(\epsilon)$  or  $\tilde{\epsilon}(\epsilon^e)$ . The scheme in Fig. 2.9 on the left depicts the full coupling. The model coupled by means of the elastic strains is shown on the right. These schemes are built based on [69, 156], where similar one dimension representations are contained, but the context is different.

Analogically to the previous section one eight-noded finite element in three dimensions and under tensile loading/unloading in statics is used to show differences in the pure and coupled models. The elastic coefficients are Young's modulus  $E = 20000$  MPa and Poisson's ratio  $\nu = 0.20$ . For pure and coupled damage models linear softening (2.19) is introduced with damage

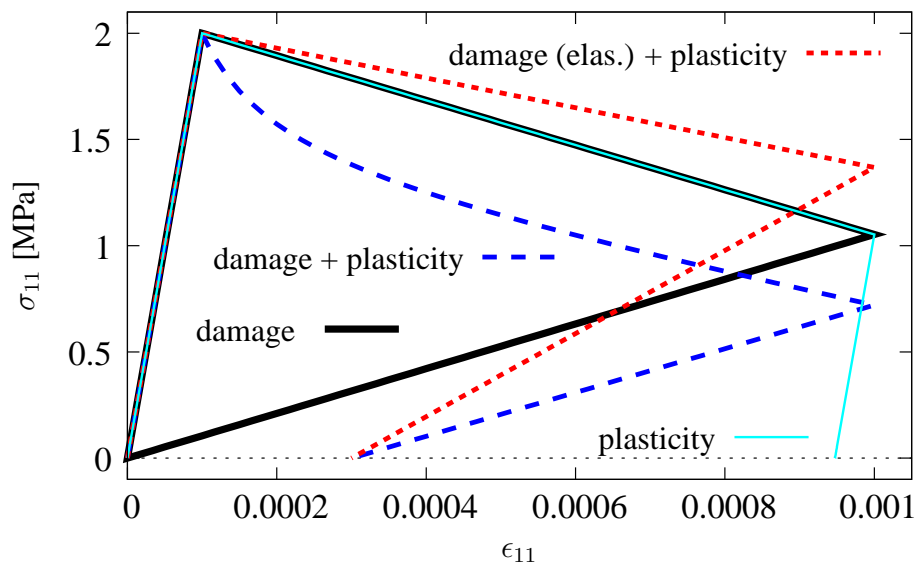


Figure 2.10: Damage, plasticity and coupled models.

threshold  $\kappa_o = 0.0001$  and ultimate value  $\kappa_u = 0.002$ . Linear hardening HMH plasticity is adopted with yield strength  $\sigma_y = 2$  MPa and hardening modulus  $h = 2E$ . This value seems to be unrealistically large, but it is known from [36] that in the coupled model plastic effects are connected only with the fictitious (effective) configuration called also the material skeleton. The part of the model related to damage theory is responsible for the development of microcracks. As it was shown in [119] an increasing value of  $h$  gives the solution which is closer to pure damage model. Pure softening plasticity is also calculated only to confront the unloading paths. In this model the yield strength is assumed as above, but to recover the same softening path like for pure damage modulus  $h$  is equal to  $-0.05E$ .

The stress-strain diagrams during the loading/unloading process are depicted in Fig. 2.10. The behaviour of pure models is obvious. It is worthy of emphasis that for coupled model different equivalent strain definitions are employed and different paths are obtained. As expected for these options irreversible strain is received and it has the same final value. Moreover, for pure damage and damage with full coupling an identical rate of stress evolution is observed from a certain moment on (see parallel diagrams in Fig. 2.10).

## 2.3 CRACK CLOSING

The coupled formulation described in the previous section does not cover the crack closure phenomenon which occurs for compression following tension (like in Fig. 2.11). As previously time  $t$  is omitted in notation. If a pure damage model is considered during unloading the constant (secant) stiffness is:

$$\mathbf{E}_{\text{sec}} = (1 - \omega) \mathbf{E} \quad (2.51)$$

In this case no residual strains remain after unloading (see also Fig. 2.10). It means that microcracks and microvoids in the material close completely. If so then the damage process should not influence the elastic behaviour under compression and the initial stiffness should be retrieved when the origin is passed once (see Fig. 2.11).

To control crack closure effect (or, more generally, a different stiffness in compression and tension) a very simple mechanism has been proposed [62, 102, 145]. The theory presented below is also explained in [117, 120, 122, 170], but similarly to [120] the Voigt's (called also matrix-vector) notation is used to make programming the FEM code easier. If it is necessary, notation with indices will be additionally employed. Firstly the tensile part of elastic strains is separated from the total elastic strains using a projection operator  $\mathbf{P}^+$ :

$$\boldsymbol{\epsilon}^{\text{e}+} = \mathbf{P}^+ \boldsymbol{\epsilon}^{\text{e}} \quad (2.52)$$

Generally the second order strain tensor corresponds to the projection operator  $\mathbf{P}^+$  defined as a the fourth order tensor, here  $\mathbf{P}^+$  is resolved to a matrix. It is assumed that only  $\boldsymbol{\epsilon}^{\text{e}+}$  is



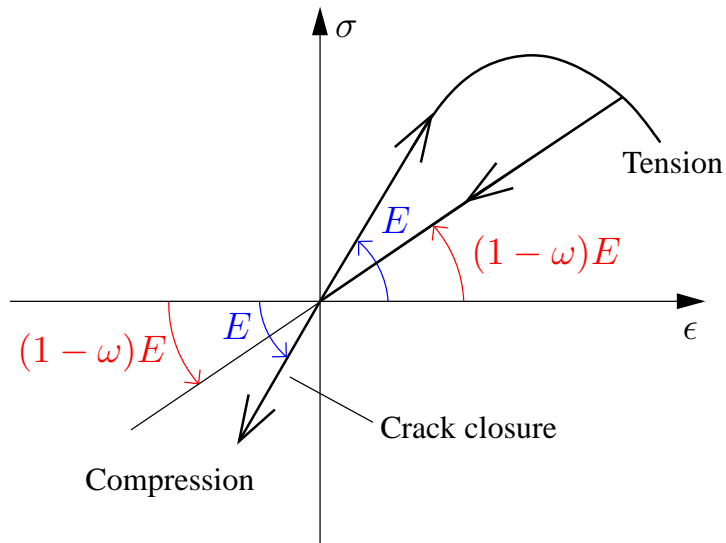


Figure 2.11: Stiffness change in crack closure phenomenon (without irreversible strains).

responsible for damage:

$$\sigma^{d+} = \omega \mathbf{E} \epsilon^{e+} \quad (2.53)$$

Further, only the tensile part of the damage stress is admitted:

$$\sigma^{d+} = (\mathbf{P}^+)^T \sigma^d \quad (2.54)$$

Now the stress-elastic strain relationship is written:

$$\sigma = \hat{\sigma} - \sigma^{d+} = \mathbf{E} \epsilon^e - \omega (\mathbf{P}^+)^T \mathbf{E} \mathbf{P}^+ \epsilon^e = \mathbf{E}_{\text{sec}} \epsilon^e \quad (2.55)$$

where the secant stiffness is distinguished as:

$$\mathbf{E}_{\text{sec}} = \mathbf{E} - \omega (\mathbf{P}^+)^T \mathbf{E} \mathbf{P}^+ \quad (2.56)$$

The key point in the above approach is a suitable formulation of the projection operator which transforms the strain tensor into its tensile part. If we assume that the projection operator  $\mathbf{P}^+$  has the following form in Voigt's notation:

$$\mathbf{P}^+ = \mathbf{T}^{-1} \mathbf{H} \mathbf{T} \quad (2.57)$$

the idea of the tensile strain projection can be enumerated as follows [89, 102]:

a) transform strain tensor to its principal directions:

$$\epsilon^{e'} = \mathbf{T} \epsilon^e \quad (2.58)$$

where matrix  $\mathbf{T}$  corresponds to the transformation from the original coordinate system to the principal directions (more detailed description below) and symbol  $'$  denotes the new coordinate system coinciding with the principal directions,

- b) choose the principal values which are greater than zero and make a new strain tensor (called positive or tensile) composed of these values:

$$\boldsymbol{\epsilon}^{e+'} = \mathbf{H} \boldsymbol{\epsilon}^{e'} \quad (2.59)$$

where ones may only be placed on the diagonal of matrix  $\mathbf{H}$ ,

- c) transform this positive strain tensor back to the original coordinate system:

$$\boldsymbol{\epsilon}^{e+} = \mathbf{T}^{-1} \boldsymbol{\epsilon}^{e+'} \quad (2.60)$$

The above actions can be depicted in the simple commutative diagram:

$$\boldsymbol{\epsilon}^e \xrightarrow{\text{a) } \mathbf{T}} \epsilon_I^e \xrightarrow{\text{b) } \mathbf{H}} \epsilon_I^{e+'} \xrightarrow{\text{c) } \mathbf{T}^{-1}} \boldsymbol{\epsilon}^{e+} \quad (2.61)$$

Here  $I = 1, 2, 3$  denotes the chosen principal direction.

For three-dimensional problems the transformation matrix  $\mathbf{T}$  with the size  $6 \times 6$  concerns elements which depend on three angles between the axes of the original coordinate system and suitable principal directions. This matrix is given explicitly in [149].

For the generalized two-dimensional problems (plane stress, plane strain, axisymmetry) it can be determined by means of one angle  $\Theta$  and its sine and cosine function

$$c_\Theta = \cos \Theta \quad s_\Theta = \sin \Theta \quad (2.62)$$

as follows:

$$\mathbf{T} = \begin{bmatrix} c_\Theta^2 & s_\Theta^2 & 0 & c_\Theta \cdot s_\Theta \\ s_\Theta^2 & c_\Theta^2 & 0 & -c_\Theta \cdot s_\Theta \\ 0 & 0 & 1 & 0 \\ -2 \cdot c_\Theta \cdot s_\Theta & 2 \cdot c_\Theta \cdot s_\Theta & 0 & c_\Theta^2 - s_\Theta^2 \end{bmatrix} \quad (2.63)$$

Now there can be distinguished two forms of the projection operator  $\mathbf{P}^+$  for 3D problems. The first one was proposed by Ortiz in [115]. If  $\mathbf{d}_I$  are unit vectors along the principal directions with components in the original coordinate system the operator in the indicial notation is introduced as:

$$P_{ijkl}^+ = H(\epsilon_1) d_{1i} d_{1j} d_{1k} d_{1l} + H(\epsilon_2) d_{2i} d_{2j} d_{2k} d_{2l} + H(\epsilon_3) d_{3i} d_{3j} d_{3k} d_{3l} \quad (2.64)$$

Naturally the second index in vectors  $\mathbf{d}_I$  points at a succeeding elements and  $H(\cdot)$  denotes the Heaviside function. Hence it can be deduced that in this option the matrix  $\mathbf{H}$  is:

$$\mathbf{H}_{Ortiz} = \text{diag}[H(\epsilon_1), H(\epsilon_2), H(\epsilon_3), 0, 0, 0] \quad (2.65)$$

and the entire operator:

$$\mathbf{P}_{Ortiz}^+ = \mathbf{T}^{-1} \mathbf{H}_{Ortiz} \mathbf{T} \quad (2.66)$$

An alternative form was proposed by Simo and Ju in [145] and afterwards simplified by Hansen in [62]. Firstly, the second order tensor must be assumed:

$$Q_{ik}^+ = H(\epsilon_1) d_{1i} d_{1k} + H(\epsilon_2) d_{2i} d_{2k} + H(\epsilon_3) d_{3i} d_{3k} \quad (2.67)$$

Based on the above relation the projection operator can be defined in indicial notation:

$$P_{ijkl}^+ = Q_{ik}^+ Q_{jl}^+ \quad (2.68)$$

It means that matrix  $\mathbf{H}$  has the following form:

$$\mathbf{H}_{SJH} = \text{diag}[H(\epsilon_1), H(\epsilon_2), H(\epsilon_3), H(\epsilon_1)H(\epsilon_2), H(\epsilon_1)H(\epsilon_3), H(\epsilon_2)H(\epsilon_3)] \quad (2.69)$$

and now the operator is:

$$\mathbf{P}_{SJH}^+ = \mathbf{T}^{-1} \mathbf{H}_{SJH} \mathbf{T} \quad (2.70)$$

For triaxial tension, when all principal values of the strain tensor are larger than zero and  $H(\epsilon_1) = H(\epsilon_2) = H(\epsilon_3) = 1$ , the following relations are obtained:

$$\mathbf{P}^+ \boldsymbol{\epsilon}^e = \boldsymbol{\epsilon}^e \quad (2.71)$$

$$(\mathbf{P}^+)^T \boldsymbol{\sigma}^d = \boldsymbol{\sigma}^d \quad (2.72)$$

Hence the secant stiffness takes the form as in Eq. (2.51). In this case  $\mathbf{H}_{Ortiz}$  degenerates to:

$$\mathbf{H}_{Ortiz} = \text{diag}[1, 1, 1, 0, 0, 0] \quad (2.73)$$

and the projection operator  $\mathbf{P}_{Ortiz}^+$  is not equal to the fourth order identity tensor or the identity matrix in the Voigt's notation. In a different manner is for the second option:

$$\mathbf{H}_{SJH} = \text{diag}[1, 1, 1, 1, 1, 1] \quad (2.74)$$

and hence  $\mathbf{P}_{SJH}^+$  becomes the fourth order identity tensor or the identity matrix. The second operator could be regarded as a superior one. However, for both cases in triaxial tension the tensile strain tensor is equal to the full strain tensor.

For triaxial compression in the model with crack closure effect the identity  $H(\epsilon_1) = H(\epsilon_2) = H(\epsilon_3) = 0$  holds and no damage is expected, it means that the projection operator becomes zero and the material behaves elastically even if in the past it has undergone a damage process in tension:

$$\mathbf{P}^+ \boldsymbol{\epsilon}^e = \mathbf{0} \quad (2.75)$$

$$\mathbf{E}_{\text{sec}} = \mathbf{E} \quad (2.76)$$

If the projection operator is incorporated, the classical elastic energy release is employed as equivalent strain measure (cf. Eq. 2.11), but with  $\epsilon$  substituted by  $\epsilon^{e+}$ :

$$\tilde{\epsilon} = \sqrt{\frac{1}{E} (\epsilon^e)^T (\mathbf{P}^+)^T \mathbf{E} \mathbf{P}^+ \epsilon^e} \quad (2.77)$$

The shape of the damage surface described by the above relation is like for Mazars definition (see Fig. 2.4). However the shape based on Eq. (2.77) for two-dimensional problems is independent of the considered state (whether plane stress or strain) and is identical to the Mazars criterion in plane strain.

Upon differentiation of Eq. (2.55) the following stress-elastic strain relationship is acquired:

$$\dot{\sigma} = \mathbf{E}_{\text{sec}} \dot{\epsilon}^e - \omega \left( \dot{\mathbf{P}}^+ \right)^T \mathbf{E} \mathbf{P}^+ \epsilon^e - \omega (\mathbf{P}^+)^T \mathbf{E} \dot{\mathbf{P}}^+ \epsilon^e - \dot{\omega} \hat{\sigma}^+ \quad (2.78)$$

Here  $\mathbf{E}_{\text{sec}}$  was introduced in Eq. (2.56) and  $\hat{\sigma}^+$  is defined as:

$$\hat{\sigma}^+ = (\mathbf{P}^+)^T \mathbf{E} \mathbf{P}^+ \epsilon^e \quad (2.79)$$

Now the derivative of the strain measure with respect to the strain tensor should be calculated in a such manner:

$$\mathbf{s}^T = \frac{d\tilde{\epsilon}}{d\epsilon} = \frac{d\tilde{\epsilon}}{d\epsilon^{e+}} \frac{d\epsilon^{e+}}{d\epsilon^e} \frac{d\epsilon^e}{d\epsilon} \quad (2.80)$$

where

$$\frac{d\epsilon^{e+}}{d\epsilon^e} = \mathbf{P}^+ + \frac{\partial \mathbf{P}^+}{\partial \epsilon^e} \epsilon^e \quad (2.81)$$

Based on Eqs (2.25) and (2.34) the relation between elastic and total strain increments is:

$$\frac{d\epsilon^e}{d\epsilon} = (\mathbf{E})^{-1} \mathbf{E}^{\text{ep}} \quad (2.82)$$

Using the latter result a tangent operator  $\mathbf{E}_{\text{tan}}$  can be introduced:

$$\mathbf{E}_{\text{tan}} = (\mathbf{E}_{\text{sec}} - \omega \mathbf{E}^*) \mathbf{E}^{-1} \mathbf{E}^{\text{ep}} \quad (2.83)$$

where

$$\mathbf{E}^* = \left[ \left( \frac{\partial \mathbf{P}^+}{\partial \epsilon^e} \right)^T \mathbf{E} \mathbf{P}^+ + \mathbf{P}^+ \mathbf{E} \frac{\partial \mathbf{P}^+}{\partial \epsilon^e} \right] \epsilon^e \quad (2.84)$$

The damage evolution determined in Eq. (2.46) needs also the definition of  $\mathcal{L}$  like in Eq. (2.48). Of course during unloading  $\dot{\omega} = 0$  is still obeyed. Therefore the tangent stress-strain relation is:

$$\dot{\sigma} = (\mathbf{E}_{\text{tan}} - \mathcal{L} \hat{\sigma}^+ \mathbf{s}^T) \dot{\epsilon} \quad (2.85)$$

If crack closing is ignored then operator  $\mathbf{E}_{\text{tan}}$  is reduced to  $(1 - \omega) \mathbf{E}^{\text{ep}}$  and  $\hat{\sigma}^+$  remains  $\hat{\sigma}$  like for the coupled model presented in the previous section.

One finite element test with static tension in one horizontal direction and then compression in the opposite direction is analyzed in two dimensions since the crack closure effect is not yet implemented for 3D problems. Here the plane finite element has four nodes. First computations are performed not only to show the differences between the inclusion of crack closing in the pure damage model, but also to examine the influence of the value of Poisson's ratio in plane strain/plane stress problems with the projection operator. Next to Poisson's ratio the stiffness is also determined by Young's modulus  $E$ , which is equal to 20000 MPa. For the damage model linear softening (2.19) is applied, where damage threshold  $\kappa_o$  is 0.0001 and the ultimate  $\kappa_u$  amounts to 0.004. If this model is applied together with plasticity, both types of coupling are compared (cf. example in the previous section). For plasticity HMH function with yield strength  $\sigma_y = 2$  MPa is introduced. After yielding linear hardening starts and the hardening modulus  $h$  equals  $2E$ . The crack closure phenomenon is incorporated by means of the projection operator  $P_{Ortiz}^+$  defined in Eq. (2.66).

In Figs 2.12 and 2.13 the loading (tension) – unloading – reloading (compression) paths are presented for horizontal stress  $\sigma_{11}$  versus corresponding strain  $\epsilon_{11}$ .

In Fig. 2.12 in the diagram for the model without the projection operator and with zero Poisson's ratio the stiffness in the reloading phase is kept from the unloading phase, hence the lack of crack closure effect is evident. Moreover, cases without the projection operator, but with Poisson's ratio equal to 0.2 (not depicted in this figure) for plane strain and plane stress produce identical paths as for the discussed diagram. If crack closing is included the behaviour is different for each case. A complete crack closing is noticed when Poisson's ratio is equal to zero. After softening and return to the origin the elastic stiffness is recovered. This is because the elements of the strain and stress tensor are not related through Poisson's ratio. For both cases (plane strain and plane stress) with non-zero Poisson's ratio the stiffness changes during

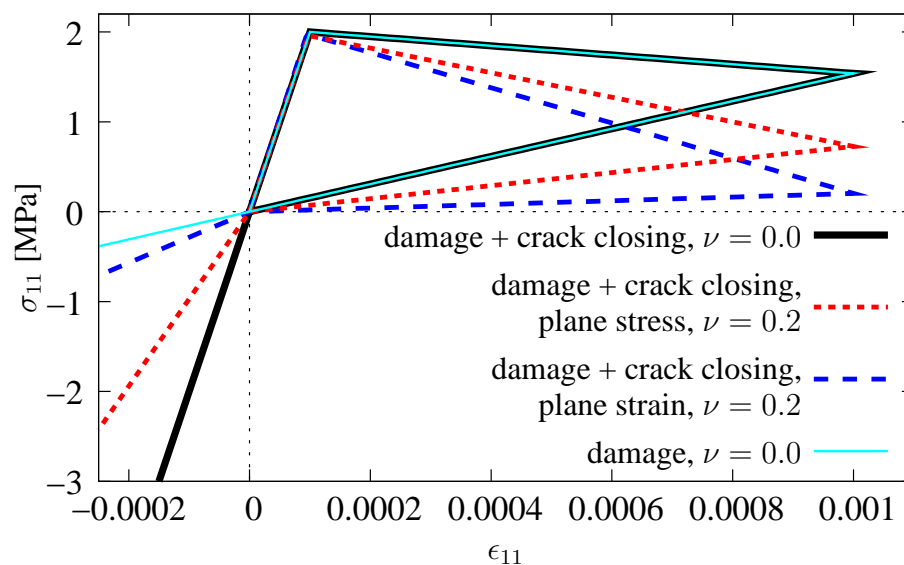


Figure 2.12: Incorporation of crack closing into scalar damage.

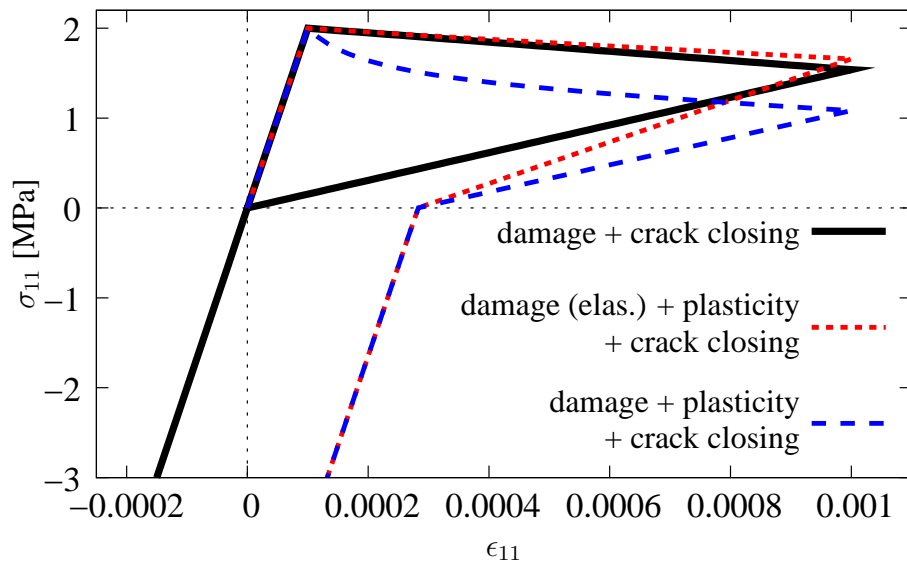


Figure 2.13: Incorporation of crack closing into coupled model.

reloading, but the elastic stiffness is not fully recovered. It is caused by different influence of the projection operator  $P^+$  on the considered problem. The contribution of  $P^+$  is visible just after the peak load is reached and different softening rates are observed. The projection operator  $P^+$  for tension in one direction contains only one non-zero component of matrix  $H$ , but for compression the operator does not become a zero matrix. The projection operator is sensitive to crossing the origin into the reloading phase. According to the theory described in page 29, for 2D domains and non-zero Poisson's ratio the original stiffness can be recovered only in biaxial tensile/compressive test.

Fig. 2.13 confronts the crack closure effect in pure and coupled models. Computations are performed only for  $\nu = 0$ . Softening paths for both options with weak and strong coupling are analogical to those presented at the end of Section 2.2. After unloading the same value of irreversible strain is obtained. Next, the initial elastic stiffness is observed during the reloading process independently of the adopted type of coupling.

## 2.4 ISOTROPIC MODEL

Departing from scalar damage, but remaining within the isotropic description, it is possible to enhance the damage model with two strain measures and/or two damage parameters. One way of such enhancement can be the decomposition of one parameter damage into two parts related to tensile and compressive actions [27, 103, 130]. However, the proposal discussed in this section results from a volumetric-deviatoric split given for example in [98]. The elastic-damage constitutive model is considered, i.e. the coupling with plasticity and crack closure effect are neglected.

The continuum damage formulation satisfies the isotropy condition if two damage parameters  $\omega_K$  and  $\omega_G$  for the volumetric and deviatoric part are considered, cf. [21,28,75,98]. The constitutive equation becomes:

$$\boldsymbol{\sigma} = [(1 - \omega_K) K \boldsymbol{\Pi} \boldsymbol{\Pi}^T + 2(1 - \omega_G) G \mathbf{Q}] \boldsymbol{\epsilon} \quad (2.86)$$

or briefly:

$$\boldsymbol{\sigma} = \mathbf{E}_{KG} \boldsymbol{\epsilon} \quad (2.87)$$

where:

$$\mathbf{E}_{KG} = (1 - \omega_K) K \boldsymbol{\Pi} \boldsymbol{\Pi}^T + 2(1 - \omega_G) G \mathbf{Q} \quad (2.88)$$

The first damage parameter  $\omega_K$  influences bulk modulus  $K$  and the second one  $\omega_G$  – shear modulus  $G$ . Moreover, the following relations are introduced:

$$\mathbf{Q} = \mathbf{Q}_0 - \frac{1}{3} \boldsymbol{\Pi} \boldsymbol{\Pi}^T \quad \mathbf{Q}_{\text{dev}} = \mathbf{I} - \frac{1}{3} \boldsymbol{\Pi} \boldsymbol{\Pi}^T \quad (2.89)$$

where:  $\boldsymbol{\Pi} = [1, 1, 1, 0, 0, 0]^T$  and  $\mathbf{Q}_0 = \text{diag}[1, 1, 1, \frac{1}{2}, \frac{1}{2}, \frac{1}{2}]$ . Note that strain and stress vectors are split into volumetric and deviatoric parts:

$$\boldsymbol{\epsilon} = \frac{1}{3} \boldsymbol{\Pi} \theta + \boldsymbol{\epsilon}_{\text{dev}} \quad (2.90)$$

$$\boldsymbol{\sigma} = \boldsymbol{\Pi} p + \boldsymbol{\xi} \quad (2.91)$$

Here the variables are respectively denoted as:  $\theta = \boldsymbol{\Pi}^T \boldsymbol{\epsilon}$  – dilatation,  $\boldsymbol{\epsilon}_{\text{dev}} = \mathbf{Q} \boldsymbol{\epsilon}$  – deviatoric strain,  $p = \frac{1}{3} \boldsymbol{\Pi}^T \boldsymbol{\sigma}$  – pressure and  $\boldsymbol{\xi} = \mathbf{Q}_{\text{dev}} \boldsymbol{\sigma}$  – deviatoric stress. The stress rate is obtained differentiating Eq. (2.86):

$$\dot{\boldsymbol{\sigma}} = \mathbf{E}_{KG} \dot{\boldsymbol{\epsilon}} - \dot{\omega}_K K \boldsymbol{\Pi} \boldsymbol{\Pi}^T \boldsymbol{\epsilon} - 2\dot{\omega}_G G \mathbf{Q} \boldsymbol{\epsilon} \quad (2.92)$$

The basic question is how the damage and the (equivalent) strain which governs it should be measured. Two approaches can be proposed.

### 2.4.1 ONE STRAIN MEASURE

The simplest case is to assume  $\kappa^d = \kappa_K^d = \kappa_G^d$ , so that one damage loading function (2.8) satisfying the Kuhn-Tucker conditions (2.10) is applied with the equivalent strain measure  $\tilde{\epsilon}$  and the damage history parameter  $\kappa^d$ . However, two different damage growth functions are distinguished:

$$\omega_K = \omega_K(\kappa^d) \quad \text{and} \quad \omega_G = \omega_G(\kappa^d) \quad (2.93)$$

This proposal will further be called "*one strain measure*".

If one history parameter  $\kappa^d$  governs the damage evolution, the rates of damage parameters  $\omega_K$  and  $\omega_G$  during loading are respectively:

$$\dot{\omega}_K = \frac{d\omega_K}{d\kappa^d} \frac{d\kappa^d}{d\tilde{\epsilon}} \frac{d\tilde{\epsilon}}{d\epsilon} \dot{\epsilon} \quad \text{and} \quad \dot{\omega}_G = \frac{d\omega_G}{d\kappa^d} \frac{d\kappa^d}{d\tilde{\epsilon}} \frac{d\tilde{\epsilon}}{d\epsilon} \dot{\epsilon} \quad (2.94)$$

and during unloading both  $\dot{\omega}_K$  and  $\dot{\omega}_G$  are equal to 0. The derivatives are denoted as:

$$\mathcal{L}_K = \frac{d\omega_K}{d\kappa^d} \frac{d\kappa^d}{d\tilde{\epsilon}} \quad \text{and} \quad \mathcal{L}_G = \frac{d\omega_G}{d\kappa^d} \frac{d\kappa^d}{d\tilde{\epsilon}} \quad (2.95)$$

and the definition in Eq. (2.49) is additionally needed. Hence the constitutive relation written in rates for the one strain measure approach is:

$$\dot{\sigma} = [\mathbf{E}_{KG} - (\mathcal{L}_K K \mathbf{\Pi} \mathbf{\Pi}^T + 2\mathcal{L}_G G \mathbf{Q}) \mathbf{s}^T] \dot{\epsilon} \quad (2.96)$$

An analogical idea is presented in [21], where so-called "single-dissipative isotropic model" is governed by one primary damage variable, but different volumetric and deviatoric stiffness degradations are distinguished. Hence like here one loading function and two damage parameters are applied.

This option has been verified by means of one-element benchmark test. The simulations of three-dimensional element with eight nodes under static tension in one direction have been performed. The general data like for example Young's modulus have been employed identical to the example in Section 2.1 (see page 21). It should be emphasized that damage threshold  $\kappa_0$ , here equal to 0.0001, influences directly the history parameter  $\kappa^d$ . Hence starting the damage process at two different instants (two thresholds) in proposal called "one strain measure" is not admitted. On the other hand the simple modification of scalar theory, which was explained above, gives a possibility to adopt of two different damage growth functions, separately for degradation of bulk modulus  $K$  and shear modulus  $G$ . It permits one to construct and then control damage evolution governed by dominating volumetric or shape failure. Ten calculated cases are juxtaposed in Table 2.1. There are presented not only detailed damage growth data and the symbol used to distinguish a given case in the computations but also diagrams of strain  $\epsilon_{11}$  versus damage  $\omega_K$  and  $\omega_G$ . These diagrams are very helpful in understanding how the additional chance to construct different damage growth functions influences the results. For example in the case called *exp,lin* (last row in Table 2.1) there is exponential softening for volumetric degradation and a linear one for the deviatoric part. In the corresponding diagram (last row and last column) it can be observed that until  $\epsilon_{11}$  nearly equals 0.0015 the parameter  $\omega_K$  is larger than  $\omega_G$  and afterwards there is a noticeable change. The reasons of this change will be clarified later in detail. Now it can only be mentioned that until  $\epsilon_{11} \approx 0.0015$  the exponential softening for the volumetric part governed by  $\omega_K$  decides about the damage evolution. Similarly to the benchmark presented in Section 2.1 such parameters have been chosen that the fracture energy for calculated cases is relevant. For instance to gain nearing fracture energy the ultimate value



Table 2.1: Tension in one direction – all cases computed by means of isotropic damage.

Symbol of case	Damage growth data		Strain-damage diagrams
	volumetric part	deviatoric part	
<i>lin</i> <span style="color:red">- - - - -</span>	linear, Eq. (2.19), $\kappa_u^K = 0.002$	linear, Eq. (2.19), $\kappa_u^G = 0.002$	
<i>lin,K</i> <span style="color:black">—</span>	linear, Eq. (2.19), $\kappa_u^K = 0.003$	linear, Eq. (2.19), $\kappa_u^G = 0.002$	
<i>lin,G</i> <span style="color:blue">- - - - -</span>	linear, Eq. (2.19), $\kappa_u^K = 0.002$	linear, Eq. (2.19), $\kappa_u^G = 0.003$	
<i>lin,K &amp; G</i> <span style="color:magenta">- - - - -</span>	linear, Eq. (2.19), $\kappa_u^K = 0.003$	linear, Eq. (2.19), $\kappa_u^G = 0.003$	
<i>exp</i> <span style="color:red">—</span>	exponential, Eq. (2.21), $\eta_K = 1000$	exponential, Eq. (2.21), $\eta_G = 1000$	
<i>exp,K</i> <span style="color:black">- - - - -</span>	exponential, Eq. (2.21), $\eta_K = 750$	exponential, Eq. (2.21), $\eta_G = 1000$	
<i>exp,G</i> <span style="color:blue">- - - - -</span>	exponential, Eq. (2.21), $\eta_K = 1000$	exponential, Eq. (2.21), $\eta_G = 750$	
<i>exp,K &amp; G</i> <span style="color:magenta">—</span>	exponential, Eq. (2.21), $\eta_K = 750$	exponential, Eq. (2.21), $\eta_G = 750$	
<i>lin,exp</i> <span style="color:blue">- - - - -</span>	linear, Eq. (2.19), $\kappa_u^K = 0.002$	exponential, Eq. (2.21), $\eta_G = 1000$	
<i>exp,lin</i> <span style="color:black">- - - - -</span>	exponential, Eq. (2.21), $\eta_K = 1000$	linear, Eq. (2.19), $\kappa_u^G = 0.002$	

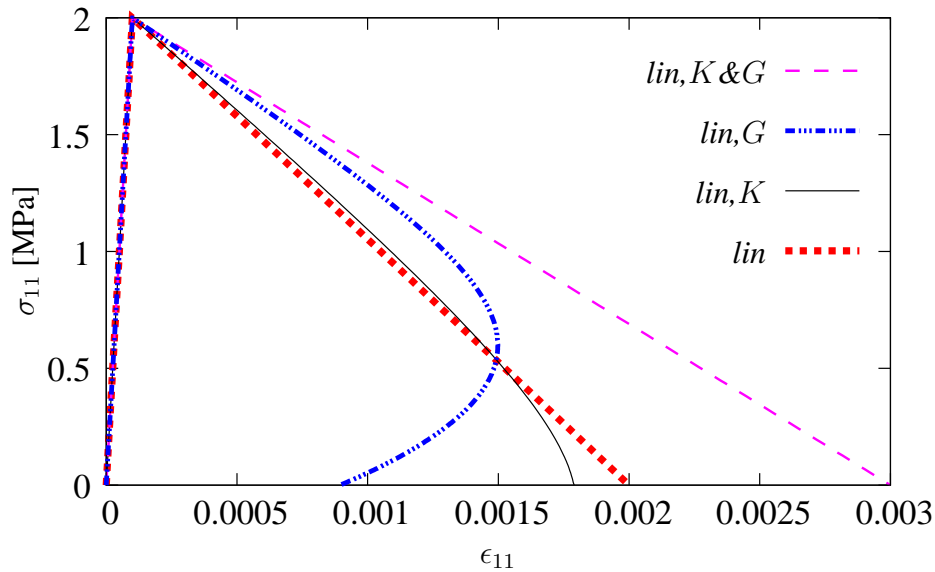


Figure 2.14: Influence of ultimate  $\kappa_u$  in linear softening for isotropic model.

$\kappa_u = 0.003$  in the linear function corresponds to the ductility parameter  $\eta_i = 750$  ( $i = K, G$ ) for the exponential one. The cases with identical data for both damage growth functions can be treated as reference. The same numerical stability parameter  $\alpha = 0.98$  in all cases with exponential softening is assigned.

Firstly in Fig. 2.14 cases with linear softening are shown. As it was expected, after the peak, diagrams for *lin, K* and *lin, G* start to descend between diagrams for *lin* and *lin, K&G*. However, it seems astonishing a nonlinear character of softening although the linear damage growth was defined for cases *lin, K* and *lin, G*. Moreover, in case *lin, G*, where the deviatoric part has greater  $\kappa_u^G$ , arc-length control has been applied during computations because strong nonlinearity and snap-back have revealed. Therefore, it suffices to change the ultimate value  $\kappa_u$  for chosen volumetric or deviatoric part in order to obtain nonlinear response. It will further be discussed in the paragraph on page 38.

Fig. 2.15 depicts stress-strain diagrams for damage growth functions related to exponential softening. The interpretation is easy since each softening branch has an exponential character. For cases *exp, K* and *exp, G* with mixed ductility parameters they run between the extreme cases *exp* and *exp, K&G*. Analogically to the cases with linear functions a certain regularity can be noted. If the fracture energy for the deviatoric part is increased (compare cases *exp* and *exp, G*), it gives a larger difference in response than for fracture energy added to the volumetric part. It is doubtful to consider fracture energy only for a chosen part of the stiffness, however in order to simplify the explanations this concept will be used.

The comparison in Fig. 2.16 shows influence of damage growth functions with a different character, i.e. first of all attention is focused on the two cases with mixed softening, namely linear-exponential called *lin, exp* and exponential-linear called *exp, lin*. The other diagrams are

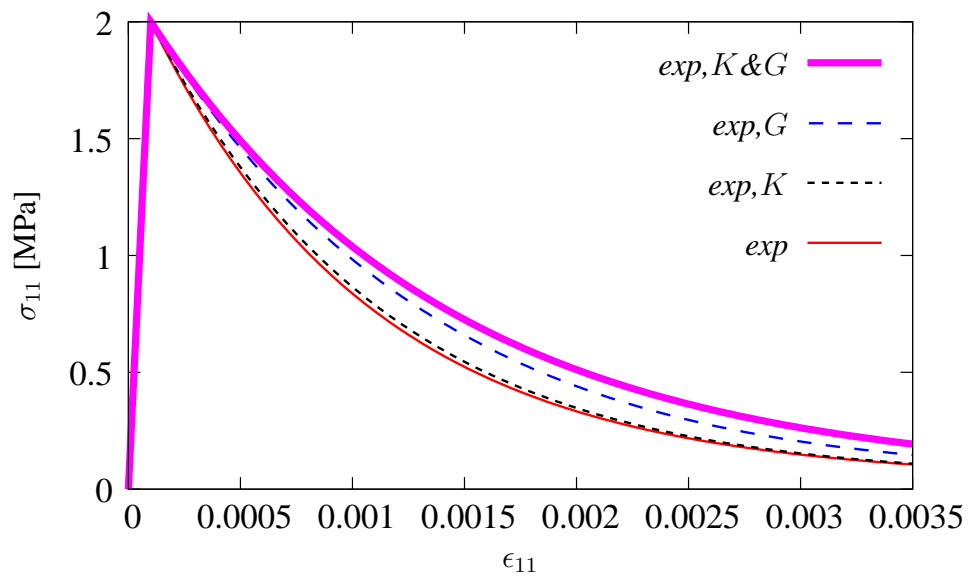


Figure 2.15: Influence of ductility parameter  $\eta_i$  ( $i = K, G$ ) in exponential softening for isotropic model.

included to explain the response for these calculated cases. The results for both simulations imply not only a nonlinear character, but as it was mentioned in page 34 (see also Table 2.1) a change in domination of damage  $\omega_K$  or  $\omega_G$  is noticed. In case *lin,exp* at first larger damage  $\omega_G$  for the deviatoric part governs the solution. Since  $\epsilon_{11}$  achieves 0.0015 damage  $\omega_K$  connected with volumetric degradation overweights. An opposite situation is observed for case *exp,lin*. Therefore until  $\epsilon_{11}$  attain 0.0015 for both computations exponential softening dominates. After exceeding this value the linear function is responsible for the drop in stiffness.

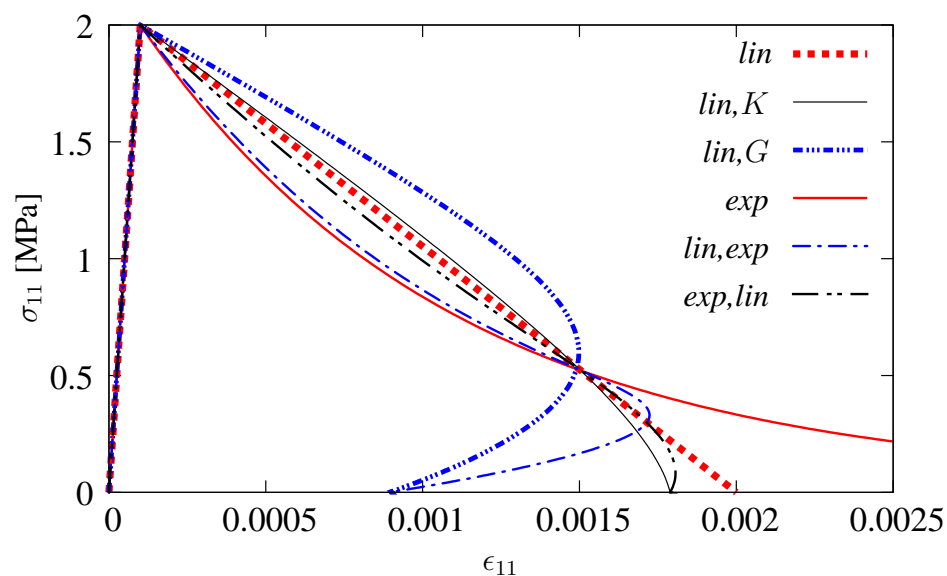


Figure 2.16: Influence of predefining damage growth functions with different character.

All the diagrams in Fig. 2.16 intersect at a point where  $\epsilon_{11} \approx 0.0015$ . Considering the basic cases *lin* and *exp*, after the peak load to this characteristic point softening branch decreases faster for case *exp*. Further if  $\epsilon_{11} > 0.0015$  the stress component  $\sigma_{11}$  decreases faster for case *lin*. Hence in cases *lin,exp* and *exp,lin* with mixed damage growth this function dominates during the evolution, which involves more intensive stiffness degradation. It is also interesting that branch for *lin,exp* finally coincides with case *lin,G* and similarly case *exp,lin* with *lin,K*. If the data gathered in Table 2.1 are confronted it turns out that both coincidences are connected with the adopted linear functions having the same ultimate value of damage history parameter. In cases *lin,exp* and *lin,G* this is  $\kappa_u^K$  for the volumetric part, opposite to *exp,lin* and *lin,K*, where identical linear softening is employed for deviatoric part with the same  $\kappa_u^G$ .

Before the next figure will be described the following definition of Poisson's ratio depending on the stiffness degradation is introduced:

$$\nu_\omega = \nu(\omega_K, K, \omega_G, G) = \frac{3(1 - \omega_K)K - 2(1 - \omega_G)G}{2[3(1 - \omega_K)K + (1 - \omega_G)G]} \quad (2.97)$$

To distinguish the Poisson's ratio which is given as an elastic material parameter from the one defined in Eq. (2.97) the subscript  $\omega$  is additionally applied. Hence, parameter  $\nu_\omega$  is computed during the damage process.

As it is shown in Fig. 2.17, if only damage growth functions are predefined for a particular case then this parameter changes. Furthermore, in the case of linear softening the value of  $\nu_\omega$  drastically tends to a lower or upper limit. These limits can be perceived as controversial results and first of all they are not physically motivated. Such extreme behaviour in simulation and as a consequence nonlinear relation between  $\epsilon_{11}$  and  $\sigma_{11}$  seems to be undisable. A completely degradation for the volumetric part (cases *lin,exp* and *lin,G*) gives finally  $\nu_\omega$  equal

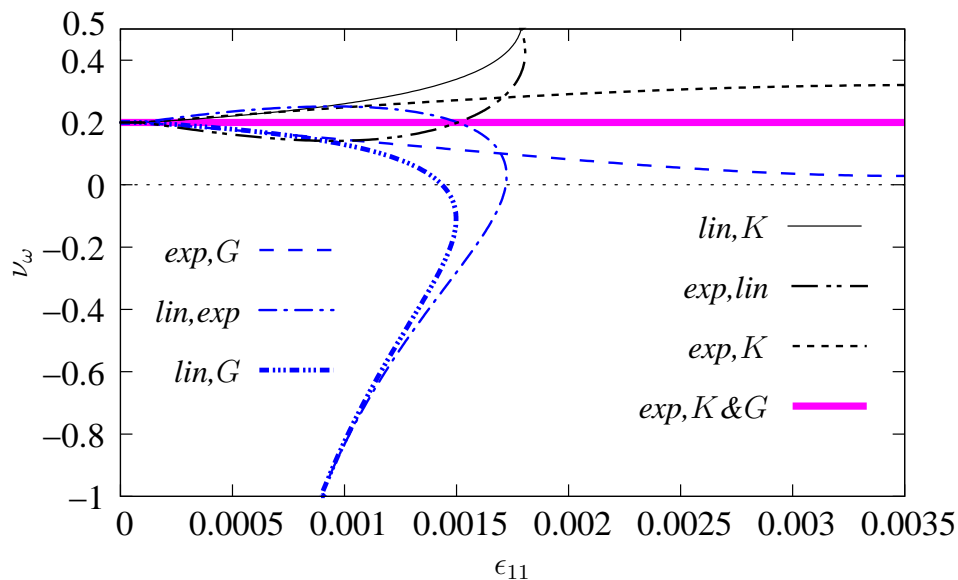


Figure 2.17: Sensitivity of Poisson's ratio  $\nu_\omega$  to adopted damage growth functions.

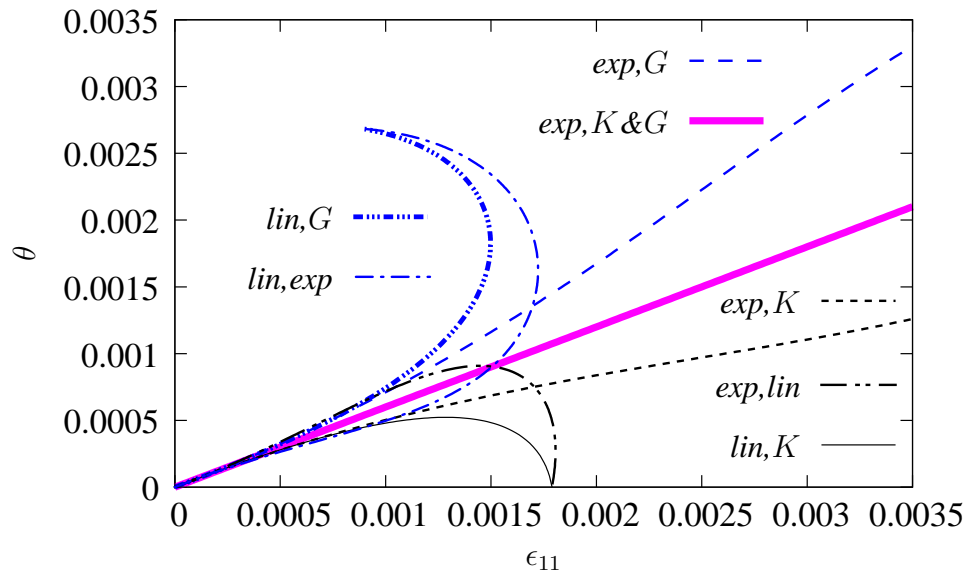


Figure 2.18: Sensitivity of dilatation  $\theta$  to adopted damage growth functions.

to  $-1$ . On the other hand the zeroed shear stiffness (cases *exp,lin* and *lin,K*) leads to  $\nu_\omega = 0.5$  like for incompressible materials (cf. [21]). Concrete is rather a material where microcracks under tension decrease the Poisson's effect during the failure process [75]. The problem is that non-physical values below zero appear and they even achieve  $-1$ . If exponential softening is used (see Fig. 2.17, case *exp,G*) a smooth drop below zero is observed, but this is not always so. Naturally the starting value of  $\nu_\omega$  and also the configuration of the considered test decide on whether  $\nu_\omega$  becomes negative. For quasi-brittle materials like concrete generally it is expected that Poisson's ratio tends to 0 during the damage evolution [21]. In this model this is not assured, hence only by means of appropriate values for the parameters of the model negative Poisson's ratio can be avoided. It is questionable whether such negative values should be admitted in the simulated process.

Fig. 2.18 provides observations mentioned in the previous paragraph connected with variable Poisson's ratio in the damage evolution. If the value of  $\nu_\omega$  reduces, the dilatancy  $\theta$  grows more intensively than linearly. Oppositely – increasing variable  $\nu_\omega$  provokes dilatancy  $\theta$  to grow slower (case *exp,K*) or leads to 0 in extreme situations (cases *exp,lin* and *lin,K*).

Summarizing case *exp,G* seems to be the most promising, but in further tests different combinations of exponential softening will be employed in order to verify the isotropic damage model not only at the point level.

## 2.4.2 TWO STRAIN MEASURES

A more difficult concept involves a total separation of damage multipliers applied to the bulk and shear modulus, so that this idea will be called "*two strain measures*". Now two damage

loading functions are employed – separately for the dilatancy:

$$f_K^d(\theta, \kappa_K^d) = \tilde{\theta}(\theta(t)) - \kappa_K^d(t) = 0 \quad (2.98)$$

and for the deviatoric (shear) strains:

$$f_G^d(\epsilon_{\text{dev}}, \kappa_G^d) = \tilde{\epsilon}_{\text{dev}}(\epsilon_{\text{dev}}(t)) - \kappa_G^d(t) = 0 \quad (2.99)$$

It remains to define functions  $\tilde{\theta}(\theta)$  and  $\tilde{\epsilon}_{\text{dev}}(\epsilon_{\text{dev}})$ . For example it is possible to divide the well-known modified von Mises formula [38] into parts related to the first and second strain invariants. If these invariants are used separately for the volumetric and deviatoric components, the following definitions can be introduced:

$$\tilde{\theta} = \frac{k-1}{k(1-2\nu)} I_1^\epsilon \quad (2.100)$$

$$\tilde{\epsilon}_{\text{dev}} = \frac{\sqrt{3kJ_2^\epsilon}}{k(1+\nu)} \quad (2.101)$$

The aim of distinguishing two history parameters  $\kappa_K^d$  and  $\kappa_G^d$  is that damage increases separately for  $\omega_K$  and  $\omega_G$ :

$$\dot{\omega}_K = \frac{d\omega_K}{d\kappa_K^d} \frac{d\kappa_K^d}{d\tilde{\theta}} \frac{d\tilde{\theta}}{d\epsilon} \dot{\epsilon} \quad \text{and} \quad \dot{\omega}_G = \frac{d\omega_G}{d\kappa_G^d} \frac{d\kappa_G^d}{d\tilde{\epsilon}_{\text{dev}}} \frac{d\tilde{\epsilon}_{\text{dev}}}{d\epsilon} \dot{\epsilon} \quad (2.102)$$

During unloading it can be assumed that either  $\dot{\omega}_K$  or  $\dot{\omega}_G$  are equal to 0. The following definitions can be introduced:

$$\mathcal{L}_K = \frac{d\omega_K}{d\kappa_K^d} \frac{d\kappa_K^d}{d\tilde{\theta}} \quad \text{and} \quad \mathcal{L}_G = \frac{d\omega_G}{d\kappa_G^d} \frac{d\kappa_G^d}{d\tilde{\epsilon}_{\text{dev}}} \quad (2.103)$$

and furthermore:

$$\mathbf{s}_K^T = \frac{d\tilde{\theta}}{d\epsilon} \quad \text{and} \quad \mathbf{s}_G^T = \frac{d\tilde{\epsilon}_{\text{dev}}}{d\epsilon} \quad (2.104)$$

For this option the constitutive relation in rates has the form:

$$\dot{\boldsymbol{\sigma}} = (\mathbf{E}_{\text{KG}} - \mathcal{L}_K \mathbf{K} \boldsymbol{\Pi} \boldsymbol{\Pi}^T \mathbf{s}_K^T - 2\mathcal{L}_G \mathbf{G} \mathbf{Q} \mathbf{s}_G^T) \dot{\epsilon} \quad (2.105)$$

A similar approach with total separation of damage parameters is described in [21], where two damage variables influences two loading functions. Such model is called in [21] "bi-dissipative isotropic model".

Although the idea described above looks attractive, it has not been implemented and can be a subject of future work.

## 2.5 WILLAM'S TEST

The tension-shear test was performed for the first time in [169] and since then it is called Willam's test. This test is often computed to verify inelastic material models at the point level. As it was noticed in [171], the responses of particular models are different even if these models in uniaxial tension exhibit a similar behaviour or are calibrated in such a manner that gives almost the same results. Many authors checked their ideas using this test, for example: comparisons between fixed, rotating and smeared crack models [49, 140], verification of bounding surface plasticity model [171], verification of multidirectional kinematic softening damage-plasticity model [106], sensitivity analysis for generalized pseudo-Rankine damage model [20] and a wide confrontation of models with respect to multi-surface plasticity [131]. From the point of view of this work the starting point can be the numerical analysis given in [113], where the results for fixed crack and damage models are collected. Although at the point level the damage model described there is analogical to the one presented in Section 2.1, but the data are incomplete. Hence the results presented in [113] compare only qualitatively to the ones calculated in this section. Eventually the adopted data are based on [131].

One finite element with four nodes in plane stress is subjected to loading in two phases:

- I. Uniaxial horizontal tension with vertical contraction due to the Poisson's effect, according to the relation between the strain increments:  $\Delta\epsilon_{11} : \Delta\epsilon_{22} : \Delta\gamma_{12} = 1 : -\nu : 0$ . In Fig. 2.19(a) the scheme of prescribed displacements corresponds to the uniaxial tensile strain state. These conditions are obeyed until the tensile strength is attained.
- II. Immediately after the tensile strength is reached the change of configuration is enforced, see Fig. 2.19(b). Now the proportions for the strain increments are arranged in the fol-

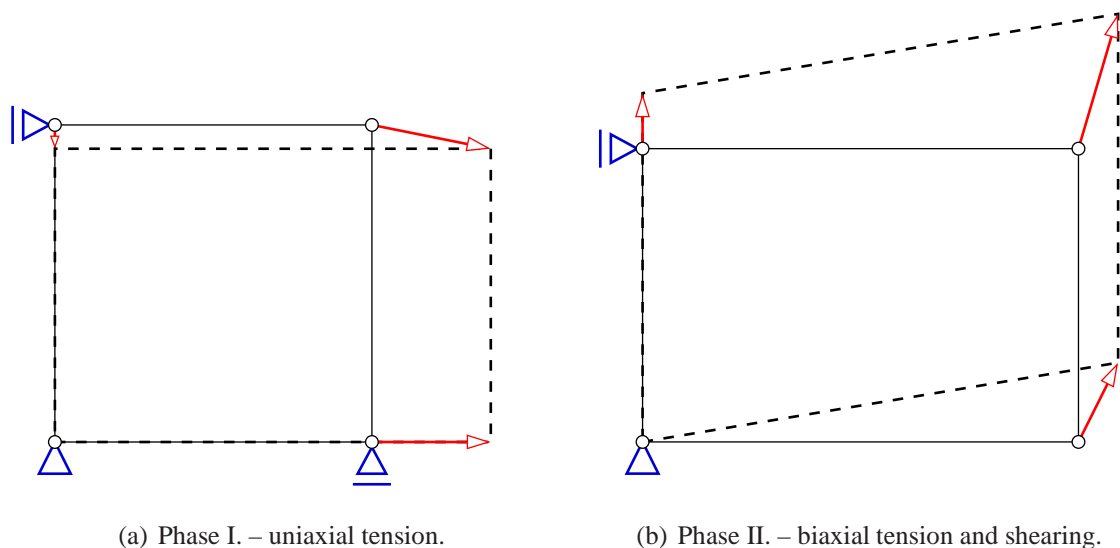
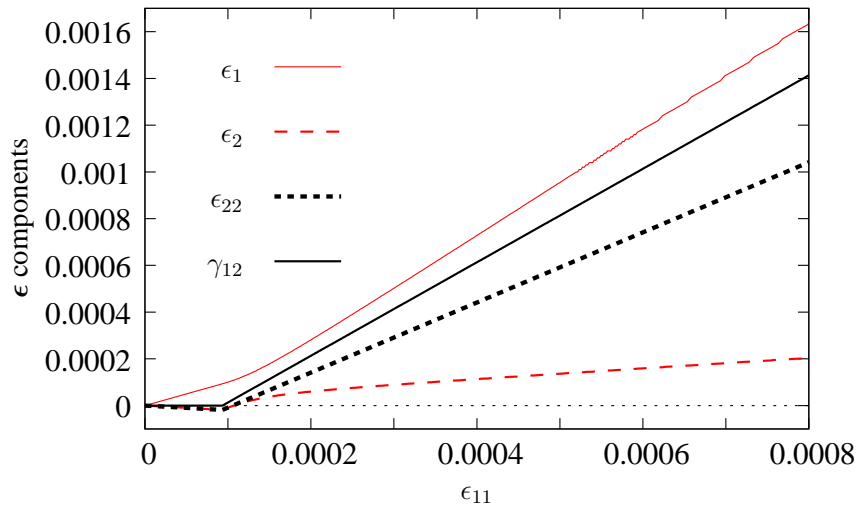
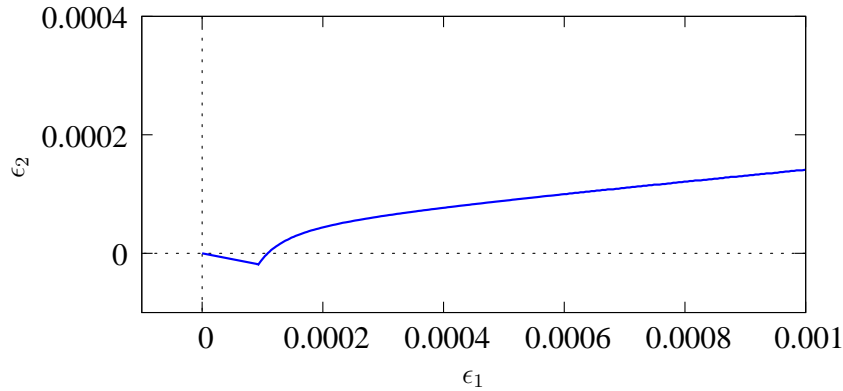


Figure 2.19: Willam's test – prescribed displacements for the corresponding strain state.

(a) Relation between  $\epsilon_{11}$  and remaining strain components.

(b) Principal strains.

Figure 2.20: Willam's test – strain evolution.

lowing way:  $\Delta\epsilon_{11} : \Delta\epsilon_{22} : \Delta\gamma_{12} = 0.5 : 0.75 : 1$ . This relation induces tension in two directions and additionally shear strain. As a consequence a rotation of principal strain axes occurs, but tension regime is preserved. At the beginning the rate of rotation is fast, but during the evolution it slows down.

As mentioned in [171] such loading process is observed during the analysis of real RC structures. Nevertheless in the literature on quasi-brittle materials there seem to be no experiments for this or similar tests with rotating principal directions [20], probably since it is difficult to be reproduced in a laboratory test. A possible verification for a given model in different biaxial states exists in the results of laboratory tests performed by Kupfer [87, 88]. This group of tests allows one to trace the experimental loading surface for concrete. A wide analysis of a numerical model at the point level using different combinations of loading in plane stress like for example in [132] can be performed and confronted with experimental results.



The adopted strain evolution for Willam's test is shown in Fig. 2.20(a) by relations between  $\epsilon_{11}$  regarded here as a history variable and the remaining strain components. The relation between principal strains is depicted in Fig. 2.20(b). The test is passed if the maximum principal stress is lower than or at most equal to the given uniaxial tensile strength [131]. The second condition is that finally all stress components should converge to zero.

The set of data are constructed as for concrete basing on [131], namely Young's modulus  $E = 32000$  MPa, Poisson's ratio  $\nu = 0.20$  and the remaining parameters are tuned to uniaxial tensile strength  $f_t = 3$  MPa, uniaxial compressive strength  $f_c = 38.3$  MPa and tensile fracture energy  $G_f = 0.11$  N/mm. In damage theory the threshold is calculated as quotient of the tensile strength and Young's modulus, so  $\kappa_o = f_t/E = 0.00009375$ . In the case of one element test the characteristic length equals the element size, which is here 100 mm. For a given fracture energy and characteristic length it is possible to determine parameters for the adopted function of damage growth. In this test exponential softening is considered. The first parameter  $\alpha$  is equal to 1.0, which means that complete loss of stiffness is admitted. The ductility parameter  $\eta = 4000$  seems to be unrealistically huge, but results in a fast material failure. If modified von Mises definition (2.15) is assumed, the ratio between compressive and tensile strength is equal to  $k = f_c/f_t = 12\frac{23}{30}$ . Additional parameters for individual cases will be listed during the description of results.

### 2.5.1 RESULTS FOR SCALAR DAMAGE

Firstly, the results for pure scalar damage model are compared and attention is focused on three different definitions of the equivalent strain measure, which were introduced in Section 2.1. In Fig. 2.21 the diagrams for stress-strain relations between corresponding components are shown for the adopted definitions. In Fig. 2.21(a) when softening starts some differences reveal, while in uniaxial tension regime the loading functions have no influence on the peak load. The most rapid decrease of  $\sigma_{11}$  is noted for modified von Mises definition (2.15). The diagrams for two other functions are rather close and this observation is also made in Figs. 2.21(b) and 2.21(c). Analyzing Fig. 2.21(b), due to Poisson's effect negative vertical strain  $\epsilon_{22}$  result from the horizontal extension and vertical stress  $\sigma_{22}$  is zero. When tensile strength is reached,  $\epsilon_{22}$  and  $\gamma_{12}$  start to grow, while both  $\sigma_{22}$  and  $\sigma_{12}$  first increase and then exhibit softening. Thus the peaks for stresses  $\sigma_{22}$  and  $\sigma_{12}$  are achieved later, when the damage process is advanced. For the modified von Mises measure the maximum values of stresses  $\sigma_{22}$  and  $\sigma_{12}$  are about 50 percent smaller than for the other definitions. Unlike the results given in [20, 171] there are no local bumps on the softening curves. For all three diagrams the modified von Mises measure produces the smallest ductility and the Mazars' measure the largest.

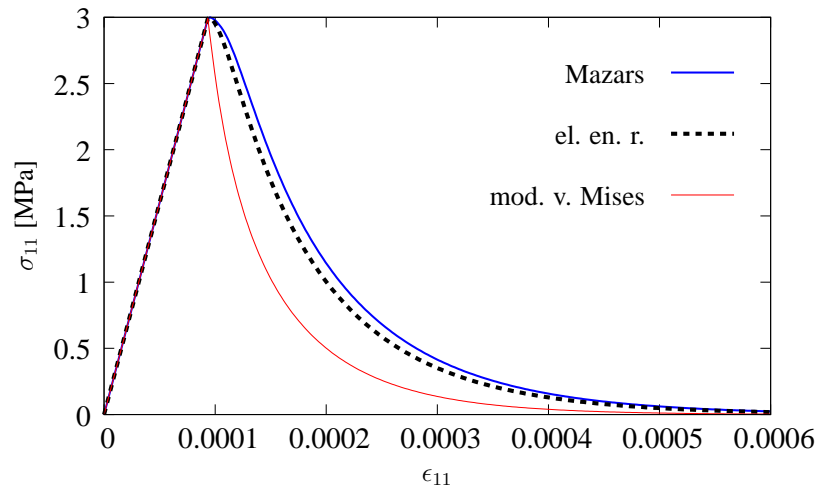
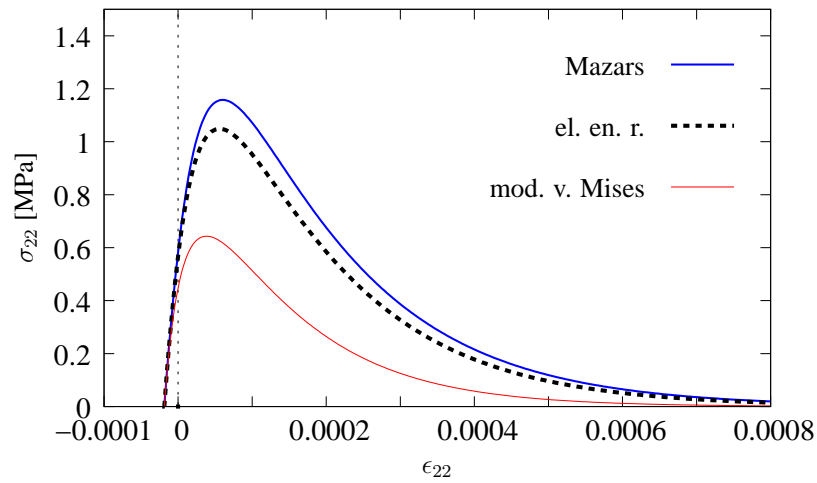
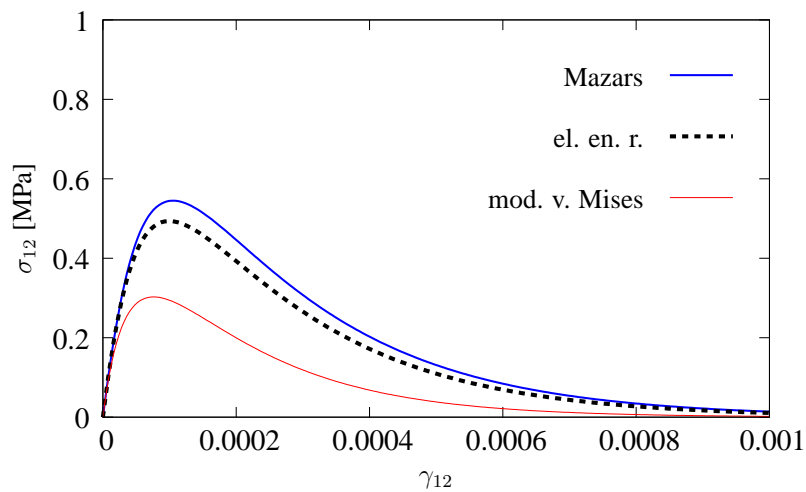
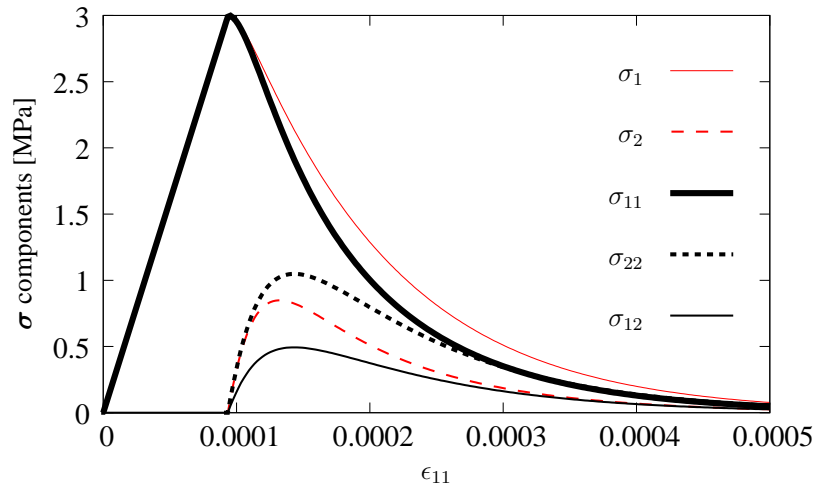
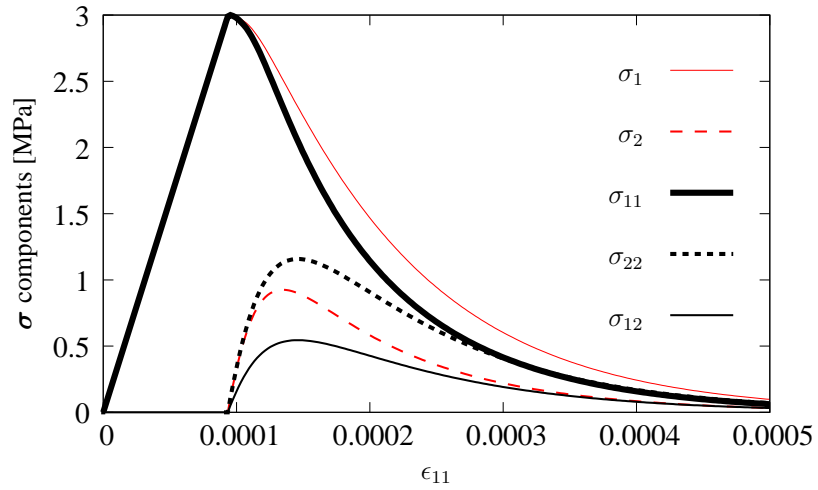
(a) Diagrams of relations  $\epsilon_{11} - \sigma_{11}$ .(b) Diagrams of relations  $\epsilon_{22} - \sigma_{22}$ .(c) Diagrams of relations  $\gamma_{12} - \sigma_{12}$ .

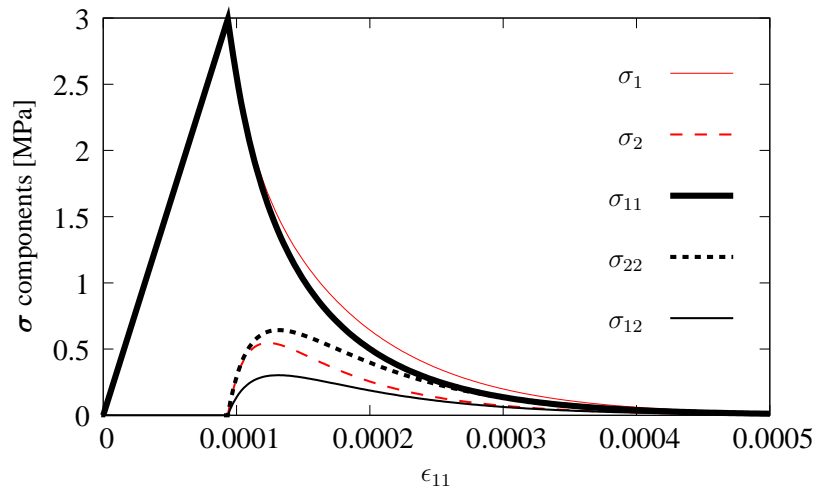
Figure 2.21: Willam's test – influence of assumed loading functions.



(a) Elastic energy release definition (2.11).



(b) Mazars definition (2.12).



(c) Modified von Mises definition (2.15).

Figure 2.22: Willam's test – comparison of stress components for different loading functions.

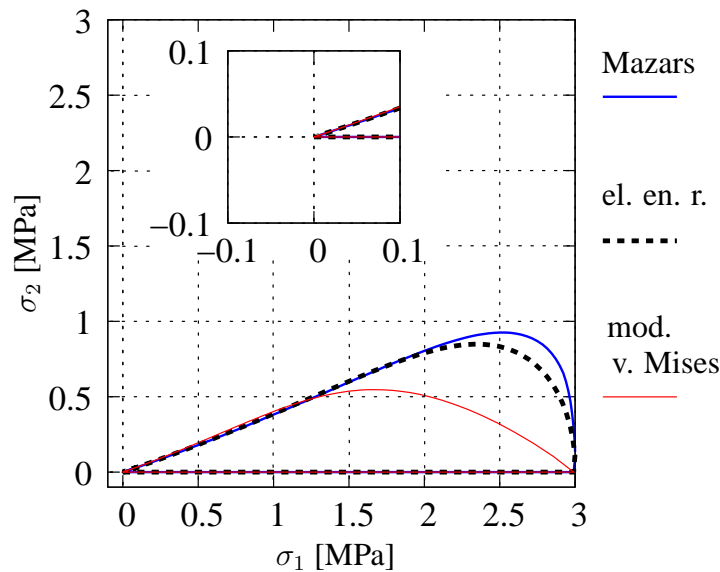


Figure 2.23: Willam's test – evolution of principal stresses for different loading functions.

Generally for all the options the uniaxial tensile strength is not exceeded and all stress components tend to zero, hence for pure scalar damage this test is passed. It is also confirmed in Figs 2.22 and 2.23. Figure 2.22 presents all stress components together with its principal values, in each subfigure for a different loading function. Figure 2.23 depicts the stress evolution in principal directions (the vicinity of the origin is zoomed above). It should be emphasized that the principal directions of the stress (and obviously strain) tensor change during the process.

### 2.5.2 RESULTS FOR COUPLED MODEL

If the coupled model is selected, plasticity with Huber-Mises-Hencky surface and linear hardening are employed. According to the general data the yield strength  $\sigma_y$  is equal to the tensile strength  $f_t$  for concrete. Two ways of coupling, namely total and elastic, are considered (see page 25). Hardening modulus  $h = 0.5E$  is adopted. This small value make it possible to bring out differences in results for a given manner of the coupling, because if  $h \rightarrow \infty$  the solution approaches pure damage (cf. [119]).

The diagrams in Fig. 2.24 show the same tendency as in the example with uniaxial tension (page 26). After the peak the descending paths run in such way that for option  $\tilde{\epsilon}(\epsilon)$  they are below and for  $\tilde{\epsilon}(\epsilon^e)$  above those resulting from the application of pure damage. A more ductile response for  $\tilde{\epsilon}(\epsilon^e)$  is especially visible in the relation  $\epsilon_{22} - \sigma_{22}$ .

Analogically to the previous subsection all stress components and also its principal values are depicted in Fig. 2.25 as functions of  $\epsilon_{11}$  (treated as history variable). This figure is divided into two subfigures for the two manners of coupling, respectively. Additionally Fig. 2.26 presents the stress evolution in principal directions. Like previously it can be noticed that the principal stresses return to zero, which satisfies one of the conditions for this test.

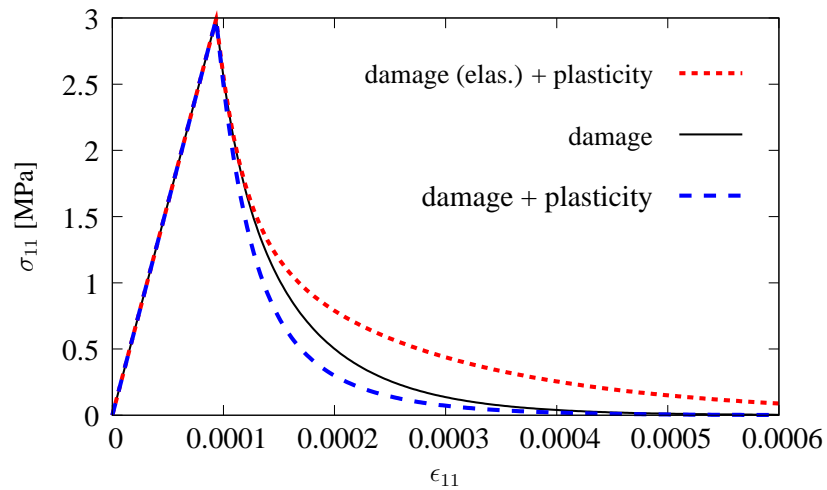
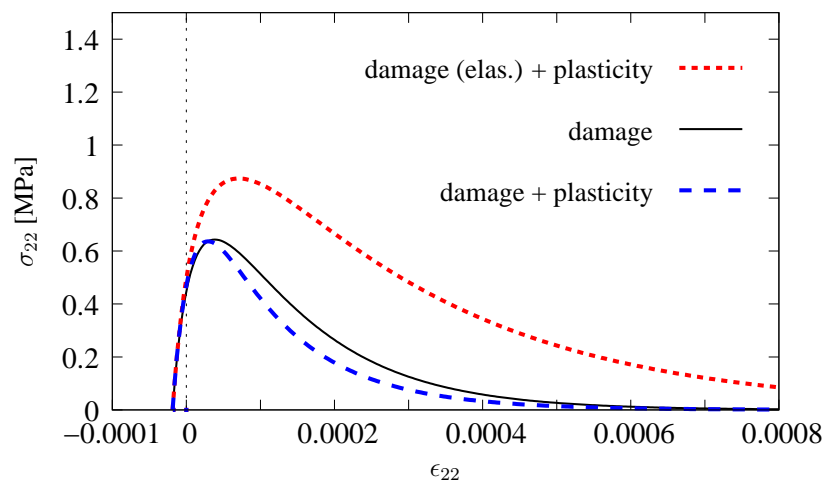
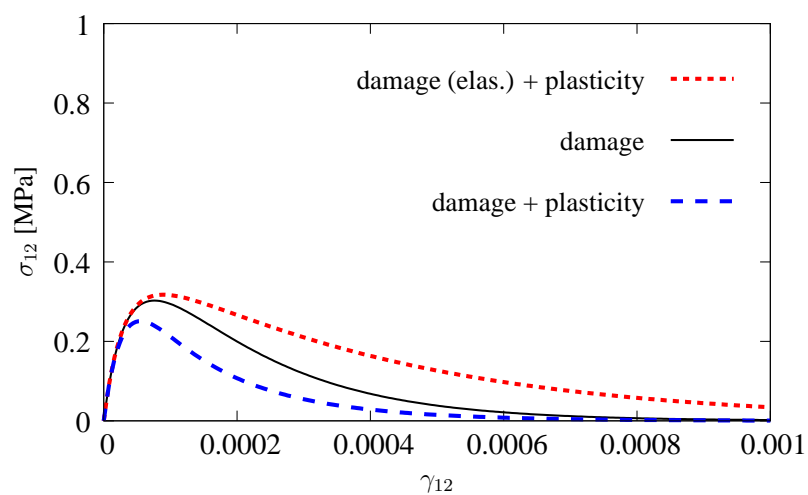
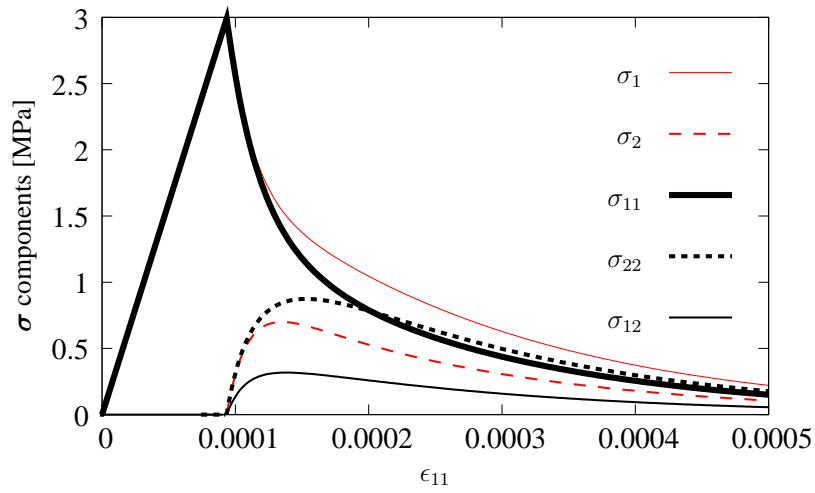
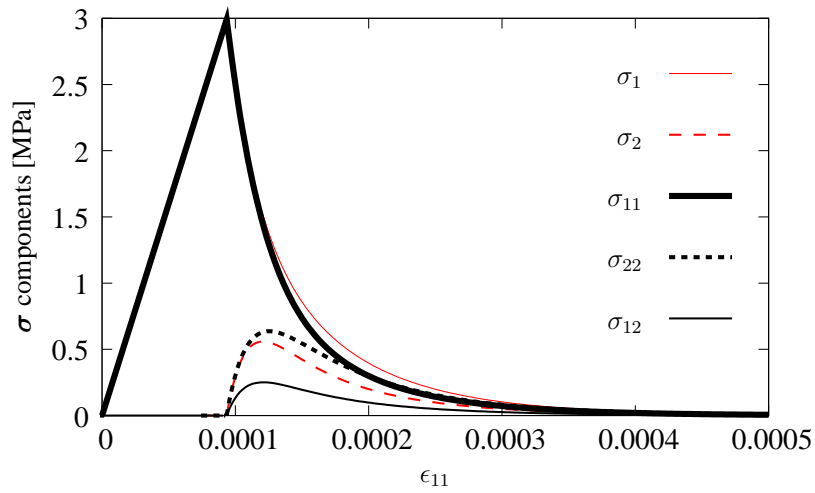
(a) Diagrams of relations  $\epsilon_{11} - \sigma_{11}$ .(b) Diagrams of relations  $\epsilon_{22} - \sigma_{22}$ .(c) Diagrams of relations  $\gamma_{12} - \sigma_{12}$ .

Figure 2.24: Willam's test – results for pure damage and coupled to plasticity.



(a) Damage (elastic) with plasticity.



(b) Damage (total) with plasticity.

Figure 2.25: Willam’s test – comparison of stress components in coupled models.

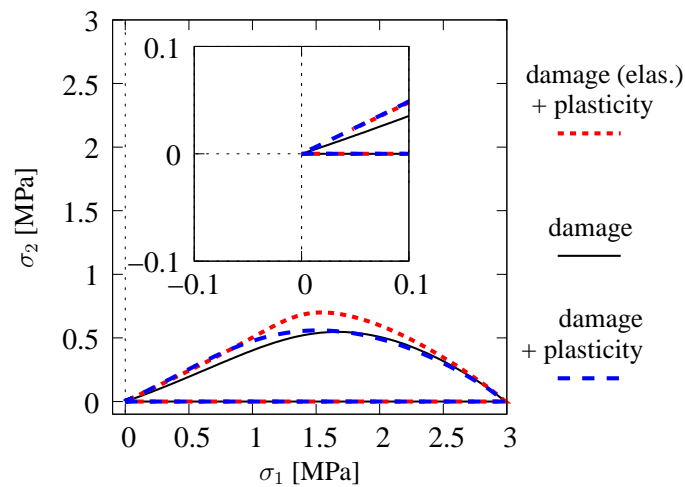
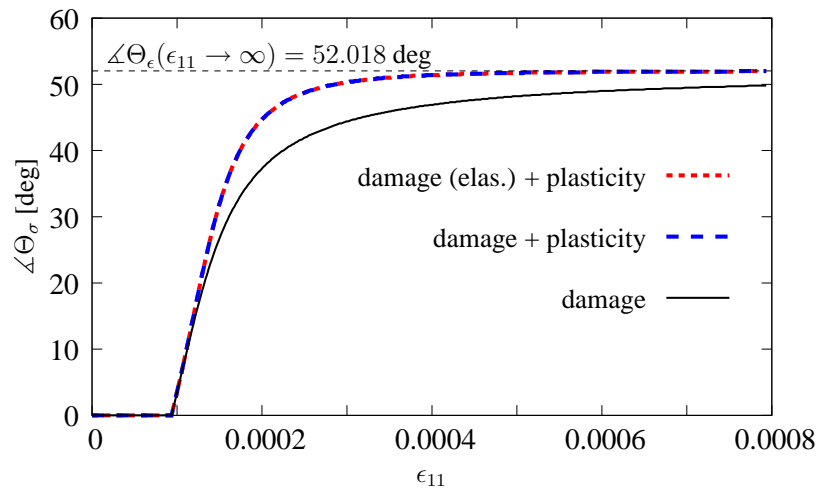
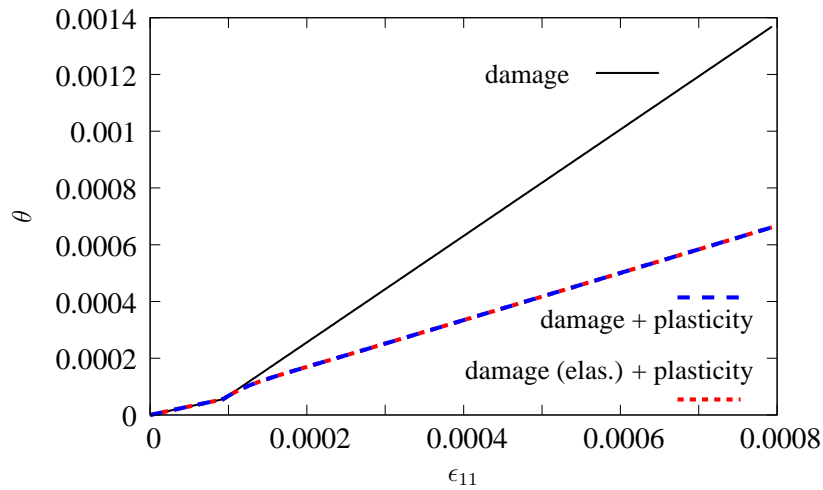


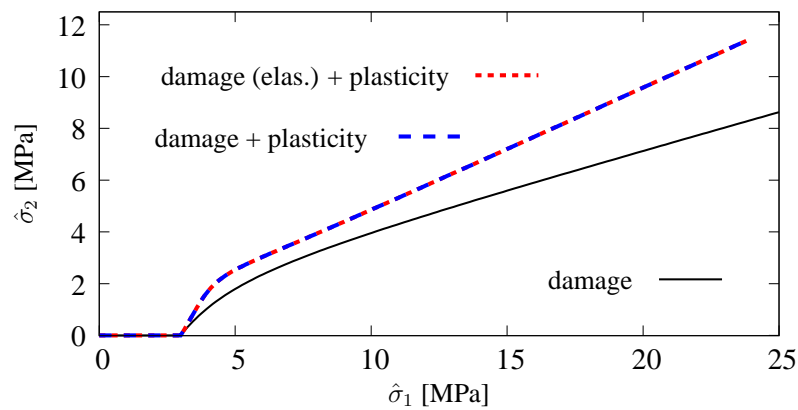
Figure 2.26: Willam’s test – evolution of principal stresses for different kinds of scalar model.



(a) Change of principal directions.



(b) Difference for dilatancy  $\theta$ .



(c) Difference for principal effective stresses.

Figure 2.27: Willam's test – differences between pure and coupled models.

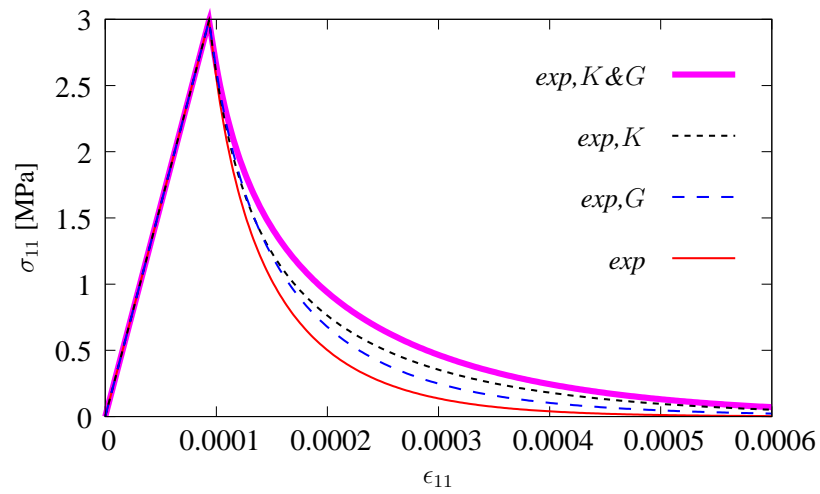
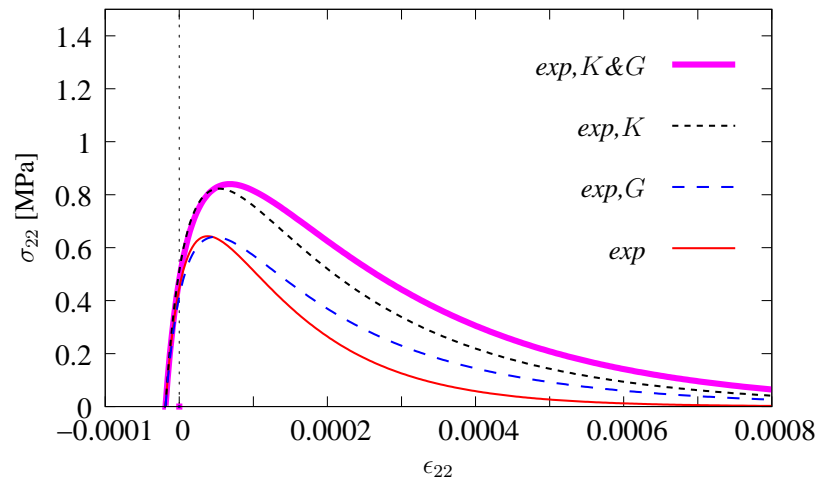
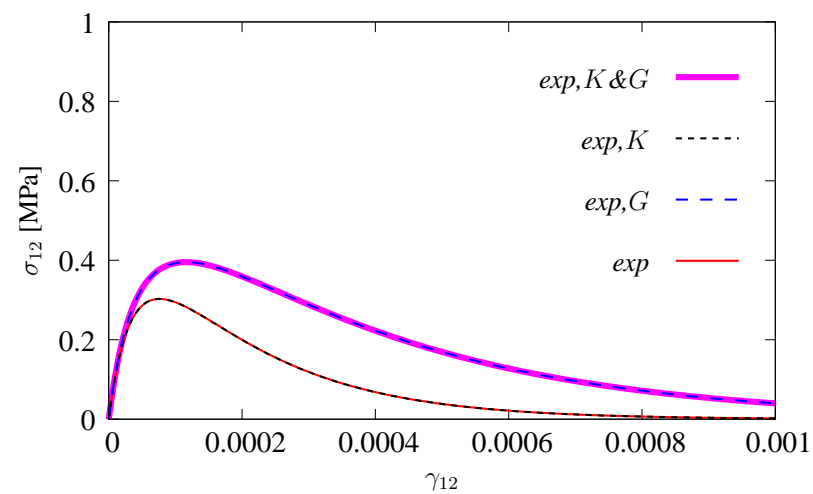
In Fig. 2.27 attention is focused on differences between pure and coupled models, considering: the change of angle of principal directions, the development of dilatancy and the relation between effective principal stresses. It is worth to underline that the response in the context of these aspects is the same whether the equivalent strain measure is based on elastic or total strains. Similarly to the results in [171] after the peak the rotation of principal direction takes place fast, then becomes slower and tends to the angle with value 52.018 deg. For pure damage angle  $\Theta_\sigma$  for principal directions in the stress space changes during evolution together with angle  $\Theta_\epsilon$  for given principal strains, since for damage without any coupling they are coaxial. For the coupled version of the model the change of angle  $\Theta_\sigma$  is faster than the change of  $\Theta_\epsilon$ . It means that the existence of plasticity accelerates the effect of rotation of principal stresses and coaxiality is not preserved. Moreover, in the final stage the angle describing the principal stress directions coincide closer with the theoretical value 52.018 deg than for the pure model. On the other hand if a plastic process is initiated, dilatancy  $\theta$  grows slower than for pure damage (see Fig. 2.27(b)). The difference is also observed in the evolution of principal effective stresses. It is shown in Fig. 2.27(c) that stronger correlation between  $\hat{\sigma}_1$  and  $\hat{\sigma}_2$  occurs for coupled models.

### 2.5.3 RESULTS FOR ISOTROPIC DAMAGE

Similarly to the computations presented in page 36 four cases with different prescribed ductility parameters are considered. The basic case *exp* is for pure scalar damage with  $\eta_K = \eta_G = 4000$ . Next two cases with different ductilities for the volumetric and deviatoric damage are calculated. The case with more smooth exponential softening for deviatoric part with parameters  $\eta_K = 4000$  and  $\eta_G = 2000$  and as effect larger volumetric damage  $\omega_K$  is called *exp,G*. The opposite data  $\eta_K = 2000$  and  $\eta_G = 4000$  are used for the case called *exp,K*, where damage for the deviatoric part governs the solution. To complete the results of Willam's test the case *exp,K&G* with both smaller parameters  $\eta_K = \eta_G = 2000$  is also analyzed. In this subsection the influence of parameters which define the damage growth function on the evolution of Poisson's ratio  $\nu_\omega$  is observed.

In Fig. 2.28 diagrams for cases *exp* and *exp,K&G* determine bounds for cases with different ductility parameters. The stress-strain diagrams for *exp,K* and *exp,G* are placed in exchanged order comparing with the example of uniaxial tension (see page 36). It seems surprising, but only apparently, because the Willam test deals with a different loading history. In Fig. 2.28(c) shear relation  $\gamma_{12}-\sigma_{12}$  is depicted. A full agreement between diagrams for *exp* and *exp,K*, and also between diagrams for *exp,K&G* and *exp,G* is characteristic in this test. It is connected with the fact that these respective cases have the same parameter  $\eta_G$  for the deviatoric part. Another interesting observation is a similar distance between descending branches for relations  $\epsilon_{11}-\sigma_{11}$  and  $\epsilon_{22}-\sigma_{22}$ .



(a) Diagrams of relations  $\epsilon_{11} - \sigma_{11}$ .(b) Diagrams of relations  $\epsilon_{22} - \sigma_{22}$ .(c) Diagrams of relations  $\gamma_{12} - \sigma_{12}$ .Figure 2.28: Willam's test – influence of ductility parameter  $\eta_i$  ( $i = K, G$ ) in isotropic model.

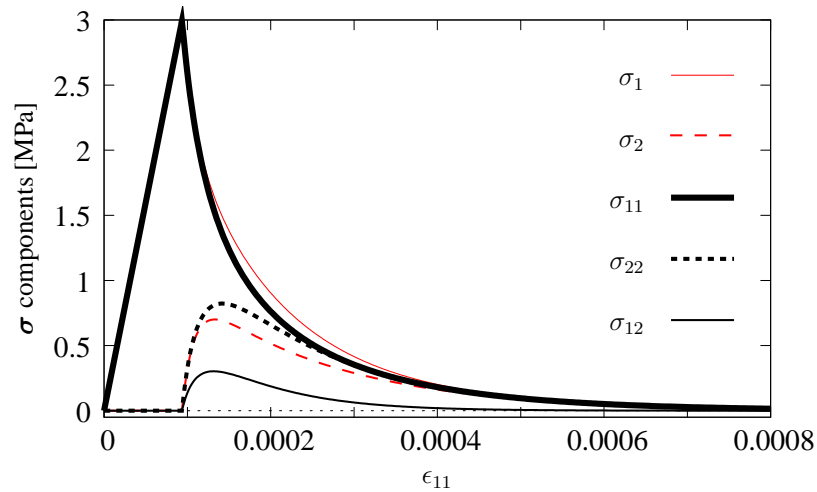
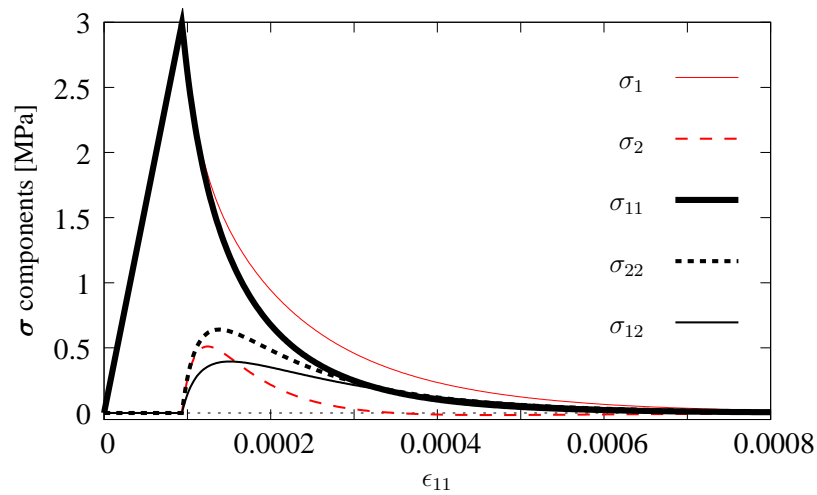
(a) *exp, K,  $\eta_K = 2000, \eta_G = 4000$ .*(b) *exp, G,  $\eta_K = 4000, \eta_G = 2000$ .*

Figure 2.29: Willam's test – comparison of stress components in isotropic model.

Again as a supplement in Fig. 2.29 the components of stress tensor together with principal stresses are presented versus strain  $\epsilon_{11}$ . The figure shows results only for the isotropic model taking into account options with mixed ductility parameters. It is noticed that for case *exp, G* the second principal stress achieves negative values. The final tendency is that all components converge to zero. Both Figs 2.30 and 2.31 show the stress evolution in principal directions. The upper Fig. 2.30 is plotted for all considered cases with  $\alpha = 1.0$ . As it is depicted in enlarged sector the zero value is finally reached. If the parameter  $\alpha$  is less than 1.0, e.g.  $\alpha = 0.97$  like for Fig. 2.31, the residual values remain. In this option the complete loss of material stiffness is avoided and as a consequence the final stresses should be non-zero.

A crucial difference between the adopted numerical stability parameters  $\alpha$  (1.0 or 0.97) is brought out in Fig. 2.32(a) during Poisson's ratio  $\nu_\omega$  evolution. If  $\alpha$  is equal to 1 the lower or

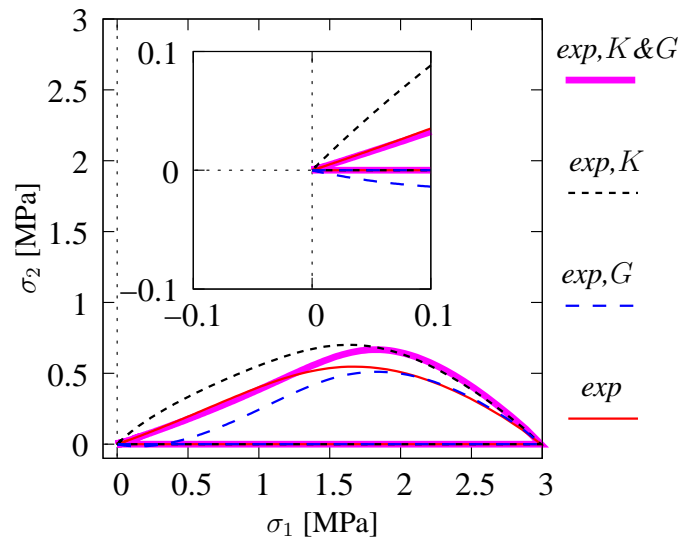


Figure 2.30: Willam's test – evolution of principal stresses for isotropic model,  $\alpha = 1.0$ .

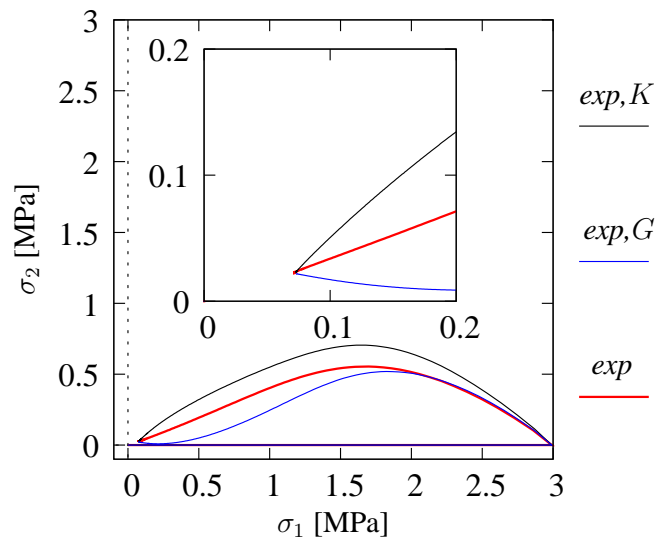
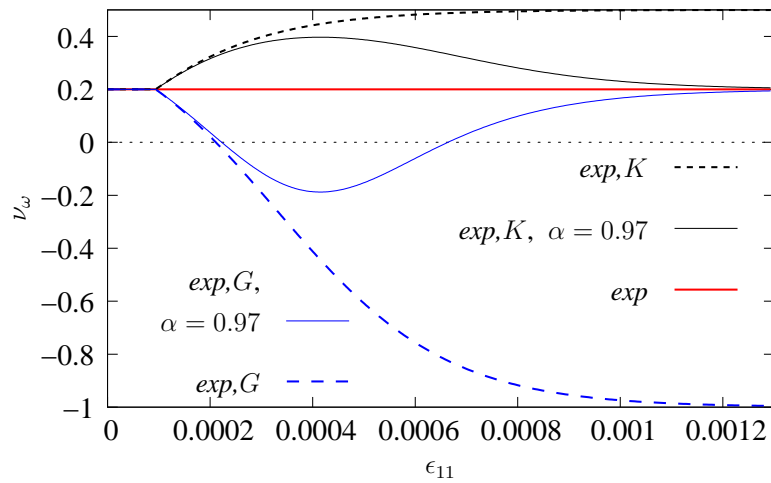
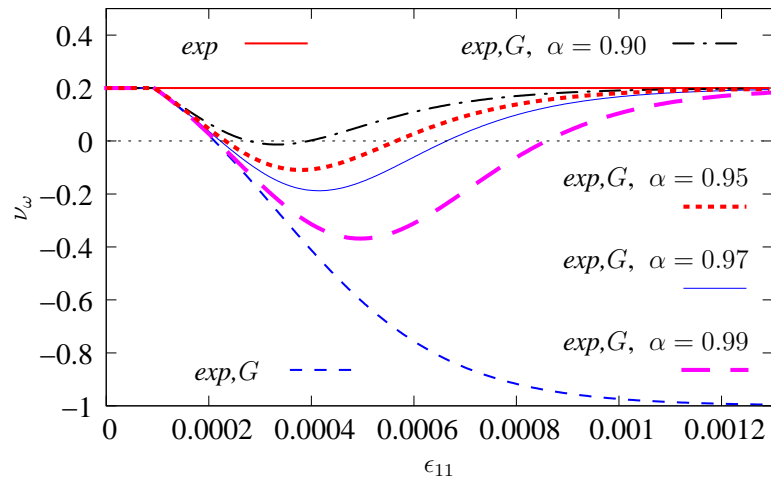
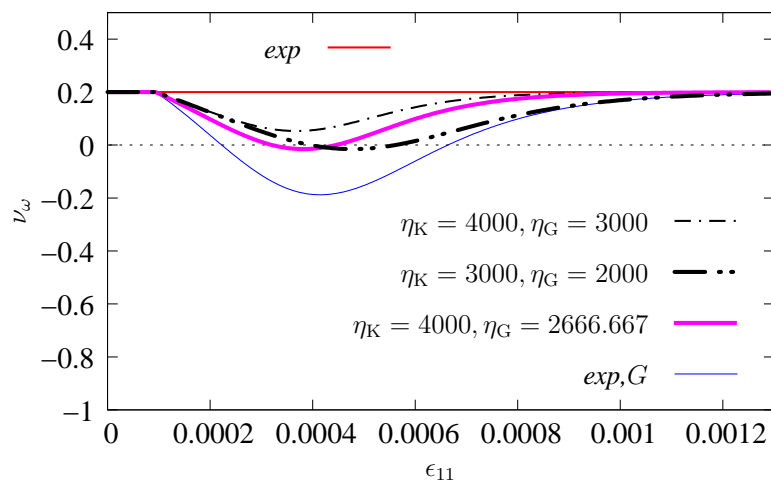


Figure 2.31: Willam's test – evolution of principal stresses for isotropic model,  $\alpha = 0.97$ .

upper limit of  $\nu_\omega$  is reached, while the value of  $\nu_\omega$  returns to the initial one for  $\alpha = 0.97$  after increasing for case *exp,K* and decreasing for case *exp,G*. It was mentioned in the previous section that for quasi-brittle materials like concrete a decreasing of Poisson's ratio is expected (see also [21]), but negative values are rather non-physical and undesirable. Attention is focused on case *exp,G*, where the values of  $\nu_\omega$  are less or at most equal to given in data. It is possible to setup both parameters  $\alpha$  and  $\eta$  separately for volumetric and deviatoric part in such way that negative Poisson's ratio can be prevented. The results in subfigures 2.32(b) and 2.32(c) confirm the above conclusion. The first manner is the reduction of the value of  $\alpha$ , but then a too large residual stresses can remain (not shown here). Secondly the proportion between ductility parameters results in a smaller or larger drop of Poisson's ratio. It turns out that cases with

(a) Different relations between parameters  $\alpha$  and  $\eta_i$  ( $i = K, G$ ).(b) Influence of  $\alpha$ .(c) Influence of different  $\eta_i$  ( $i = K, G$ ),  $\alpha = 0.97$ .Figure 2.32: Willam's test – sensitivity of Poisson's ratio  $\nu_\omega$  in isotropic model.

parameters  $\eta_K = 4000$ ,  $\eta_G = 2666.667$  and  $\eta_K = 3000$ ,  $\eta_G = 2000$  have an identical lower limit. The smaller the difference between  $\eta_K$  and  $\eta_G$  is, the less drastical evolution of Poisson's ratio is noticed. This holds only if  $\alpha < 1.0$  (see Fig. 2.32(c)).

Summarizing this section the results for all the options of the model satisfy the conditions to pass the Willam test.



## CHAPTER 3

# FINITE ELEMENTS FOR GRADIENT DAMAGE

### 3.1 PROPOSALS OF GRADIENT ENHANCEMENT FOR DAMAGE

The damage theory coupled to plasticity and additionally including the crack closure effect, presented in the previous chapter, has been formulated in the local approach, so it of course does not ensure a proper numerical reproduction of failure processes in plain or reinforced concrete (see Section 1.2 and Appendix A). For softening materials like concrete, when the tangent stiffness becomes negative, in the formulation for statics the loss of ellipticity occurs. Analogically the loss of hyperbolicity is noticed in the formulation for dynamics. Mathematically the ill-posedness of the IBVP is the cause that an infinite number of solutions can be received. Physically it is connected with the onset of strain localization which is then observable in the considered domain. The zone of localization has a discrete form (line or surface). In numerical modelling the loss of well-posedness results in a spurious mesh sensitivity. This well-known problem can be overcome using different regularization techniques (see details in Section 1.2). In the dissertation it is assumed that the plasticity model exhibits hardening, so that softening can only be caused by damage. Therefore, the damage theory is made nonlocal, while the plasticity theory remains standard.

The consideration starts from the assumption that a given stress state at a material point  $\boldsymbol{x}$  corresponding to time instant  $t$  during the loading history depends not only on state variables at this point but also on points in the neighbourhood. The non-locality in the damage theory (cf. [7, 10, 129]) can be introduced by a relation of the damage measure  $\omega$  with the equivalent strain measure  $\tilde{\epsilon}$  treated as non-local (averaged):

$$\bar{\epsilon}(\boldsymbol{x}) = \int_{\mathcal{B}} g(\boldsymbol{x}, \boldsymbol{s}_x) \tilde{\epsilon}(\boldsymbol{s}_x) dV \quad (3.1)$$

Here  $\boldsymbol{s}_x$  denotes the source point around which the non-local weight function  $g(\boldsymbol{x}, \boldsymbol{s}_x)$  is spanned.

The weight function is correlated with distance  $r$  between points  $\mathbf{s}_x$  and  $\mathbf{x}$  in domain  $\mathcal{B}$ :

$$r = \|\mathbf{x} - \mathbf{s}_x\| \quad (3.2)$$

The function  $g$  is non-negative and monotonically decreasing with the increase of distance  $r$  [68]. Therefore the smaller is the distance from the considered point  $\mathbf{x}$ , the stronger is the influence of the stress state at the origin  $\mathbf{s}_x$ . During averaging according to Eq. (3.1) an arbitrary constant field should not be modified [17, 72]. Next to boundaries the weight function  $g$  is scaled to prevent changing the uniform field, so the presence of a boundary does not modify the symmetry of the efficient weighting. Different averaging techniques in the proximity of boundaries are proposed and compared in [72]. The weight function  $g(r)$  is usually accepted as the Gauss distribution:

$$g(r) = \exp\left(-\frac{r^2}{2l^2}\right) \quad (3.3)$$

where  $l$  denotes an internal length parameter. An alternative distribution is the so-called bell-shaped function, applied for example in [68].

In this thesis a gradient-enhanced model according to [55, 117, 125, 126] has been selected from among the group of models producing mesh-independent results. Generally, applying higher-order gradients of a considered field can be motivated physically by two different concepts, as illustrated in [5]. If regularization of certain discontinuities is demanded, higher-order gradients smooth the heterogeneity of this field. The opposite way is introducing the heterogeneity into the considered field in order to obtain its exact representation in the microstructure. In Fig. 3.1 the strain field in one dimension is depicted before (on the left) and after (on the right) the operation of applying higher-order gradients.

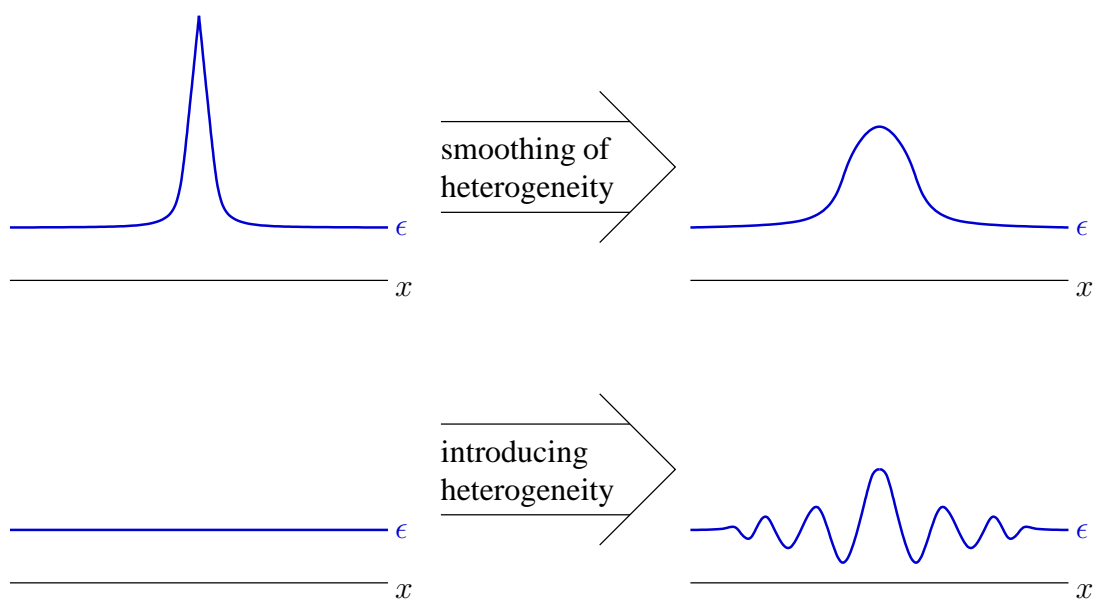


Figure 3.1: Two consequences of using higher-order gradients. Based on [5].



Eq. (3.1) valid for non-local damage can be rewritten upon the Taylor series expansion of the equivalent strain measure  $\tilde{\epsilon}$ . Then it gives due to the isotropy of the weighting function the following expression (odd terms disappear):

$$\bar{\epsilon}(\mathbf{x}) = \tilde{\epsilon}(\mathbf{x}) + c\nabla^2\tilde{\epsilon}(\mathbf{x}) + d\nabla^4\tilde{\epsilon}(\mathbf{x}) + e\nabla^6\tilde{\epsilon}(\mathbf{x}) + \dots \quad (3.4)$$

where  $\nabla^2 = \frac{\partial^2}{\partial x^2} + \frac{\partial^2}{\partial y^2} + \frac{\partial^2}{\partial z^2}$  and  $\nabla^{2n} = (\nabla^2)^n$ . The successive coefficients  $c$ ,  $d$  and so on can be related to an internal length parameter as  $c = \frac{1}{2}l^2$ ,  $d = \frac{1}{8}l^4$  and so on [4]. The expansion in Eq. (3.4) truncated after the second order term gives an explicit gradient enhancement for averaged strain measure  $\bar{\epsilon}$ :

$$\bar{\epsilon}(\mathbf{x}) = \tilde{\epsilon}(\mathbf{x}) + c\nabla^2\tilde{\epsilon}(\mathbf{x}) \quad (3.5)$$

The averaged strain measure  $\bar{\epsilon}$  is then calculated from the local equivalent strain measure  $\tilde{\epsilon}$  and its second-order derivatives. As discussed in [127] the second-order derivative is a local quantity, so as a consequence the explicit gradient model remains local. The truly non-local character could be guaranteed only if each term in the Taylor series expansion was included. Derivations presented in [127] suggest that the explicit gradient model is not able to describe the cracking phenomenon properly.

On the other hand a so-called implicit gradient enhancement can be obtained as follows. The second derivative from both sides of Eq. (3.4) is multiplied by parameter  $c$ :

$$c\nabla^2\bar{\epsilon}(\mathbf{x}) = c\nabla^2\tilde{\epsilon}(\mathbf{x}) + c^2\nabla^4\tilde{\epsilon}(\mathbf{x}) + cd\nabla^6\tilde{\epsilon}(\mathbf{x}) + \dots \quad (3.6)$$

Next the term  $c\nabla^2\tilde{\epsilon}(\mathbf{x})$  is derived from Eq. (3.6) and substituted into Eq. (3.4). Neglecting again the fourth and higher order terms the relationship below is obtained:

$$\bar{\epsilon}(\mathbf{x}) - c\nabla^2\bar{\epsilon}(\mathbf{x}) = \tilde{\epsilon}(\mathbf{x}) \quad (3.7)$$

in which the  $\nabla^2$  operator acts on the averaged strain. Gradient terms of orders higher than two are indirectly contained in the implicit enhancement, so that now the truly non-local character is preserved, as confirmed in [127]. It is also shown there that this implicit enhancement is formally equivalent with the non-local approach if a specific weighting function  $g$  is selected. In this thesis the regularization is performed for damage using Eq. (3.7) and moreover that model is coupled to local hardening plasticity. Relation (3.7) is called the averaging Helmholtz equation or the diffusion equation. It involves the second gradients of the averaged strain  $\bar{\epsilon}$ . The fourth gradients can be also included, but it requires advanced spatial discretization like for example the Element-Free Galerkin method (see [3]). The parameter  $c > 0$  has a unit of length squared and it is connected with the internal length scale  $l$  of a material. The relation  $c = \frac{1}{2}l^2$  is derived for instance in [4]. In this work the parameter  $c$  is assumed to be constant, however, with some modifications in the formulation, it can be made a function of  $\tilde{\epsilon}$  or  $\bar{\epsilon}$ . These three-field formulations, which treat the parameter  $c$  as variable depending on the gradient activity, are investigated in [55]. They are called failure based transient-gradient damage (with nodal

values of continuous damage  $\omega$ ) or strain based transient-gradient damage (with nodal values of gradient activity variable). It is presented in [124] that for the implicit gradient enhancement the loss of ellipticity is avoided. The characteristic determinant derived from the acoustic tensor for the gradient damage is positive for all  $\omega < 1$ , so during failure process, after the onset of localization, but until the total loss of the stiffness ( $\omega = 1$ ), the governing system of equations remains elliptic. The damage theory combined with plasticity, but with averaging of  $\tilde{\epsilon}$  in a non-local integral manner, is employed in [17].

Instead of the gradient enhancement of the equivalent strain  $\tilde{\epsilon}$  it is possible to determine the damage history parameter  $\kappa^d$  as a nonlocal variable by a similar expansion like in Eq. (3.4) and neglecting the fourth and higher order terms:

$$\bar{\kappa}^d = \kappa^d + c\nabla^2\kappa^d \quad (3.8)$$

It is emphasized that the damage history parameter  $\kappa^d$  continuously increases during the loading process since it is remembered as a maximum value of the equivalent strain  $\tilde{\epsilon}$ . In numerical analysis this difference may reveal for example during unloading. Non-local damage combined with local plasticity, where  $\kappa^d$  is smoothed by an integral as in Eq. (3.1), is presented in [61]. The proposals of gradient enhancement for this and other variables are set together in [34]. For example the damage parameter can be directly averaged as follows:

$$\bar{\omega} = \omega + c\nabla^2\omega \quad (3.9)$$

The interpretation of parameter  $c$  can be different for different versions of the gradient enhancement. The spatial gradient of considered variable can also be introduced directly into a damage loading function in the stress space like for instance the averaged damage parameter in [26]. For so-called stress-based damage models a damage strain tensor written in a vector form can be introduced [34]:

$$\epsilon^d = \omega \epsilon \quad (3.10)$$

Furthermore, this field can be enhanced using equivalent damage strain measure  $\tilde{\epsilon}^d = \tilde{\epsilon}^d(\epsilon^d)$ :

$$\bar{\tilde{\epsilon}}^d = \tilde{\epsilon}^d + c\nabla^2\tilde{\epsilon}^d \quad (3.11)$$

Because of the definition of the loading function in the stress space two last proposals remind gradient plasticity (cf. [35, 116]). Analogically to non-local damage based on the averaging of the displacement field  $\mathbf{u}$  as in [70], the implicit gradient enhancement can be formulated with Helmholtz equations for the displacements:

$$\bar{\mathbf{u}} - c\nabla^2\bar{\mathbf{u}} = \mathbf{u} \quad (3.12)$$

The averaging equation can also be constructed for the effective plastic strain measure:

$$\bar{\kappa}^p - c\nabla^2\bar{\kappa}^p = \kappa^p \quad (3.13)$$

However, this averaging refers to plasticity-induced damage model elaborated in [47], where the damage parameter  $\omega$  is inserted in the yield function:

$$f^P(\boldsymbol{\sigma}, \kappa^P, \bar{\kappa}^P) = \tilde{\sigma}(\boldsymbol{\sigma}) - [1 - \omega(\bar{\kappa}^P)] \sigma_y(\kappa^P) \quad (3.14)$$

Here  $\tilde{\sigma}$  is an equivalent stress measure for stress tensor, cf. Eq. (2.28). The yield strength  $\sigma_y$  is calculated from the plastic history parameter  $\kappa^P$ , treated here as a local equivalent measure. Ductile damage  $\omega$  is a function of nonlocal equivalent measure strain  $\bar{\kappa}^P$ . The damage parameter reduces the yield strength  $\sigma_y$ . This approach seems to be particularly useful for materials like metals, for details see [47]. There are also anisotropic gradient damage models, where analogically to Eq. (3.7) each component of the strain tensor is averaged, cf. [34, 84]. Moreover, according to the theory shown in [83, 154] Helmholtz equation can be interpreted as a condition of balance of micro-momentum. For the strain tensor it is determined as in [83]:

$$\operatorname{div} \boldsymbol{\tau} - \bar{\boldsymbol{\epsilon}} = -\boldsymbol{\epsilon} \quad (3.15)$$

where  $\boldsymbol{\tau} = \boldsymbol{\tau}(\nabla \bar{\boldsymbol{\epsilon}})$  is a certain third-order tensor analogical to the couple-stress tensor in micropolar models. This interpretation is motivated by the interaction of microdefects. For anisotropic materials like layered composites the damage tensor is determined, which corresponds to fiber failure, in-plane matrix failure and out-of-plane matrix failure. In this case a specific set of higher-order variables like in [58] should describe the damage process, so that a multifield formulation is created. Each averaging equation mentioned in this section should be completed with suitable boundary conditions.

## 3.2 GRADIENT DAMAGE WITH ONE OR TWO PARAMETERS

### 3.2.1 GRADIENT SCALAR DAMAGE WITH PLASTICITY – DYNAMICS

#### FORMULATION AND SPACE DISCRETIZATION

A certain domain  $\mathcal{B}$ , occupied by the material body, with boundary  $\partial\mathcal{B}$  is considered and the following identities are valid:

$$\partial\mathcal{B} = \partial\mathcal{B}_{\boldsymbol{t}} \cup \partial\mathcal{B}_{\boldsymbol{u}} \quad \partial\mathcal{B}_{\boldsymbol{t}} \cap \partial\mathcal{B}_{\boldsymbol{u}} = \emptyset \quad (3.16)$$

where  $\partial\mathcal{B}_{\boldsymbol{t}}$  denotes part of boundary with given tractions and  $\partial\mathcal{B}_{\boldsymbol{u}}$  is part of boundary with prescribed displacements. In boundary conditions listed in Table 3.1 vector  $\mathcal{N}$  is the outward normal to the surface of domain  $\mathcal{B}$ . Small strains and motion in time with no damping effects are assumed. Like in the previous chapter time  $t$  will occur in notation if it is necessary for clear explanation.

Table 3.1: Set of initial boundary value problem (IBVP) equations.

PROBLEM EQUATIONS	
Equations of motion:	$\mathbf{L}^T \boldsymbol{\sigma} + \mathbf{b} = \rho \ddot{\mathbf{u}}$ (2.1)
Kinematic equations:	$\boldsymbol{\epsilon} = \mathbf{L} \mathbf{u}$ (2.2)
Constitutive equations	
(damage + plasticity + crack closing):	$\dot{\boldsymbol{\sigma}} = (\mathbf{E}_{\text{tan}} - \mathcal{L} \hat{\boldsymbol{\sigma}}^+ \mathbf{s}^T) \dot{\boldsymbol{\epsilon}}$ (2.85)
BOUNDARY CONDITIONS	
for tractions $\mathbf{t}$ :	$\mathcal{N}^T \boldsymbol{\sigma} = \hat{\mathbf{t}}$ on $\partial \mathcal{B}_t$
for displacements $\mathbf{u}$ :	$\mathbf{u} = \hat{\mathbf{u}}$ on $\partial \mathcal{B}_u$
INITIAL CONDITIONS	
for displacements $\mathbf{u}$ :	$\mathbf{u}(t = 0) = \mathbf{u}_0$
for velocity $\dot{\mathbf{u}}$ :	$\dot{\mathbf{u}}(t = 0) = \mathbf{v}_0$

From the previous section it is assumed that the IBVP, summarized in Table 3.1, is regularized by means of the averaging Helmholtz equation (3.7). Now the following non-standard natural boundary condition is postulated:

$$\mathcal{N}^T \nabla \bar{\boldsymbol{\epsilon}} = 0 \quad \text{on} \quad \partial \mathcal{B} \quad (3.17)$$

After introducing gradient enhancement into the formulation the damage evolution (2.8) has a nonlocal character. Hence a loading function, in which the averaged strain  $\bar{\boldsymbol{\epsilon}}$  governs the damage progress instead of the local equivalent strain  $\tilde{\boldsymbol{\epsilon}}$ , is employed:

$$f^d(\boldsymbol{\epsilon}, \kappa^d) = \bar{\boldsymbol{\epsilon}}(\bar{\boldsymbol{\epsilon}}(\boldsymbol{\epsilon}(t))) - \kappa^d(t) = 0 \quad (3.18)$$

The weak form of equations of motion (2.1) is obtained multiplying them by a variation of the displacement field  $\delta \mathbf{u}$  and integrating:

$$\int_{\mathcal{B}} \delta \mathbf{u}^T (\mathbf{L}^T \boldsymbol{\sigma} + \mathbf{b} - \rho \ddot{\mathbf{u}}) dV = 0 \quad (3.19)$$

Further Green's formula is applied and natural boundary conditions (Table 3.1) are used:

$$\int_{\mathcal{B}} \delta \mathbf{u}^T \mathbf{L}^T \boldsymbol{\sigma} dV = \int_{\partial \mathcal{B}} \delta \mathbf{u}^T \mathcal{N}^T \boldsymbol{\sigma} dS - \int_{\mathcal{B}} (\mathbf{L} \delta \mathbf{u})^T \boldsymbol{\sigma} dV \quad (3.20)$$

Substituting  $\boldsymbol{\epsilon} = \mathbf{L} \mathbf{u}$  the following relation is constructed:

$$\int_{\mathcal{B}} \delta \boldsymbol{\epsilon}^T \boldsymbol{\sigma} dV + \int_{\mathcal{B}} \delta \mathbf{u}^T \rho \ddot{\mathbf{u}} dV = \int_{\mathcal{B}} \delta \mathbf{u}^T \mathbf{b} dV + \int_{\partial \mathcal{B}} \delta \mathbf{u}^T \mathbf{t} dS \quad (3.21)$$

The weak form of Helmholtz equation (3.7) is derived below. The variation of the averaged strain measure  $\delta \bar{\boldsymbol{\epsilon}}$  is introduced:

$$\int_{\mathcal{B}} \delta \bar{\boldsymbol{\epsilon}} (\bar{\boldsymbol{\epsilon}} - c \nabla^2 \bar{\boldsymbol{\epsilon}}) dV = \int_{\mathcal{B}} \delta \bar{\boldsymbol{\epsilon}} \tilde{\boldsymbol{\epsilon}} dV \quad (3.22)$$

The Green's formula results in:

$$\int_{\mathcal{B}} \delta \bar{\epsilon} c \nabla^2 \bar{\epsilon} dV = \int_{\partial \mathcal{B}} \delta \bar{\epsilon} c \mathcal{N}^T \nabla \bar{\epsilon} dS - \int_{\mathcal{B}} (\nabla \delta \bar{\epsilon})^T c \nabla \bar{\epsilon} dV \quad (3.23)$$

Using non-standard natural boundary condition (3.17) the Helmholtz equation in the weak form is determined as:

$$\int_{\mathcal{B}} \delta \bar{\epsilon} \bar{\epsilon} dV + \int_{\mathcal{B}} (\nabla \delta \bar{\epsilon})^T c \nabla \bar{\epsilon} dV = \int_{\mathcal{B}} \delta \bar{\epsilon} \tilde{\epsilon} dV \quad (3.24)$$

Independent interpolations of displacements  $\mathbf{u}$  and averaged strain measure  $\bar{\epsilon}$  are employed in the semi-discrete linear system and a two-field formulation ensues. The primary fields are interpolated in this way:

$$\mathbf{u} = \mathbf{N} \mathbf{a} \quad \text{and} \quad \bar{\epsilon} = \mathbf{h}^T \mathbf{e} \quad (3.25)$$

where  $\mathbf{N}$  and  $\mathbf{h}$  contain suitable shape functions. From the above interpolations the secondary fields  $\epsilon$  and  $\nabla \bar{\epsilon}$  can be computed:

$$\epsilon = \mathbf{B} \mathbf{a} \quad \text{and} \quad \nabla \bar{\epsilon} = \mathbf{g}^T \mathbf{e} \quad (3.26)$$

where  $\mathbf{B} = \mathbf{L} \mathbf{N}$  and  $\mathbf{g}^T = \nabla \mathbf{h}^T$ . To derive matrix equations additionally variations are interpolated:

$$\delta \mathbf{u} = \mathbf{N} \delta \mathbf{a} \quad \text{and} \quad \delta \bar{\epsilon} = \mathbf{h}^T \delta \mathbf{e} \quad (3.27)$$

$$\delta \epsilon = \mathbf{B} \delta \mathbf{a} \quad \text{and} \quad \nabla \delta \bar{\epsilon} = \mathbf{g}^T \delta \mathbf{e} \quad (3.28)$$

and also the time derivatives are employed:

$$\dot{\epsilon} = \mathbf{B} \dot{\mathbf{a}} \quad \text{and} \quad \dot{\bar{\epsilon}} = \mathbf{N} \dot{\mathbf{a}} \quad (3.29)$$

The discretized equations of motion are obtained:

$$\delta \mathbf{a}^T \int_{\mathcal{B}} \mathbf{B}^T \boldsymbol{\sigma} dV + \delta \mathbf{a}^T \int_{\mathcal{B}} \mathbf{N}^T \rho \mathbf{N} \ddot{\mathbf{a}} dV = \delta \mathbf{a}^T \int_{\mathcal{B}} \mathbf{N}^T \mathbf{b} dV + \delta \mathbf{a}^T \int_{\partial \mathcal{B}} \mathbf{N}^T \mathbf{t} dS \quad (3.30)$$

and additionally:

$$\delta \mathbf{e} \int_{\mathcal{B}} \mathbf{h} \mathbf{h}^T \mathbf{e} dV + \delta \mathbf{e} \int_{\mathcal{B}} c \mathbf{g} \mathbf{g}^T \mathbf{e} dV = \delta \mathbf{e} \int_{\mathcal{B}} \mathbf{h} \tilde{\epsilon} dV \quad (3.31)$$

The above discretized averaging equation can also be written in this form:

$$\delta \mathbf{e} \int_{\mathcal{B}} (\mathbf{h} \mathbf{h}^T + c \mathbf{g} \mathbf{g}^T) \mathbf{e} dV = \delta \mathbf{e} \int_{\mathcal{B}} \mathbf{h} \tilde{\epsilon} dV \quad (3.32)$$

Identities (3.30) and (3.32) must hold for any admissible  $\delta \mathbf{a}$  and  $\delta \mathbf{e}$ . Therefore:

$$\int_{\mathcal{B}} \mathbf{B}^T \boldsymbol{\sigma} dV + \int_{\mathcal{B}} \mathbf{N}^T \rho \mathbf{N} \ddot{\mathbf{a}} dV = \int_{\mathcal{B}} \mathbf{N}^T \mathbf{b} dV + \int_{\partial \mathcal{B}} \mathbf{N}^T \mathbf{t} dS \quad (3.33)$$

$$\int_{\mathcal{B}} (\mathbf{h} \mathbf{h}^T + c \mathbf{g} \mathbf{g}^T) \mathbf{e} dV = \int_{\mathcal{B}} \mathbf{h} \tilde{\epsilon} dV \quad (3.34)$$

## TIME DISCRETIZATION (LINEARIZATION)

The IBVP is linearized, hence at nodal points the increments of the primary fields from time  $t$  to time  $t + \Delta t$  must be introduced according to the following decomposition:

$$\mathbf{a}^{t+\Delta t} = \mathbf{a}^t + \Delta \mathbf{a} \quad \text{and} \quad \mathbf{e}^{t+\Delta t} = \mathbf{e}^t + \Delta \mathbf{e} \quad (3.35)$$

Analogically – at the integration points:

$$\boldsymbol{\epsilon}^{t+\Delta t} = \boldsymbol{\epsilon}^t + \Delta \boldsymbol{\epsilon} \quad \text{hence} \quad \tilde{\boldsymbol{\epsilon}}^{t+\Delta t} = \tilde{\boldsymbol{\epsilon}}^t + \Delta \tilde{\boldsymbol{\epsilon}} \quad (3.36)$$

$$\boldsymbol{\sigma}^{t+\Delta t} = \boldsymbol{\sigma}^t + \Delta \boldsymbol{\sigma} \quad (3.37)$$

$$\bar{\boldsymbol{\epsilon}}^{t+\Delta t} = \bar{\boldsymbol{\epsilon}}^t + \Delta \bar{\boldsymbol{\epsilon}} \quad \text{hence} \quad \omega^{t+\Delta t} = \omega^t + \Delta \omega \quad (3.38)$$

For implicit time integration the equations of motion then become:

$$\int_{\mathcal{B}} \mathbf{B}^T (\boldsymbol{\sigma}^t + \Delta \boldsymbol{\sigma}) \, dV + \int_{\mathcal{B}} \mathbf{N}^T \rho \mathbf{N} \ddot{\mathbf{a}}^{t+\Delta t} \, dV = \int_{\mathcal{B}} \mathbf{N}^T \mathbf{b}^{t+\Delta t} \, dV + \int_{\partial \mathcal{B}} \mathbf{N}^T \mathbf{t}^{t+\Delta t} \, dS \quad (3.39)$$

and averaging equation is derived as:

$$\int_{\mathcal{B}} (\mathbf{h} \mathbf{h}^T + c \mathbf{g} \mathbf{g}^T) (\mathbf{e}^t + \Delta \mathbf{e}) \, dV = \int_{\mathcal{B}} \mathbf{h} (\tilde{\boldsymbol{\epsilon}}^t + \Delta \tilde{\boldsymbol{\epsilon}}) \, dV \quad (3.40)$$

Based on Eq. (2.78) or Eq. (2.85) the constitutive relation is taken into account in its incremental version:

$$\Delta \boldsymbol{\sigma} = \mathbf{E}_{\text{tan}}^t \Delta \boldsymbol{\epsilon} - \Delta \omega (\hat{\boldsymbol{\sigma}}^+)^t \quad (3.41)$$

where  $\mathbf{E}_{\text{tan}}^t$  was introduced in Eq. (2.83),  $(\hat{\boldsymbol{\sigma}}^+)^t$  in Eq. (2.79) and the increment of damage  $\Delta \omega$  depends on  $\Delta \bar{\boldsymbol{\epsilon}}$ :

$$\Delta \omega = \left[ \frac{\partial \omega}{\partial \kappa^d} \right]^t \left[ \frac{\partial \kappa^d}{\partial \bar{\boldsymbol{\epsilon}}} \right]^t \Delta \bar{\boldsymbol{\epsilon}} \quad (3.42)$$

In the relation above instead of  $\mathcal{L}$ , defined in Eq. (2.48), a similar identity is applied:

$$\mathcal{G}^t = \left[ \frac{\partial \omega}{\partial \kappa^d} \right]^t \left[ \frac{\partial \kappa^d}{\partial \bar{\boldsymbol{\epsilon}}} \right]^t \quad (3.43)$$

Now interpolations of primary fields (3.25) and their derivatives (3.26) are used:

$$\Delta \boldsymbol{\epsilon} = \mathbf{B} \Delta \mathbf{a} \quad \text{and} \quad \Delta \bar{\boldsymbol{\epsilon}} = \mathbf{h}^T \Delta \mathbf{e} \quad (3.44)$$

and hence Eq. (2.85) in the incremental form is as follows:

$$\Delta \boldsymbol{\sigma} = \mathbf{E}_{\text{tan}}^t \mathbf{B} \Delta \mathbf{a} - \mathcal{G}^t (\hat{\boldsymbol{\sigma}}^+)^t \mathbf{h}^T \Delta \mathbf{e} \quad (3.45)$$

Finally rewriting Eq. (3.39) into a matrix form:

$$\mathbf{K}_{aa} \Delta \mathbf{a} + \mathbf{K}_{ae} \Delta \mathbf{e} + \mathbf{M}_{aa} \ddot{\mathbf{a}}^{t+\Delta t} = \mathbf{f}_{\text{ext}}^{t+\Delta t} - \mathbf{f}_{\text{int}}^t \quad (3.46)$$

The definitions for the submatrices and the right-hand side vectors derived from the equations of motion are assumed as follows:

$$\mathbf{K}_{aa} = \int_{\mathcal{B}} \mathbf{B}^T \mathbf{E}_{\text{tan}}^t \mathbf{B} \, dV \quad (3.47)$$

$$\mathbf{K}_{ae} = - \int_{\mathcal{B}} \mathcal{G}^t \mathbf{B}^T (\hat{\boldsymbol{\sigma}}^+)^t \mathbf{h}^T \, dV \quad (3.48)$$

$$\mathbf{f}_{\text{ext}}^{t+\Delta t} = \int_{\mathcal{B}} \mathbf{N}^T \mathbf{b}^{t+\Delta t} \, dV + \int_{\partial\mathcal{B}} \mathbf{N}^T \mathbf{t}^{t+\Delta t} \, dS \quad (3.49)$$

$$\mathbf{f}_{\text{int}}^t = \int_{\mathcal{B}} \mathbf{B}^T \boldsymbol{\sigma}^t \, dV \quad (3.50)$$

The mass matrix is defined in the standard way:

$$\mathbf{M}_{aa} = \int_{\mathcal{B}} \mathbf{N}^T \rho \mathbf{N} \, dV \quad (3.51)$$

In Eq. (3.40) the increment of equivalent strain measure  $\Delta\tilde{\epsilon}$  is computed from the interpolated displacement increment  $\Delta\mathbf{a}$ :

$$\Delta\tilde{\epsilon} = \left[ \frac{d\tilde{\epsilon}}{d\boldsymbol{\epsilon}} \right]^t \Delta\boldsymbol{\epsilon} = [\mathbf{s}^T]^t \mathbf{B} \Delta\mathbf{a} \quad (3.52)$$

and Eq. (3.40) can be rewritten in the matrix form:

$$\mathbf{K}_{ea} \Delta\mathbf{a} + \mathbf{K}_{ee} \Delta\mathbf{e} = \mathbf{f}_{\epsilon}^t - \mathbf{f}_e^t \quad (3.53)$$

The matrices and vectors in Eq. (3.53) are like in the formulation presented in [125]:

$$\mathbf{K}_{ea} = - \int_{\mathcal{B}} \mathbf{h} [\mathbf{s}^T]^t \mathbf{B} \, dV \quad (3.54)$$

$$\mathbf{K}_{ee} = \int_{\mathcal{B}} (\mathbf{h} \mathbf{h}^T + c \mathbf{g} \mathbf{g}^T) \, dV \quad (3.55)$$

$$\mathbf{f}_{\epsilon}^t = \int_{\mathcal{B}} \mathbf{h} \tilde{\epsilon}^t \, dV \quad (3.56)$$

$$\mathbf{f}_e^t = \mathbf{K}_{ee} \mathbf{e}^t \quad (3.57)$$

Finally, this gradient damage formulation can be written as a coupled matrix problem similar to gradient plasticity [150]:

$$\begin{bmatrix} \mathbf{M}_{aa} & 0 \\ 0 & 0 \end{bmatrix} \begin{bmatrix} \ddot{\mathbf{a}}^{t+\Delta t} \\ \ddot{\mathbf{e}}^{t+\Delta t} \end{bmatrix} + \begin{bmatrix} \mathbf{K}_{aa} & \mathbf{K}_{ae} \\ \mathbf{K}_{ea} & \mathbf{K}_{ee} \end{bmatrix} \begin{bmatrix} \Delta\mathbf{a} \\ \Delta\mathbf{e} \end{bmatrix} = \begin{bmatrix} \mathbf{f}_{\text{ext}}^{t+\Delta t} - \mathbf{f}_{\text{int}}^t \\ \mathbf{f}_{\epsilon}^t - \mathbf{f}_e^t \end{bmatrix} \quad (3.58)$$

### 3.2.2 GRADIENT ISOTROPIC DAMAGE – DYNAMICS

#### FORMULATION AND SPACE DISCRETIZATION

This section concerns the derivation of isotropic damage with a similar gradient enhancement. The governing equations of the IBVP are almost the same like for scalar damage (cf. Table 3.1), but instead of Eq. (2.85) the relation defined in Eq. (2.96) or Eq. (2.105) is included. In the previous chapter (see Section 2.4) two specifications of loading and damage growth functions were presented. In this subsection the averaging procedure is presented for the isotropic model.

If one-measure approach is assumed, the Helmholtz equation (3.7) is still the basis of the two-field formulation like for scalar gradient damage.

In the option with two averaged strain measures two damage loading functions for two averaged strain measures are introduced:

$$f_K^d(\theta, \kappa_K^d) = \bar{\theta} \left( \tilde{\theta}(\theta(t)) \right) - \kappa_K^d(t) = 0 \quad (3.59)$$

$$f_G^d(\epsilon_{\text{dev}}, \kappa_G^d) = \bar{\epsilon}_{\text{dev}} \left( \tilde{\epsilon}_{\text{dev}}(\epsilon_{\text{dev}}(t)) \right) - \kappa_G^d(t) = 0 \quad (3.60)$$

Therefore, two different averaging equations must be introduced:

$$\bar{\theta} - c_K \nabla^2 \bar{\theta} = \tilde{\theta} \quad (3.61)$$

$$\bar{\epsilon}_{\text{dev}} - c_G \nabla^2 \bar{\epsilon}_{\text{dev}} = \tilde{\epsilon}_{\text{dev}} \quad (3.62)$$

and in result a three-field formulation is obtained.

A similar, but much more complicated approach to anisotropic gradient damage model according to the microplane theory was proposed in [83, 84].

Further, attention is focused only on the one-measure idea. The weak form and discretization in space are the same as for scalar gradient damage, so only the discretization in time will be explained, assuming that Eqs (3.33) and (3.34) are the starting point.

#### TIME DISCRETIZATION (LINEARIZATION) – ONE MEASURE

The linearization procedure at the nodal point and at the integration point are the same as for scalar gradient damage apart from the damage parameters. Both are obtained from the averaged strain measure discretization (cf. Eq. (3.38)):

$$\omega_K^{t+\Delta t} = \omega_K^t + \Delta\omega_K \quad \text{and} \quad \omega_G^{t+\Delta t} = \omega_G^t + \Delta\omega_G \quad (3.63)$$

The equations of motion presented in the incremental version in Eq. (3.39) hold and the implicit time integration is used. Next Eq. (3.41) for the scalar theory is replaced by the incremental constitutive relation derived starting from Eq. (2.92) or Eq. (2.96) for the isotropic model with one averaged strain measure:

$$\Delta\sigma = E_{KG}^t \Delta\epsilon - \Delta\omega_K K \Pi \Pi^T \epsilon^t - 2\Delta\omega_G G Q \epsilon^t \quad (3.64)$$



where  $\mathbf{E}_{\text{KG}}^t$  was defined in Eq. (2.88). The increments of damage are computed from the averaged strain measure increments  $\Delta\bar{\epsilon}$ :

$$\Delta\omega_{\text{K}} = \left[ \frac{\partial\omega_{\text{K}}}{\partial\kappa^{\text{d}}} \right]^t \left[ \frac{\partial\kappa^{\text{d}}}{\partial\bar{\epsilon}} \right]^t \Delta\bar{\epsilon} \quad \text{and} \quad \Delta\omega_{\text{G}} = \left[ \frac{\partial\omega_{\text{G}}}{\partial\kappa^{\text{d}}} \right]^t \left[ \frac{\partial\kappa^{\text{d}}}{\partial\bar{\epsilon}} \right]^t \Delta\bar{\epsilon} \quad (3.65)$$

where the derivatives determined in instant  $t$  are:

$$\mathcal{G}_{\text{K}}^t = \left[ \frac{\partial\omega_{\text{K}}}{\partial\kappa^{\text{d}}} \right]^t \left[ \frac{\partial\kappa^{\text{d}}}{\partial\bar{\epsilon}} \right]^t \quad \text{and} \quad \mathcal{G}_{\text{G}}^t = \left[ \frac{\partial\omega_{\text{G}}}{\partial\kappa^{\text{d}}} \right]^t \left[ \frac{\partial\kappa^{\text{d}}}{\partial\bar{\epsilon}} \right]^t \quad (3.66)$$

If the interpolation of the displacements and averaged strain measure in the incremental notation is employed like in Eq. (3.44) the damage increments can be calculated as:

$$\Delta\omega_{\text{K}} = \mathcal{G}_{\text{K}}^t \mathbf{h}^{\text{T}} \Delta\mathbf{e} \quad \text{and} \quad \Delta\omega_{\text{G}} = \mathcal{G}_{\text{G}}^t \mathbf{h}^{\text{T}} \Delta\mathbf{e} \quad (3.67)$$

and further the incremental stress-strain relation is:

$$\Delta\boldsymbol{\sigma} = \mathbf{E}_{\text{KG}}^t \mathbf{B} \Delta\mathbf{a} - [\mathcal{G}_{\text{K}}^t K \boldsymbol{\Pi} \boldsymbol{\Pi}^{\text{T}} + 2\mathcal{G}_{\text{G}}^t G \mathbf{Q}] \boldsymbol{\epsilon}^t \mathbf{h}^{\text{T}} \Delta\mathbf{e} \quad (3.68)$$

Therefore the equations of motion (3.39) change into the matrix form:

$$\mathbf{K}_{aa}^{\text{KG}} \Delta\mathbf{a} + \mathbf{K}_{ae}^{\text{KG}} \Delta\mathbf{e} + \mathbf{M}_{aa} \ddot{\mathbf{a}}^{t+\Delta t} = \mathbf{f}_{\text{ext}}^{t+\Delta t} - \mathbf{f}_{\text{int}}^t \quad (3.69)$$

In comparison to the scalar theory in the equation above only submatrices  $\mathbf{K}_{aa}^{\text{KG}}$  and  $\mathbf{K}_{ae}^{\text{KG}}$  must be defined anew:

$$\mathbf{K}_{aa}^{\text{KG}} = \int_{\mathcal{B}} \mathbf{B}^{\text{T}} \mathbf{E}_{\text{KG}}^t \mathbf{B} \, dV \quad (3.70)$$

$$\mathbf{K}_{ae}^{\text{KG}} = - \int_{\mathcal{B}} \mathbf{B}^{\text{T}} [\mathcal{G}_{\text{K}}^t K \boldsymbol{\Pi} \boldsymbol{\Pi}^{\text{T}} + 2\mathcal{G}_{\text{G}}^t G \mathbf{Q}] \boldsymbol{\epsilon}^t \mathbf{h}^{\text{T}} \, dV \quad (3.71)$$

It should be emphasized that the averaging equation (3.40) has the matrix form exactly like for scalar gradient damage, hence Eq. (3.53) is in force.

Eventually, the following matrix system of equations is used:

$$\begin{bmatrix} \mathbf{M}_{aa} & 0 \\ 0 & 0 \end{bmatrix} \begin{bmatrix} \ddot{\mathbf{a}}^{t+\Delta t} \\ \ddot{\mathbf{e}}^{t+\Delta t} \end{bmatrix} + \begin{bmatrix} \mathbf{K}_{aa}^{\text{KG}} & \mathbf{K}_{ae}^{\text{KG}} \\ \mathbf{K}_{ea} & \mathbf{K}_{ee} \end{bmatrix} \begin{bmatrix} \Delta\mathbf{a} \\ \Delta\mathbf{e} \end{bmatrix} = \begin{bmatrix} \mathbf{f}_{\text{ext}}^{t+\Delta t} - \mathbf{f}_{\text{int}}^t \\ \mathbf{f}_{\epsilon}^t - \mathbf{f}_e^t \end{bmatrix} \quad (3.72)$$

### 3.3 IMPLEMENTATION OF TWO-FIELD FINITE ELEMENTS

In the described gradient damage formulations the displacements  $\mathbf{u}$  and the averaged strain measure  $\bar{\epsilon}$  are approximated independently. After interpolation and discretization the incremental nodal displacements  $\Delta\mathbf{a}$  and the increments of nodal averaged strain measure  $\Delta\mathbf{e}$  are solved for in each time step. Hence the nodal values  $\mathbf{a}$  and  $\mathbf{e}$  are updated using implicit time-integration, which is based on the standard Newmark algorithm for nonlinear problems. This means that within time steps we apply the Newton-Raphson method to retrieve internal equilibrium.

The algorithm for statics, which is the internal iteration in a time step, is described for example in [36, 117, 122].

Below the Newmark algorithm for nonlinear problems in dynamics connected with iterative procedure for considered models will be presented. The following general denotation must be introduced for clarity of the presented algorithm. The mass matrix is:

$$\mathbf{M} = \begin{bmatrix} \mathbf{M}_{aa} & 0 \\ 0 & 0 \end{bmatrix} \quad (3.73)$$

The tangent operator, which is non-symmetric for the scalar and isotropic model, is respectively determined as:

$$\mathbf{K}^t = \begin{bmatrix} \mathbf{K}_{aa} & \mathbf{K}_{ae} \\ \mathbf{K}_{ea} & \mathbf{K}_{ee} \end{bmatrix} \quad \text{and} \quad \mathbf{K}^t = \begin{bmatrix} \mathbf{K}_{aa}^{\text{KG}} & \mathbf{K}_{ae}^{\text{KG}} \\ \mathbf{K}_{ea} & \mathbf{K}_{ee} \end{bmatrix} \quad (3.74)$$

The degrees of freedom (dofs) vector for nodal quantities consists of the nodal displacements and nodal averaged strains:

$$\mathbf{q} = \begin{bmatrix} \mathbf{a} \\ \mathbf{e} \end{bmatrix} \quad (3.75)$$

As a consequence the increments and accelerations of the primary fields can be written as:

$$\Delta \mathbf{q} = \begin{bmatrix} \Delta \mathbf{a} \\ \Delta \mathbf{e} \end{bmatrix} \quad \text{and} \quad \ddot{\mathbf{q}}^{t+\Delta t} = \begin{bmatrix} \ddot{\mathbf{a}}^{t+\Delta t} \\ \ddot{\mathbf{e}}^{t+\Delta t} \end{bmatrix} \quad (3.76)$$

Eventually general vectors for external and internal forces are created:

$$\mathbf{F}_{\text{ext}}^{t+\Delta t} = \begin{bmatrix} \mathbf{f}_{\text{ext}}^{t+\Delta t} \\ 0 \end{bmatrix} \quad \text{and} \quad \mathbf{F}_{\text{int}}^t = \begin{bmatrix} -\mathbf{f}_{\text{int}}^t \\ \mathbf{f}_{\epsilon}^t - \mathbf{f}_e^t \end{bmatrix} \quad (3.77)$$

Further in the notation the upper index  $t + \Delta t$  will be omitted presuming that a quantity without the time indicator is the most up-to-date. After that the system of equations (3.58) or (3.72) is:

$$\mathbf{M} \ddot{\mathbf{q}} + \mathbf{K}^t \Delta \mathbf{q} = \mathbf{F}_{\text{ext}} + \mathbf{F}_{\text{int}}^t \quad (3.78)$$

Now the derivation needed for the Newmark method is presented according to in [150]. Based on the linear approximation of time derivatives, the relations below are exploited:

$$\dot{\mathbf{q}} = \dot{\mathbf{q}}^t + [(1 - \gamma_N) \ddot{\mathbf{q}}^t + \gamma_N \ddot{\mathbf{q}}] \Delta t \quad (3.79)$$

$$\mathbf{q} = \mathbf{q}^t + \dot{\mathbf{q}}^t \Delta t + \left[ \left( \frac{1}{2} - \beta_N \right) \ddot{\mathbf{q}}^t + \beta_N \ddot{\mathbf{q}} \right] (\Delta t)^2 \quad (3.80)$$

where  $\gamma_N$  and  $\beta_N$  are parameters that set the stability and accuracy of the Newmark method. The difference between  $\mathbf{q}$  and  $\mathbf{q}^t$  gives the incremental nodal vector for succeeding time instants:

$$\Delta \mathbf{q} = \mathbf{q} - \mathbf{q}^t \quad (3.81)$$

The following set of the coefficients is introduced in order to abbreviate the notation:

$$c_0 = \frac{1}{\beta_N (\Delta t)^2} \quad c_1 = \frac{1}{\beta_N \Delta t} \quad c_2 = \frac{1}{2\beta_N} - 1 \quad (3.82)$$

$$c_3 = (1 - \gamma_N)\Delta t \quad c_4 = \gamma_N\Delta t \quad (3.83)$$

The first three of them and Eq. (3.81) are useful in the definition of the acceleration vector for instant  $t + \Delta t$  derived from Eq. (3.80):

$$\ddot{\mathbf{q}} = c_0 \Delta \mathbf{q} - c_1 \dot{\mathbf{q}}^t - c_2 \ddot{\mathbf{q}}^t \quad (3.84)$$

After the substitution of the above result into Eq. (3.78) the incremental equation can be solved:

$$\widehat{\mathbf{K}} \Delta \mathbf{q} = \widehat{\mathbf{F}} \quad (3.85)$$

where:

$$\widehat{\mathbf{K}} = \mathbf{K}^t + c_0 \mathbf{M} \quad (3.86)$$

$$\widehat{\mathbf{F}} = \mathbf{F}_{\text{ext}} + \mathbf{M} (c_1 \dot{\mathbf{q}}^t + c_2 \ddot{\mathbf{q}}^t) + \mathbf{F}_{\text{int}}^t \quad (3.87)$$

The matrix  $\widehat{\mathbf{K}}$  can be called the dynamic tangent matrix and the vector  $\widehat{\mathbf{F}}$  denotes the effective load vector (see [150]). Next the incremental correction vector for  $i$ -th internal iteration used to obtain equilibrium in the time step is:

$$d\mathbf{q}^{(i)} = \mathbf{q}^{(i)} - \mathbf{q}^{(i-1)} \quad (3.88)$$

so that:

$$\Delta \mathbf{q}^{(i)} = \Delta \mathbf{q}^{(i-1)} + d\mathbf{q}^{(i)} \quad (3.89)$$

The above suggest computing the last nodal quantity as:

$$\mathbf{q}^{(i)} = \mathbf{q}^t + \Delta \mathbf{q}^{(i-1)} + d\mathbf{q}^{(i)} = \mathbf{q}^t + \Delta \mathbf{q}^{(i)} \quad (3.90)$$

and hence its acceleration:

$$\ddot{\mathbf{q}}^{(i)} = c_0 d\mathbf{q}^{(i)} + \ddot{\mathbf{q}}^{(i-1)} \quad (3.91)$$

The equations of motion with the incremental correction for the  $i$ -th internal iteration take the form:

$$\mathbf{M} \ddot{\mathbf{q}}^{(i)} + \mathbf{K}^{(i-1)} d\mathbf{q}^{(i)} = \mathbf{F}_{\text{ext}} + \mathbf{F}_{\text{int}}^{(i-1)} \quad (3.92)$$

or briefly:

$$\widehat{\mathbf{K}}^{(i-1)} d\mathbf{q}^{(i)} = \widehat{\mathbf{R}} \quad (3.93)$$

Here matrix  $\widehat{\mathbf{K}}^{(i-1)}$  and the residual force vector  $\widehat{\mathbf{R}}$  are defined as:

$$\widehat{\mathbf{K}}^{(i-1)} = \mathbf{K}^{(i-1)} + c_0 \mathbf{M} \quad (3.94)$$

Table 3.2: The algorithm of Newmark method for gradient damage model.

1. Determine constants:	$c_0 = \frac{1}{\beta_N(\Delta t)^2}, c_1 = \frac{1}{\beta_N \Delta t}, c_2 = \frac{1}{2\beta_N} - 1,$	Eq. (3.82)
	$c_3 = (1 - \gamma_N)\Delta t, c_4 = \gamma_N \Delta t$	Eq. (3.83)
2. Initialize for $t = 0$ :	$\mathbf{q}^0, \dot{\mathbf{q}}^0, \ddot{\mathbf{q}}^0$	
3. Compute:	$\widehat{\mathbf{K}} = \mathbf{K}^t + c_0 \mathbf{M}$	Eq. (3.86)
	$\widehat{\mathbf{F}} = \mathbf{F}_{\text{ext}} + \mathbf{M} (c_1 \dot{\mathbf{q}}^t + c_2 \ddot{\mathbf{q}}^t) + \mathbf{F}_{\text{int}}^t$	Eq. (3.87)
4. Solve:	$\widehat{\mathbf{K}} \Delta \mathbf{q} = \widehat{\mathbf{F}}$	Eq. (3.85)
5. $i = 1$ :	$\Delta \mathbf{q}^{(0)} = \Delta \mathbf{q}$	
6. Internal iteration:		
6.1.	$\ddot{\mathbf{q}}^{(i-1)} = c_0 \Delta \mathbf{q}^{(i-1)} - c_1 \dot{\mathbf{q}}^t - c_2 \ddot{\mathbf{q}}^t$	Eq. (3.84)
6.2. IF coupling		
	THEN resolve plasticity	Eq. (2.28)
6.3. IF crack closing		
	THEN compute projection operator $\mathbf{P}^+$	Eq. (2.57)
6.4. Resolve damage		Eq. (2.8)
6.5. Compute current stress $\boldsymbol{\sigma}$		
	and $\mathbf{E}_{\text{tan}}$ (or $\mathbf{E}_{\text{KG}}$ for isotropic model)	
6.6. Update $\mathbf{K}^{(i-1)}$ and $\mathbf{F}_{\text{int}}^{(i-1)}$		
6.7. Compute:	$\widehat{\mathbf{K}}^{(i-1)} = \mathbf{K}^{(i-1)} + c_0 \mathbf{M}$	Eq. (3.94)
	$\widehat{\mathbf{R}} = \mathbf{F}_{\text{ext}} - \mathbf{M} \ddot{\mathbf{q}}^{(i-1)} + \mathbf{F}_{\text{int}}^{(i-1)}$	Eq. (3.95)
7. Solve:	$\widehat{\mathbf{K}}^{(i-1)} d\mathbf{q}^{(i)} = \widehat{\mathbf{R}}$	Eq. (3.93)
8. Update:	$\Delta \mathbf{q}^{(i)} = \Delta \mathbf{q}^{(i-1)} + d\mathbf{q}^{(i)}$	Eq. (3.89)
9. Check convergence:	IF not converged	
	THEN $i = i + 1$ and GO TO point 6.	
	ELSE $\Delta \mathbf{q} = \Delta \mathbf{q}^{(i)}$	
10. Calculate new:	$\ddot{\mathbf{q}} = c_0 \Delta \mathbf{q} - c_1 \dot{\mathbf{q}}^t - c_2 \ddot{\mathbf{q}}^t$	Eq. (3.84)
	$\dot{\mathbf{q}} = \dot{\mathbf{q}}^t + c_3 \ddot{\mathbf{q}}^t + c_4 \ddot{\mathbf{q}}$	Eq. (3.79)
	$\mathbf{q} = \mathbf{q}^t + \Delta \mathbf{q}$	Eq. (3.90)
11. Next time step:	GO TO point 3.	


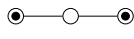
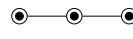
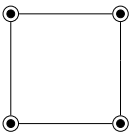
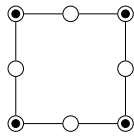
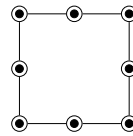
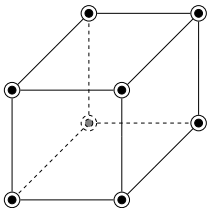
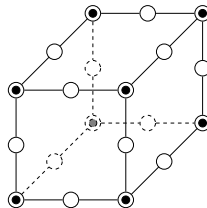
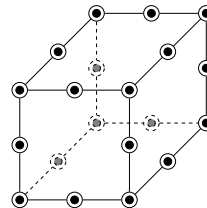
$$\widehat{\mathbf{R}} = \mathbf{F}_{\text{ext}} - \mathbf{M} \ddot{\mathbf{q}}^{(i-1)} + \mathbf{F}_{\text{int}}^{(i-1)} \quad (3.95)$$

Based on the derivation presented above the algorithm from Table 3.2 is employed in the implementation.

The finite elements (FEs) are programmed in the FEAP package [158] using three variants of  $C^0$ -continuous interpolation. For the implicit gradient formulation the  $C^0$ -continuous shape functions are sufficient [125]. Quadrilaterals are available in two-dimensional problems, brick

elements – in three dimensions. In Table 3.3 each element is reviewed, the orders of interpolations, numbers of nodes, degrees of freedom (dofs) and integration points (ips) are compared. Generally, in the first option elements with analogical linear interpolation of both the displacements and the averaged strain are shown. In the thesis these FEs will be called Q4/4 for 2D problems and consequently B8/8 for 3D problems. In the second option quadratic interpolation of the displacements and linear of the averaged strain is assumed, hence a different number of dofs at the corner and midside nodes is required. Hence these FEs in 2D and 3D problems will be called Q8/4 and B20/8, respectively. For the last group of elements (fourth column) – quadratic interpolation of both quantities is introduced. The elements for this third option are

Table 3.3: Available elements for gradient damage model.

1D elements			
$a/e$	lin/lin	quad/lin	quad/quad
nodes	2/2	3/2	3/3
dofs	4	5	6
ips	1	2	2
2D elements			
abbreviation	Q4/4	Q8/4	Q8/8
$a/e$	lin/lin	quad/lin	quad/quad
nodes	4/4	8/4	8/8
dofs	12	20	24
ips	4/1	4	4
3D elements			
abbreviation	B8/8	B20/8	B20/20
$a/e$	lin/lin	quad/lin	quad/quad
nodes	8/8	20/8	20/20
dofs	32	68	80
ips	8	8	27

● -  $a/e$     ○ -  $a$

called Q8/8 for 2D problems and B20/20 for 3D problems. Although the second interpolation option could be optimal, the other possibilities can give stable results, since the analyzed problem is coupled rather than mixed. Thus it is mentioned in [147] that so-called inf-sup condition does not have to be obeyed. Oscillations which may appear for some secondary fields, like for example stress field, have local character i.e. occur only in the zone where damage varies quickly. In any case care should be taken with respect to volumetric locking and excessive shear stiffness, but well-established solutions such as for example  $\bar{B}$  formulation [67] can be adopted just as for ordinary displacement-based elements. The first option with linear interpolation for both fields is implemented in 2D also with possibility of using one sampling point with an hourglass control (for details see next section).

### 3.4 PROPERTIES OF ELEMENTS AND HOURGLASS CONTROL

Firstly in this section attention is focused on the description of the spectral analysis of a single FE including different types of interpolation and integration. One two- or three-dimensional FE with unit dimensions is subjected to tension in one direction. The elastic (weaker) coupling of HMH plasticity with linear hardening and the damage model with linear softening (2.19) is adopted. Loading-unloading path is executed like in Fig. 3.2, in order to detect respective differences in each phase. The computations of the eigenproblem for the tangent operator  $\mathbf{K}$  in each phase are performed for incremental steps marked on the  $\sigma_{11}-\epsilon_{11}$  diagram. The following material data are adopted: Young's modulus  $E = 20000$  MPa, Poisson's ratio  $\nu = 0.20$ , damage threshold  $\kappa_o = 0.0001$ , ultimate damage is for  $\kappa_u = 0.002$ , yield strength  $\sigma_y = 2$  MPa and hardening modulus  $h = E/2$ . The internal length parameter  $c$  can be optionally equal to 1 or 0. It permits one to check the influence of the regularization in FE. The spectrum of eigenvalues will

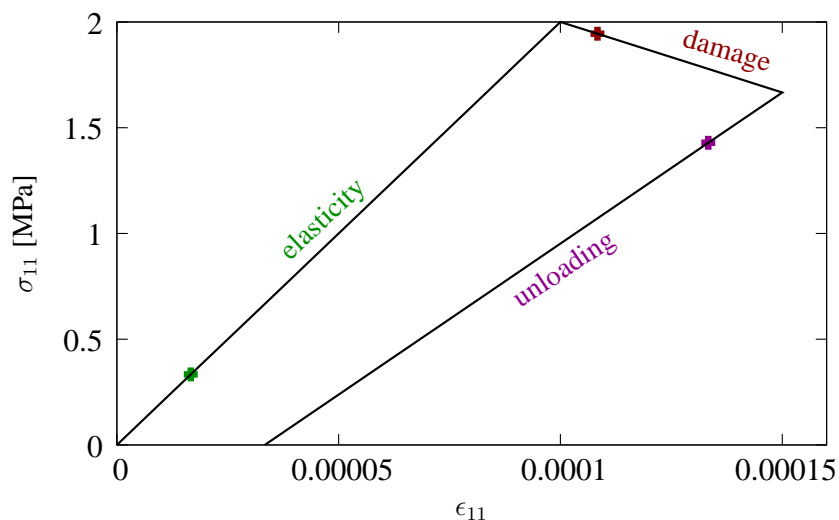


Figure 3.2: Loading-unloading path used in spectral analysis.

be shown in tables for the whole tangent operator  $\mathbf{K}$  and for particular submatrices, respectively  $\mathbf{K}_{aa}$  which is connected with the equilibrium equations and  $\mathbf{K}_{ee}$  – with the averaging equation.

### 3.4.1 FOUR-NODED ELEMENT – SPECTRAL ANALYSIS

Now the analysis is limited to four-noded element called Q4/4, where linear interpolation is employed. In Tables 3.4 and 3.5 there are summarized numbers of positive, zero and negative eigenvalues for different phases of the loading process. Computations with full integration (FI) are correct with respect to the FE quality. The accepted precision is equal to  $1.0^{-10}$ , so that absolute eigenvalue less than this limit is assumed to be zero. Three zero eigenvalues are admitted in the case with FI and as is depicted in Figs 3.3–3.5 they correspond to rigid motions of the element. A negative eigenvalue for  $\mathbf{K}$  appears after the peak during the damage progress and is related to softening in the material model. The non-negative spectrum is restored during unloading. When reduced integration (RI) without any hourglass control is applied, more than three zero eigenvalues appear. Moreover, they originate not only from  $\mathbf{K}_{aa}$ , but also from  $\mathbf{K}_{ee}$ . If  $c = 1$  then altogether six such eigenvalues are present, if  $c = 0$  – the number rises to eight. Extra-zero i.e. spurious eigenvalues can be interpreted by means of specially constructed eigenforms as explained below.

Eigenvectors, which correspond to the eigenvalue spectrum, are depicted in the following way. In every figure coefficients of the eigenvector are split into the part related to displacement dofs  $\mathbf{a}$  and the part connected with dofs  $\mathbf{e}$  for averaged strain measure. The subvectors for the displacement dofs in each direction can be illustrated as a deformed element in the plane. Therefore, the real space of the displacements is plotted blue in the figures. It is emphasized

Table 3.4: Eigenvalues for Q4/4,  $c = 1$ .

(a) FI.									(b) RI.										
s. eigs	Elasticity			Damage			Unloading			s. eigs	Elasticity			Damage			Unloading		
	+	0	-	+	0	-	+	0	-		+	0	-	+	0	-	+	0	-
$\mathbf{K}_{aa}$	5	3	0	5	3	0	5	3	0	$\mathbf{K}_{aa}$	3	5	0	3	5	0	3	5	0
$\mathbf{K}_{ee}$	4	0	0	4	0	0	4	0	0	$\mathbf{K}_{ee}$	3	1	0	3	1	0	3	1	0
$\mathbf{K}$	9	3	0	8	3	1	9	3	0	$\mathbf{K}$	6	6	0	5	6	1	6	6	0

Table 3.5: Eigenvalues for Q4/4,  $c = 0$ .

(a) FI.									(b) RI.										
s. eigs	Elasticity			Damage			Unloading			s. eigs	Elasticity			Damage			Unloading		
	+	0	-	+	0	-	+	0	-		+	0	-	+	0	-	+	0	-
$\mathbf{K}_{aa}$	5	3	0	5	3	0	5	3	0	$\mathbf{K}_{aa}$	3	5	0	3	5	0	3	5	0
$\mathbf{K}_{ee}$	4	0	0	4	0	0	4	0	0	$\mathbf{K}_{ee}$	1	3	0	1	3	0	1	3	0
$\mathbf{K}$	9	3	0	8	3	1	9	3	0	$\mathbf{K}$	4	8	0	3	8	1	4	8	0

that in each phase the tangent operator  $\mathbf{K}$  is non-symmetric, so imaginary parts of components of eigenvectors in the spectral analysis are admitted. If an eigenvector component is complex, its imaginary and real parts are marked by "iu-ru" and "iv-rv", respectively, for the horizontal or vertical axis. In this case the imaginary part of the vector will additionally be presented using a light blue shape of FE. This shape reminds the FE deformation, however the physical interpretation can be performed only if the whole eigenvector is real. An analogical situation is for the averaged strain dofs. The components of eigenvector for this field are shown as shifted vertically and they are marked by the red color. The mark "iASM-rASM" in magenta color denotes the existence of real and imaginary parts of eigenvector component. The magenta shape of FE in vertical direction attempts such representation of a complex number as well. All these illustrations of eigenvectors are called eigenforms or eigenmodes.

Figures 3.3–3.11 collect eigenforms for three specific cases, namely:

- Figs 3.3–3.5: for FE Q4/4 using FI and  $c = 1$ ,
- Figs 3.6–3.8: for FE Q4/4 using RI and  $c = 1$ ,
- Figs 3.9–3.11: for FE Q4/4 using RI and  $c = 0$ .

A detailed interpretation for the first case in the elastic phase (Fig. 3.3) can easily be offered. Eigenmodes for which eigenvalues are positive and blue deformed FE is plotted correspond to the combination of basic states of deformation like tension/compression, shearing and bending. As mentioned in page 73, FE eigenforms for three zero eigenvalues combine the rigid body modes despite the fact that imaginary parts activate. The most interesting are eigenforms marked red related to the averaged strain space for zero values of displacement dofs (inactive deformations). The product  $\mathbf{h} \mathbf{h}^T$  in submatrix  $\mathbf{K}_{ee}$  is the source of a constant field of averaged strain since the eigenvalue equals 0.25 (second row and column in Fig. 3.3). Eigenmodes for both eigenvalues equal 1.0833 make similar linear distributions of averaged strain measure and probably they come from the product  $c \mathbf{g} \mathbf{g}^T$  in submatrix  $\mathbf{K}_{ee}$ . The counterpart for eigenvalue equal to 0.69444 is the vector with a so-called twisted mode for the averaged strain space. Basic vectors for a separated single field (displacement or averaged strain) can be illustrated like in [13]. They constitute a base and their non-zero contributions determine the rank of the tangent operator. After the peak in the damage phase two eigenforms change the character (Fig. 3.4). It is noticed that non-zero values in eigenvectors arise for both subspaces: displacement and averaged strain fields. Indeed, the coupling in the formulation is visible for these modes and one of them corresponds to the negative eigenvalue. If the process falls into unloading the eigenforms are analogical to the elastic phase, see Fig. 3.5.

In the second case, where reduced integration (RI) is applied, the eigenforms agree with the eigenvalue spectrum. Six zero eigenvalues from operator  $\mathbf{K}$  are separated in such a way that five of them originate from the part connected with submatrix  $\mathbf{K}_{aa}$  and the last one - from submatrix  $\mathbf{K}_{ee}$ . It exactly complies with illustrations in Figs 3.6–3.8. Apart from the eigenforms,



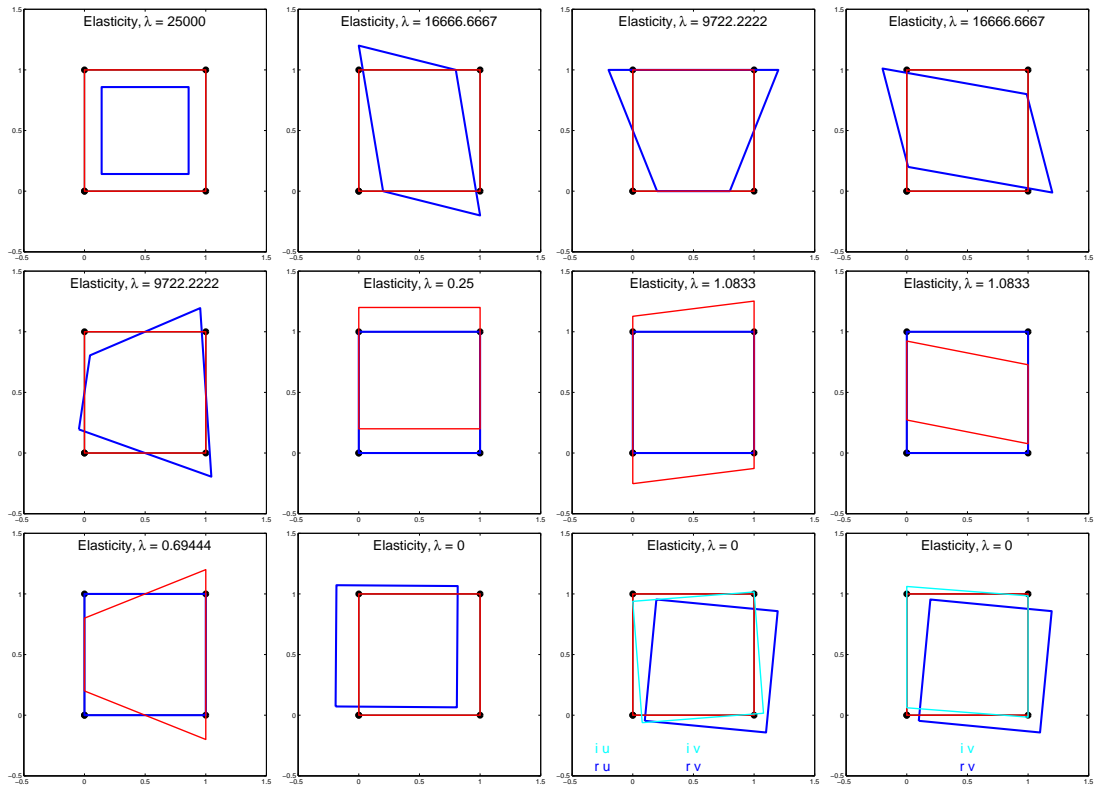


Figure 3.3: Eigenforms for Q4/4, FI,  $c = 1$ , elastic phase.

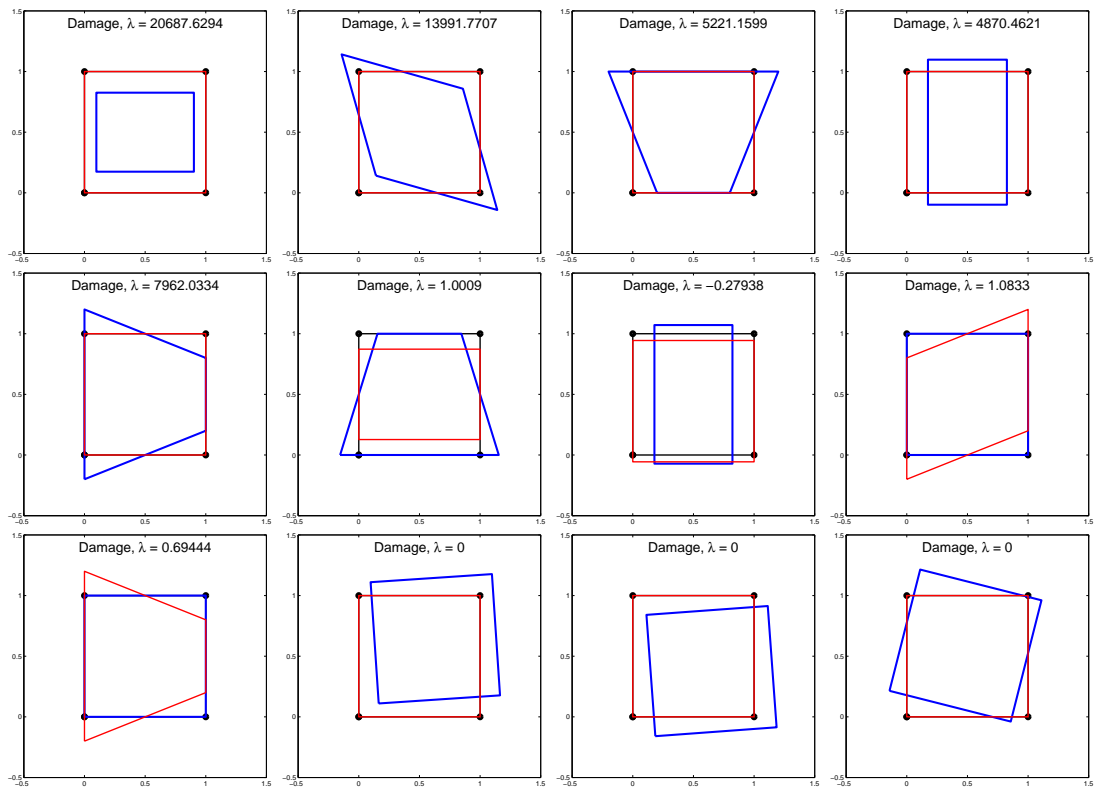


Figure 3.4: Eigenforms for Q4/4, FI,  $c = 1$ , damage phase.

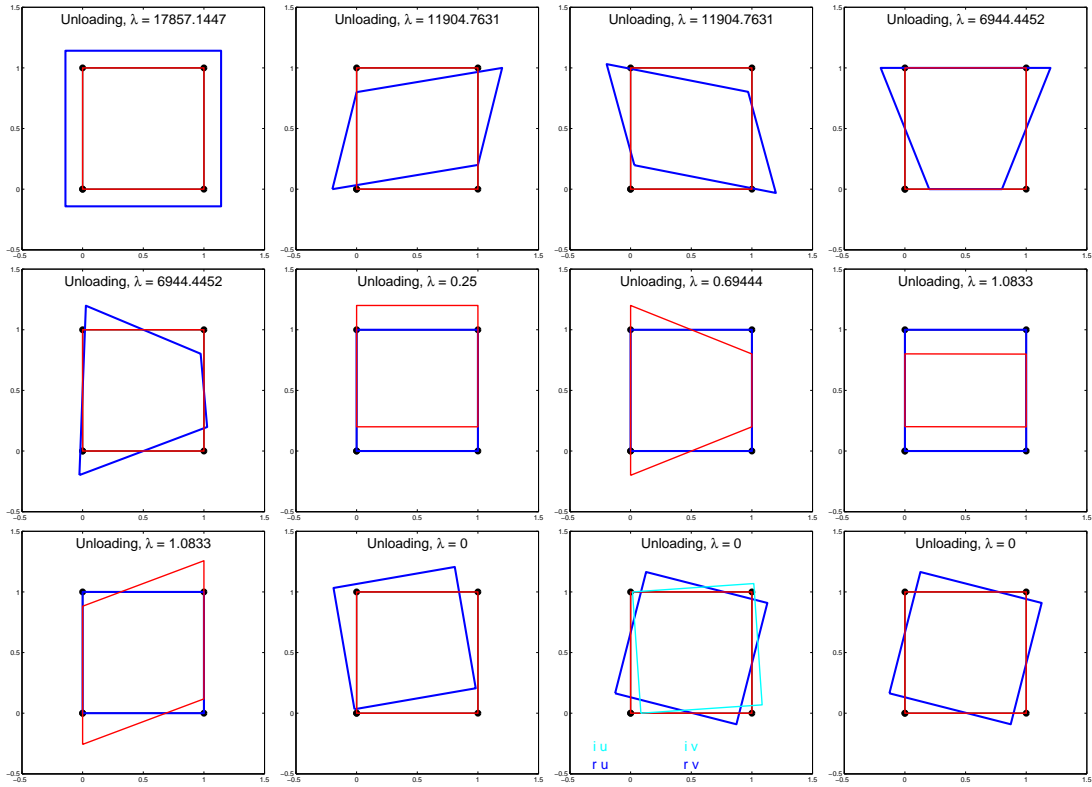


Figure 3.5: Eigenforms for Q4/4, FI,  $c = 1$ , unloading.

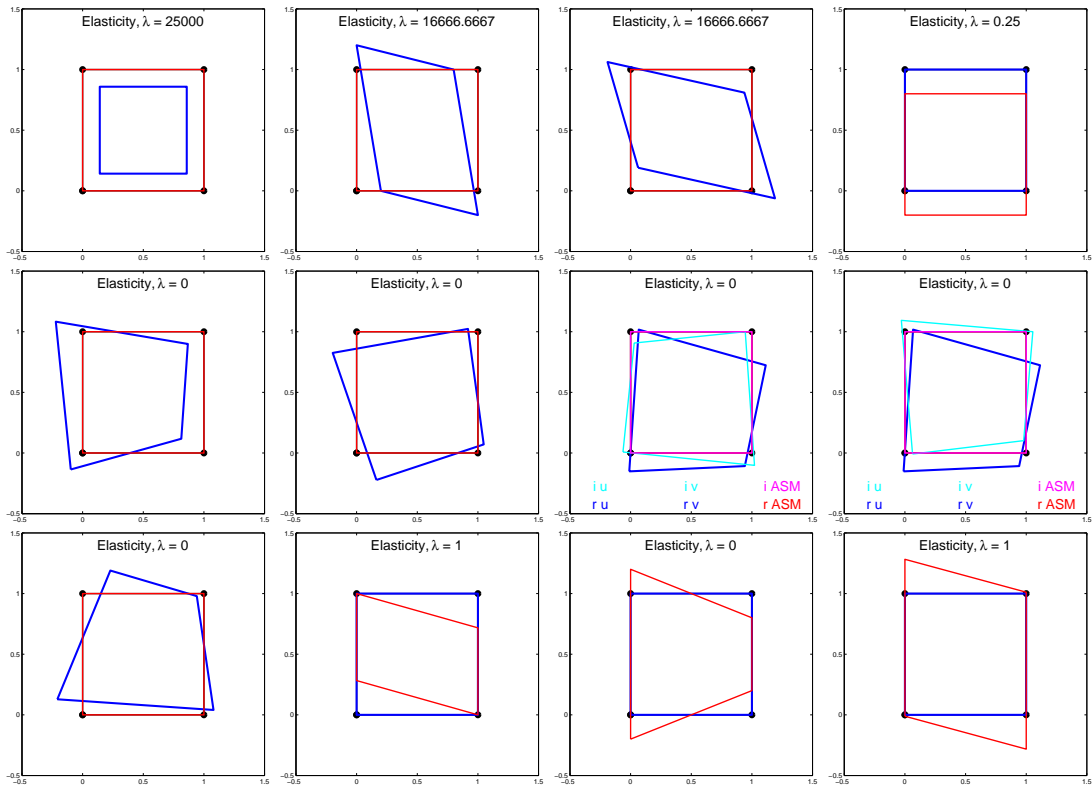


Figure 3.6: Eigenforms for Q4/4, RI,  $c = 1$ , elastic phase.

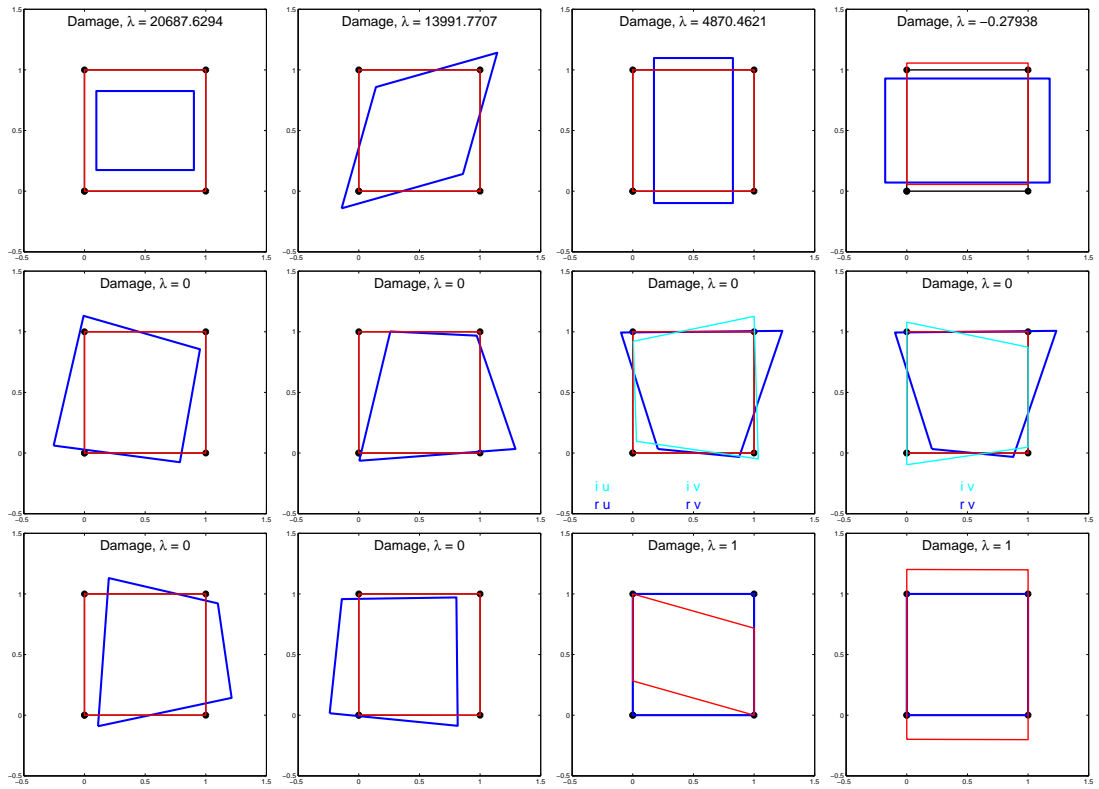


Figure 3.7: Eigenforms for Q4/4, RI,  $c = 1$ , damage phase.

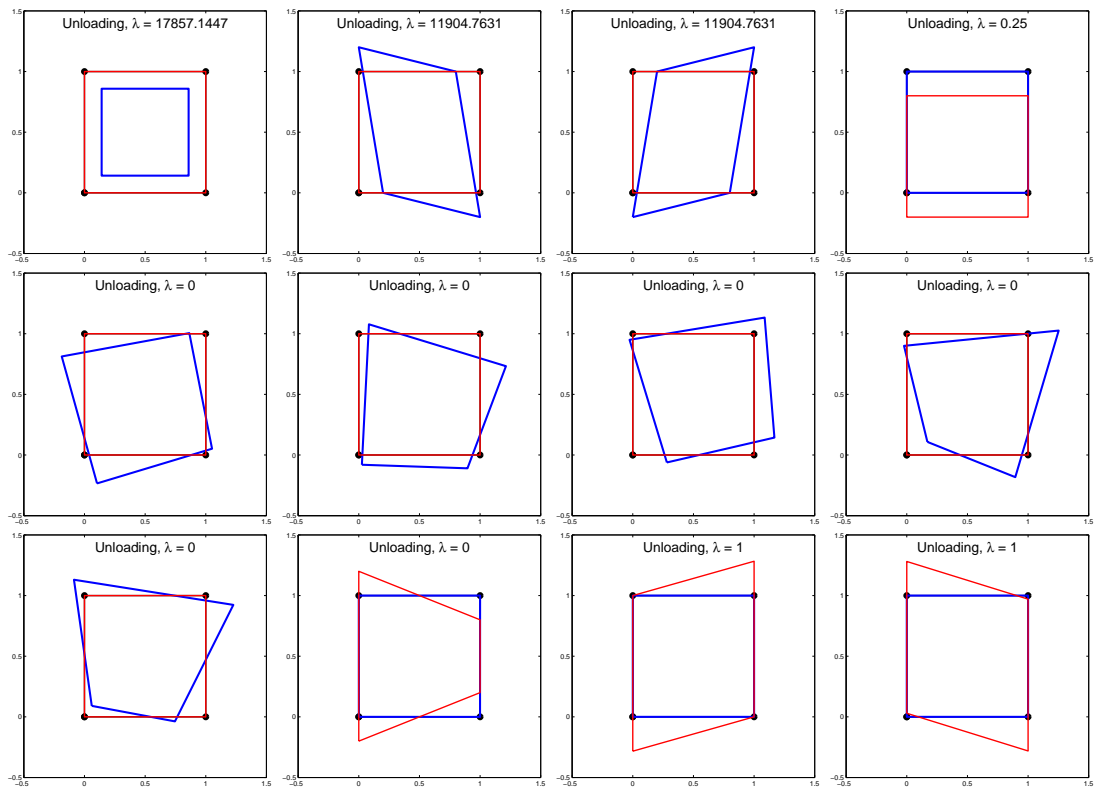


Figure 3.8: Eigenforms for Q4/4, RI,  $c = 1$ , unloading.

where interpretations can be made similarly to the description given in the previous paragraph, the remaining group creates so-called spurious hourglass modes. The vectors corresponding to five zero eigenvalues produce deformed shapes which are combinations of rigid body and in plane bending modes in the displacement field (blue color), cf. Fig. 3.6. Moreover, due to the coupled problem the sixth spurious hourglass mode with a twisted form in the averaged strain space in the elastic phase (third row and column in Fig. 3.6) changes into a non-zero eigenform for displacement dofs and zero form for the averaged strain measure (third row and second column in Fig. 3.7).

The spectrum for the case where RI is used and  $c = 0$  encloses even eight zero eigenvalues. Like previously the eigenforms, depicted in Figs 3.9–3.11, for five of them are associated with spurious modes coming from rigid motions combined with bending. They are non-zero only in the real and imaginary space of the displacements. Identically to previous cases, for the eigenvalue which is equal to 0.25 the constant function is obtained for the averaged strain space (red lines), see first row and last column in Fig. 3.9. Hence this distribution comes from the product  $\mathbf{h} \mathbf{h}^T$  in submatrix  $\mathbf{K}_{ee}$ . After the damage progress starts the eigenvalue becomes negative. Only this mode with the constant field for averaged strain dofs modifies in such a manner that the whole eigenvector is non-zero, again cf. first row and last column, but in Fig. 3.10. That eigenvalue with the corresponding eigenform are recovered during unloading (Fig. 3.11). Three subsequent eigenvalues equal to 0 with spurious eigenforms also correspond to the averaged strain measure. If RI is employed the main difference between the spectrum for  $c = 1$  and  $c = 0$  is in the number of zero eigenvalues and as a consequence – in improper modes. From one for  $c = 1$  the number grows to three for  $c = 0$ . The gradient term coming from the averaging action is eliminated. Hence the product  $c \mathbf{g} \mathbf{g}^T$  in submatrix  $\mathbf{K}_{ee}$  contributes nothing ( $c = 0$ ), thus now linear distributions for the averaged strain field are missing in eigenmodes in each phase.

Anyway, if FE Q4/4 is applied in computations with one integration point (RI), so-called hourglass control must be incorporated in both primary fields in the formulation. Additional spurious eigenforms, which reveal for the displacements and for the averaged strain measure, confirm that hourglass control also known as mesh-stabilization is needed. It permits one to prevent pathology in solutions for the considered problem discretized by meshes with elements Q4/4 and one sampling (integration) point in a FE. It is common that if standard elements with RI are used and improper hourglass modes have any influence on the results, it could lead to singularity of the assembled tangent operator  $\mathbf{K}$  for the structure and the stable numerical analysis become impossible. On the other hand FI can be less effective, especially for large simulated problems. Furthermore under certain boundary conditions FI can cause a locking phenomenon in the mesh. Therefore, beside ideas similar to the  $\bar{B}$  formulation, the concept of computations using one point integration in a FE with hourglass control seems to be attractive for non-linear analysis.

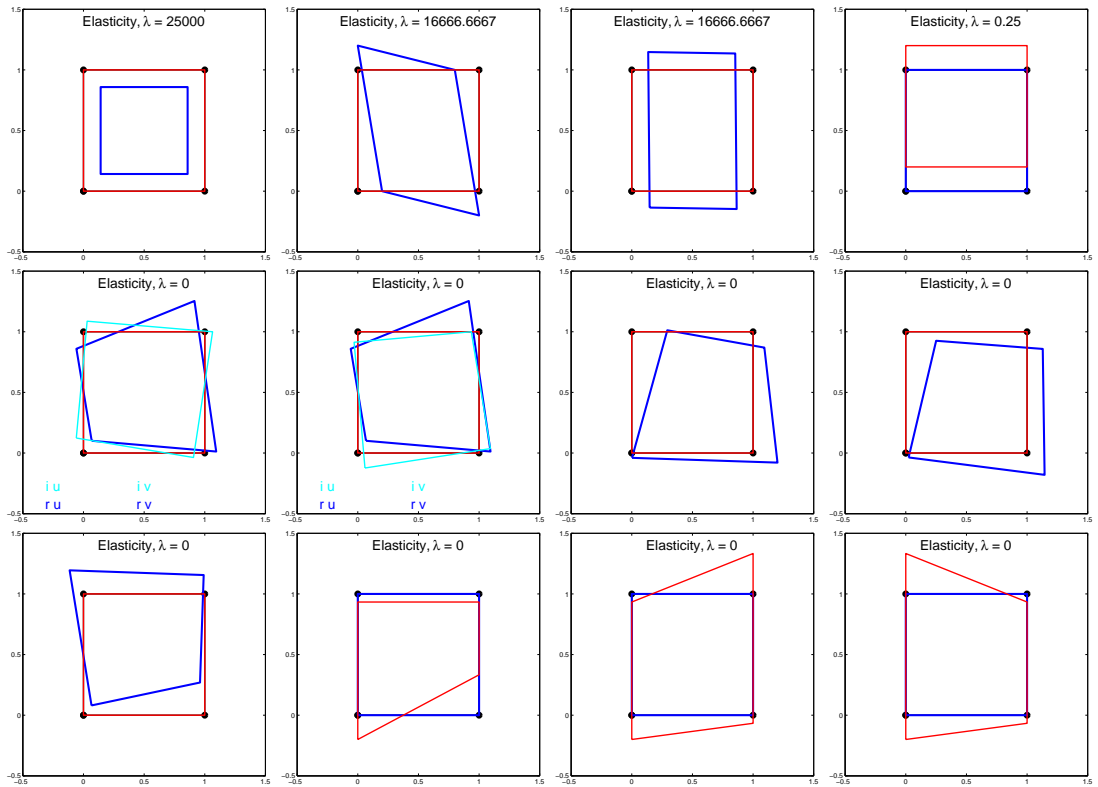


Figure 3.9: Eigenforms for Q4/4, RI,  $c = 0$ , elastic phase.

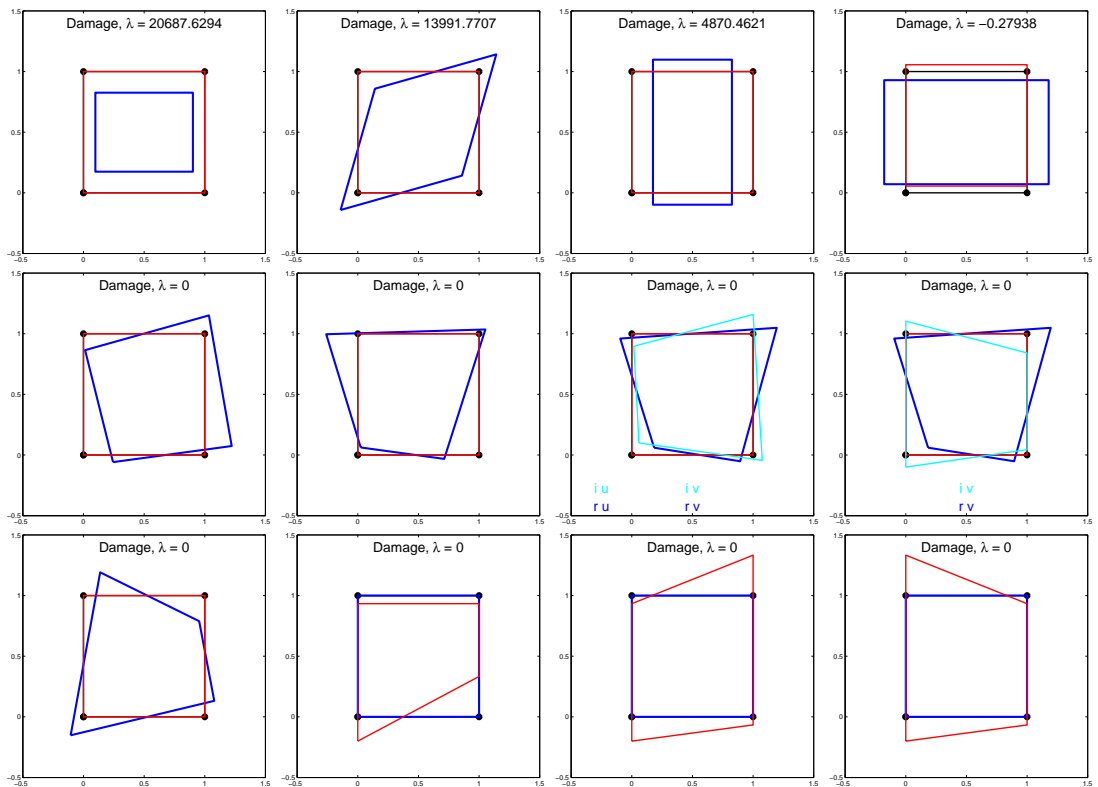
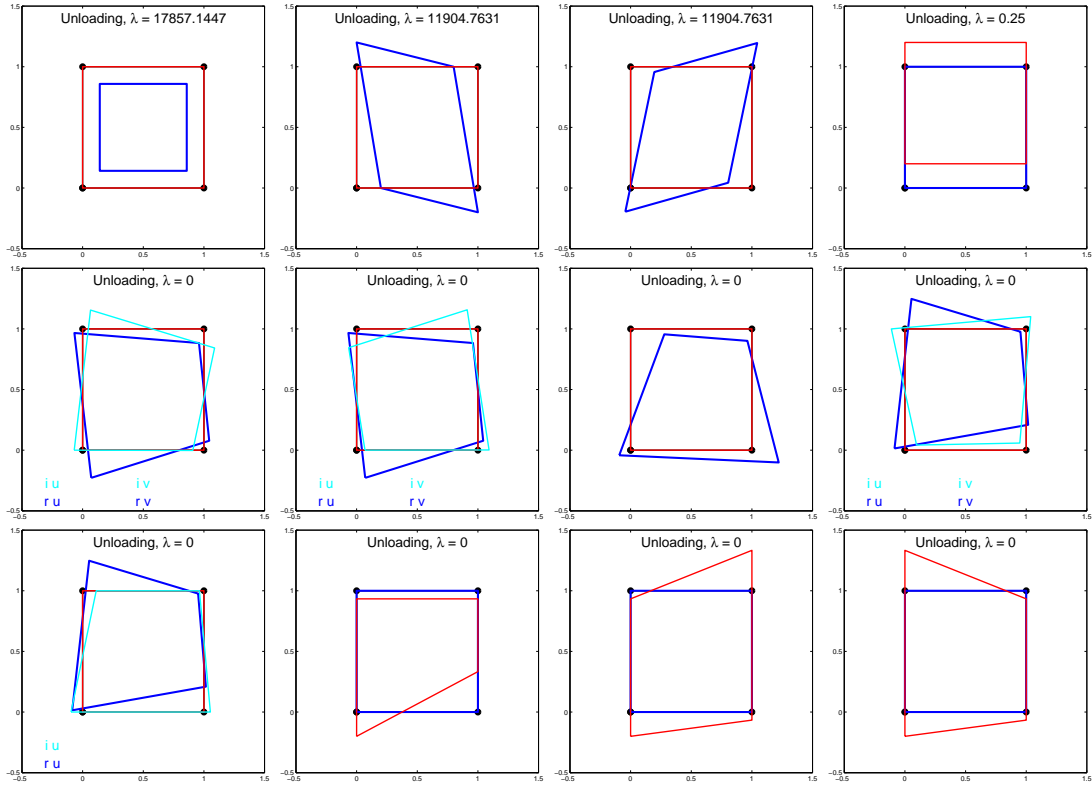


Figure 3.10: Eigenforms for Q4/4, RI,  $c = 0$ , damage phase.

Figure 3.11: Eigenforms for Q4/4, RI,  $c = 0$ , unloading.

### 3.4.2 STABILIZED FOUR-NODED ELEMENT

#### VARIATIONAL EQUATIONS

The standard (static) boundary value problem is considered in this subsection. Now the equations of motion (2.1) are reduced to the equilibrium equations, since  $\rho \ddot{\mathbf{u}} = 0$  in Eq. (2.1). The governing equations are summarized in Table 3.1, but the additional averaging equation (3.7) enhances the formulation in order to overcome the mesh-dependence. The constitutive relations for scalar damage theory combined with hardening plasticity are valid. The corresponding boundary conditions are assumed. As shown in Sections 3.2 and 3.3, apart from the approximation of displacements  $\mathbf{u}$ , the averaged strain measure  $\bar{\mathbf{e}}$  is also employed as a secondary discretized field to regularize the problem. Introducing the spatial interpolation of both fields in the weak form two variational equations can be built as follows (cf. [77, 162]):

$$R_1(\delta \mathbf{a}, \mathbf{a}, \mathbf{e}) = \delta \mathbf{a}^T \int_{\mathcal{B}} \mathbf{B}^T \boldsymbol{\sigma}(\mathbf{a}, \mathbf{e}) dV - \delta \mathbf{a}^T \int_{\mathcal{B}} \mathbf{N}^T \mathbf{b} dV - \delta \mathbf{a}^T \int_{\partial \mathcal{B}} \mathbf{N}^T \mathbf{t} dS \quad (3.96)$$

and

$$R_2(\mathbf{a}, \delta \mathbf{e}, \mathbf{e}) = \delta \mathbf{e}^T \int_{\mathcal{B}} (\mathbf{h} \mathbf{h}^T + c \mathbf{g} \mathbf{g}^T) \mathbf{e} dV - \delta \mathbf{e}^T \int_{\mathcal{B}} \mathbf{h} \tilde{\mathbf{e}}(\mathbf{a}) dV \quad (3.97)$$

Finally, the variational equations can be written in a general form:

$$R(\delta \mathbf{a}, \mathbf{a}, \delta \mathbf{e}, \mathbf{e}) = R_1(\delta \mathbf{a}, \mathbf{a}, \mathbf{e}) + R_2(\mathbf{a}, \delta \mathbf{e}, \mathbf{e}) = 0 \quad (3.98)$$

## STABILIZATION OF EQUILIBRIUM EQUATIONS

The mixed  $\mathbf{u} - p$  formulation in [29, 162] and the mixed formulation for second order continuum in [77] are the starting point for the derivations below. For example the stabilization in the  $\mathbf{u} - p$  formulation presented in [29, 162] is mathematically motivated. It is possible to apply one integration point and control hourglass modes in the solution of equilibrium equations by the Galerkin least-square (GLS) method like in [77, 178]. A stabilization term is added to Eq. (3.96):

$$R_1(\delta \mathbf{a}, \mathbf{a}, \mathbf{e}) + R_1^{\text{stab}}(\delta \mathbf{a}, \mathbf{a}, \delta \mathbf{e}, \mathbf{e}) = 0 \quad (3.99)$$

The term  $R_1^{\text{stab}}$  can be defined according to the GLS method [178] and for continuous fields is written as follows:

$$R_1^{\text{stab}}(\delta \mathbf{u}, \mathbf{u}, \delta \bar{\epsilon}, \bar{\epsilon}) = \sum_{e=1}^{n_{el}} \int_{B^e} (\mathbf{L}^T \boldsymbol{\sigma}(\delta \mathbf{u}, \delta \bar{\epsilon}))^T \boldsymbol{\varphi} (\mathbf{L}^T \boldsymbol{\sigma}(\mathbf{u}, \bar{\epsilon}) + \mathbf{b}) \, dV \quad (3.100)$$

The stabilization scaling matrix  $\chi_1$  is assumed as below:

$$\chi_1 = \frac{\chi h_e^2}{2G} \mathbf{I} \quad (3.101)$$

Here  $\chi$  is an arbitrary, but possibly small value,  $h_e$  is a characteristic length of finite element, for example its diagonal and  $G$  is shear modulus. A further explanation of the definition of  $\chi_1$  and the analysis of units are given in detail in [29].

The weighting part of the stabilization term for the equilibrium equations can be written in the following manner:

$$\mathbf{P}_1(\delta \mathbf{u}, \delta \bar{\epsilon}) = \mathbf{L}^T \boldsymbol{\sigma}(\delta \mathbf{u}, \delta \bar{\epsilon}) = \mathbf{L}^T [(1 - \omega^t(\delta \bar{\epsilon})) \mathbf{E} \boldsymbol{\epsilon}^e(\delta \mathbf{u})] \quad (3.102)$$

As was done with the plastic part in [29], to avoid the linearization of the damage part in Eq.(3.102), the damage contribution is omitted and only the elastic one kept. Further, instead of  $\mathbf{P}_1(\delta \mathbf{u}, \delta \bar{\epsilon})$  its discrete counterpart  $\mathbf{P}_1(\delta \mathbf{a})$  is introduced:

$$\mathbf{P}_1(\delta \mathbf{a}) = \mathbf{L}^T \mathbf{E} \mathbf{B} \delta \mathbf{a} = \mathbf{G}_a^e \delta \mathbf{a} \quad (3.103)$$

where an additional matrix is defined:  $\mathbf{G}_a^e = \mathbf{L}^T \mathbf{E} \mathbf{B}$ .

The equilibrium is obtained at time step  $t + \Delta t$  in subsequent iterations  $i$ :

$$\boldsymbol{\sigma}_{i+1}^{t+\Delta t} = \boldsymbol{\sigma}_i^{t+\Delta t} + d\boldsymbol{\sigma} \quad (3.104)$$

In the following considerations the superscript  $t + \Delta t$  will be skipped. The definition below is introduced:

$$\mathbf{R}_{\sigma, i+1} = \mathbf{L}^T \boldsymbol{\sigma}_{i+1}(\mathbf{u}, \bar{\epsilon}) \quad (3.105)$$

to obtain:

$$\mathbf{R}_{\sigma,i+1} + \mathbf{b} = \mathbf{L}^T(\boldsymbol{\sigma}_i + d\boldsymbol{\sigma}) + \mathbf{b} = \mathbf{R}_{\sigma,i} + d\mathbf{R}_{\sigma} + \mathbf{b} \quad (3.106)$$

The constitutive equation (2.45) in rate form for the damage theory coupled to plasticity can be rewritten:

$$\dot{\boldsymbol{\sigma}} = (1 - \omega) \mathbf{E}^{\text{ep}} \dot{\boldsymbol{\epsilon}} - \dot{\omega} \hat{\boldsymbol{\sigma}} \quad (3.107)$$

The following expression for  $d\mathbf{R}_{\sigma}$  is then derived:

$$d\mathbf{R}_{\sigma} = \mathbf{L}^T [(1 - \omega^t) \mathbf{E}^{\text{ep}} \mathbf{B} da - \mathcal{G}^t \mathbf{E} \boldsymbol{\epsilon}^t \mathbf{h}^T de] \quad (3.108)$$

Further definitions are introduced:

$$\mathbf{E}_{aa} = (1 - \omega^t) \mathbf{E}^{\text{ep}} \quad (3.109)$$

$$\mathbf{E}_{ae} = -\mathcal{G}^t \mathbf{E} \boldsymbol{\epsilon}^t \quad (3.110)$$

so that:

$$d\mathbf{R}_{\sigma} = \mathbf{L}^T (\mathbf{E}_{aa} \mathbf{B} da + \mathbf{E}_{ae} \mathbf{h}^T de) \quad (3.111)$$

Finally, we obtain the residual part:

$$\begin{aligned} \mathbf{R}_{\sigma,i+1} &= \mathbf{R}_{\sigma,i} + \mathbf{L}^T \mathbf{E}_{aa} \mathbf{B} da + \mathbf{L}^T \mathbf{E}_{ae} \mathbf{h}^T de + \mathbf{b} \\ &= \mathbf{R}_{\sigma,i} + \mathbf{G}_a^{\text{epd}} da + \mathbf{G}_e^{\text{epd}} de + \mathbf{b} \end{aligned} \quad (3.112)$$

In the above relation we have:  $\mathbf{G}_a^{\text{epd}} = \mathbf{L}^T \mathbf{E}_{aa} \mathbf{B}$  and  $\mathbf{G}_e^{\text{epd}} = \mathbf{L}^T \mathbf{E}_{ae} \mathbf{h}^T$ .

According to these derivations the stabilization term (3.100) is equal to:

$$R_1^{\text{stab}} = \sum_{e=1}^{nel} \int_{\mathcal{B}^e} (\mathbf{G}_a^e \delta \mathbf{a})^T \chi_1 (\mathbf{R}_{\sigma,i} + \mathbf{G}_a^{\text{epd}} da + \mathbf{G}_e^{\text{epd}} de + \mathbf{b}) dV \quad (3.113)$$

When the following definitions are introduced:

$$\bar{\mathbf{K}}_{aa} = \int_{\mathcal{B}^e} (\mathbf{G}_a^e)^T \chi_1 \mathbf{G}_a^{\text{epd}} dV \quad (3.114)$$

$$\bar{\mathbf{K}}_{ae} = \int_{\mathcal{B}^e} (\mathbf{G}_a^e)^T \chi_1 \mathbf{G}_e^{\text{epd}} dV \quad (3.115)$$

$$\bar{\mathbf{f}} = \int_{\mathcal{B}^e} (\mathbf{G}_a^e)^T \chi_1 (\mathbf{R}_{\sigma,i} + \mathbf{b}) dV \quad (3.116)$$

the final matrix form can be written as:

$$\begin{bmatrix} \mathbf{K}_{aa} + \bar{\mathbf{K}}_{aa} & \mathbf{K}_{ae} + \bar{\mathbf{K}}_{ae} \\ \mathbf{K}_{ea} & \mathbf{K}_{ee} \end{bmatrix} \begin{bmatrix} da \\ de \end{bmatrix} = \begin{bmatrix} \mathbf{f}_{\text{ext}} - \mathbf{f}_{\text{int}} - \bar{\mathbf{f}} \\ \mathbf{f}_{\epsilon} - \mathbf{f}_e \end{bmatrix} \quad (3.117)$$



## STABILIZATION OF AVERAGING EQUATION

In a similar manner a stabilization term can be added to the averaging variational equation (3.97):

$$R_2(\mathbf{a}, \delta \mathbf{e}, \mathbf{e}) + R_2^{\text{stab}}(\delta \mathbf{a}, \mathbf{a}, \delta \mathbf{e}, \mathbf{e}) = 0 \quad (3.118)$$

In fact, in [29, 162] the sign before term  $R_2$  is changed to preserve the positive definiteness of the tangent operator. Here the sign remains positive. Apparently simple to perform, an analogical GLS method seems questionable for the averaging equation. Below three proposals are presented and it is explained, why this doubt appears. The third approach is a method based on the idea presented in [13].

1. GALERKIN LEAST-SQUARE (GLS) METHOD. In this approach for continuous fields  $R_2^{\text{stab}}$  is determined as:

$$R_2^{\text{stab}}(\mathbf{u}, \delta \bar{\epsilon}, \bar{\epsilon}) = \sum_{e=1}^{n_{el}} \int_{\mathcal{B}^e} (\delta \bar{\epsilon} - c \nabla^2 \delta \bar{\epsilon})^T \chi_2 (\bar{\epsilon} - c \nabla^2 \bar{\epsilon} - \tilde{\epsilon}(\mathbf{u})) \, dV \quad (3.119)$$

where  $\chi_2$  is the following stabilization scaling factor:

$$\chi_2 = \frac{\chi h_e^2}{2c} \quad (3.120)$$

This coefficient is calculated according to a dimensional analysis in [29]. The definitions of quantities  $\chi$  and  $h_e$  are as previously,  $c$  is connected with the internal length parameter  $l$  as usual. After discretization and linearization, presented in details in Appendix B, it turns out that for rectangular elements  $\nabla^2 \mathbf{h}^T = \mathbf{0}$ , so then this method does not remove spurious singular modes. Clearly, in this case  $\bar{\mathbf{K}}_{ee}$  is defined by the product  $\mathbf{h} \mathbf{h}^T$  like the original operator  $\mathbf{K}_{ee}$ , so that the hourglass control fails. It can be confirmed by a spectral analysis (see also Appendix B).

2. GRADIENT GALERKIN LEAST-SQUARE (GGLS) METHOD. The idea of this method is taken from [63]. Here for continuous fields  $R_2^{\text{stab}}$  has the form:

$$R_2^{\text{stab}}(\mathbf{u}, \delta \bar{\epsilon}, \bar{\epsilon}) = \sum_{e=1}^{n_{el}} \int_{\mathcal{B}^e} \nabla (\delta \bar{\epsilon} - c \nabla^2 \delta \bar{\epsilon})^T \chi_2 \nabla (\bar{\epsilon} - c \nabla^2 \bar{\epsilon} - \tilde{\epsilon}(\mathbf{u})) \, dV \quad (3.121)$$

where the stabilization scaling matrix  $\chi_2$  is now expressed as:

$$\chi_2 = \chi h_e^2 \mathbf{I} \quad (3.122)$$

Unfortunately, like for GLS method, after discretization and linearization (shown in Appendix B), the stabilization operator  $\bar{\mathbf{K}}_{ee}$  in the matrix equation arises as a result of multiplying matrix  $\mathbf{g}$  and its transposition. An identical term is included in  $\mathbf{K}_{ee}$ , so that hourglass control cannot work. As for GLS method the spectral analysis can verify this observation.

3. OPERATOR  $\gamma$  METHOD. According to [13], if RI is used in four-noded quadrilateral, the results can be stabilized properly by means of the so-called operator  $\gamma$  method (or shortly:  $\gamma$  method). Analogically to the analysis performed there for the Laplace equation, in this approach  $R_2^{\text{stab}}$  is taken into account as:

$$R_2^{\text{stab}}(\delta\bar{\epsilon}, \bar{\epsilon}) = \sum_{e=1}^{n_{el}} \int_{B^e} \delta\bar{g}^T \chi_2 \bar{g} dV \quad (3.123)$$

where  $\chi_2$  is defined in Eq. (3.120). The field  $\bar{g}$  denotes a certain additional gradient connected with the averaged strain field. Discretization must be introduced in a such way that it should satisfy the condition [13]:

$$\bar{g} = 0 \quad (3.124)$$

for any nodal values associated with a linear distribution of  $\bar{\epsilon}$ . On the other hand the identity  $\bar{g} \neq 0$  should be valid if only the distribution of  $\bar{\epsilon}$  is in the so-called improper null-space. In this case the rank of  $\mathbf{K}_{ee}$ , which is equal to 3 for RI (three positive eigenvalues), should be increased to 4 and the hourglass control should be properly introduced. Hence, after [13] operator  $\gamma$  is adopted, which should not influence the linear fields, but affects in the improper null-space:

$$\gamma^T = a [\mathbf{t}_e - (\mathbf{t}_e^T \mathbf{x}_e) \mathbf{g}_x - (\mathbf{t}_e^T \mathbf{y}_e) \mathbf{g}_y] \quad (3.125)$$

where in the above relation additional element quantities must be defined [13]:

$$\mathbf{t}_e^T = [-1, 1, -1, 1] \quad \mathbf{g} = [\mathbf{g}_x \ \mathbf{g}_y] \quad (3.126)$$

$$\mathbf{x}_e^T = [x_{e1}, x_{e2}, x_{e3}, x_{e4}] \quad \mathbf{y}_e^T = [y_{e1}, y_{e2}, y_{e3}, y_{e4}] \quad (3.127)$$

The parameter  $a$  can be equal to 1, because it is an arbitrary constant. The vector  $\mathbf{t}_e$  constitutes in 2D a the twisted form. The nodal coordinates are gathered in vectors  $\mathbf{x}_e$  and  $\mathbf{y}_e$ , the second index in their components refers to consecutive nodes. It should be emphasized that the derivatives of shape functions  $\mathbf{g}$  for the averaged strain field are separated in Eq. (3.125). Analogically to the proceeding in the previous subsection the discretization of the stabilization term  $R_2^{\text{stab}}$  is performed as follows:

$$\bar{g} = \gamma^T \mathbf{e} \quad \text{and} \quad \delta\bar{g} = \gamma^T \delta\mathbf{e} \quad (3.128)$$

where the discretized  $\delta\bar{g}$  can be treated as the weighting part  $\mathbf{P}_2(\delta\mathbf{e})$ .

Linearization of the residual can easily be derived:

$$\bar{g}_{i+1} = \bar{g}_i + d\bar{g} = \bar{g}_i + \gamma^T d\mathbf{e} \quad (3.129)$$

Therefore, the term  $R_2^{\text{stab}}$  has the form:

$$R_2^{\text{stab}} = \sum_{e=1}^{n_{el}} \int_{B^e} \gamma \chi_2 (\bar{g}_i + \gamma^T d\mathbf{e}) dV \quad (3.130)$$

For the  $\gamma$  method an additional matrix and vector are introduced:

$$\bar{\mathbf{K}}_{ee} = \int_{B^e} \chi_2 \gamma \gamma^T dV \quad (3.131)$$

$$\bar{\mathbf{f}}_e = \int_{B^e} \chi_2 \gamma \bar{g}_i dV \quad (3.132)$$

in order to obtain the final matrix form:

$$\begin{bmatrix} \mathbf{K}_{aa} + \bar{\mathbf{K}}_{aa} & \mathbf{K}_{ae} + \bar{\mathbf{K}}_{ae} \\ \mathbf{K}_{ea} & \mathbf{K}_{ee} + \bar{\mathbf{K}}_{ee} \end{bmatrix} \begin{bmatrix} d\mathbf{a} \\ d\mathbf{e} \end{bmatrix} = \begin{bmatrix} \mathbf{f}_{\text{ext}} - \mathbf{f}_{\text{int}} - \bar{\mathbf{f}} \\ \mathbf{f}_\epsilon - \mathbf{f}_e - \bar{\mathbf{f}}_e \end{bmatrix} \quad (3.133)$$

It can be shown that an analogical approach for the first stabilization term, i.e. for the equilibrium equations, is equivalent to the one applied in the previous subsection in the GLS method. However, this equivalence is valid only for the four-noded FE. The GLS method seems to be more general, since the derivation is prepared for elements with an arbitrary number of nodes. The disadvantage of the  $\gamma$  method is the lack of such versatility: in 2D it can be employed only for the four-noded element. The elaboration of the formulation with an effective stabilization for the 3D B8/8 element requires further research and the above derivation can constitute its initial point.

#### SPECTRAL ANALYSIS FOR STABILIZED FINITE ELEMENT

The accepted proposal of stabilized FE can be verified again using the spectral analysis. The data for the considered eigenproblem has been shown at the beginning of this section. A single element with RI and stabilization of the first or both variational equations is computed. The stabilization scaling factor  $\chi$  in each case is equal to 0.0001. The parameter  $c = 1$  represents the active averaging of the problem, so the case with  $c = 0$  is not considered in this analysis. Table 3.6 summarizes the spectrum of eigenvalues. It is clearly shown that the stabilization defined according to Eq. (3.117) ensures the suitable spectrum of eigenvalues only for submatrix  $\mathbf{K}_{aa} + \bar{\mathbf{K}}_{aa}$ , which is connected with the variational equilibrium equation (Table 3.6 on the left). One additional zero eigenvalue results from the unstabilized averaged strain field in the element. This spurious representation can be corrected by means of the idea like in Eq. (3.133). It is confirmed not only in Table 3.6 on the right, but also in the figures below.

Table 3.6: Eigenvalues for stabilized Q4/4,  $c = 1$ ,  $\chi = 0.0001$ .

(a) RI with stabilization according to Eq. (3.117).									(b) RI with stabilization according to Eq. (3.133).										
	Elasticity			Damage			Unloading				Elasticity			Damage			Unloading		
s. eigs	+	0	-	+	0	-	+	0	-	s. eigs	+	0	-	+	0	-	+	0	-
$\mathbf{K}_{aa} + \bar{\mathbf{K}}_{aa}$	5	3	0	5	3	0	5	3	0	$\mathbf{K}_{aa} + \bar{\mathbf{K}}_{aa}$	5	3	0	5	3	0	5	3	0
$\mathbf{K}_{ee}$	3	1	0	3	1	0	3	1	0	$\mathbf{K}_{ee} + \bar{\mathbf{K}}_{ee}$	4	0	0	4	0	0	4	0	0
$\mathbf{K} + \bar{\mathbf{K}}$	8	4	0	7	4	1	8	4	0	$\mathbf{K} + \bar{\mathbf{K}}$	9	3	0	8	3	1	9	3	0

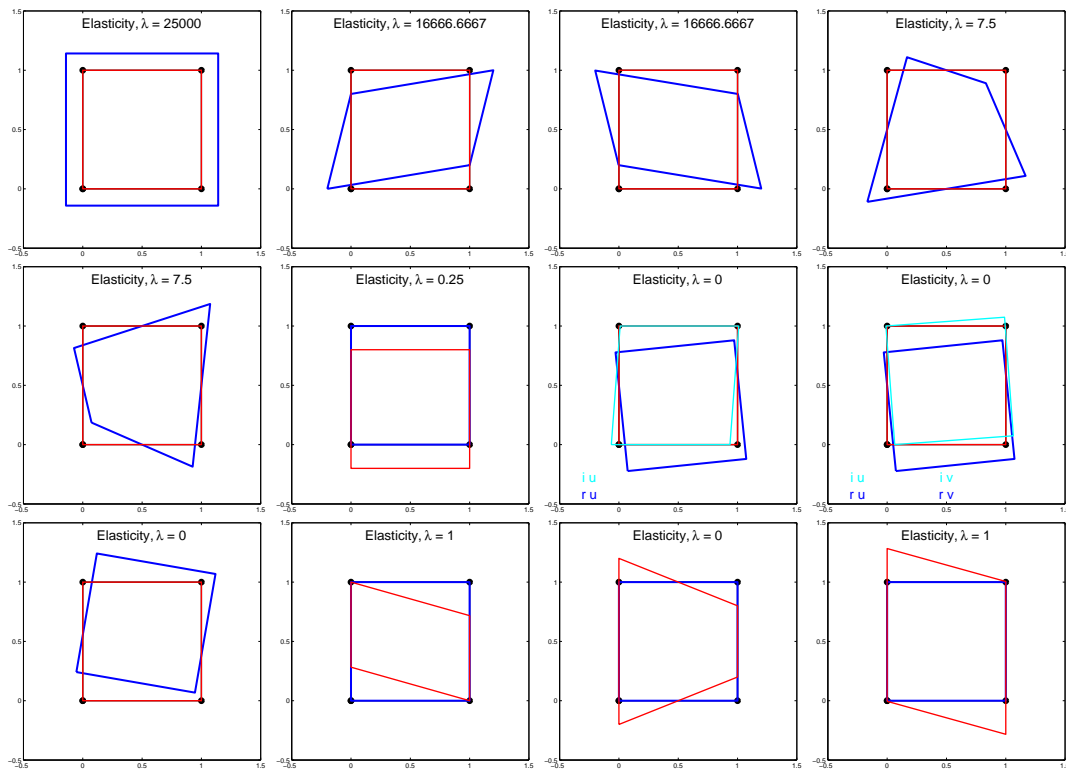


Figure 3.12: Eigenforms for Q4/4, RI with stabilization according to Eq. (3.117),  $c = 1$ ,  $\chi = 0.0001$ , elastic phase.

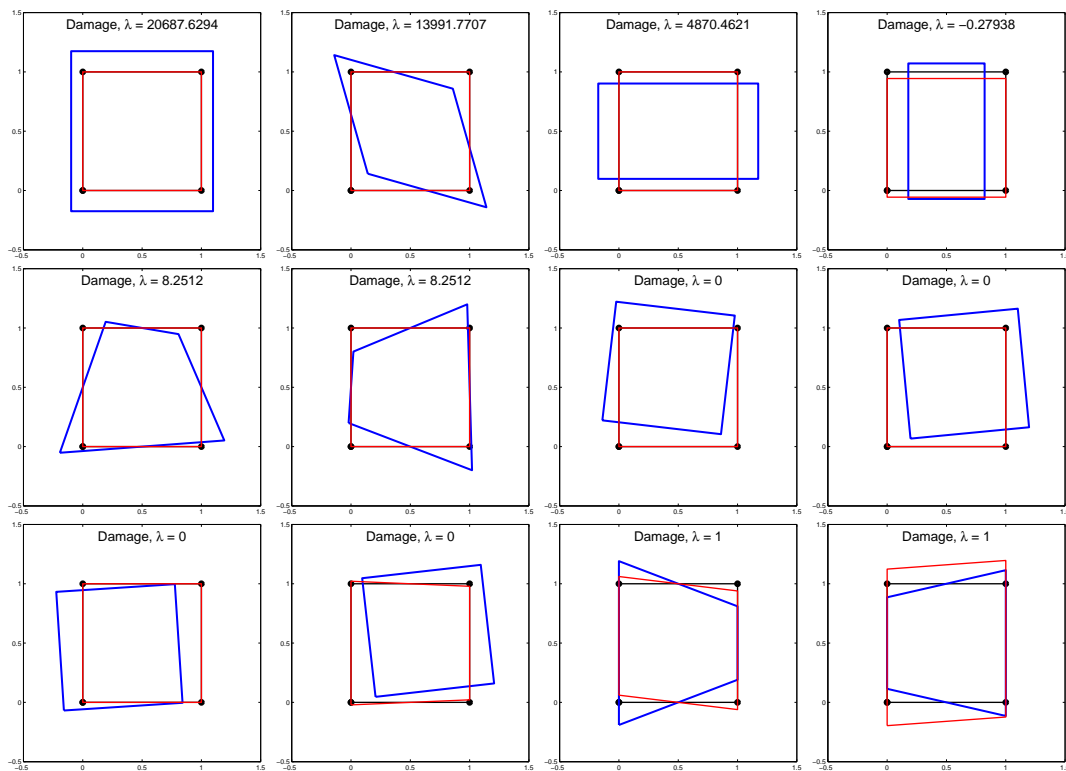


Figure 3.13: Eigenforms for Q4/4, RI with stabilization according to Eq. (3.117),  $c = 1$ ,  $\chi = 0.0001$ , damage phase.

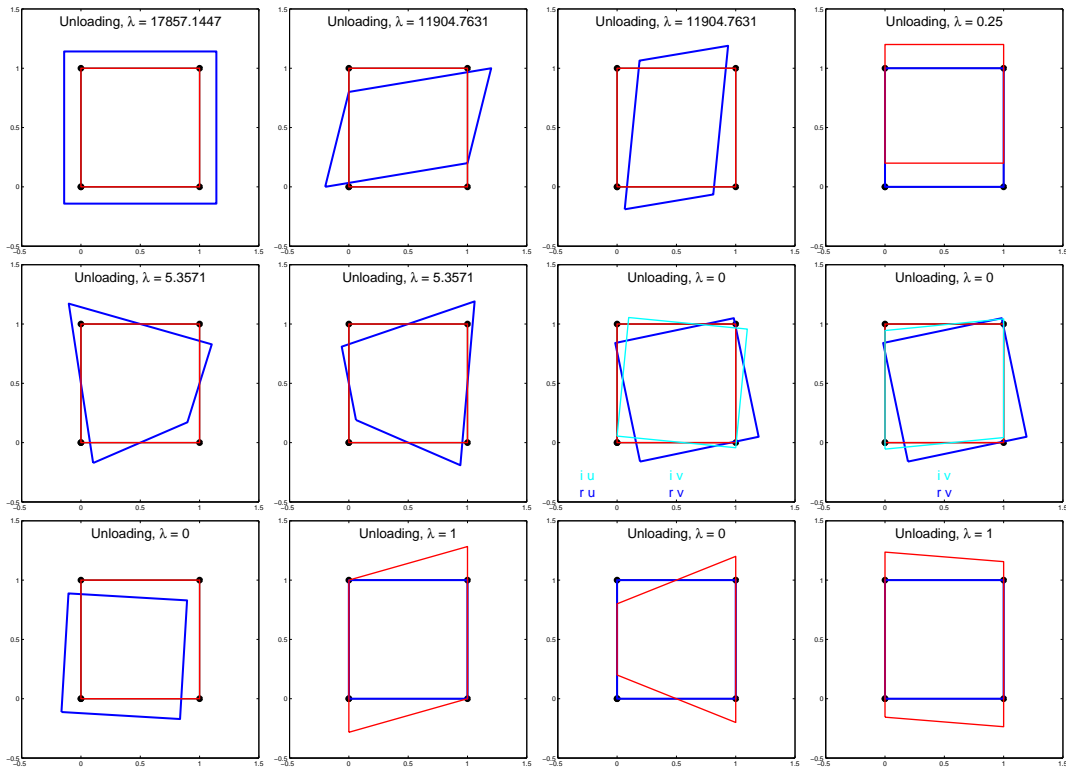


Figure 3.14: Eigenforms for Q4/4, RI with stabilization according to Eq. (3.117),  $c = 1$ ,  $\chi = 0.0001$ , unloading.

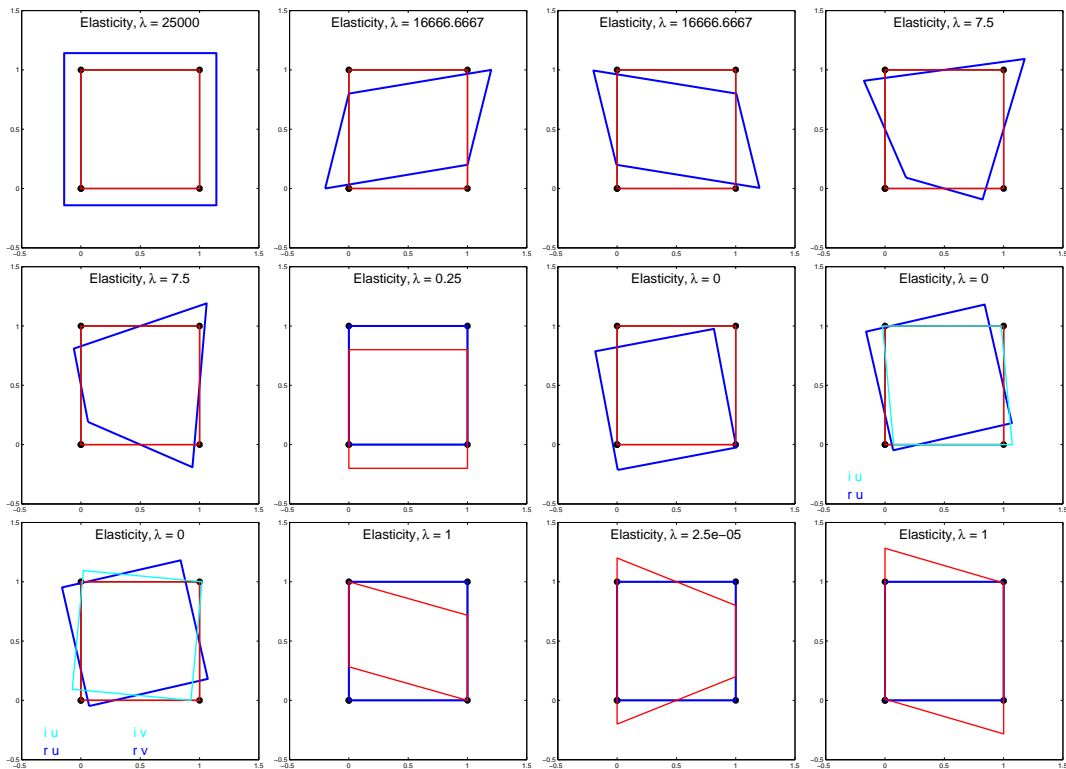


Figure 3.15: Eigenforms for Q4/4, RI with stabilization according to Eq. (3.133),  $c = 1$ ,  $\chi = 0.0001$ , elastic phase.

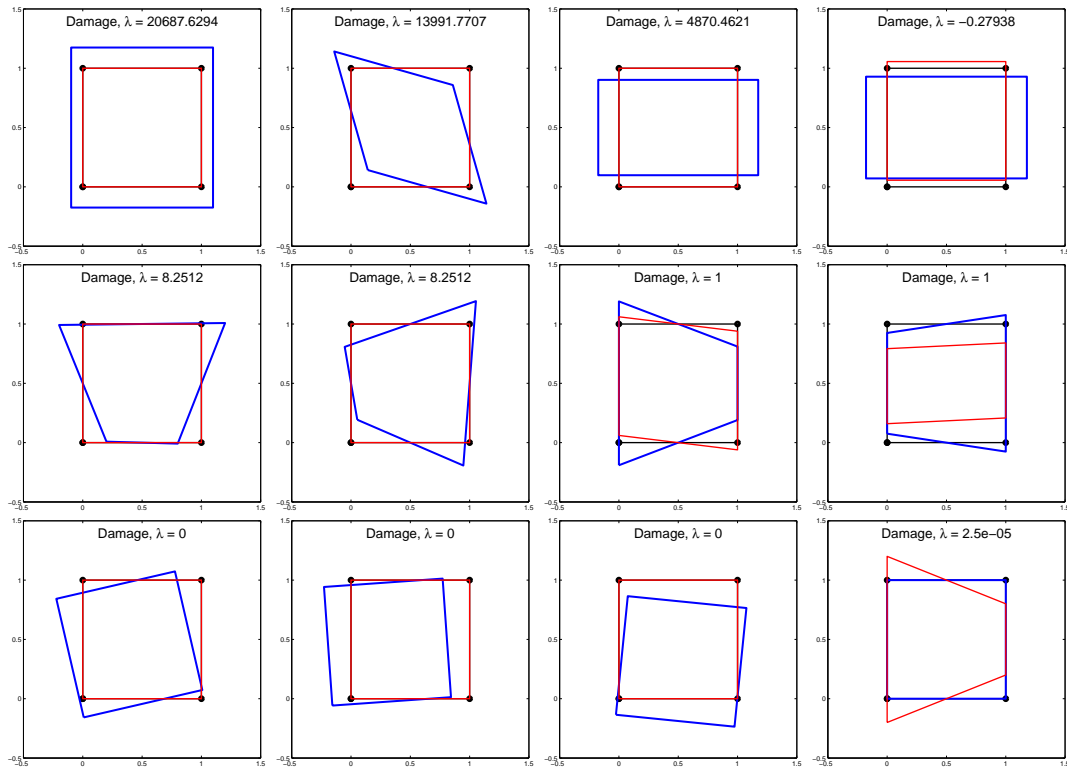


Figure 3.16: Eigenforms for Q4/4, RI with stabilization according to Eq. (3.133),  $c = 1$ ,  $\chi = 0.0001$ , damage phase.

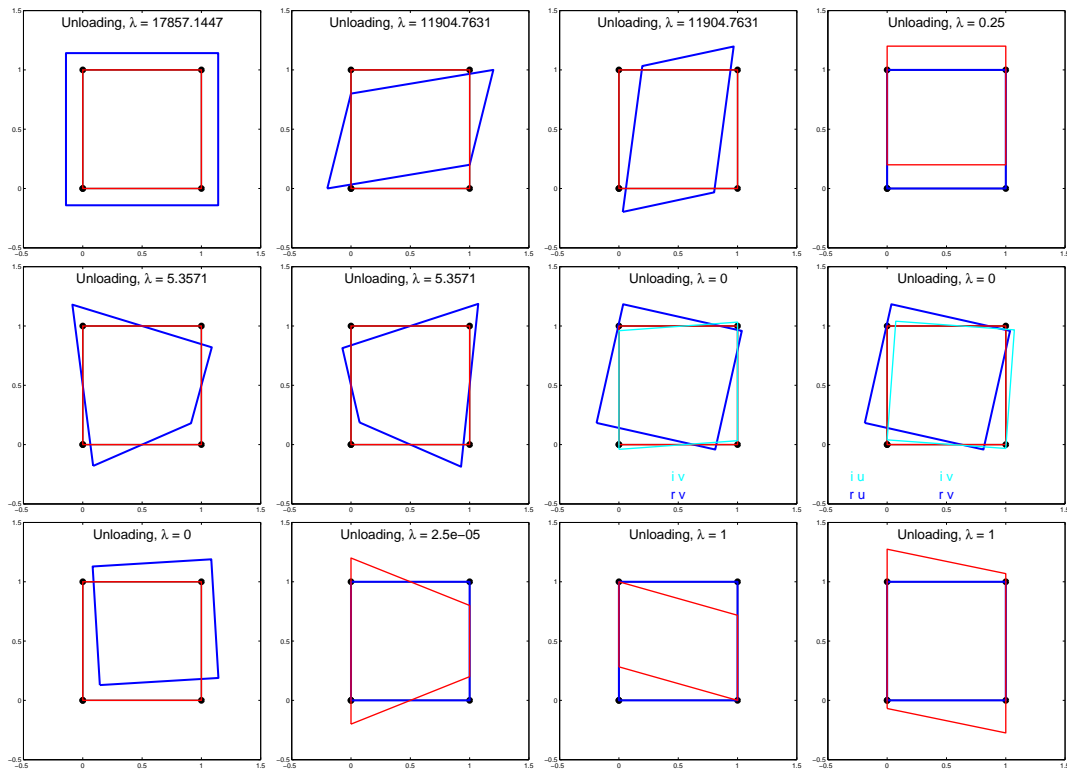


Figure 3.17: Eigenforms for Q4/4, RI with stabilization according to Eq. (3.133),  $c = 1$ ,  $\chi = 0.0001$ , unloading.

All figures with groups of eigenforms are presented in accordance with the rules discussed in page 74. Figures 3.12–3.14 are connected with the case where only the first variational equation in the formulation is stabilized. In comparison to Figs 3.6–3.8, where RI without stabilization has been applied in FE, the spurious eigenforms for the displacement field vanish. However, as emphasized in the previous paragraph, one zero eigenvalue is still present and the corresponding eigenvector represents a spurious eigenform. In the elastic and unloading phases (Figs 3.12 and 3.14) it is a twisted mode in the averaged strain space, but in the damage phase (third row and second column in Fig. 3.13) their influence on eigenforms is not completely clear. The tendency is similar to the case in Fig. 3.7, where the coupling between the displacement and averaged strain fields is of importance. Like there, now the eigenform has non-zero values for the displacement dofs, but in such a way, that they are visualized like a rigid body motion. Simultaneously the twisted mode in the averaged strain space is preserved, but the values of components in the eigenvector are close to zero. In the damage phase apart from the negative eigenvalue, the coupling is also present for eigenvalues equal to 1, while in other phases eigenforms for the averaged strain measure are only active. The observed behaviour seems surprising, in fact it is caused by the averaging process ( $c = 1$ ) and the coupling of both fields in the model. The eigenmodes in the averaged strain space (marked by red) remind a linear distribution, while in the displacement space (marked by blue) – the twisted form in the vertical direction is activated.

The eigenmodes in Figs 3.15–3.17 are composed as previously, but now the stabilization for the whole tangent operator  $\mathbf{K} + \bar{\mathbf{K}}$  is adopted, see Eq. (3.133). Three eigenforms with zero eigenvalues correspond to the combination of rigid motions. The eigenform with the non-zero eigenvalue and the twisted mode in the averaged strain space are the same in each phase, which means that stabilization is fully initiated. Moreover, the second field is stabilized by the  $\gamma$  method, where operator  $\gamma$  for a rectangular element is reduced to the twist vector  $t_e$ . Like previously the coupling of variational equations can be observed if eigenforms for eigenvalues equal to 1 are illustrated in the damage phase, where linear functions for the averaged strain dofs together with the twisted form in vertical direction for displacement dofs are obtained.

When one-point reduced integration RI is applied in the four-noded FE mesh then for effective computations a stabilization must be assured in the formulation. In this subsection the possibility of stabilization in such finite elements has been proposed and verified in the spectral analysis. As demonstrated, the stabilization terms are needed in both variational equations, in order to ensure a proper quality of FE and finally stable numerical results. However, in the discussed approach two different methods of stabilization for the given equation have been assumed.

## 3.4.3 OTHER ELEMENTS – SPECTRAL ANALYSIS

This subsection is devoted to a brief presentation of the spectral analysis performed for other elements. The implemented FEs are illustrated in Table 3.3, so far only element Q4/4 has been investigated (1D elements are neglected in the analysis). The general data and the loading path, which are representative for the model considered in this work, has been described at the beginning of this section. The eigenforms are not computed, because their analysis would be analogical to the results presented for element Q4/4.

The numbers of positive, zero and negative eigenvalues shown at the top of Table 3.7 are evaluated for element Q8/4 with four integration points. It means that for the displacement dofs RI is applied, but for the averaged strain field FI is employed. Apart from three zero eigenvalues connected as usual with the rigid motions, the extra spurious mode is possible due to the fourth zero eigenvalue. This singularity reveals in each phase of the loading process and comes from the submatrix  $\mathbf{K}_{aa}$  in the tangent operator  $\mathbf{K}$ . However, it is known (cf. for example [178]) that the zero eigenvalue and the spurious form are removed when more elements than one are assembled in the mesh. Like previously one negative eigenvalue appears in the damage phase (just after the peak) and the reason is the onset of softening in the material model.

The above explanations are additionally verified when FE Q8/8 is tested. If FI with nine sampling points is used (Table 3.7, at the bottom, on the left) only three zero eigenvalues are calculated and as mentioned in the previous paragraph this is correct. Similarly to Q8/4, four points are now used for RI. Also here one additional zero eigenvalue together with its spurious eigenform disappear from the discretized problem if more than one FE is assumed.

Table 3.7: Eigenvalues for other 2D elements,  $c = 1$ .(a) Q8/4, 20 dofs,  $a - \text{RI}$ ,  $e - \text{FI}$ .

s. eigs	Elasticity			Damage			Unloading		
	+	0	-	+	0	-	+	0	-
$\mathbf{K}_{aa}$	12	4	0	12	4	0	12	4	0
$\mathbf{K}_{ee}$	4	0	0	4	0	0	4	0	0
$\mathbf{K}$	16	4	0	15	4	1	16	4	0

(b) Q8/8, 24 dofs, FI.

s. eigs	Elasticity			Damage			Unloading		
	+	0	-	+	0	-	+	0	-
$\mathbf{K}_{aa}$	13	3	0	13	3	0	13	3	0
$\mathbf{K}_{ee}$	8	0	0	8	0	0	8	0	0
$\mathbf{K}$	21	3	0	20	3	1	21	3	0

(c) Q8/8, 24 dofs, RI.

s. eigs	Elasticity			Damage			Unloading		
	+	0	-	+	0	-	+	0	-
$\mathbf{K}_{aa}$	12	4	0	12	4	0	12	4	0
$\mathbf{K}_{ee}$	8	0	0	8	0	0	8	0	0
$\mathbf{K}$	20	4	0	19	4	1	20	4	0



Table 3.8: Eigenvalues for 3D elements,  $c = 1$ .

(a) B8/8, 32 dofs, FI.										(b) B8/8, 32 dofs, RI.											
		Elasticity			Damage			Unloading					Elasticity			Damage			Unloading		
s. eigs		+	0	-	+	0	-	+	0	-	s. eigs		+	0	-	+	0	-	+	0	-
$K_{aa}$		18	6	0	18	6	0	18	6	0	$K_{aa}$		6	18	0	6	18	0	6	18	0
$K_{ee}$		8	0	0	8	0	0	8	0	0	$K_{ee}$		4	4	0	4	4	0	4	4	0
$K$		26	6	0	25	6	1	26	6	0	$K$		10	22	0	9	22	1	10	22	0

(c) B20/8, 68 dofs, $a - RI, e - FI$ .										
		Elasticity			Damage			Unloading		
s. eigs		+	0	-	+	0	-	+	0	-
$K_{aa}$		48	12	0	48	12	0	48	12	0
$K_{ee}$		8	0	0	8	0	0	8	0	0
$K$		56	12	0	55	12	1	56	12	0

(d) B20/20, 80 dofs, FI.										(e) B20/20, 80 dofs, RI.											
		Elasticity			Damage			Unloading					Elasticity			Damage			Unloading		
s. eigs		+	0	-	+	0	-	+	0	-	s. eigs		+	0	-	+	0	-	+	0	-
$K_{aa}$		54	6	0	54	6	0	54	6	0	$K_{aa}$		48	12	0	48	12	0	48	12	0
$K_{ee}$		20	0	0	20	0	0	20	0	0	$K_{ee}$		20	0	0	20	0	0	20	0	0
$K$		74	6	0	73	6	1	74	6	0	$K$		68	12	0	67	12	1	68	12	0

Table 3.8 summarizes the eigenvalue analysis for three-dimensional elements. The data and the loading path are identical to the previous computations.

The most elementary discretization with the so-called brick elements B8/8 is adopted, where linear interpolation and eight nodes for both fields are used. Results for FI (eight sampling points) are shown in Table 3.8 at the top on the left. As expected, the spectrum in each phase is analogical to the one for Q4/4 with FI. Six zero eigenvalues correspond to the motions of the rigid body in 3D space and one negative eigenvalue occurs in the damage phase. For RI one integration point is used. In this case in the tangent operator  $K$  sixteen additional zero eigenvalues are observed. Twelve of them originate in part  $K_{aa}$  derived from the variational equilibrium equations. The next four result from submatrix  $K_{ee}$ , which is constructed based on the variational averaging equation. Moreover, if  $c = 0$  is used in  $K_{ee}$ , only one positive eigenvalue is noticed (these results are not presented). It means that the non-zero parameter  $c$  and as a consequence the averaging operation contributes three proper modes into 3D FE. However, to ensure stable computations for B8/8 with RI hourglass control must be introduced. In this thesis in the 3D tests and examples only FI is employed. The stabilization of B8/8 can be considered in future research.

For completeness the eigenvalue numbers for other 3D elements are listed at the bottom of Table 3.8. In brief, the results are fully analogical to the ones presented before in Table 3.7.



## CHAPTER 4

# TESTING OF FINITE ELEMENTS

### 4.1 BAR WITH IMPERFECTION UNDER STATIC TENSION

The simulation of uniaxial tension for a bar with imperfection in the middle is the most basic and typical test in physically nonlinear mechanics. In the zone where the specimen is made from a weaker material, it has a smaller cross-section, a notch or another kind of abatement, the phenomenon of localization is triggered. Numerical analysis allows one to observe if and how applied models can simulate the stiffness degradation in the specimen. In a load-displacement diagram, after reaching the peak load, a softening branch is expected. Because of general character of the test it can be run for ductile materials like metals as well as for brittle materials like concrete and rocks. The character of this test permits one to compare different numerical models, but not necessarily to confront them with experiments. Usually, the results for this test are performed to verify a new model and present its properties, for example the gradient scalar damage model was firstly used for this test in [125], where analytical and numerical solutions were obtained. Geometrically non-linear version of gradient damage (e.g. in [154]) was also tested using the simulation of the tensile bar with imperfection. Similarly, the coupling of scalar damage with hardening plasticity was checked by means of this test, cf. [36, 119]. For completeness of the thesis some results of this test, which were presented previously in different works by other authors, are computed. Indeed, their connection with new results serves the purpose of verification of the considered numerical model.

The bar has an imperfection in the middle of the specimen. A reduction of selected geometrical or physical quantity by 10 per cent depends on the used model. The test is depicted in Fig. 4.1. The general data are summarized in Table 4.1. The basic data for gradient damage are presented in Table 4.2. They can be optionally changed, in order to observe a certain aspect of the model. The bar is computed subsequently by means of 1D, 2D and 3D finite elements. The load control and the arc length method are used because the snapback effect is possible. Moreover, for the majority of computations equal steps are assumed in order to show the evolution of variables, which are illustrated as surfaces spanned along the bar and pseudo-time axis in second direction.

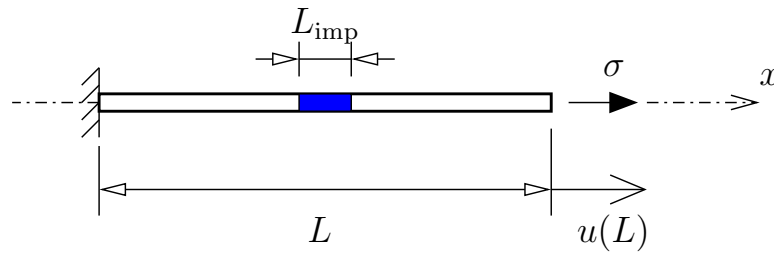


Figure 4.1: Bar with imperfection for localization test in tension.

Table 4.1: General problem data.

Geometry:	length: $L = 100$ mm
	weaker central zone: $L_{\text{imp}} = 10$ mm
	imperfection: 10%
Material:	Young's modulus: $E = 2 \times 10^4$ MPa

Table 4.2: Basic data for gradient damage model (also with plasticity).

Pure gradient damage:	
internal length parameter:	$c = 4 \text{ mm}^2$ ( $l = 2.83$ mm)
threshold:	$\kappa_o = 0.0001$
damage growth function:	linear softening, $\kappa_u = 0.0125$
Gradient damage with plasticity:	
tensile strength:	$\sigma_y = 5$ MPa
yield function:	HMH, linear hardening, $h = E$

#### 4.1.1 1D SIMULATIONS

For computations with one-dimensional finite elements a smaller cross-section is assumed as the imperfection in the middle of the bar. For all analyzed options the elements with quad/lin interpolation are employed. Quadratic polynomials for the displacement field together with linear interpolation for the averaged strain dofs seems to be optimal [124], because oscillations of secondary fields are avoided. For the 1D problem the stress is calculated as  $\sigma = (1 - \omega) E \epsilon$ . As shown in [124, 147] if lin/lin FE is used for discretization the combination of linear distribution of damage and piecewise constant strain field for elements gives an oscillating stress field. Somehow, it is confirmed in [147] that for the numerical solution of the imperfect bar, discretized with 80 FEs, oscillations occur in the zone where damage varies quickly and this effect can be overcome by means of postprocessing. All three types of 1D elements (see the top in Table 3.3) give a similar, stable solution. The load-displacement diagrams, presented in [117, 122], are close to each other. A comparison of elements in 2D and 3D problems, where different interpolation is used, will be performed later.

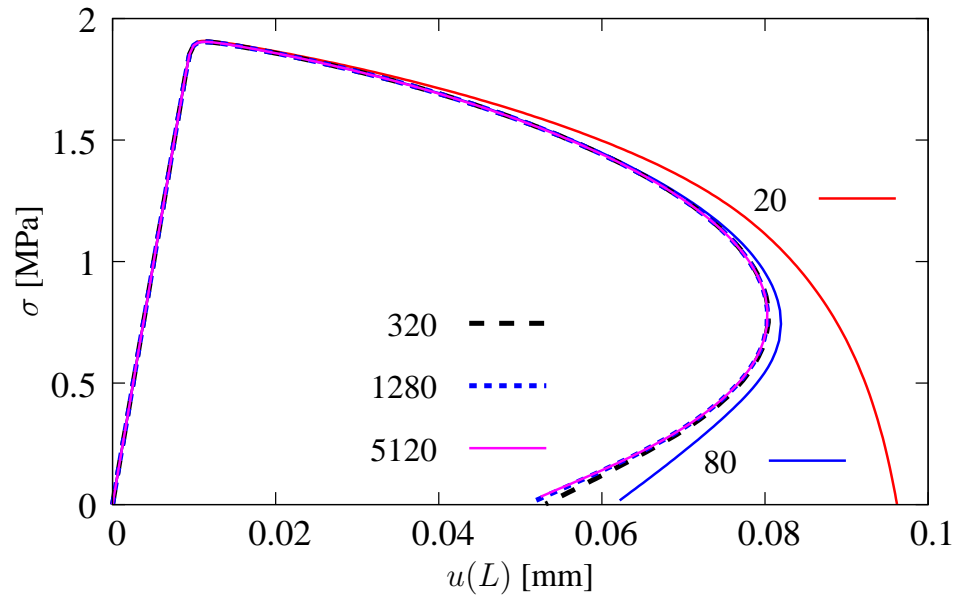
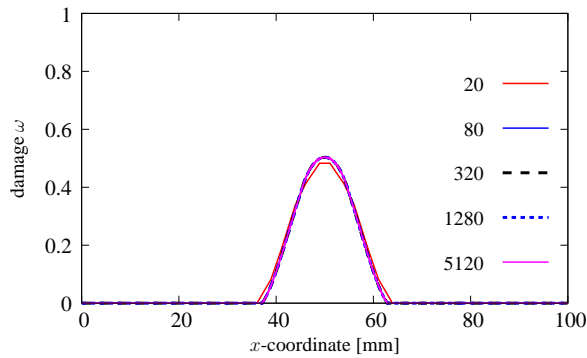
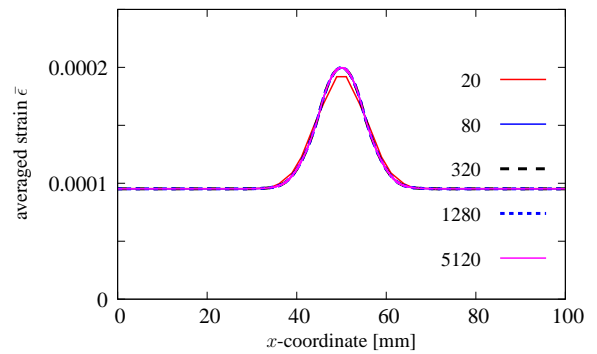


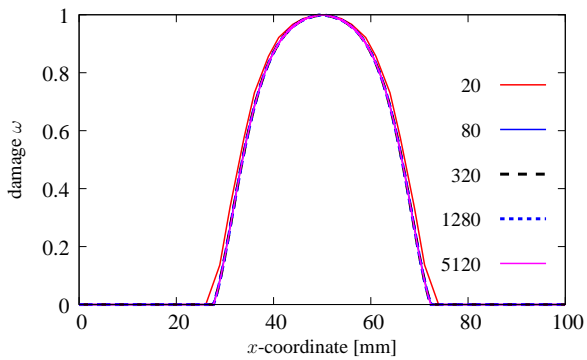
Figure 4.2: Tensile bar with imperfection in 1D. Stress-displacement diagrams for different numbers of elements.



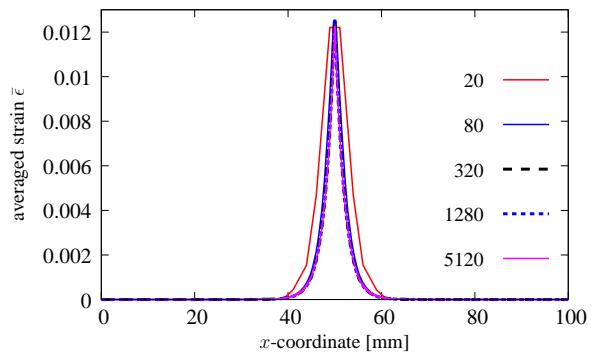
(a) Damage distribution, after peak load.



(b) Averaged strain, after peak load.



(c) Damage distribution, final state.



(d) Averaged strain, final state.

Figure 4.3: Tensile bar with imperfection in 1D. Results for different numbers of elements – mesh-independence.

The basic issue is to check if the analyzed model is spuriously sensitive to FE discretization. Starting from 20 elements each next mesh is constructed multiplying the previous number by 4 up to 5120 elements. The results, depicted in Figs 4.2 and 4.3, demonstrate the same tendency as the ones presented in [125]. As expected, the gradient damage model is mesh-objective. However, the stress-displacement diagram for 20 elements in Fig. 4.2 departs from the others. For this coarse mesh the internal length is smaller than the length of a single FE ( $2.83 \text{ mm} < 5 \text{ mm}$ ), so the size of the element determines the width of the localization zone. Even so, the averaged strain and damage distributions are similar for the whole set of meshes (see Fig. 4.3). Generally, localization occurs in a zone broader than one FE and the problem is regularized. The snap-back effect appears in the advanced phase of the loading, when a growing part of the localization zone runs into unloading and the active process is observed only in the narrowing part of the bar in the center (see Fig. 4.3(d)). The results converge to a certain solution, which is governed by the internal length parameter and is insensitive to the adopted mesh.

From now on the 1D analysis for the uniaxial tension test is limited to the mesh with 80 elements along the bar. Here the influence of the internal length scale is verified. Figs 4.4 and 4.5 collect the results for different values of parameter  $c$ . According to the observation in [125], the larger the internal length parameter is, the higher the peak stress is obtained. The difference is not too significant, but noticeable (see Fig. 4.4). Moreover, the increasing value of  $c$  not only causes the widening of the localization zone like in Fig. 4.5, but also delays the onset of the snap-back. If  $c = 0$  is adopted then oscillating distributions occur. It is known that in this case they are governed by discretization. The length  $l$  and accordingly adjusted  $c$  should be larger

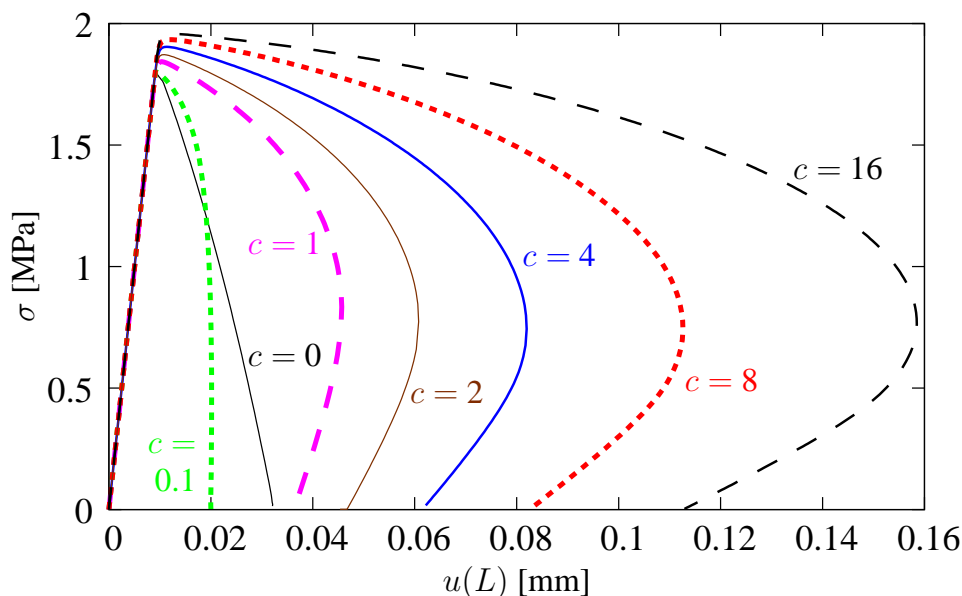


Figure 4.4: Tensile bar with imperfection in 1D. Stress-displacement diagrams for different values of internal length parameter.

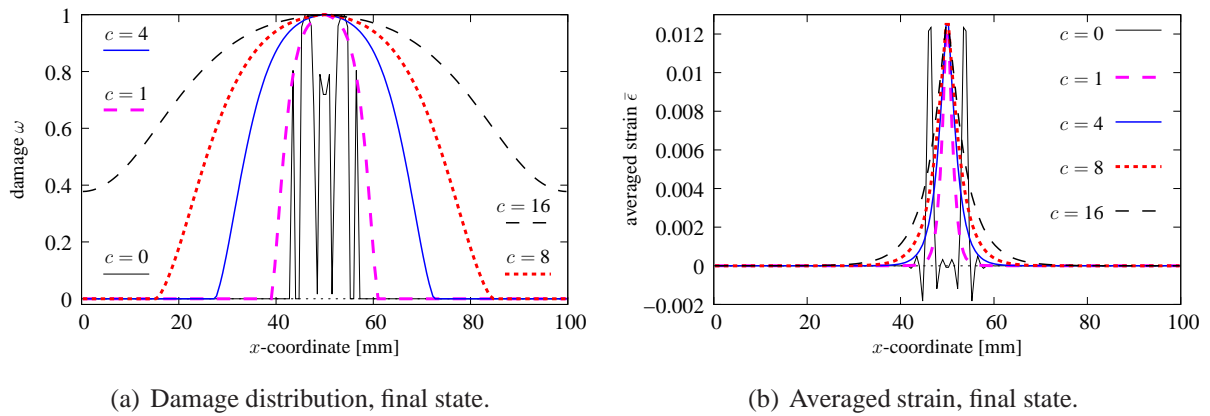
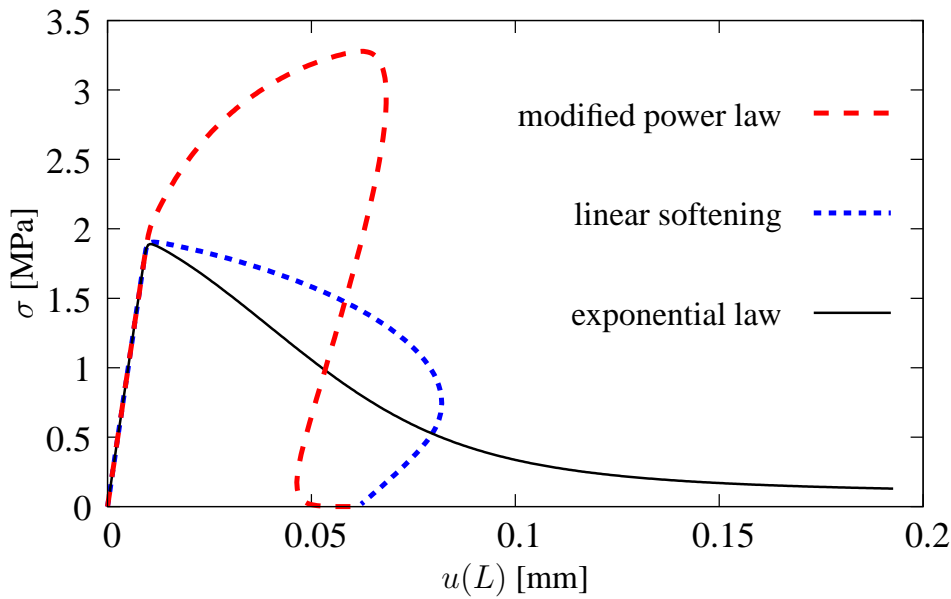


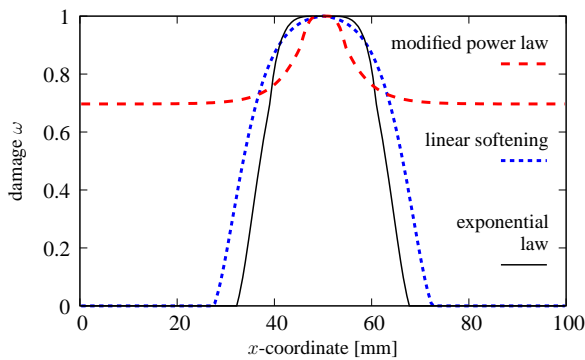
Figure 4.5: Tensile bar with imperfection in 1D – internal length influence.

than the size of FE, in order to invoke efficient regularization. On the other hand, if  $c = 16$  is introduced the regularized zone is so wide that the whole bar is damaged. It seems to be unrealistic, hence the value of the parameter  $c$  should be properly selected. Indeed, the internal length parameter  $l$  (and of course  $c$ ) is connected with the microstructure of the material. For quasi-brittle materials like concrete the adequate value of the parameter can be associated with the maximum aggregate size [10].

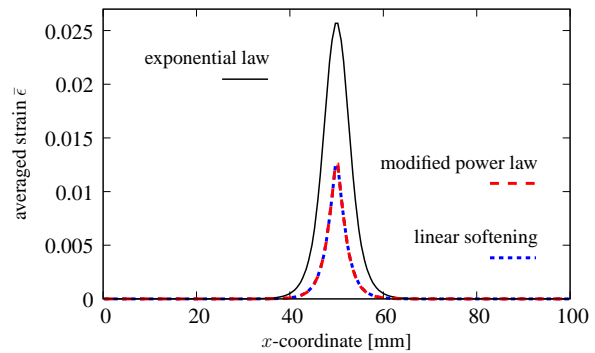
Further computations are performed for different damage growth functions, with reference to the analysis at the material point level (one FE) presented in Section 2.1. The basic option with linear softening remains without changes as in Table 4.2. For exponential softening, defined in Eq. (2.21), model parameters are:  $\alpha = 0.96$  and  $\eta = 200$ . If the modified power law in Eq. (2.20) is employed, the ultimate parameter is as for linear softening, i.e.  $\kappa_u = 0.0125$ . The exponents in this law are  $\alpha = 5.0$  and  $\beta = 0.6$ . The convergence analysis for this damage growth function is performed for example in [55, 85] and an additional parameter study can be found in [55]. The modified power law was applied to computations for polymers [55], so this function will be omitted in next examples. The parameters for all the above cases correspond to a similar value of fracture energy, however the damage progress is quite different. Fig. 4.6(a) illustrates non-linear stress-elongation paths for the assumed damage growth laws. Differences are also visible in damage distributions along the bar at the final state (see Fig. 4.6(b)). For linear and exponential softening the damaged and undamaged regions are distinguished. In the active zone damage spreads similarly to cosine function. If the modified power law is employed the whole bar is damaged despite the fact that  $c$  still equals 4. The problem of evidently too wide damage zone can be solved for example like in [55], where the constant parameter  $c$  is substituted by a function of equivalent or averaged strain measure. Nevertheless, the final distribution of averaged strain  $\bar{\epsilon}$  has the same character for all cases. The largest averaged strain for the exponential law corresponds to a much larger elongation of the bar. Obviously the adopted damage growth function has negligible influence on the averaged strain distribution.



(a) Stress-displacement diagrams.



(b) Damage distribution, final state.



(c) Averaged strain, final state.

Figure 4.6: Tensile bar with imperfection in 1D – different damage growth.

The results for gradient damage combined with hardening plasticity, discussed in [36, 119], are supplemented in the present and next paragraphs. The basic data for the model are given in Table 4.2. The start of the plastic process is slightly delayed with reference to damage initiation. The equivalent strain can optionally be a function of the elastic or total strain tensor, so in 1D respectively  $\tilde{\epsilon} = \epsilon^e$  constitutes the so-called weak coupling and  $\tilde{\epsilon} = \epsilon$  – the strong coupling. The stress-displacement diagrams for the coupled model are depicted in Fig. 4.7 together with the equilibrium path for pure gradient damage. For the weak coupling the response is more ductile than for the pure model. On the other hand the more brittle process is observed if the strong coupling is assumed. As noticed in [119] and confirmed in these calculations, the larger the value of the hardening parameter  $h$ , the closer the solution is to pure gradient damage. This relation holds true for both options of the coupling (see Fig. 4.7).



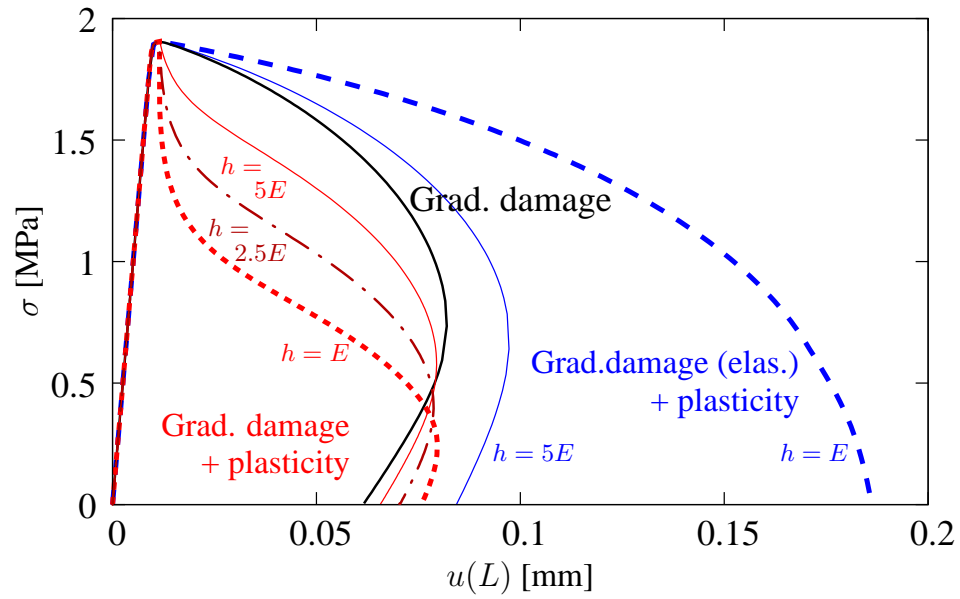


Figure 4.7: Tensile bar with imperfection in 1D – stress-displacement diagrams for gradient damage and hardening plasticity.

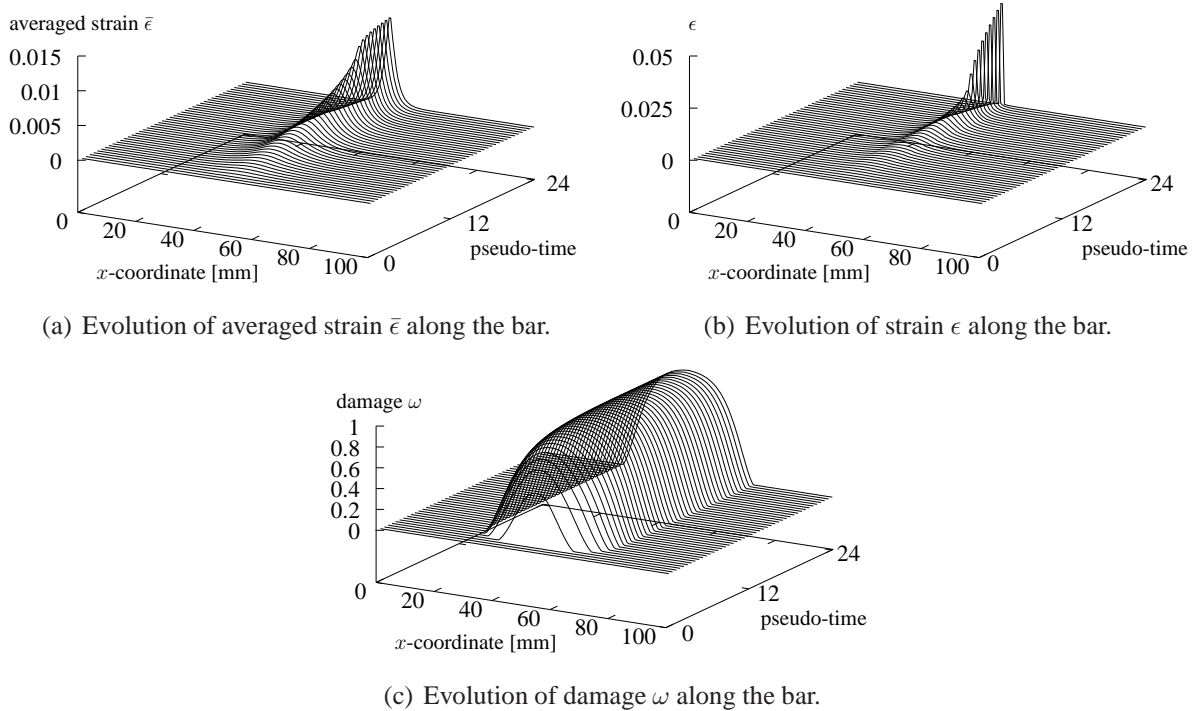


Figure 4.8: Pure gradient damage – evolution of chosen variables.

In the end the evolutions of characteristic variables are shown in Figs 4.8–4.10. The growth of averaged strain measure  $\bar{\epsilon}$  along the bar is slower for the coupled models, but the maximum value is almost equal and amounts to nearly  $1.25 \times 10^{-2}$  for the pure and both coupled models. The axial strain  $\epsilon$  evolution differs. Moreover, as proved in [85], an increasing number

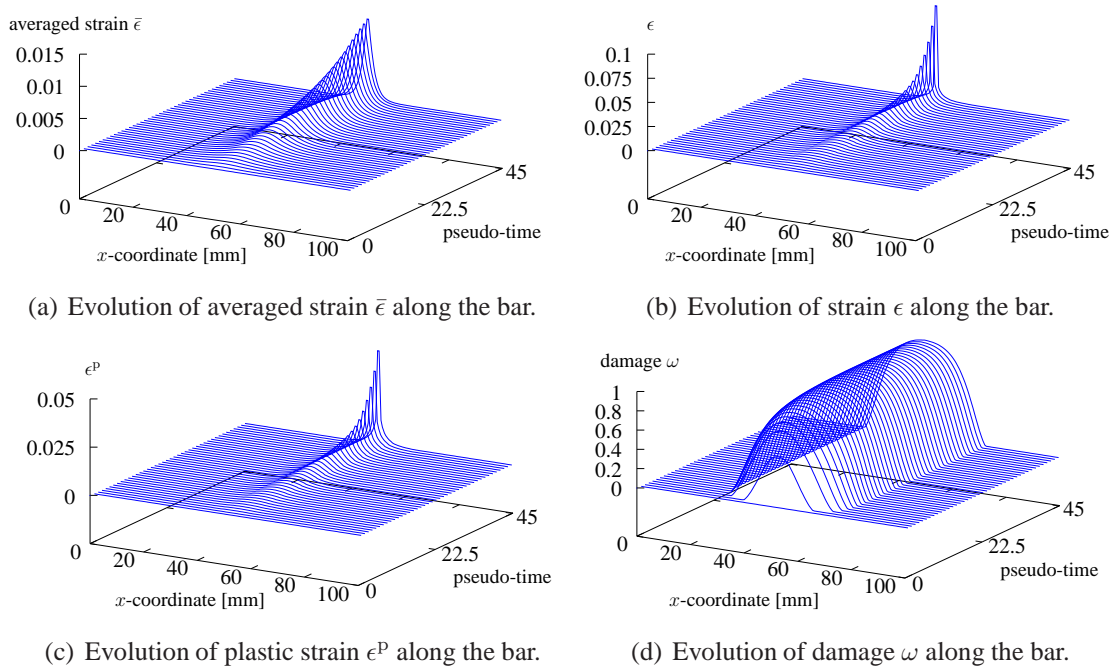


Figure 4.9: Weak coupling of gradient damage and plasticity – evolution of chosen variables.

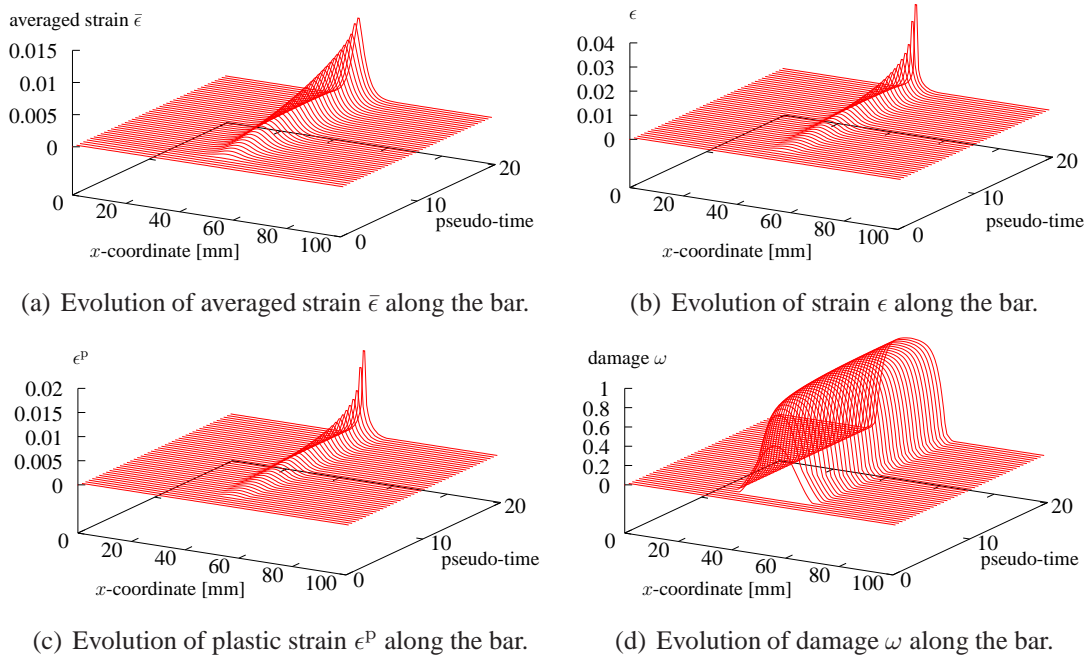


Figure 4.10: Strong coupling of gradient damage and plasticity – evolution of chosen variables.

of elements in the bar results in the convergence of the axial strain distribution to Dirac delta function at the final state. It is observed that the zone with non-zero plastic strain  $\epsilon^p$  occupies nearly half of the whole bar for both coupling options. The averaged, axial and plastic strain distributions, which are made during the loading process, are quite similar. For the weak coupling the damage evolution is like for the pure model. This is because the lack of contribution of the plastic part into the damage growth is involved. If the strong coupling is employed then the mutual interaction causes that the damage zone along the bar is active in a thinner band. A concise presentation of gradient damage based on the benchmark of the bar with imperfection in 1D and also a comparison with gradient plasticity is performed in [118].

#### 4.1.2 2D AND 3D SIMULATIONS

In two- and three-dimensional configurations a physical imperfection is introduced, however it has the same meaning as in the previous computations. Now the damage threshold is reduced by 10 % in the middle of the bar. Firstly, 2D elements with different types of integration are tested. Next, the isotropic gradient model with one or two damage parameters is verified. Finally, the confrontation focuses on 3D elements with different interpolation options.

In this part FE Q4/4 is checked with different combinations of integration schemes. The basic data are summarized in Tables 4.1 and 4.2. Additionally Poisson's ratio  $\nu$  is equal to zero. Plane stress is assumed, where both thickness  $T$  and width  $B$  equal 5 mm. Arc length control computations with varying steps size adapted along the loading path are employed. In Fig. 4.11 stress-elongation diagrams are presented. Three approaches, described in Chapter 3,

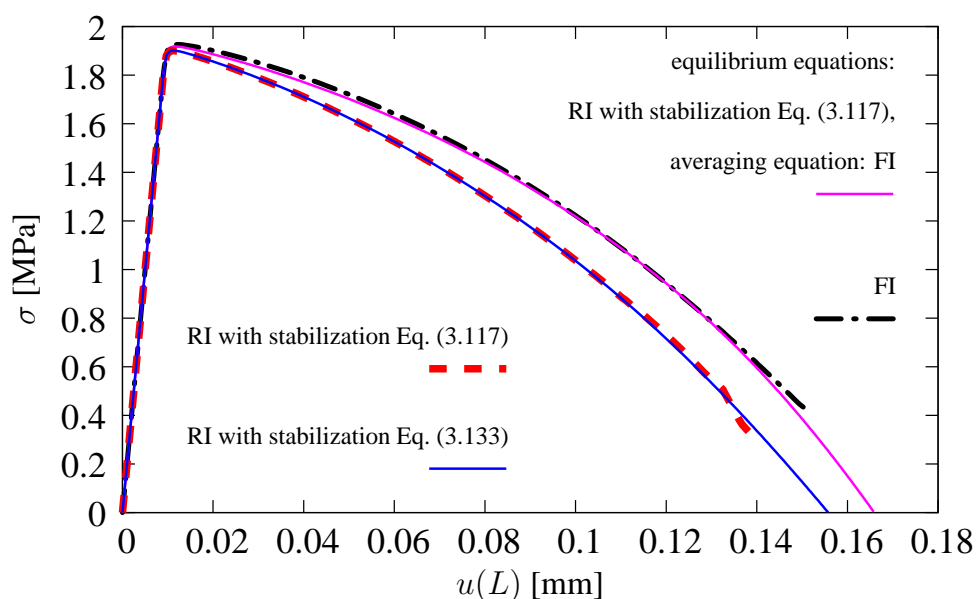


Figure 4.11: Tensile bar with imperfection in 2D. Stress-displacement diagrams - different types of integration in FE Q4.

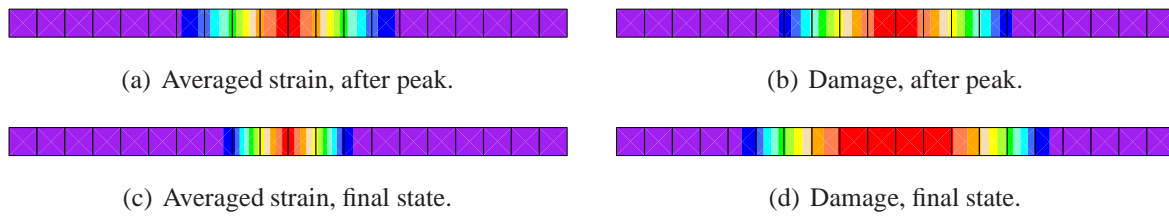


Figure 4.12: Results for bar with imperfection – elements Q4 with FI.

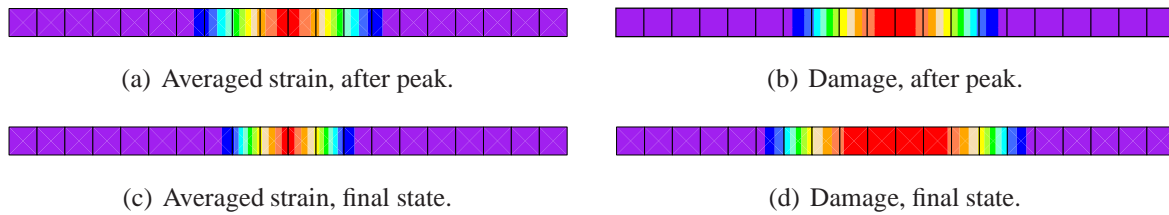


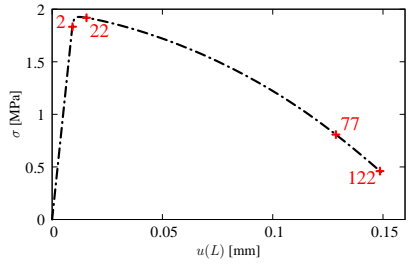
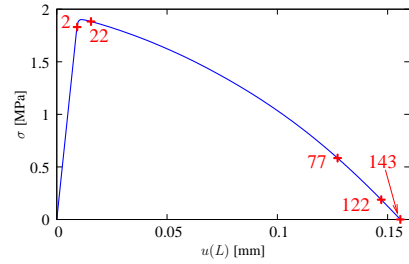
Figure 4.13: Results for bar with imperfection – elements Q4 with RI and stabilization according to Eq. (3.133),  $\chi = 0.000001$ .

are compared. They are in turn: full integration (FI) and reduced integration (RI) with stabilization according to Eq. (3.117) or Eq. (3.133). If the elements are stabilized, the coefficient  $\chi = 0.000001$  is introduced. Apart from that, a fourth option is calculated. In this option the equilibrium equations are formulated and implemented together with stabilization, so RI is applied, but the derivation as for standard FEs is valid for the averaging equation, where FI is preferred. The element with such mixed integration is not practical, because finally five sampling points are required. However, the computations for this type of integration are performed in order to show one more alternative.

Generally, if FI is employed for the second or both discretized fields, the relation between elongation  $u(L)$  and the stress  $\sigma$  is like for a slightly stiffer bar. The diagram in Fig. 4.11 for FI ends before the stress approaches zero, but it is connected with the fact that the damage history parameter reaches the ultimate value  $\kappa_u$  and an unwanted change of the stiffness or unloading is obtained. For RI and stabilization according to Eq. (3.117), which does not assure a proper FE without spurious eigenmodes, computations diverge in the advanced state of deformation. For fully correct paths, namely for these where FI or RI with stabilization like in Eq. (3.133) are applied, the averaged strain and damage distributions in two phases are shown in Figs 4.12 and 4.13. Both variables have similar distributions just after the peak load and also in the final state.

At the end of this part a convergence study is performed similarly to [94]. Two basic types of integration are confronted in Table 4.3. Four or five characteristic steps are chosen according to the figures placed at the top of this table. A drastically different number of active integration points (ips) is observed as the consequence of the adopted integration in a single FE. It is confirmed that the solution reaches quadratic convergence in every step for both alternative cases.

Table 4.3: Convergence study – bar with imperfection. Two types of integration.

type ips (1 FE)	FI $2 \times 2 = 4$	RI + stabilization, Eq. (3.133) $1 \times 1 = 1$		
				
Step no.	Relative energy norm	Active ips	Relative energy norm	Active ips
2	1.00000000000000E+00	8	1.00000000000000E+00	2
	5.321187441983860E+02	8	5.763488320259804E+02	2
	2.534990264376641E-04	8	6.048211715158885E-04	2
	1.770959355358748E-10	8	1.304413629483436E-09	2
	8.617827040306284E-23	8	6.008164724480290E-21	2
22	1.00000000000000E+00	40	1.00000000000000E+00	8
	-9.779478750996960E-06	40	-3.149860222058139E-04	8
	1.548406070066814E-10	40	-7.542830989034233E-12	8
	3.871666510054424E-11	40	-1.885723762863035E-12	8
	1.260922539766909E-19	40	4.655693122775198E-24	8
77	1.00000000000000E+00	12	1.00000000000000E+00	4
	-6.737739431886433E-02	12	-8.738447627994261E-02	4
	-1.936878713736846E-19	12	1.595955486024598E-16	4
		12	-3.543616722096119E-27	4
122	1.00000000000000E+00	12	1.00000000000000E+00	4
	-8.424036872173256E-02	12	-5.664603859365940E-01	4
	-3.265570463637080E-20	12	6.614336369593637E-19	4
143			1.00000000000000E+00	4
			-6.109566557762603E-01	4
			3.162731767832675E-19	4

The two-dimensional bar with imperfection is also tested using the isotropic model, where different parameters for the damage growth function are introduced. The general data still hold for the considered benchmark. Since, as shown in Section 2.4, the solution for linear softening at the level of a material point is less stable than for exponential softening, so only the latter function is employed. The gradient damage with volumetric-deviatoric split and linear softening has been numerically verified, but results are questionable, especially if the load carrying capacity is exhausted for either the volumetric or deviatoric damage measures and Poisson's ratio  $\nu_\omega$  attains 0.5 or non-physical value  $-1$ . The initial value of  $\nu_\omega$  equals 0.2 for each analyzed case. Differently from the previously presented computations, now the plane strain configuration is proposed. It extends the analysis performed in this section. At the beginning two

Table 4.4: Bar with imperfection – cases computed by means of isotropic gradient damage.

Symbol of case	Parameters for exponential softening		Damage growth
	volumetric part	deviatoric part	
<i>exp</i> ———	$\eta_K = 600$	$\eta_G = 600$	more intensive
<i>exp, K</i> - - - -	$\eta_K = 200$	$\eta_G = 600$	$\omega_K < \omega_G$
<i>exp, G</i> - - - -	$\eta_K = 600$	$\eta_G = 200$	$\omega_K > \omega_G$
<i>exp, K &amp; G</i> ———	$\eta_K = 200$	$\eta_G = 200$	less intensive

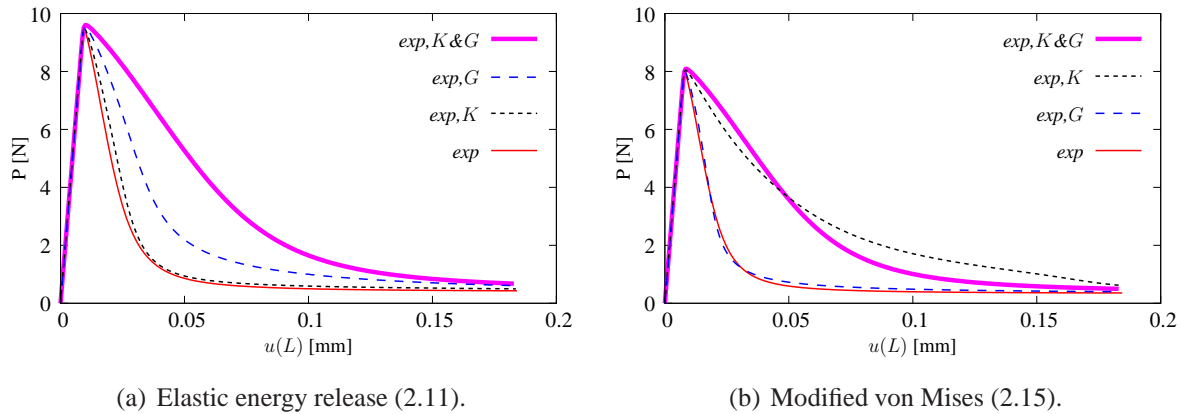
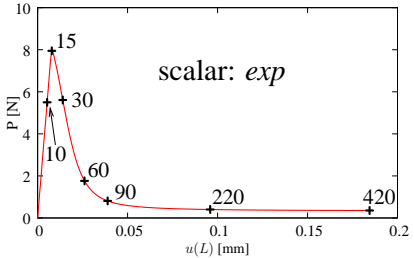
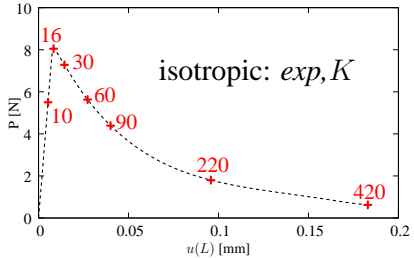


Figure 4.14: Tensile bar with imperfection (2D). Isotropic gradient damage. Load-displacement diagrams – different types of equivalent strain measure.

different damage loading functions are considered: elastic energy release EER definition (2.11) or modified von Mises definition (2.15). Computations are limited to the case with 80 elements Q8/4, where quad/lin interpolation is introduced. Like previously, the arc length control is used, but here the loading path is divided into equal steps. The width  $B$  equals 5 mm.

The load-elongation diagrams for the two adopted equivalent strain measures are illustrated in Fig. 4.14. A given value of the load is calculated as the sum of horizontal reactions on the left boundary. The relations between damage growth parameters  $\eta_K$  and  $\eta_G$  for exponential softening are listed in Table 4.4, thus four cases are distinguished. For cases *exp* and *exp, K & G* the model is in fact scalar, so the diagrams are different with reference to ductility, independently of the employed damage loading function. Isotropic properties appear for cases *exp, K* and *exp, G*, where deviatoric or volumetric damage dominates. For the EER loading function (2.11) the diagrams for cases *exp, K* and *exp, G* run between the bounding cases *exp* and *exp, K & G* and the diagram for *exp, G* is more ductile. On the other hand, for the modified von Mises definition (2.15) this does not hold and moreover, the diagram for *exp, K* is more ductile. Therefore, the shape of the damage loading function and additionally the non-zero Poisson's ratio decide about the response in this test although the bar is under tension in one direction. Next, the analysis is focused on the computations in which the modified von Mises definition is adopted.

Table 4.5: Convergence study – bar with imperfection. Scalar vs isotropic models.

Model				
Step no.	Relative energy norm	Active ips	Relative energy norm	Active ips
10	1.000000000000000E+00 6.545127804761267E+01 7.237258773905286E-27	0 0 0	1.000000000000000E+00 6.545127804761267E+01 7.237258773905286E-27	0 0 0
<i>exp</i> : 15 <i>exp, K</i> : 16 (peak)	1.000000000000000E+00 1.332232373671283E+02 5.283882949851624E-02 1.517076421774993E-05 1.271296475843388E-12 1.631334537801833E-26	32 40 40 40 40 40	1.000000000000000E+00 7.104307390597425E+01 2.828519453667412E-03 2.195920115196281E-08 3.044556460158339E-19	56 60 60 60 60
30	1.000000000000000E+00 -7.145757073494839E+00 -2.523525035112035E-12 -6.308773112513990E-13 6.502890662243225E-25	64 64 64 64 64	1.000000000000000E+00 -8.050307462407983E-01 1.529335843988511E-13 3.823338587620005E-14 1.759515922801841E-27	100 100 100 100 100
60	1.000000000000000E+00 -1.033016859561164E+00 7.135799125742083E-15 3.647482047565556E-27	52 52 52 52	1.000000000000000E+00 -5.097062669130918E-01 3.283294745214887E-15 8.208230538840247E-16 2.052057119854064E-16 5.130140402320353E-17	68 68 68 68 68 68
90	1.000000000000000E+00 -4.733095888274573E-02 1.587455443544377E-16 8.742964699372276E-27	60 60 60 60	1.000000000000000E+00 -2.813217273957667E-01 2.287022780935627E-16 5.717548206029520E-17	52 52 52 52
220	1.000000000000000E+00 -8.145727820349697E-05 7.918728946372482E-20	84 84 84	1.000000000000000E+00 -1.979850284683554E-02 7.956711042408951E-19	56 56 56
420	1.000000000000000E+00 -1.703893288677314E-06 3.747828894113349E-22	100 100 100	1.000000000000000E+00 -2.546419098702699E-03 8.311343950960651E-20	80 80 80

Before the results for various quantities are presented in detail, the convergence study is confronted in Table 4.5 for two chosen options: *exp* and *exp, K*, as representatives of the scalar and isotropic models. The convergence study for case *exp, K & G* is similar to *exp* and accordingly

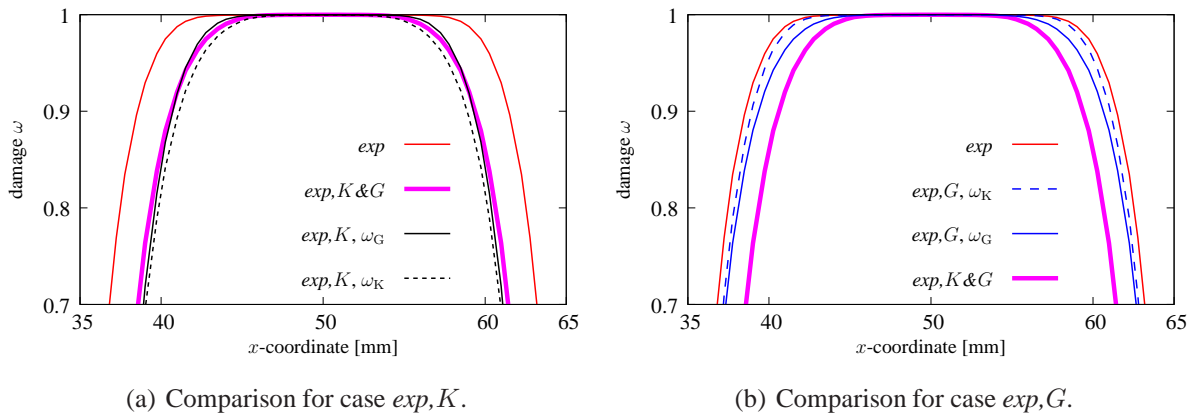


Figure 4.15: Tensile bar with imperfection (2D). Isotropic gradient damage. Damage distribution along the bar in final state.

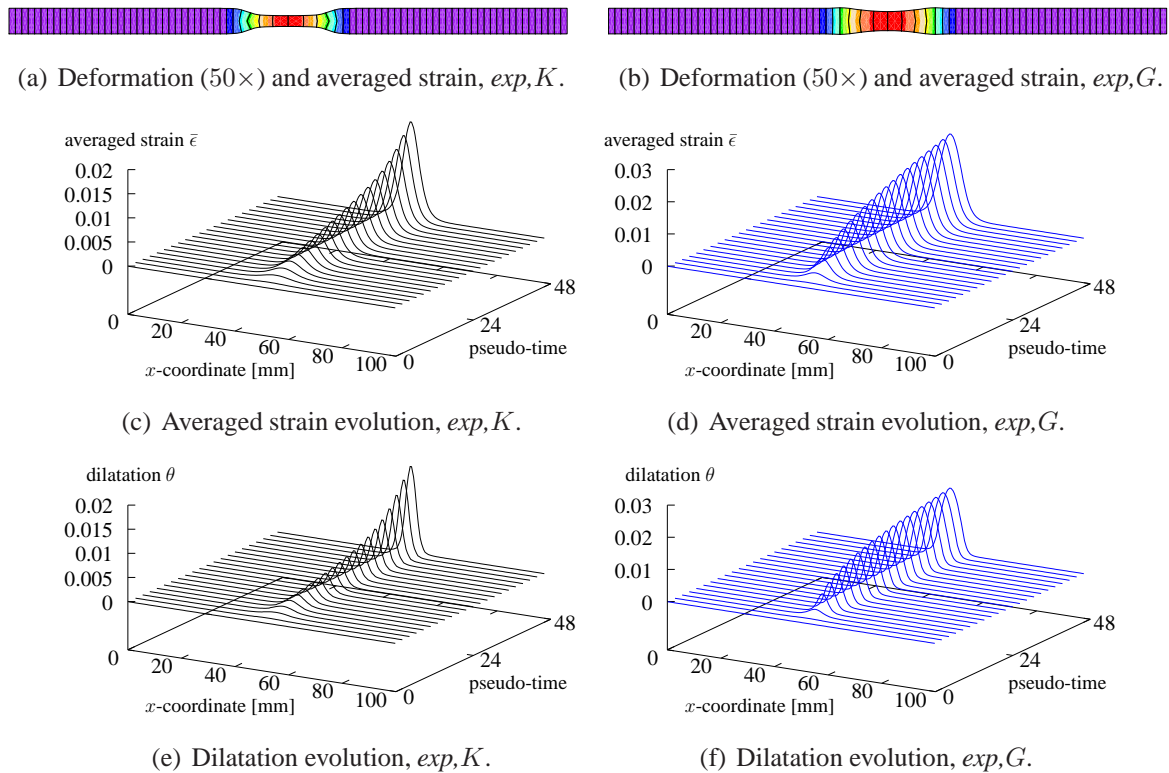


Figure 4.16: Tensile bar with imperfection (2D). Isotropic gradient damage. Deformation and strain state.

*exp, G* – to *exp, K*. It can be noticed that the quadratic convergence is lost near the peak load, but it is recovered for subsequent steps. The number of iterations during respective steps is almost the same for both analyzed cases. Moreover, the value of the relative energy norm diminishes in a similar manner.

Figs 4.15 and 4.16 show the results for two options, where ductility parameters  $\eta_i$  ( $i = K, G$ ) in the damage growth laws are different. The final damage distributions are depicted in



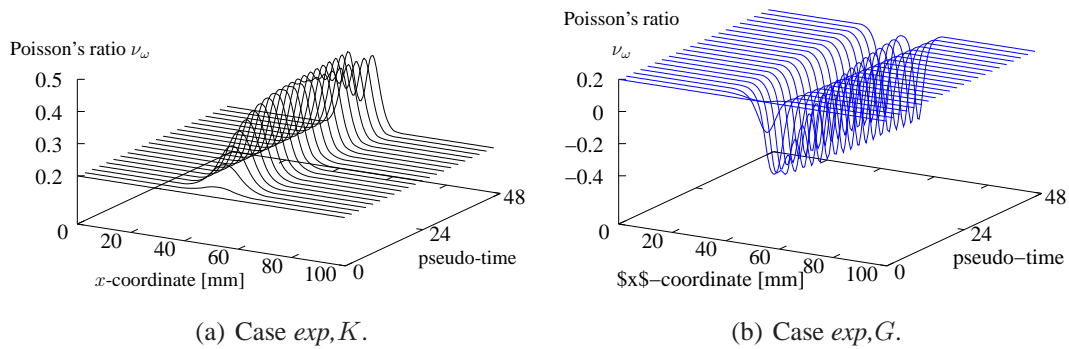


Figure 4.17: Bar with imperfection (2D). Isotropic gradient damage. Poisson's ratio evolution.

Fig. 4.15. It should be emphasized that the ranges of horizontal and vertical axes are shorten in order to clearly show the relations between parameters  $\omega_K$  and  $\omega_G$ , because the differences are rather small. Generally, the results for case *exp,K* are presented on the left and the results for *exp,G* are on the right. Final deformations, enlarged 50 times, together with the averaged strain patterns are illustrated in Figs 4.16(a) and 4.16(b). If case *exp,K* is considered the deformation produces a thinner localization band than for the *exp,G* option. Besides, in case *exp,G*, where volumetric degradation dominates, the bar can exhibit volume growth in the localization zone. It is caused by Poisson's ratio  $\nu_\omega$  decreasing below zero. These results looks non-physical, so they are not included in the analysis. The evolution of averaged strain  $\bar{\epsilon}$  and dilatation  $\theta$  during the damage evolution is similar for both cases, as shown in Fig. 4.16.

The Poisson's ratio distributions are compared in Fig. 4.17. The parameter  $\nu_\omega$  increases up to 0.45 in the zone of localization for the case *exp,K* where  $\omega_G > \omega_K$ . However, in advanced state this value reduces in the middle of the bar where damage is equal almost to 1, but close to this zone where difference between  $\omega_G$  and  $\omega_K$  still holds Poisson's ratio is approximately 0.45. An analogical situation is noticed in case *exp,G* where  $\omega_K > \omega_G$ . Now the evolution of the Poisson's ratio is inverted, i.e. it decreases in the zone of localization and then in the middle of the bar the initial value is retrieved. As mentioned in Section 2.4, for concrete it is expected that Poisson's ratio tends to 0 during the fracture evolution [21], but it does not drop below this value. It is possible to setup data in such a way that the negative Poisson's ratio is avoided, cf. results for the isotropic model in Section 2.5. On the other hand, maybe the deviatoric degradation (case *exp,K*) should be dominating, so it is still unclear which type of isotropic damage is more proper for concrete. Hence, in the next chapter both options will be considered.

Finally a short comparison for 3D elements is performed. The general data are again summarized in Tables 4.1 and 4.2 including the return to the linear softening law. The pure gradient damage model is computed. Five different types of interpolation and mesh divisions are confronted. Load-elongation diagrams are presented in Fig. 4.18. In Table 4.6 not only the important features for analyzed cases are characterized, but also the times of computations are shown. This computational time for each option is rather approximated, although all

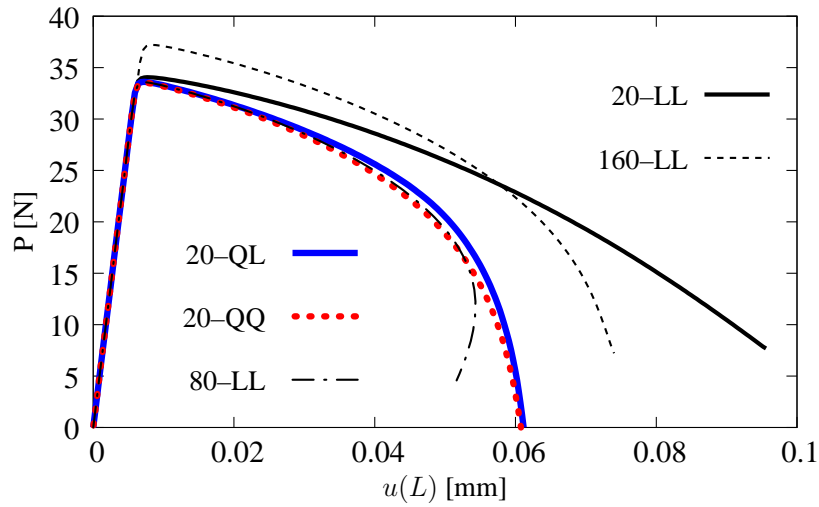


Figure 4.18: Tensile bar with imperfection in 3D. Load-displacement diagrams.

Table 4.6: Bar with imperfection – different 3D discretizations.

abbreviation	20-LL	80-LL	160-LL	20-QL	20-QQ
used FE	B8/8	B8/8	B8/8	B20/8	B20/20
interpolation	lin/lin	lin/lin	lin/lin	quad/lin	quad/quad
discretization	$20 \times 1 \times 1$	$80 \times 1 \times 1$	$40 \times 2 \times 2$	$20 \times 1 \times 1$	$20 \times 1 \times 1$
elements	20	80	160	20	20
nodes	84	324	369	248	248
dofs	336	1296	1476	828	992
equations	164	644	975	324	488
steps	231	141	176	152	151
iterations	772	675	756	730	720
iteration/step	3.34	4.79	4.30	4.80	4.77
total time (CPU) [s]	34.93	148.06	367.52	117.33	211.39
CPU time/step [s]	0.1512	1.0501	2.0882	0.7719	1.3999
CPU time/iteration	0.0452	0.2193	0.4861	0.1607	0.2936

measurements have been performed on the same processor called Intel Xeon with clock 2.4 GHz and RAM size of 4 GB. As expected, the fastest time is for case 20-LL. If more exact results are needed, a better idea is to enhance interpolation in FE than to refine the mesh. Introducing quad/lin interpolation into 3D elements in this simple test causes a triple increase of computational time, but quadratic interpolation for both fields costs over 6 times more. In large scale 3D problems discretized with fine meshes of twenty-noded FEs too much time can be consumed, so FE B8/8 with linear interpolation is chosen despite the fact that the solution can then produce less accurate results. The damage patterns at the final instant are depicted in Fig. 4.19.

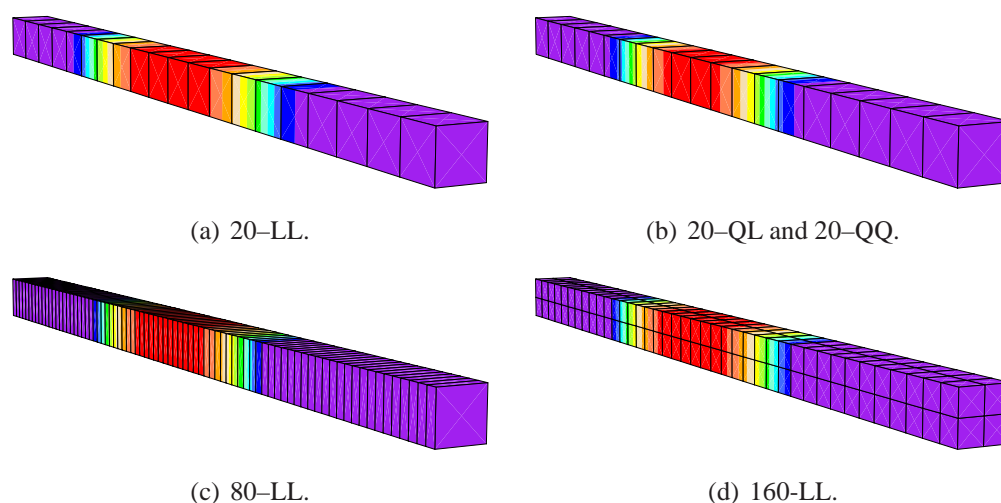


Figure 4.19: Results for bar with imperfection. 3D elements, damage – final distribution.

## 4.2 TWO TESTS FOR DYNAMICS

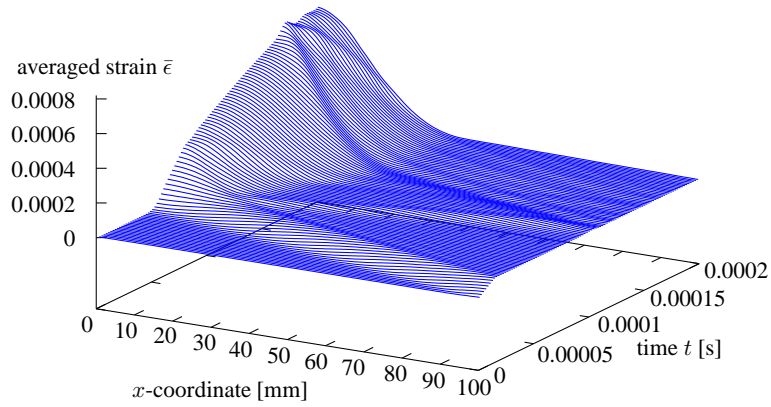
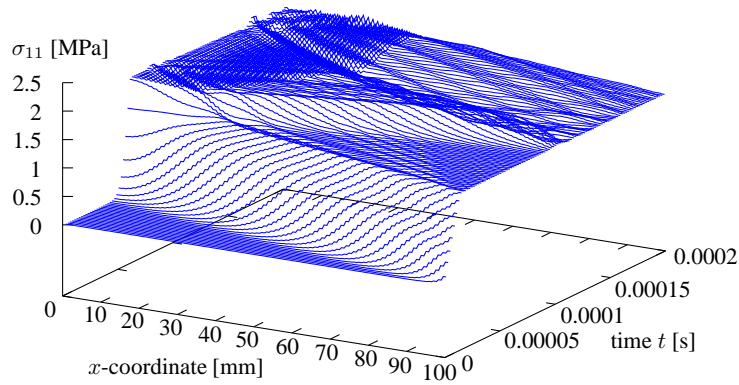
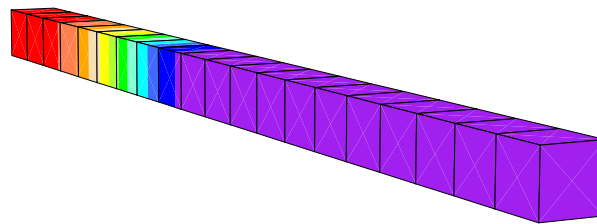
### 4.2.1 BAR UNDER IMPACT LOADING\*

The experimental review and mathematical foundations of softening phenomena in wave propagation can be found for example in [135]. A solution for a bar loaded at both sides or fixed at one and loaded at the other is presented in [8] and [150]. The analytical solution of a classical strain-softening bar in dynamics explains the mechanism of propagating waves before and after a reflection on a boundary. When the stress exceeds the elastic limit after the reflection of the wave front, softening occurs, imaginary wave speeds are obtained and hence waves do not propagate (a standing wave appears). When the propagating wave stops, strain localization is observed, which can lead to cracking in the solid. In a local continuum a displacement discontinuity accompanies the standing wave and the strain at the place of localization can be defined as a Dirac delta function. Hence, in the local approach the zone of intense deformation is limited to a discrete line (curve) or plane (surface), the IBVP loses hyperbolicity and the finite element solution reveals mesh sensitivity.

In this example it will be confirmed that among different regularization techniques also the gradient-dependent model can be applied for the wave propagation problem in softening materials and cracking phenomena under a pulse loading are suitably simulated. As the simplest test a bar extended in one dimension is considered. Almost the same benchmark has been computed to verify and compare various numerical models for example in [150]. In order to analyze wave propagation a time-dependent load at the right end of the bar is applied and the stress wave propagates to the left supported end. The stress attempts to double upon reflection, which results in damage and a standing wave related to softening.

---

\*Based on example presented in [173]

(a) Evolution of averaged strain measure  $\bar{\epsilon}$  along the bar in time.(b) Evolution of stress  $\sigma$  along the bar in time.(c) Evolution of damage  $\omega$  along the bar in time

(d) 3D contour plot of damage distribution (20 el., final instant).

Figure 4.20: Results for the bar under one-dimensional dynamic tension.

The length of the bar is  $L = 100$  mm, width  $B = 5$  mm and thickness  $T = 5$  mm. The data for the gradient damage model (scalar, without plasticity) are as follows: Young's modulus  $E = 20000$  MPa, Poisson's ratio  $\nu = 0.0$ , density  $\rho = 5000$  kg/m<sup>3</sup>, internal length  $l = 2\sqrt{2}$  mm. A linear damage growth as in Eq. (2.19) is assumed with threshold  $\kappa_0 = 0.0001$  and ultimate value  $\kappa_u = 0.0125$ . Linear-constant type of the pulse loading is adopted (as shown on the right-hand side of Fig. 4.21), where for instant  $t_1 = 1.5 \times 10^{-5}$  s the traction intensity  $P_1 = 0.75f_t$  is reached ( $f_t$  is the tensile strength). The time step is  $2 \times 10^{-6}$  s. The mesh contains 20 or 80 elements for the 2D analysis and 20 elements for 3D.

In Figs 4.20(a)–4.20(c) three surface plots for the case with 80 two-dimensional elements are shown: averaged strain measure  $\bar{\epsilon}$ , stress  $\sigma$  and damage parameter  $\omega$  are plotted against time and length of the bar. For the averaged strain it can be observed how the propagating wave changes into a standing wave, although the elastic part of the propagating energy results in small humps. In Fig. 4.20(b) a superposition of waves (values of stresses are not smoothed) is noticed. Damage initiates when the front of the wave reflects on the support, cf. Fig. 4.20(c). The results for all the applied meshes are similar. The final damage state for the 3D mesh is depicted in contour plot 4.20(d).

In this test the behaviour of the propagating wave in the gradient damage model is obtained, which seems to be similar to other mesh-independent softening models (see for example [150]). Due to the gradient terms the propagation is dispersive and hyperbolicity of the governing equations is preserved.

#### 4.2.2 DYNAMIC DIRECT TENSION TEST<sup>†</sup>

The aim of this test is a two-dimensional analysis of tensile wave propagation in a reinforced concrete damaging bar. The results of this test are compared with those for plain concrete bar (cf. also [118]) and the differences in dynamic response are examined.

As shown in Fig. 4.21, a bar supported along both symmetry axes and loaded with a time-dependent normal traction at both ends is considered. The reinforcement is located along the axis of the bar. The length of the bar is  $L = 250$  mm, width  $B = 60$  mm. The plane stress configuration with thickness  $T = 50$  mm is analyzed. Figure 4.21 also shows the employed discretization, where the central zone is refined because localization is expected there. Eight-noded two-field gradient damage elements for concrete and elastic truss finite elements for the reinforcement are introduced. Full bond between steel and concrete is assumed.

For the gradient damage model of concrete the material data are as follows: Young's modulus  $E = 18000$  MPa, Poisson's ratio  $\nu = 0.0$ , density  $\rho = 2320$  kg/m<sup>3</sup>. Exponential damage growth function (see Eq. (2.21)) is used with  $\kappa_0 = 0.00188$  (tensile strength  $f_t = 3.4$  MPa),  $\alpha = 0.99$  and  $\eta = 500$ . The modified von Mises definition of the equivalent strain (2.15)

<sup>†</sup>Based on example presented in [175]

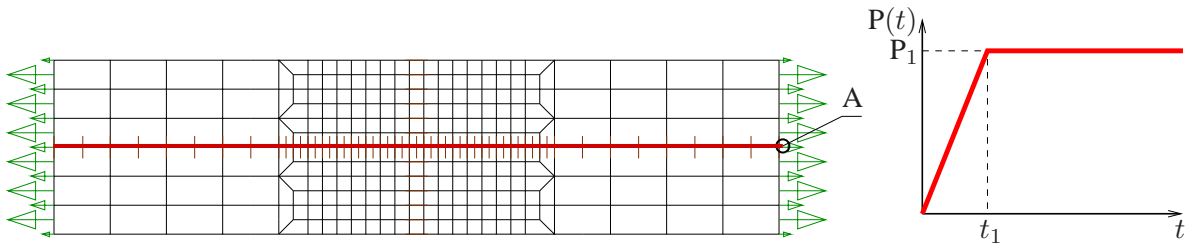


Figure 4.21: Dynamic direct tension test.

is employed. Three values of the internal length scale parameter, namely  $l = 2/4/8$  mm, are considered. The steel reinforcement is modelled with  $E = 200000$  MPa,  $\nu = 0.0$  and  $\rho = 7800$  kg/m<sup>3</sup> and cross section  $A_r = 30$  mm<sup>2</sup> (the reinforcement ratio equals 1%). The time step is  $2 \times 10^{-6}$  s, in Fig. 4.21 time  $t_1 = 3 \times 10^{-5}$  s and the traction intensity is  $P_1 = 2.4$  MPa.

The diagrams depicted in Fig. 4.22 confront the behaviour of the bar with and without the reinforcement. For plain concrete the elongation tends to infinity due to fracture, while for reinforced concrete the axial displacement oscillates around a certain state. Nevertheless, for both responses a standing wave and localization are observed in the centre of the bar (cf. Figs 4.23(e) and 4.23(f)).

Figure 4.23 shows the internal length influence for plain and reinforced concrete. The elongation-time diagrams for plain concrete, which are presented in Fig. 4.23(a), demonstrate that the smaller the value of parameter  $l$  is, the faster the elongation grows. Figure 4.23(b) points out that for reinforced concrete together with the decrease of  $l$  the amplitude of elon-

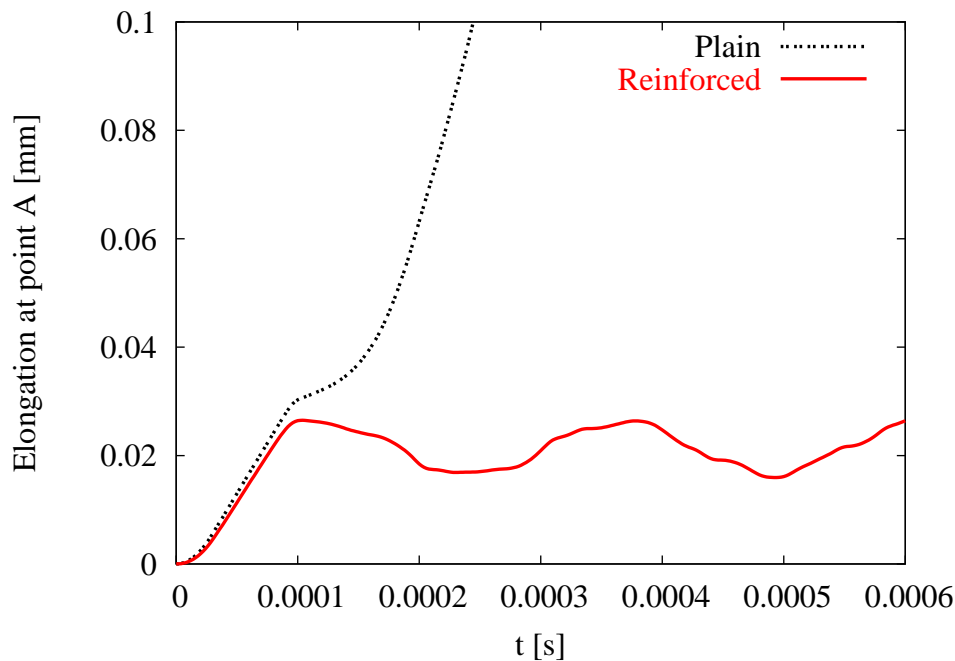


Figure 4.22: Elongation history for plain vs reinforced concrete.

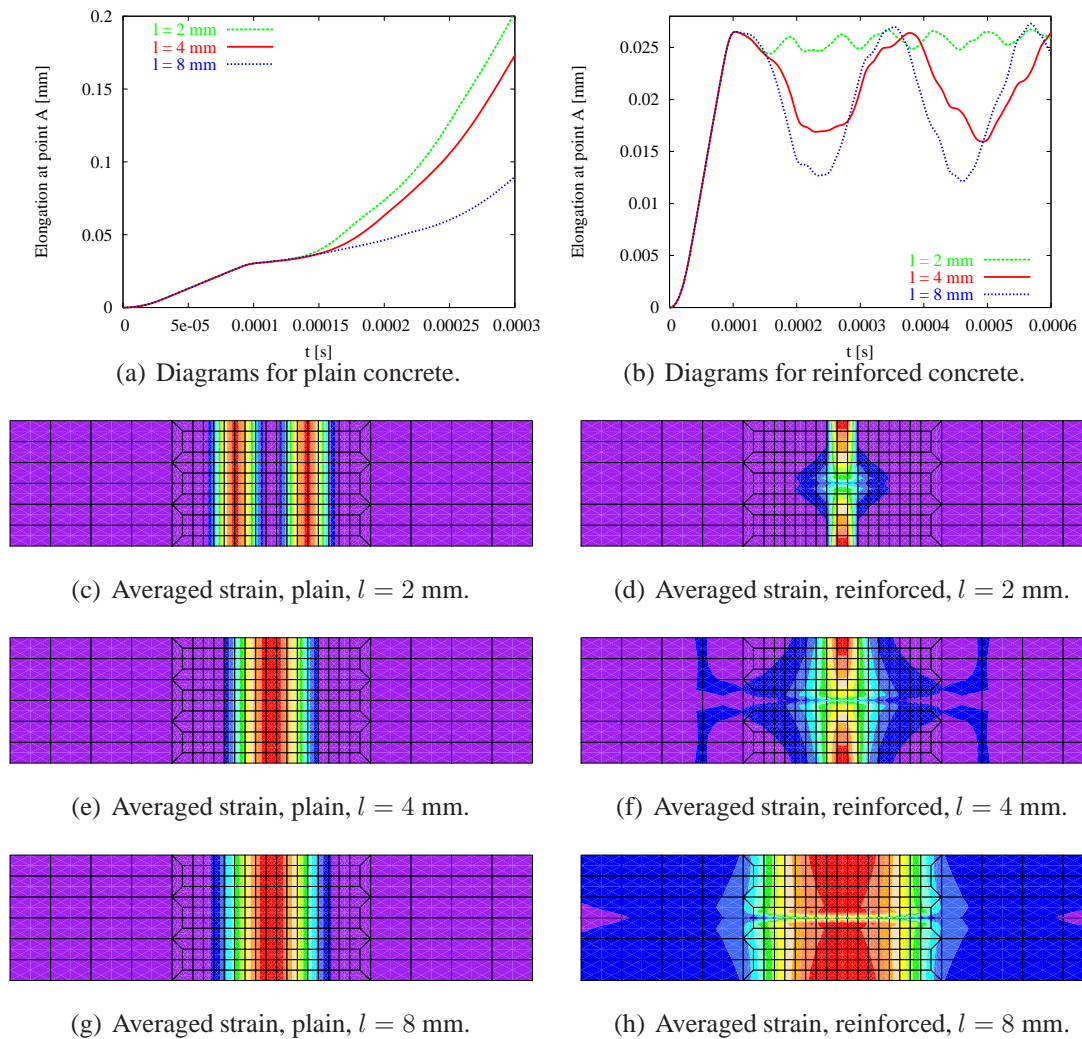


Figure 4.23: Internal length influence for plain and reinforced concrete bar.

gation during vibrations decreases. For  $l = 2$  mm a much smaller period of the vibrations occurs. A similar upper limit of the elongation for each  $l$  is observed, which is related to the reinforcement action.

All contour plots in Fig. 4.23, which illustrate the averaged strain distribution, are performed for the time instant  $t = 0.0006$  s (after 300 time steps). Comparing the results, for plain concrete and  $l = 2$  mm (Fig. 4.23(c)) two separated zones of localization appear, which is probably a numerical effect. For the other cases one central zone emerges, which is consistent with the analytical solution for the strain-softening bar presented in [8]. The standing decohesion wave is located exactly in the centre. The general tendency for gradient-enhanced models that the width of the zone increases together with larger  $l$  is valid. For plain concrete the localization zones are perpendicular to the bar axis and the averaged strain contours form even bands, which is expected due to the loading direction (for a non-zero Poisson's ratio the distribution of the averaged strain looks similarly).

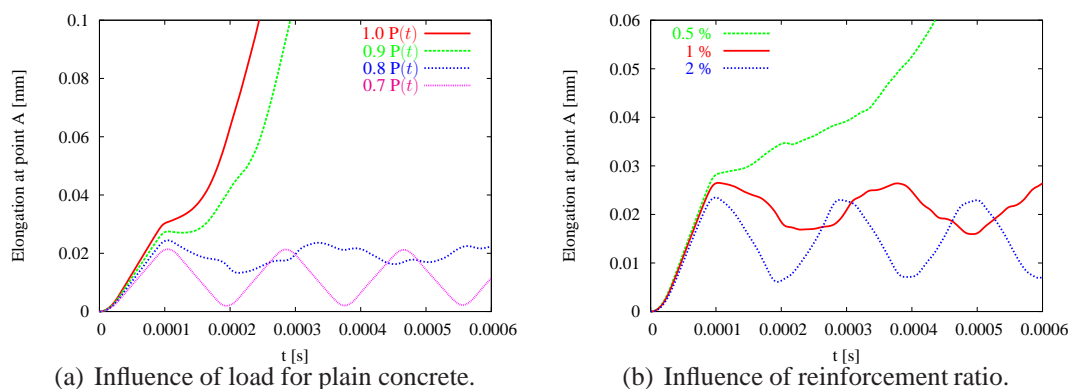


Figure 4.24: Sensitivity of results to load intensity and reinforcement ratio.

On the right-hand side of Fig. 4.23 the averaged strain distribution for reinforced concrete is shown. Here, like for plain concrete, with the growth of  $l$  the zone of localization enlarges. A new visible effect is that the reinforcement delays the progress of cracking along the whole width. Along the bar axis localization does not seem to occur. The most active zones are the farthest from the reinforcement, but similarly to plain concrete the standing wave and damage zone are placed in the central part of the tensile bar. The full bond between concrete and the rebar influences the shape of the damage zones, which do not look very realistic. In reality more than one localized cracks, which gradually develop in the vertical direction next to the reinforcement, are observed. However, the existence of the reinforcement in this simulation suppresses evolution of the localized zone, cf. diagrams in Figs 4.23(a) and 4.23(b). To simulate this behaviour a proper representation of bond slip and, from the numerical point of view, the implementation of interface elements can be adopted like in [153].

The elongation-time diagrams in Fig. 4.24(a) present the dependence on the load scaling factor for the plain concrete test with  $l = 4$  mm. The limit load factor when either the elongation goes to infinity or oscillations occur is between 0.8 and 0.9. For  $0.7 P(t)$  the standing wave does not appear, which means that the elastic energy dominates the solution. The influence of the reinforcement ratio is considered in Fig. 4.24(b). For the smallest cross section of the reinforcement the specimen behaves similarly to the tests with plain concrete, when the standing wave is noticed and the elongation tends to infinity. The results for 2% of reinforcement show similar oscillations to the case  $0.7 P(t)$  for plain concrete. In fact, it is difficult to assess whether the propagating wave changes into a standing one, but the damage zone arises (not presented).



## CHAPTER 5

# NUMERICAL MODEL APPLICATIONS

### 5.1 CANTILEVER BEAM UNDER LOAD REVERSALS

A cantilever beam (similar to a half of three-point bending test) subjected to reversed loading is analyzed. The beam together with the employed FE mesh are illustrated in Fig. 5.1. This test was also solved and discussed in [117, 122], so the results presented below extend the ones previously shown. The elements Q8/4 with quadratic/linear interpolation and  $2 \times 2$  Gauss integration are adopted. The dimensions of the beam are shown in Fig. 5.1 and the thickness is 50 mm. The vertical force is exerted along the left edge under deformation control of all vertical degrees of freedom. The load is first applied upwards, so tensile fibers are at the bottom. Then after an unloading stage the load changes the sign and the upper fibers are under increasing tension, followed by unloading again. The nodes at the clamped edge are fully constrained.

The elastic constants are as follows: Young's modulus  $E = 40000 \text{ N/mm}^2$  and Poisson's ratio  $\nu = 0.0$ . The reasons why this particular value of Poisson's ratio is chosen will be discussed later. The material data for pure damage are assumed as follows: modified von Mises definition (2.15) of the strain measure with threshold  $\kappa_o = 0.000075$ , exponential damage evolution (2.21) with  $\alpha = 0.92$  and  $\eta = 300$ , gradient influence factor  $c = 4 \text{ mm}^2$ .

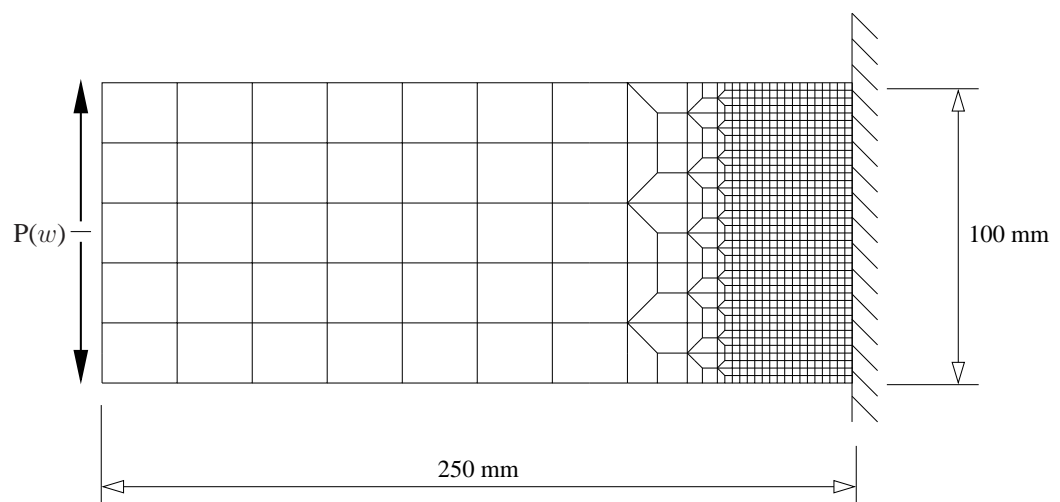


Figure 5.1: Cantilever beam under load reversals together with FE mesh.

If the crack closure is activated, it provides a possibility to retrieve the original elastic stiffness when compression follows tensile damage at a point, and also makes it unnecessary to use the modified von Mises definition of the strain measure. This is because with the projection operator  $P^+$  the definition of elastic energy release rate in Eq. (2.77) is sensitive to the sign of loading and in triaxial compression no damage occurs (see Section 2.3, page 29). Therefore, the cantilever test is repeated with this equivalent strain measure and the crack closing effect is incorporated by means of  $P^+$  according to the Ortiz definition (2.66).

Next, the weak coupling with the hardening plasticity theory is added to the model which results in irreversible strains. In this option the equivalent strain  $\tilde{\epsilon}$  depends only on the elastic part of the strain tensor. The HMM criterion is used with yield strength  $\sigma_y = 4.5 \text{ N/mm}^2$  and modulus  $h = E/2$ . The damage and plastic processes start simultaneously.

Fig. 5.2 shows the relationship between the total force exerted at the left edge and vertical displacement  $w$  of the middle node of the edge for the three considered options, namely: pure damage without and with the crack closure projection and finally coupled damage-plasticity together with crack closing. The upward load causes damage starting at the bottom near the clamped edge (cf. Fig. 5.5 and also crack patterns in [122]). Obviously all paths involve softening, but for the coupled model the process is less rapid. Unloading shows the stiffness degradation due to the accumulated damage. The pure model without and with activated crack closing does not exhibit differences in diagrams until the origin is passed. For the model without crack closure effect the original stiffness is not retrieved. The crack closure takes place if operator  $P^+$  is included in computations. The unloading path for the coupled model with crack closing ends

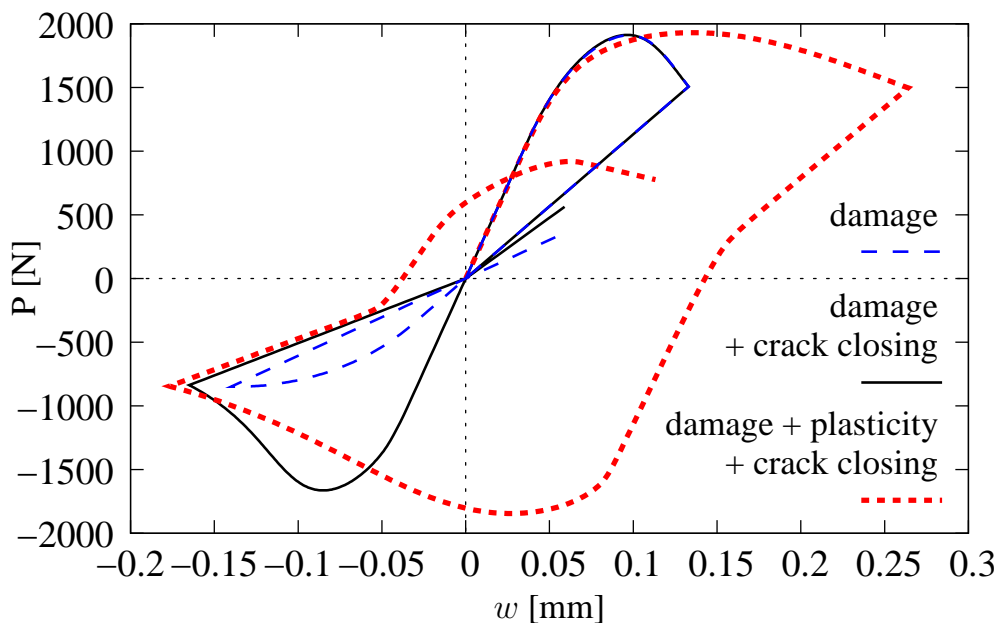


Figure 5.2: Cantilever beam under load reversals – load-displacement diagrams.

before the load value drops to zero. There are clearly visible irreversible strains and also the return to the initial stiffness. The active damage process starts under reversed loading, before the deflection of the beam changes the sign.

Now attention is focused on the results for the case when damage-plasticity together with the crack closure effect is analyzed. Figures 5.3 and 5.4 present the distribution of the horizontal stress  $\sigma_{11}$  along the vertical line A-A during the loading process (at points marked on the equilibrium path). The line A-A runs along the height of the beam crossing the integration points in the second column of elements from the clamped edge, see Fig. 5.3(a). After the elastic limit is reached, it is visible in Figs 5.3(c)–5.3(e) that the value of the tensile strength calculated as  $f_t = \kappa_o E = 3$  MPa is not exceeded and the zone corresponding to this value grows from the bottom. Figure 5.3(f) is plotted for point 5, when unloading is advanced, but crack closing is not entered yet. The next figure is made for point 6, just after the crack closure effect activates. At this moment negative stresses appear at the bottom of the section. The return to the original stiffness is observed in the diagram (Fig. 5.3(a)), so a sufficient number of integration points cross into compression and from that moment on crack closing is noticed as the general behaviour of the beam. Figure 5.4(a) shows that the tensile strength is reached at the upper side. The most negative value in the stress distribution is obtained at point 9, when the largest vertical displacement downwards is forced. After that the beam returns again to the state, where tensile fibers are at the bottom. Starting from point 10 in Fig. 5.4(c) negative stresses appear at the top and the second increase of the global stiffness is reproduced. The stress distributions was prepared without any smoothing, so some disturbances near the lower and upper boundaries are observed.

Figures 5.5 and 5.6 present the crack patterns at the state when the largest vertical displacement  $w$  is observed in the two directions. The secondary damage zone develops at the top near the clamped edge at smaller stress, since the primary damage weakened the critical cross-section. Observe that in this model the attained damage level is remembered at a point irrespective of any change of the sign of strains, so in the secondary phase two damage zones are visible although the averaged strain measure plot shows the active zone. This test has been computed for  $\nu = 0$ , since for the zero Poisson effect the tangent stiffness operator  $\mathbf{E}_{\text{tan}}$  takes a particular form for which discontinuities in the stress-strain response are avoided [23].

In fact, for  $\nu = 0.2$  the solution diverges if crack closure is activated (hence this case is not shown in the thesis, see [117, 122]). As noticed in [23], due to the unilateral character of the crack closure phenomenon a discontinuity (Heaviside function) is introduced in the formulation and this might be the cause of numerical difficulties. The problem can be solved in different ways. For example, a modification of the crack closing algorithm along the lines proposed in [53] can be formulated and implemented. This requires the introduction of a certain continuous

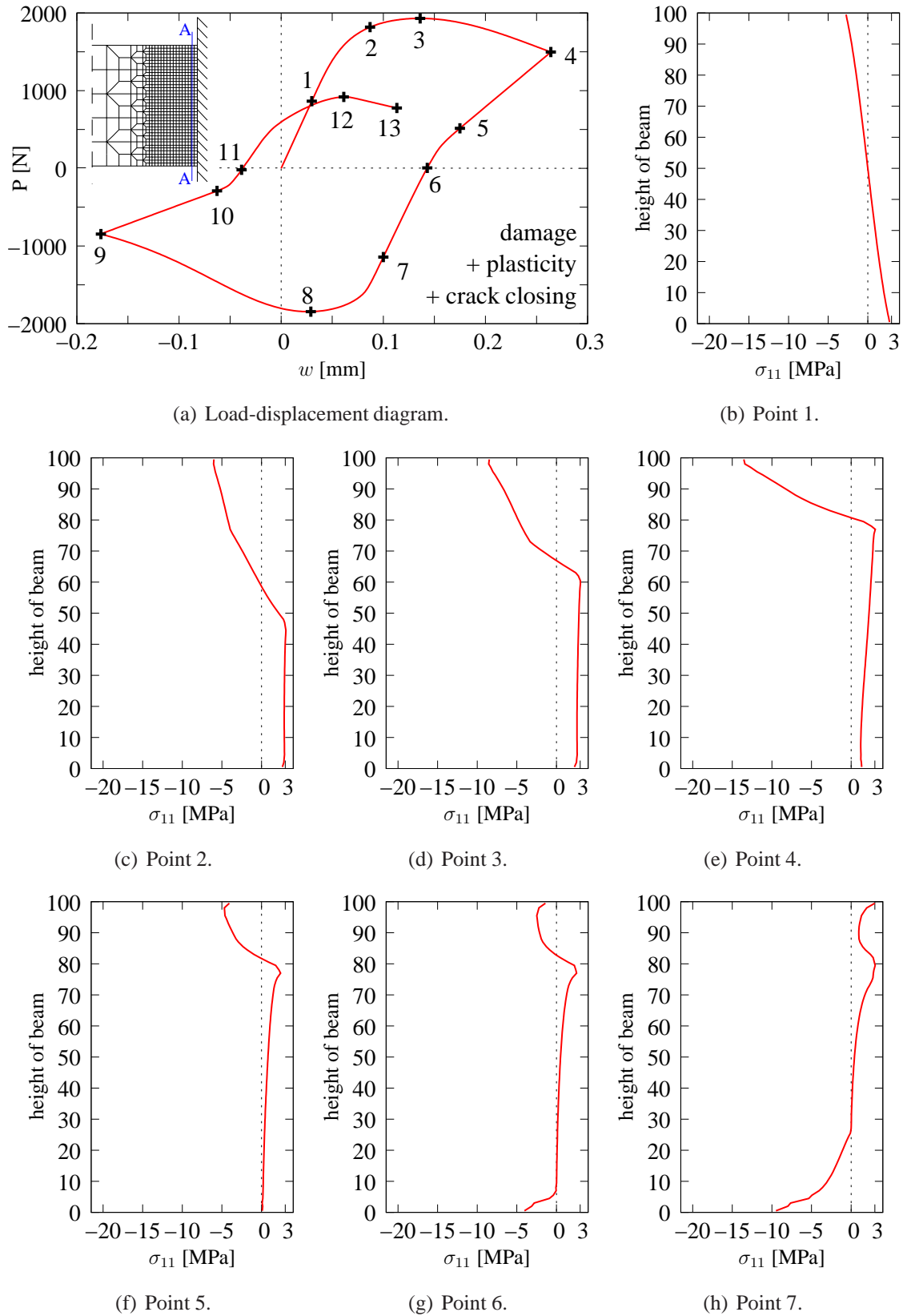


Figure 5.3: Cantilever beam under load reversals – evolution of stress  $\sigma_{11}$  along line A-A.

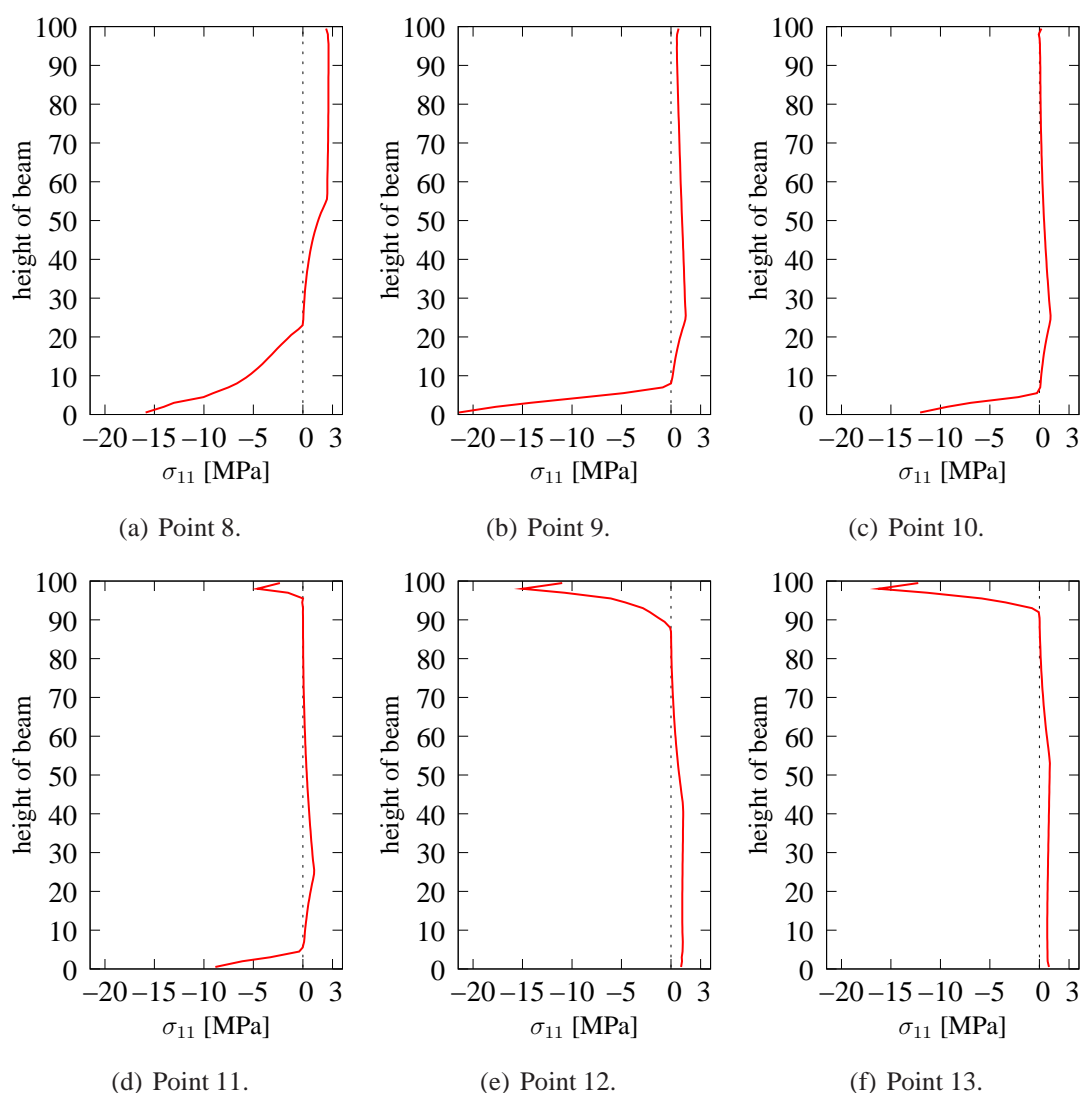


Figure 5.4: Cantilever beam, load reversals – evolution of stress  $\sigma_{11}$ , line A-A (continued).

function in the projection operator. Then, if crack closing is activated, the change of the stiffness does not involve any jumps. It is physically motivated, because the experimental observation is that microdefects do not close suddenly but rather gradually.

As has been noticed in [55], the damage predictions of the model with a constant gradient influence factor  $c$  and the exponential damage evolution law may be unrealistic for two-dimensional configurations, since the damage zone tends to broaden instead of evolving into a crack when failure is approached, cf. Figs 5.5(c) and 5.6(c). The coupling to plasticity does not solve this problem. If a localized final damage pattern is to be simulated, the gradient-damage model should be improved, for instance by making the gradient influence factor variable and adopting a different damage law, see [55]. An other idea is to remove totally damaged finite elements from the discretized mesh during the solution like in [124], however the application of this approach together with crack closing is problematic.

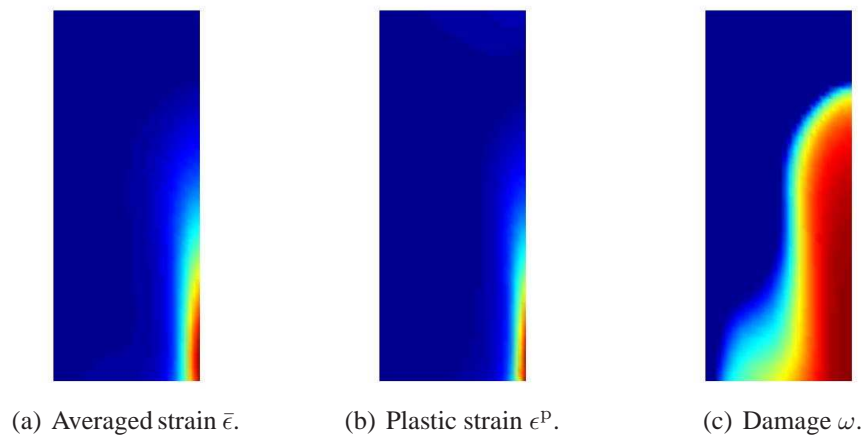


Figure 5.5: Part of cantilever near clamped edge. Damage coupled to plasticity and crack closing – contour plots for maximum upward displacement  $w$ .

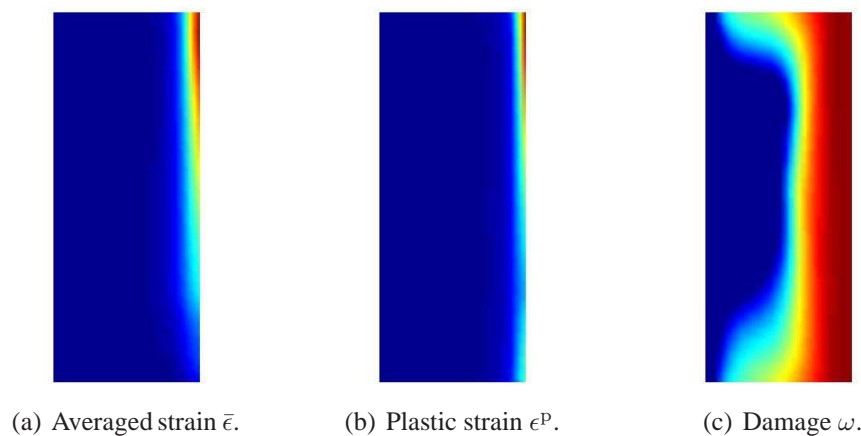
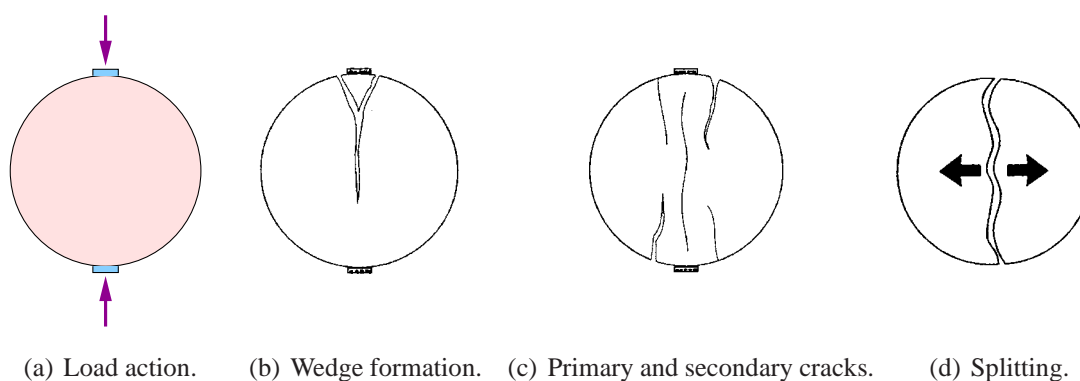


Figure 5.6: Part of cantilever near clamped edge. Damage coupled to plasticity and crack closing – contour plots for maximum downward displacement  $w$ .

## 5.2 BRAZILIAN SPLIT TEST

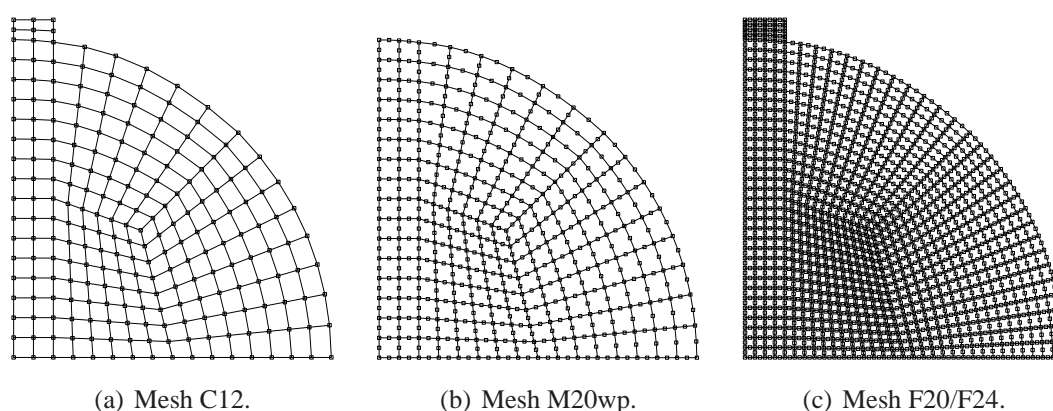
### 5.2.1 APPLICATION OF SCALAR DAMAGE

This example presents the behaviour of the gradient damage model in the so-called Brazilian test (see Fig. 5.7). Under the influence of compression primary and secondary cracks form [137,138], when splitting inside the specimen is observed. This phenomenon is used to establish the concrete tensile strength, because the compression between the loading platens induces the perpendicular tensile force action in the middle. In the numerical simulation, according to the experiment (see for example [137, 167]), localization is expected in the vertical central zone of the specimen between load-transferring strips as is shown e.g. in [49, 138]. The cylinder specimen is simulated in plane strain, but plane stress [172] or 3D analyses [142] are also possible.



(a) Load action. (b) Wedge formation. (c) Primary and secondary cracks. (d) Splitting.

Figure 5.7: Idea of Brazilian split test. Subfigures (b), (c) and (d) quoted from [137].



(a) Mesh C12.

(b) Mesh M20wp.

(c) Mesh F20/F24.

Figure 5.8: Exemplary meshes for Brazilian test.

Due to a double symmetry and in order to reduce the computation time only a quarter of the domain (with radius equal to 40 mm) is considered. The general geometry data are based on [49, 172]. The load is applied to the specimen indirectly via a stiff platen (width - 5 mm, height - 2.5 mm). The platen is perfectly connected with the specimen. The meshes selected for this case are shown in Figs 5.8(a) and 5.8(c). The applied discretizations are listed in Table 5.1. The influence of mesh refinement will be discussed in the next paragraph. To compare, direct loading without the platen can be considered, see mesh M20wp in Fig. 5.8(b). The load acts downwards at the top of the platen or in the case without platen at the edge part equivalent to the platen. The material data are presented in Table 5.2. No coupling with plasticity is included in the model (pure gradient damage). Because of a possible snapback response the test is computed using the arc length method. In the calculations selective integration is applied for lin/lin interpolation (FE Q4/4) and  $2 \times 2$  integration for the remaining elements.

The vertical displacement at the top of the platen on the symmetry axis is measured, which grows with the applied loading. In Figs 5.9 and 5.10 load-displacement diagrams for the used meshes are presented. For no solution a softening curve is obtained like in [49], instead a snapback response is observed which is connected with the splitting process. In Fig. 5.9 two

Table 5.1: Brazilian test – discretizations used in simulations.

COARSE MESHES			
name	C12 (Fig. 5.8(a))	C20	C24
used FE	Q4/4	Q8/4	Q8/8
interpolation	lin/lin	quad/lin	quad/quad
dofs/element	12	20	24
nodes/sym.edge	17	17	17
elems/sym.edge	16	8	8
MEDIUM MESHES			
name	M12	M20	M24
used FE	Q4/4	Q8/4	Q8/8
interpolation	lin/lin	quad/lin	quad/quad
dofs/element	12	20	24
nodes/sym.edge	33	33	33
elems/sym.edge	32	16	16
FINE MESHES			
name	F12	F20 (Fig. 5.8(c))	F24 (Fig. 5.8(c))
used FE	Q4/4	Q8/4	Q8/8
interpolation	lin/lin	quad/lin	quad/quad
dofs/element	12	20	24
nodes/sym.edge	65	65	65
elems/sym.edge	64	32	32

Table 5.2: Brazilian test – material model data.

---

SPECIMEN: damaging  
 Young's modulus:  $E_c = 37700$  MPa  
 Poisson's ratio:  $\nu = 0.15$

Equivalent strain measure: modified von Mises definition,  $k = 10$

Damage growth function: exponential softening,  $\alpha = 0.99$ ,  $\eta = 600$

Fracture energy:  $G_f = 0.075$  N/mm  
 Internal length scale:  $l = 6$  mm, i.e.  $c = 18.0$   
 Threshold:  $\kappa_o = 7.9576 \times 10^{-5}$

---

PLATEN: elastic  
 Young's modulus:  $E_s = 10 \cdot E_c$   
 Poisson's ratio:  $\nu = 0.15$

---



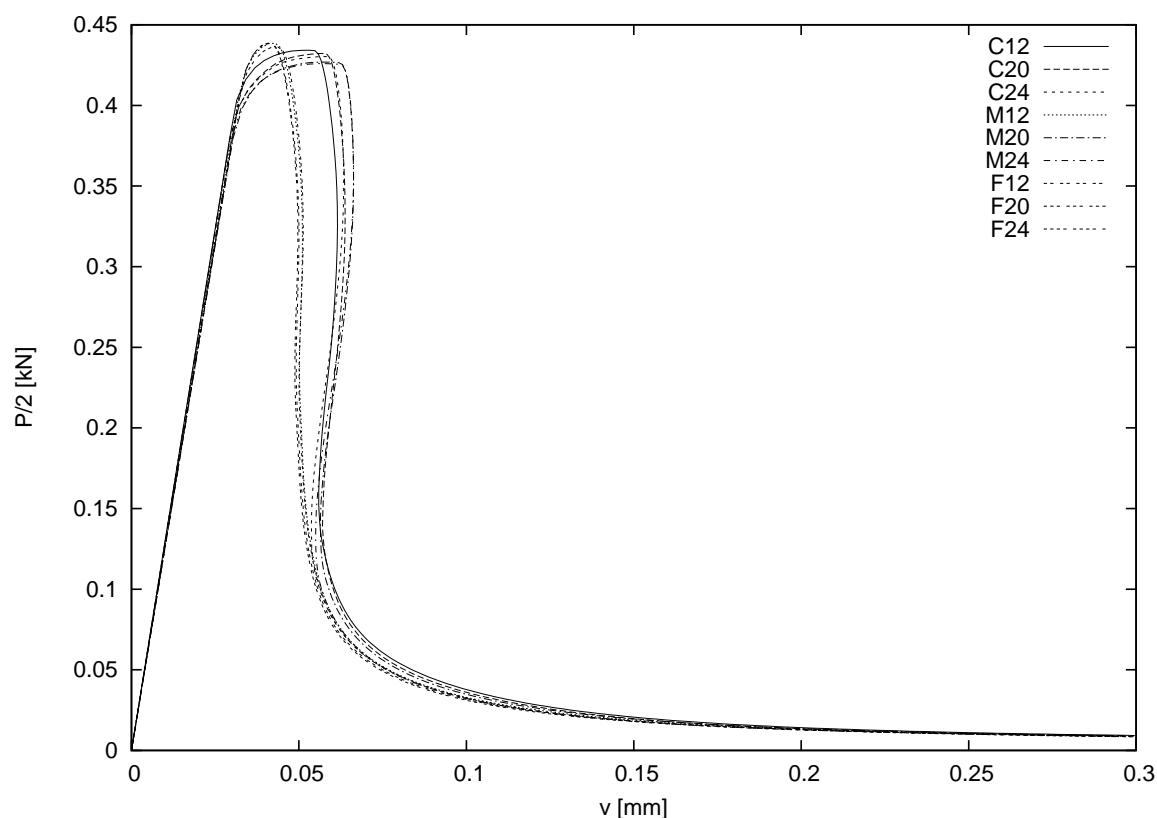


Figure 5.9: Load-displacement diagrams for used meshes in Brazilian test – summary.

groups of diagrams are noticed. One group shows a sharper drop after a longer peak phase. It is for solutions performed with coarse meshes, and M20 or M24. The second group of branches (fine meshes and M12) show the response with a more distinct peak and the snapback is less pronounced. An explanation why the solution for mesh M12 belongs to the second group can be found if we compare the mesh density and especially integration point density for the meshes. In this context the ratio of refinement for mesh M12 is the same as for meshes F20 and F24 (see Table 5.1).

A difference between the solutions for meshes M20/M24 and M12 is observed, as is depicted in Fig. 5.10(b), hence an improvement of the approximation can slightly influence the loading path. However, in general the results are almost independent of the mesh. In the final stage, the loading paths go to the same residual load level.

The contour plots in Figs 5.11–5.13 show the mesh independence of the results. The failure mode associated with primary crack formation [137, 138] is seen, it means that a crack appears exactly under the loading platen along the vertical symmetry axis. All the plots are shown for the final points of the loading paths. The deformation presented in Fig. 5.12(b) seems to be similar to [16, 49], but apart from the splitting a small concentration of strains in the area under the platen is observed here (see also contour plots 5.11(a), 5.12(a) and 5.13(a) for the horizontal normal strain  $\epsilon_{11}$ ). Probably the concentration is induced just after the primary crack formation

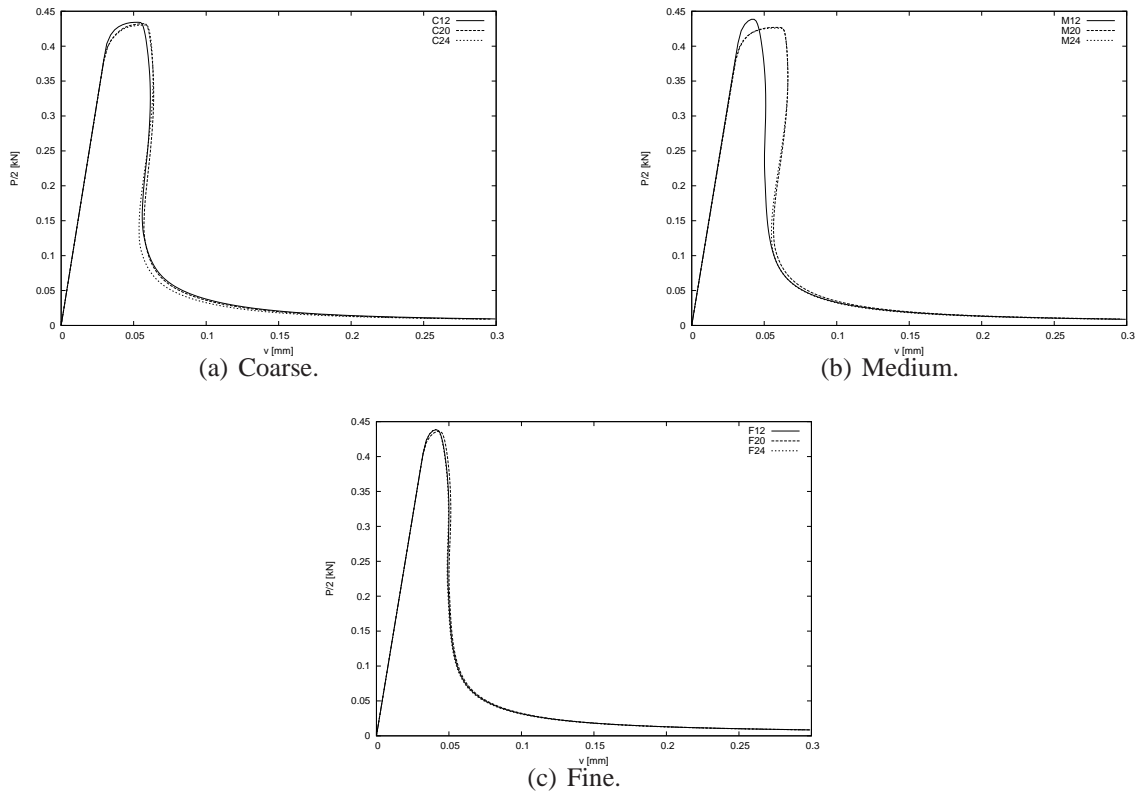


Figure 5.10: Load-displacement diagrams for coarse, medium and fine meshes in Brazilian test.

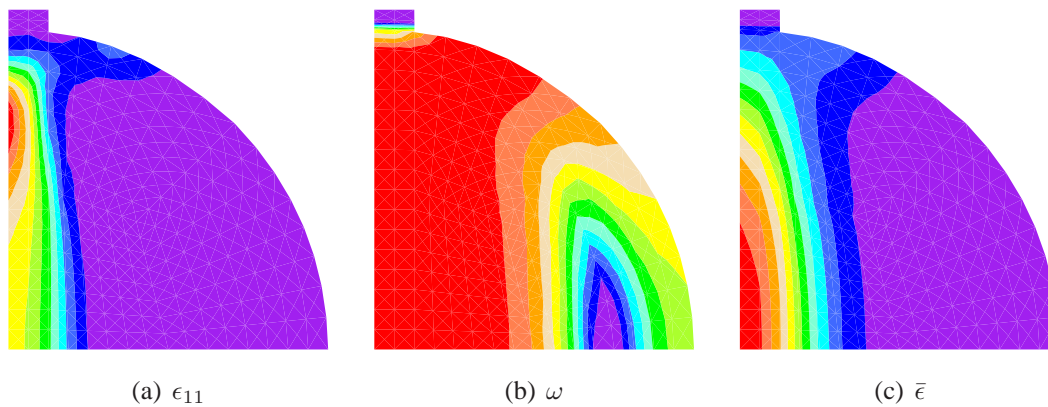


Figure 5.11: Brazilian test. Contour plots for mesh C12.

and it can depend on the value of the internal length parameter. The broad damage zones as in the cantilever subjected to load reversals are perceived.

The internal length parameter, which is incorporated in the Helmholtz equation (3.7), decides in the Brazilian test whether or not and how the splitting phenomenon appears. The diagrams in Fig. 5.14 show that with the decreasing value of  $l$  the material becomes more brittle. When the parameter equals 3 mm the splitting phenomenon during the process does not occur. It is reflected in the contour plots (Fig. 5.15) and in the diagram with the monotonically softening curve. The loading path for  $l$  equal to 12 mm, first exhibits a gradual softening stage

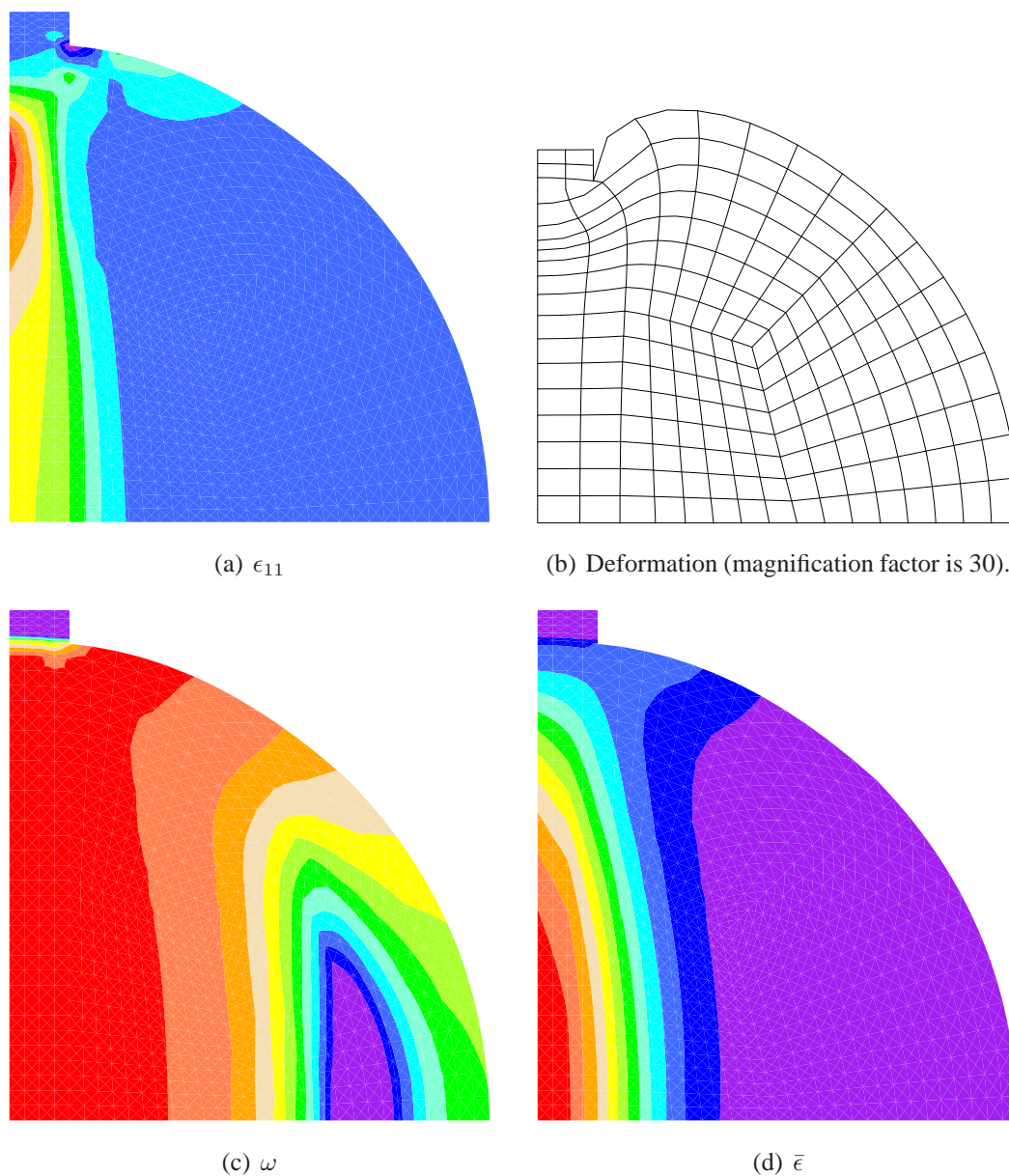


Figure 5.12: Brazilian test. Contour plots for mesh M20.

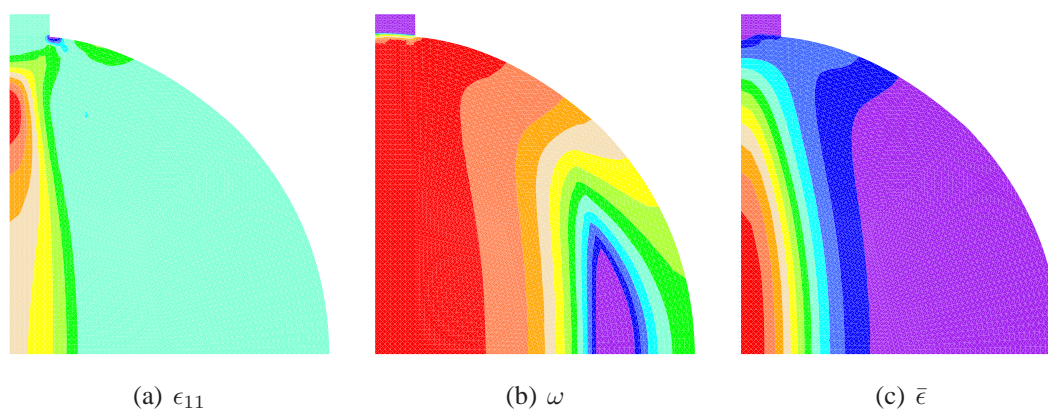


Figure 5.13: Brazilian test. Contour plots for mesh F24.

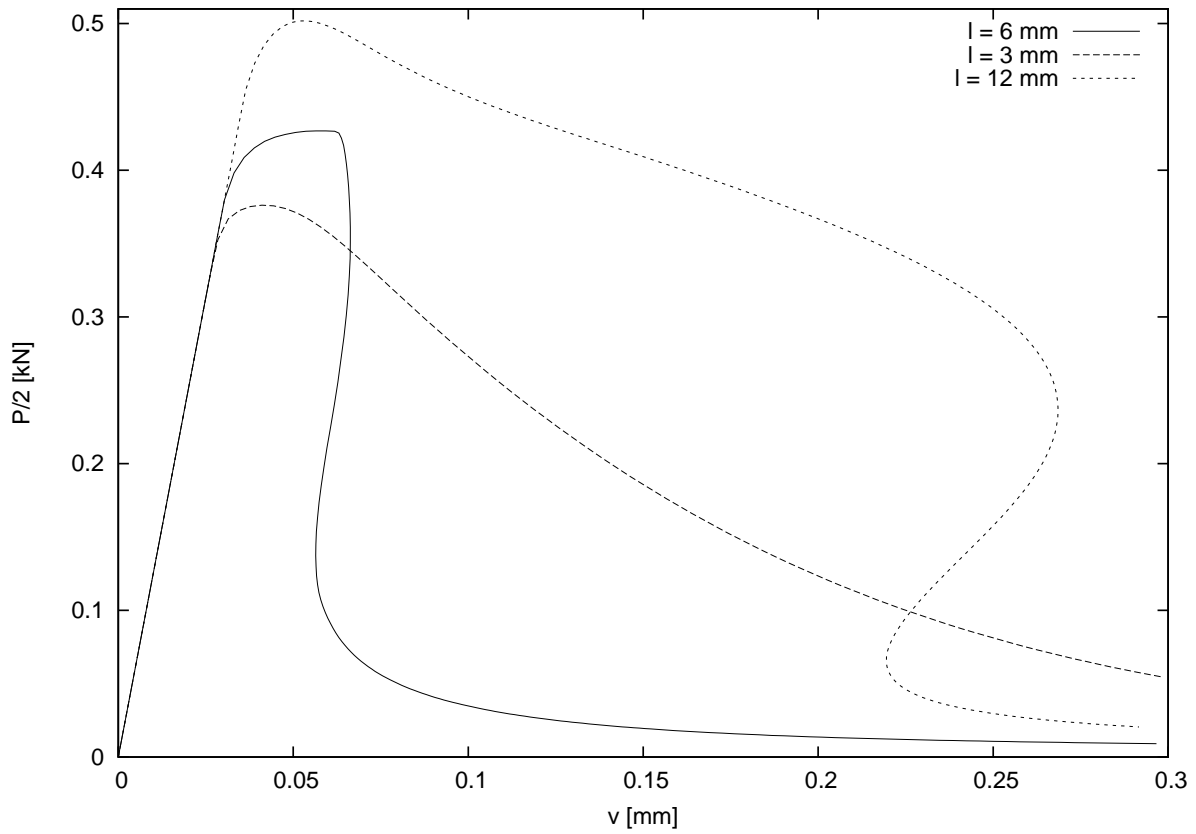


Figure 5.14: Brazilian test. Influence of internal length scale – diagrams.

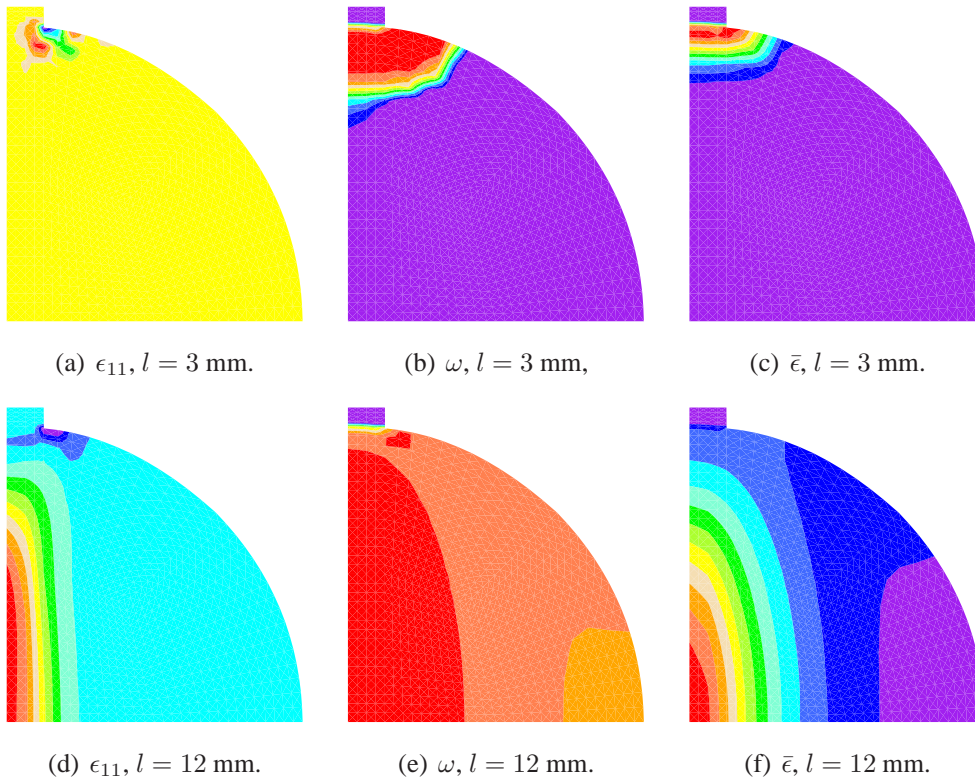


Figure 5.15: Brazilian test. Influence of internal length scale – contour plots.

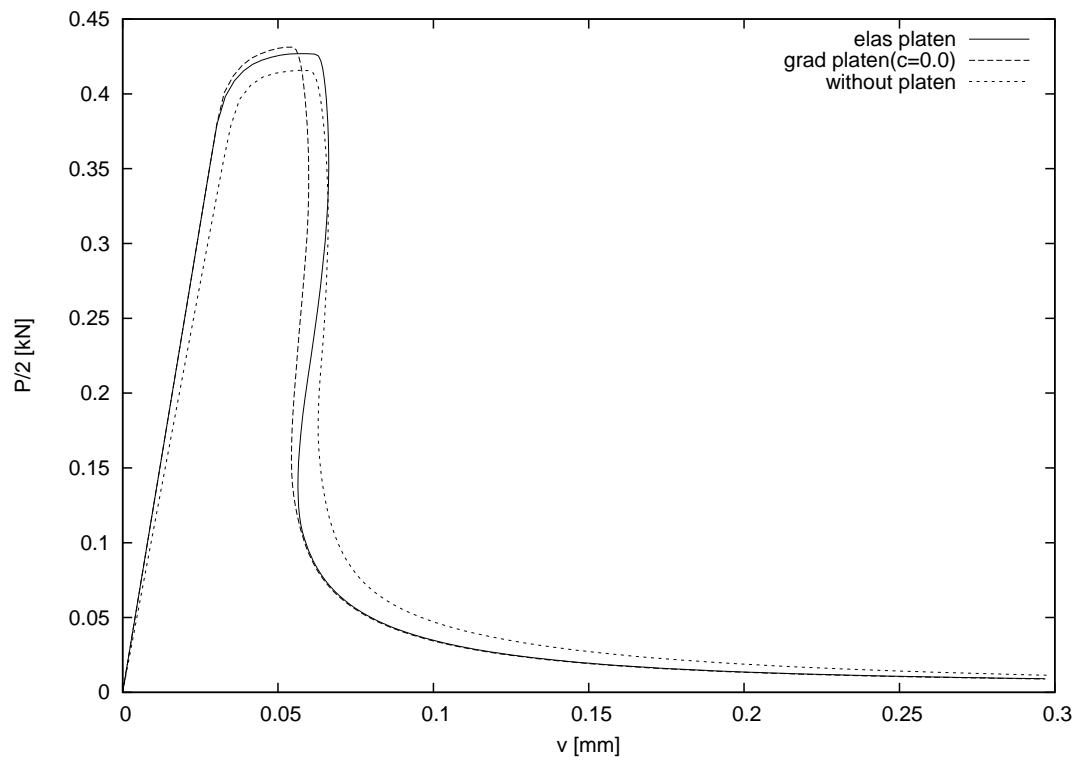


Figure 5.16: Brazilian test. Influence of platen definition – diagrams.

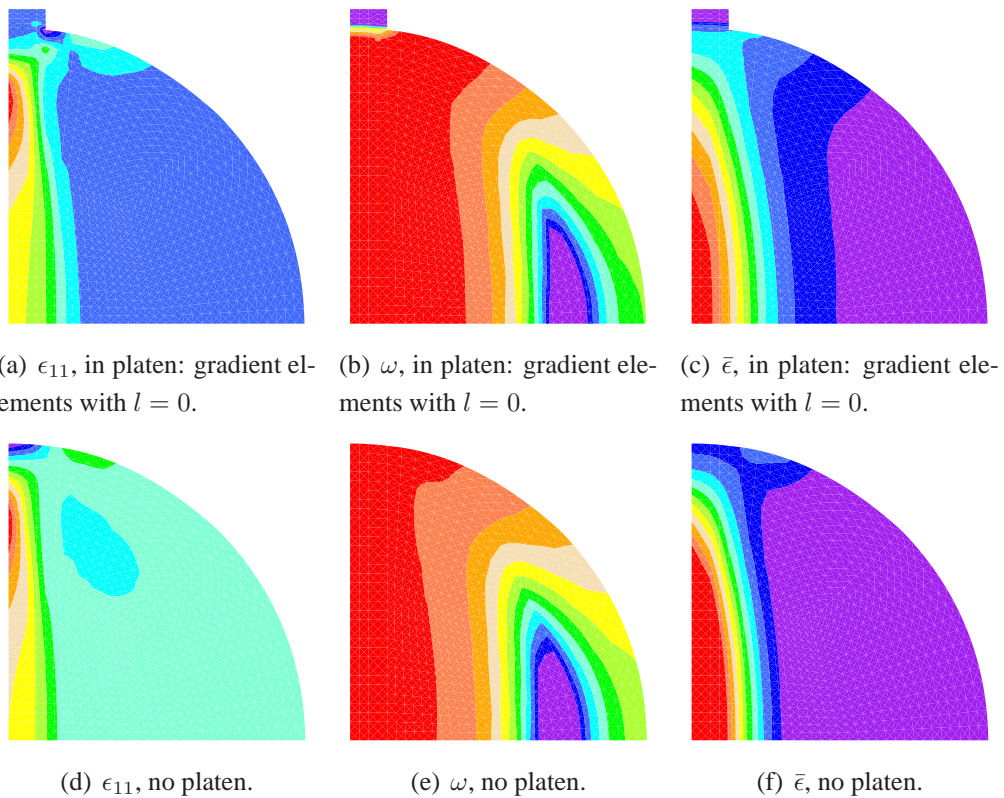


Figure 5.17: Brazilian test. Influence of platen – contour plots (M20/M20wp).

and then a snapback drop, in contrast with the diagram for  $l = 6$  mm. The higher the value of  $l$  the more delayed the snapback is. Moreover, if Figs 5.12 and 5.15(d)–5.15(f) are confronted it can be concluded that the localization zone broadens together with the increase of the internal length scale. In the last case ( $l = 12$  mm) the concentration of strains in the area under the platen almost vanishes, as is depicted in Fig. 5.15(d).

In Fig. 5.16 load-displacement diagrams are compared for the same mesh M20, but for different platen representations. For the second case gradient elements (and not standard ones) are used in the platen with  $E_s = 10 \cdot E_c$  and  $l = 0.0$ . The model called M20wp does not have a platen, so the load acts directly on the specimen. The character of the splitting process is analogical. The load-displacement paths run very closely to each other, only the case without platen exhibits a slightly smaller initial stiffness. The small differences between the elastic platen and the gradient platen are in the neighbourhood of the peak and the reason lies in the release of the constraints for the averaged strain measure field in the connection. It is visible if attention is focused on the joint in contour plots 5.17(a)–5.17(c) (see also Fig. 5.12). However, the splitting process and final localization zone for the considered cases give a quite similar image, so the definition of the platen is insignificant.

### 5.2.2 CONFRONTATION WITH ISOTROPIC DAMAGE

The splitting effect and the snapback response in the Brazilian test is not simple to obtain in numerical computations, because damage can localize directly under the platen (see the case with  $l = 3$  mm in the previous subsection). In this subsection attention is focused on the comparison of the isotropic damage model with one and two parameters. In fact, different mechanical models have been verified numerically using this test, for example: in [24] plasticity theories are analyzed, in [49] rotating crack and plasticity models are confronted, in [106] multidirectional kinematic softening damage-plasticity and fixed crack models are tested. Here it will be shown that in the gradient model not only the internal length parameter decides about the results of the test, but also other parameters of the model, for instance the choice of the damage growth function.

Now one discretization, namely mesh M20, is considered. Geometry and material data

Table 5.3: Brazilian test – cases computed by means of isotropic gradient damage.

Symbol of case	Parameters for exponential softening		Damage growth
	volumetric part	deviatoric part	
<i>exp</i> ———	$\eta_K = 1200$	$\eta_G = 1200$	more intensive
<i>exp, K</i> - - - - -	$\eta_K = 600$	$\eta_G = 1200$	$\omega_K < \omega_G$
<i>exp, G</i> - - - - -	$\eta_K = 1200$	$\eta_G = 600$	$\omega_K > \omega_G$
<i>exp, K &amp; G</i> ———	$\eta_K = 600$	$\eta_G = 600$	less intensive

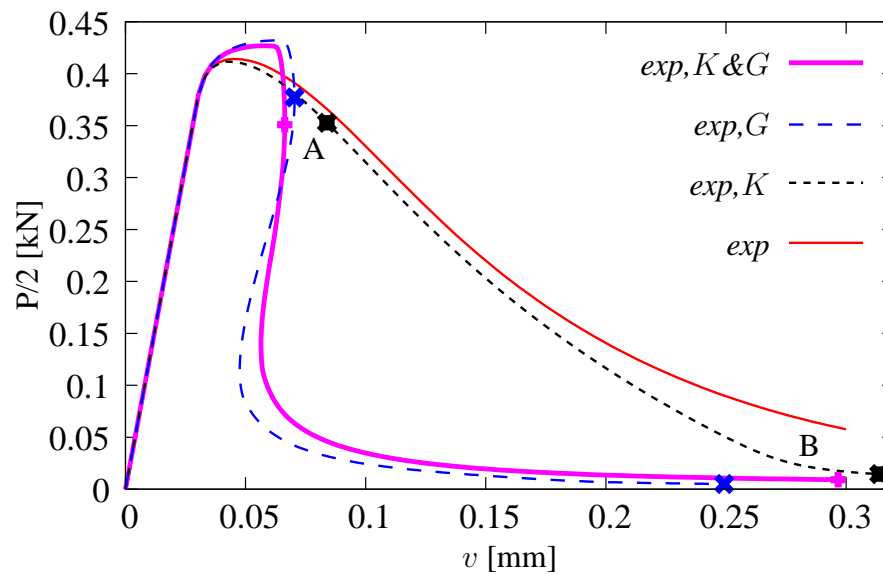
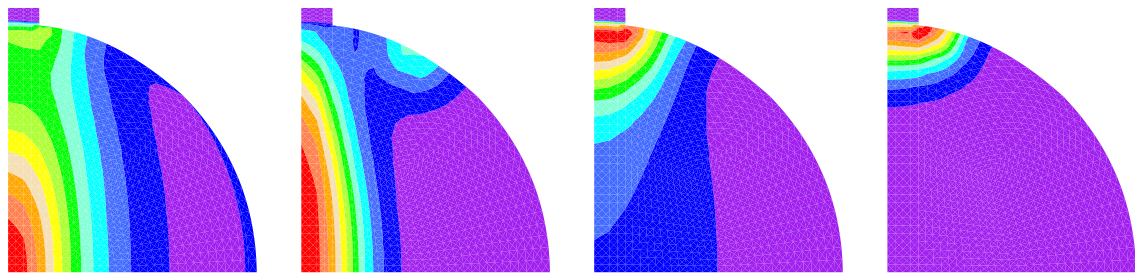


Figure 5.18: Brazilian test. Influence of ductility parameter  $\eta_i$  ( $i = K, G$ ) in isotropic model – load-displacement diagrams.



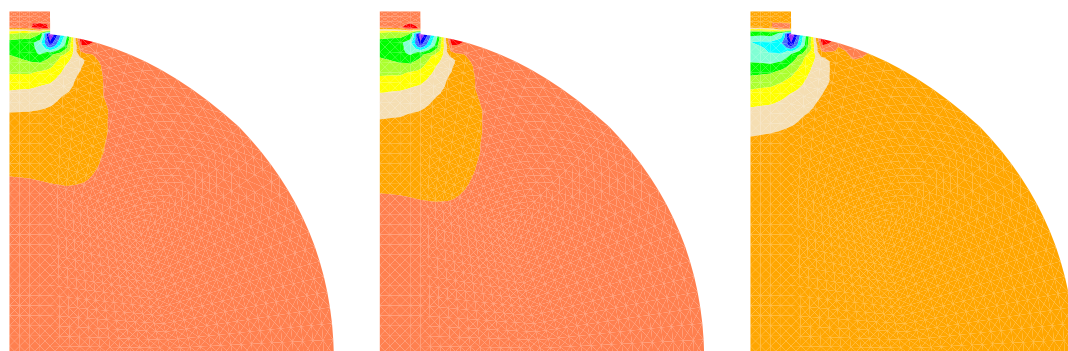
(a) Case *exp,G*, point A. (b) Case *exp,G*, point B. (c) Case *exp,K*, point A. (d) Case *exp,K*, point B.

Figure 5.19: Brazilian test. Contour plots of averaged strain  $\bar{\epsilon}$  for isotropic model.

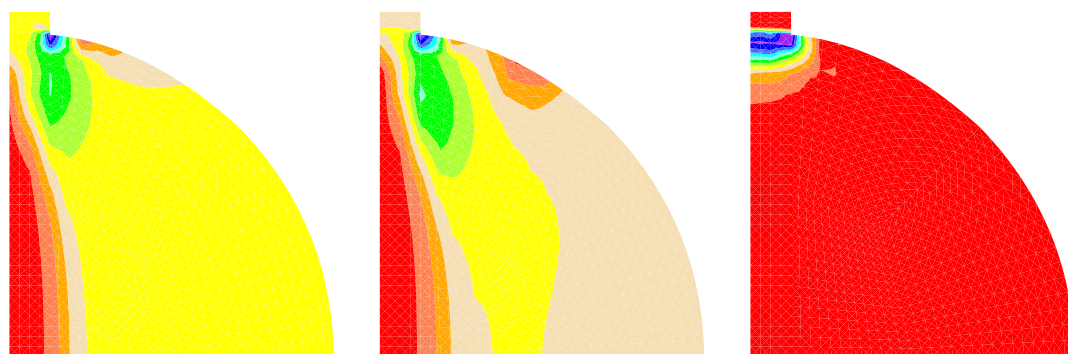
(Table 5.2) are like previously, but four options of damage growth are analyzed. Table 5.9 summarizes the damage growth parameters. Again the arc length method and  $2 \times 2$  integration are employed.

Load-displacement diagrams in Fig. 5.18 are traced for the four considered cases. It is noticed that for cases *exp,K* and *exp* the softening paths are monotonic and without any snapback. The same value of parameter  $\eta_G = 1200$  governs the solution. On the other hand, for cases *exp,G* and *exp,K&G* the snapback response is retrieved. This means that deviatoric damage is more important in the stiffness degradation and decides about the proper behaviour in the Brazilian test. Contour plots in Figs 5.19–5.22 are presented for the peak and the final state (in Fig. 5.18 the respective points A and B are marked).

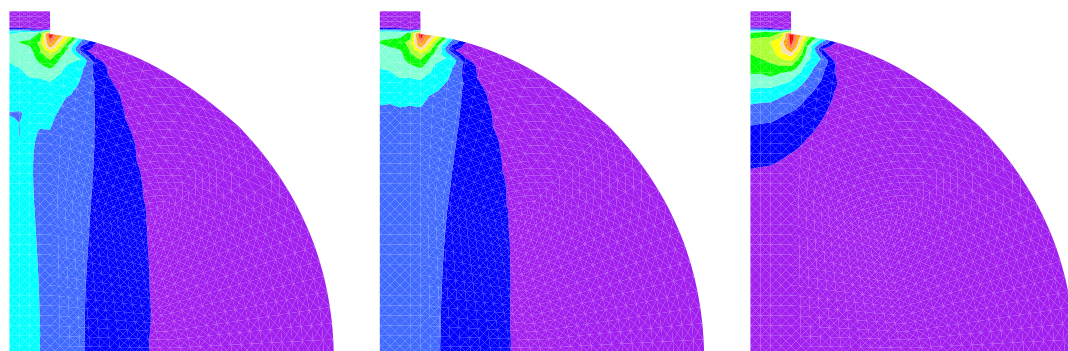
The splitting is obtained only for the cases which correspond to the larger value of fracture energy  $G_f$  for the deviatoric part, i.e. the ductility  $\eta_G = 600$ . It is confirmed by means of Figs 5.19 and 5.20, where the distributions of averaged strain and strain invariants are plotted



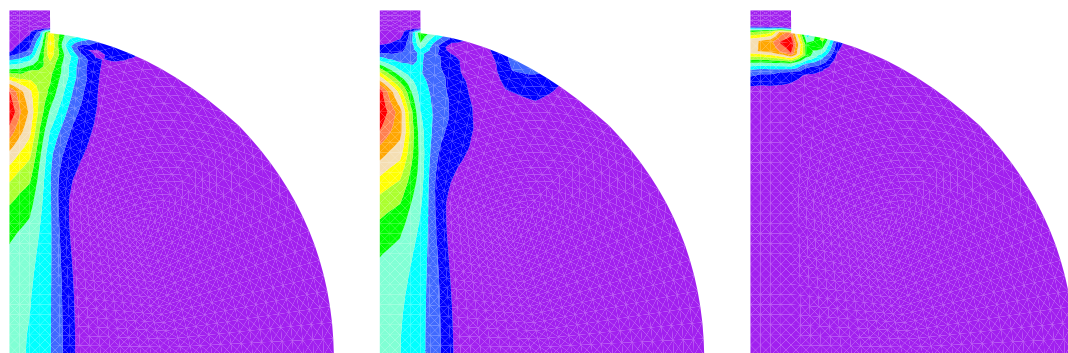
(a) Case *exp,K&G*, point A,  $I_1^\epsilon$ . (b) Case *exp,G*, point A,  $I_1^\epsilon$ . (c) Case *exp,K*, point A,  $I_1^\epsilon$ .



(d) Case *exp,K&G*, point B,  $I_1^\epsilon$ . (e) Case *exp,G*, point B,  $I_1^\epsilon$ . (f) Case *exp,K*, point B,  $I_1^\epsilon$ .



(g) Case *exp,K&G*, point A,  $J_2^\epsilon$ . (h) Case *exp,G*, point A,  $J_2^\epsilon$ . (i) Case *exp,K*, point A,  $J_2^\epsilon$ .



(j) Case *exp,K&G*, point B,  $J_2^\epsilon$ . (k) Case *exp,G*, point B,  $J_2^\epsilon$ . (l) Case *exp,K*, point B,  $J_2^\epsilon$ .

Figure 5.20: Contour plots of strain invariants for isotropic model in Brazilian test.



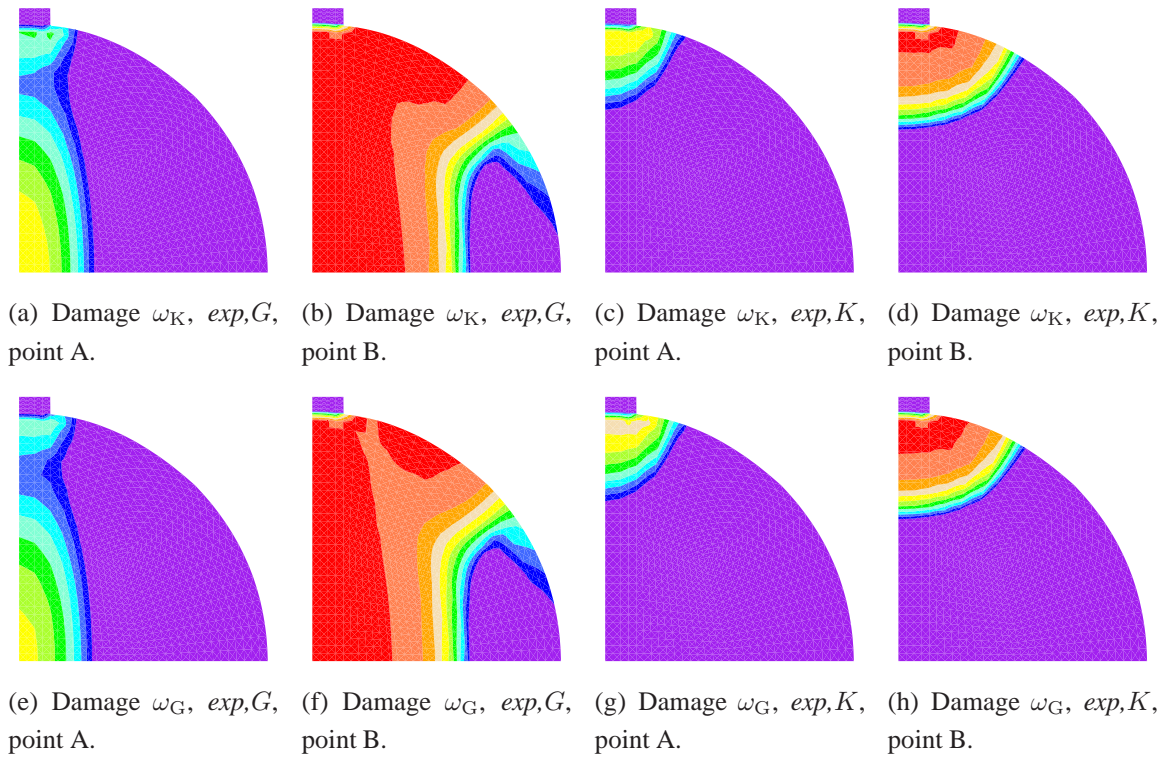


Figure 5.21: Damage patterns for isotropic model in Brazilian test.

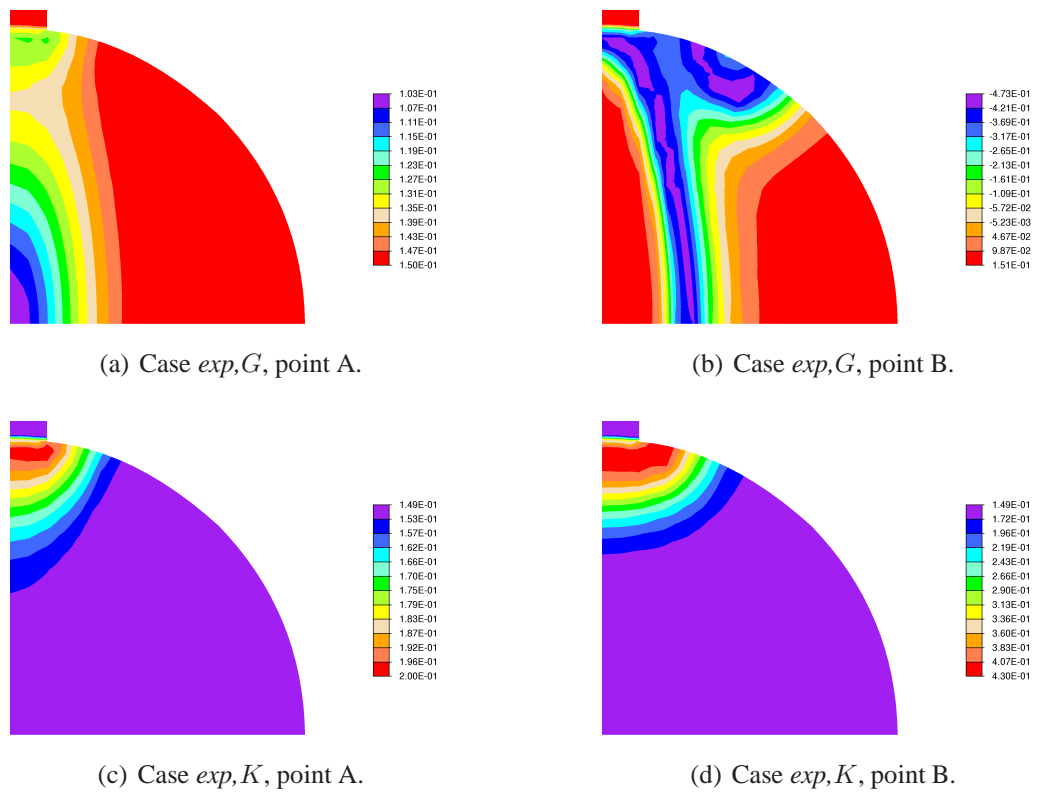


Figure 5.22: Change of Poisson's ratio  $\nu_w$  for isotropic model in Brazilian test.

for the two stages (points A and B). The lack of noticeable splitting effect in the pattern occurs only for the first invariant  $I_1^\epsilon$  after the peak (point A), cf. Figs 5.20(a)–5.20(c). Contour plots in Figs 5.20(j) and 5.20(k) for the second invariant  $J_2^\epsilon$  in final state resemble a wedge formation like in Fig. 5.7(b). The interaction between the compressive loading and the tensile response seems to be transferred via the deviatoric characteristics in the model.

Figure 5.21 shows the damage patterns for cases  $exp,G$  and  $exp,K$ . According to the assumptions included in Table 5.9, the domination of damage  $\omega_K$  in case  $exp,G$  and inversely  $\omega_G$  – in case  $exp,K$  is visible. The variable distribution of Poisson's ratio  $\nu_\omega$  during the process is depicted in Fig. 5.22. The splitting effect observed for case  $exp,G$  is expected in the Brazilian test, so the coincidence with the decrease of  $\nu_\omega$  during the process is suitable for concrete. However, the problem with negative values is observed. In Fig. 5.22(b) they are noted in zones of the damage front, where the strain gradient is more intensive. Recommendations from Section 2.5 could partly overcome the problem with negative values, but the main idea in this subsection was to confront the model with one and two damage parameters.

### 5.3 FOUR-POINT BENDING\*

This benchmark is referred to a reinforced concrete beam, which was analyzed experimentally under dynamic loading by Eibl et al. [46]. Subsequently, numerical analyses were performed by Sluys [151, 152] and Pijaudier-Cabot et al. [45], using various cracking models.

The data are setup on the basis of [151]. The geometry data are presented in Table 5.4 and Fig. 5.23. Two supports are introduced at the bottom of the beam, while the loading is imposed at two points at the top. Plane stress conditions for concrete and full bond between steel and concrete are assumed. Steel is modelled as elastic-ideal-plastic (here shortly called "plastic") material in uniaxial stress state using truss finite elements. In the experiment concrete was additionally reinforced by Dramix fibers (1.2% volume) and hence the presence of fibers gives an additional physical motivation to the gradient enhancement and increased ductility of the model. The basic material model data are summarized in Table 5.5. Computations are performed for three different FE meshes, namely: coarse -  $56 \times 8$ , medium -  $112 \times 16$  and fine -  $168 \times 24$  elements for the concrete matrix.

The parameters of the gradient damage model are  $\kappa_\omega = 95.6 \times 10^{-6}$ ,  $\alpha = 0.96$  and  $\eta = 350$ . The internal length scale takes three values  $l = 4/16/96$  mm. Finite elements with a linear interpolation of both the displacements and averaged strain are used. Full integration (FI) is applied, with the exception of the beam without the reinforcement and statical load. In this case also stabilized elements with one integral point are adopted and a comparison is carried out.

For dynamics the beam is loaded by impact like in the experiment [46], with slightly different load histories for the left and right forces, as shown in Fig. 5.23. The experimental response

---

\*Section based on [175] and [174]

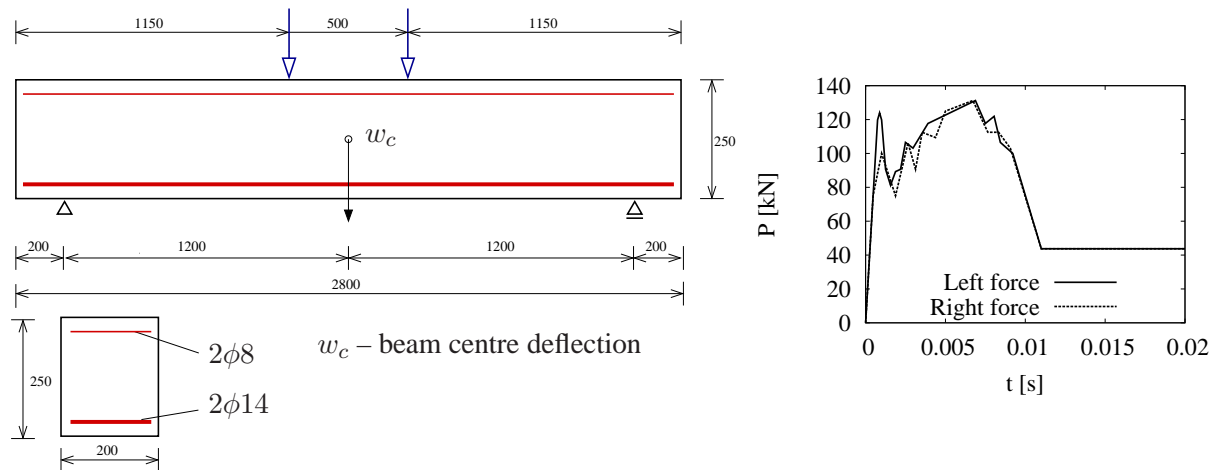


Figure 5.23: RC beam in four point bending.

Table 5.4: Four point bending – geometry data for beam.

length: $L = 2800$ mm,	height: $B = 250$ mm,	thickness: $T = 200$ mm
lower reinforcement: $A_r = 308$ mm <sup>2</sup> ( $2\phi 14$ ) located at 31.25 mm from bottom		
upper reinforcement: $A_r = 100.5$ mm <sup>2</sup> ( $2\phi 8$ ) located at 218.75 mm from bottom		
span between supports: 2400 mm,	distance between load points: 500 mm	

Table 5.5: General material data in four point bending test.

	FIBER REINF. CONCRETE:	STEEL REINFORCEMENT:
Young's modulus	$E_c = 32940$ MPa	$E_s = 245390$ MPa
Poisson's ratio	$\nu_c = 0.2$	$\nu_s = 0.3$
Compressive strength	$f_c = 31.50$ MPa	$f_y = 638$ MPa
Tensile strength	$f_t = 3.15$ MPa	as above
Density	$\rho = 2320$ kg/m <sup>3</sup>	$\rho = 7800$ kg/m <sup>3</sup>

is known up to time  $t = 0.011$  s. In computations constant final values of the forces are kept for a longer time. The load control is used.

In the case of static loading the forces have exactly the same values, and displacement control is used.

### 5.3.1 STATICS – PLAIN CONCRETE

Firstly, the static response of the beam without reinforcement is examined to assess the width of the fracture process zone  $w_f$  and determine the proper internal length parameter  $l$ . Figures 5.24(a), 5.24(b) and 5.24(c) show the load-deflection diagrams for different values of  $l$  and in each case for three mesh densities used in computations (here only FI is employed). From these

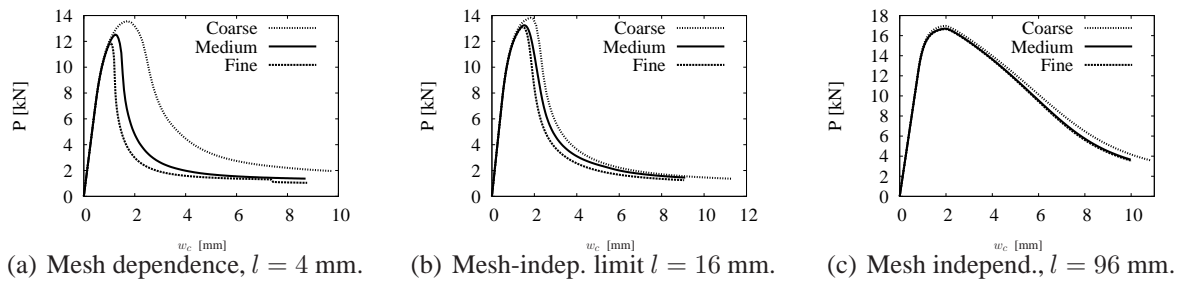


Figure 5.24: Diagrams for plain concrete beam.

results and the contour plots of the averaged strain presented in Fig. 5.26 it is concluded that  $l = 16$  mm is the value for which mesh sensitivity is almost removed. Then, for the coarse mesh one broader damage zone is still observed, while for the medium and fine meshes two "cracks" occur. For the medium mesh the width of the fracture band  $w_f$  measured on the averaged strain contour plot is equal to about four times the element size (approximately 100 mm), so  $w_f \approx 6l$ . It is only a rough estimation, but it is similar to gradient plasticity [35], where  $w_f = 2\pi l$ . For smaller values, the size of the element determines the solution (cf. the diagrams in Fig. 5.24(a)). On the other hand for a large  $l$  like 96 mm, mesh-independent results (Fig. 5.24(c)) are obtained, but strain localization does not occur. Moreover, the increase of the internal length produces a similar peak load due to averaging over a wider area.

Secondly, like in [174], the influence of the type of integration is examined. For one-point integration and stabilization in single FE the scaling factor  $\chi$  is equal to 0.0001. From the comparison of diagrams in Fig. 5.25 the general tendency of results obtained from computations

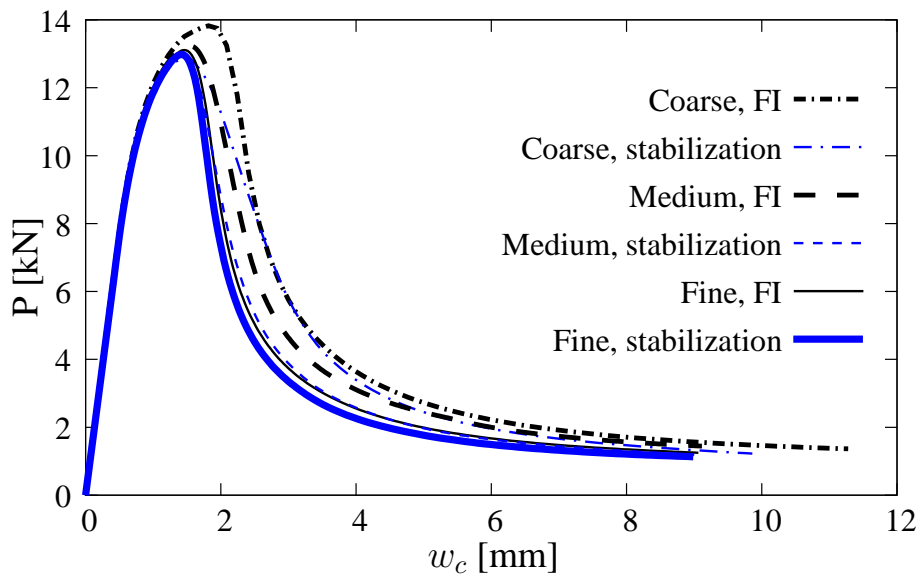


Figure 5.25: Load-deflection diagrams – influence of meshes and integration types.

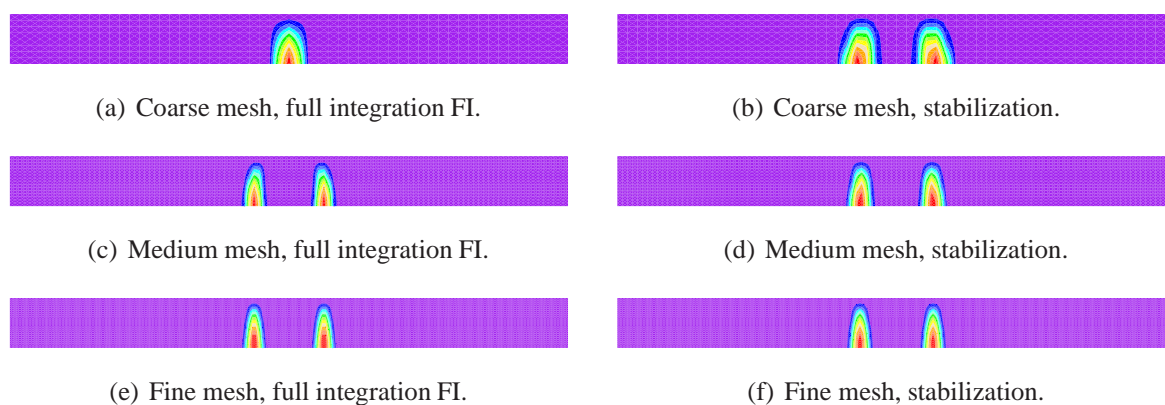


Figure 5.26: Averaged strain distribution for plain concrete beam.

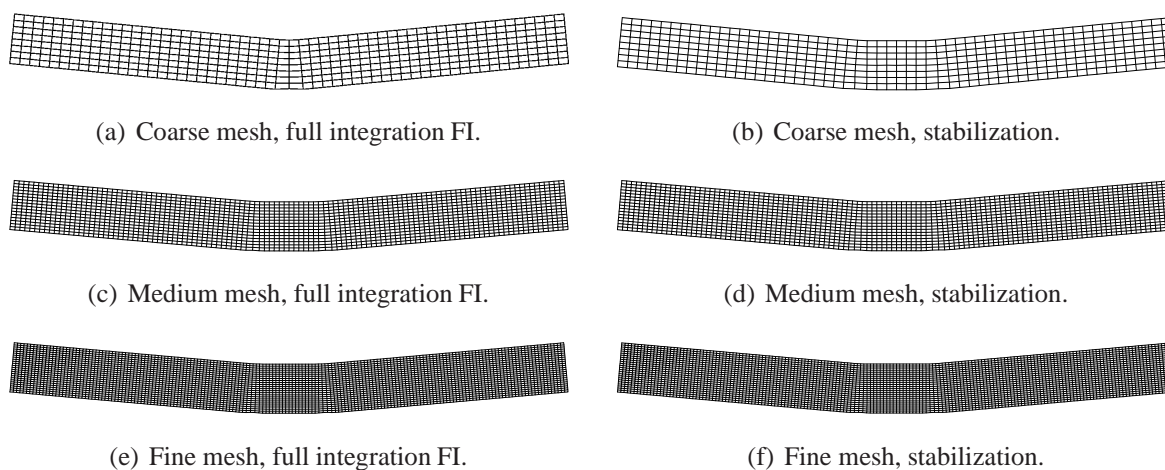


Figure 5.27: Deformation for plain concrete beam.

with reduced integration (i.e. with stabilized FEs) is that a slightly smaller load carrying capacity is obtained than for computations with full integration. As expected, the simulated behaviour gives the response as for a slightly less stiff beam. The general character of diagrams does not differ significantly. The diagrams for the fine mesh are the nearest to one another.

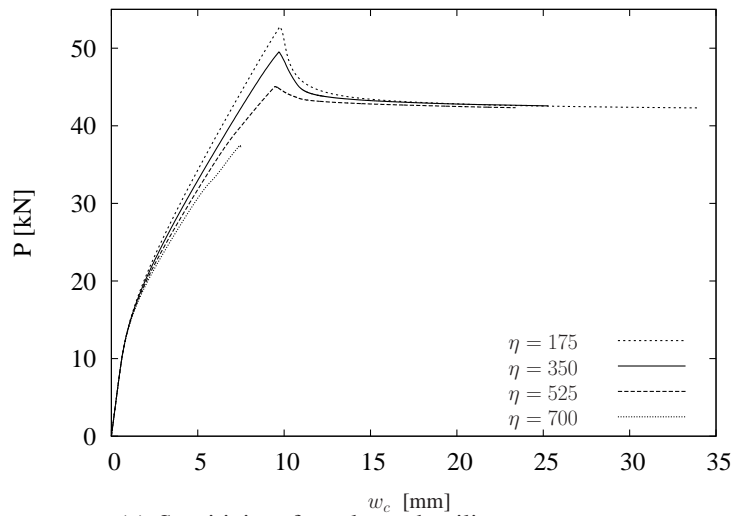
From Fig. 5.27 with the deformations of the meshes and Fig. 5.26 with the corresponding contour plots of the averaged strain measure it is noticed that two zones of localization are simulated. An exception is constituted by the case with coarse mesh and full integration. Of course these zones can be associated with cracking of the beam. It is also confirmed in Figs 5.26(a) and 5.27(a) that among the calculated cases, the solution for the coarse mesh and full integration leads to the stiffest model. However, according to the plastic hinges theory in bars, both forms of deformation, both crack patterns and hence one or two localization zones are admissible.

In brief it can be concluded that the reduced integration results in a slightly less stiff response of the model, which is consistent with what is known about the influence of integration quadrature on FEM results.

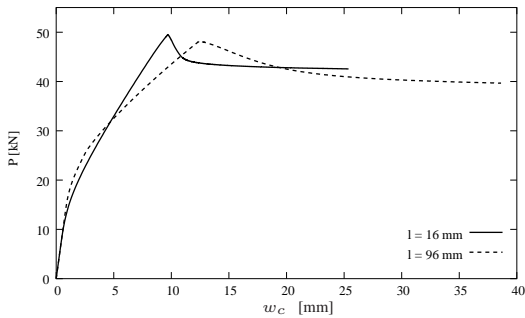
5.3.2 STATICS – REINFORCED CONCRETE

In this subsection attention is focused on the aspects of the material model and on the selection of its suitable parameters. Hence, the computations are performed only for the medium mesh and full integration.

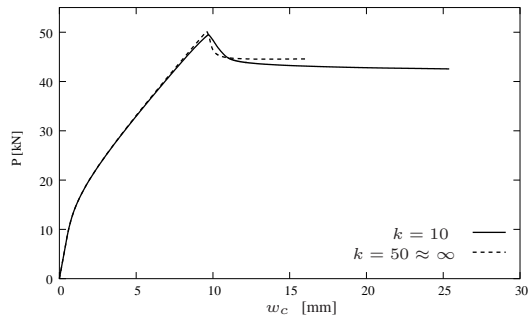
A comparison of the diagrams for the RC beam is presented in Fig. 5.28. When the carrying capacity of concrete is reached, the load is transmitted to the reinforcement and a change of the



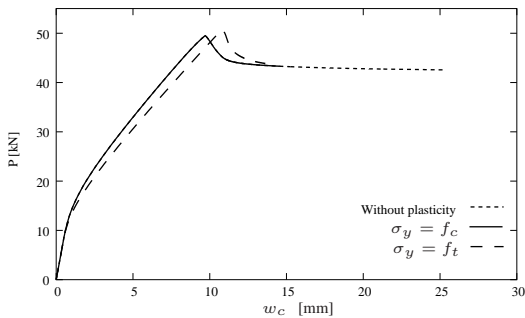
(a) Sensitivity of results to ductility parameter  $\eta$ .



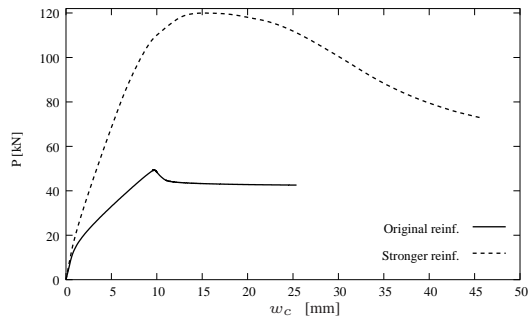
(b) Dependence on internal length scale.



(c) Influence of compressive/tensile strength ratio.



(d) Influence of coupling to plasticity.



(e) Differences for two reinforcement ratios.

Figure 5.28: Comparison of load–deflection diagrams for RC beam.

slope for each load-deflection path is observed. The peak points are connected with reaching the yield strength for the reinforcement. The character of each particular path near the peak and further in the final phase depends on the selection of parameters. However, a general tendency is that the numerical results converge to the ultimate force computed from the theoretical limit state of the reinforced concrete beam in bending, namely 42 kN. In Fig. 5.28(a) the diagrams are compared for different values of ductility parameter  $\eta$  for concrete. For a smaller value of  $\eta$  the material is more ductile, fracture energy  $G_f$  and the value of the peak load are larger. In the absence of tension stiffening the peak would not appear and a direct transition into the yielding branch would be noticed. For  $\eta = 700$  the computations diverge before the peak, probably because the assumed fracture energy of concrete is too small.

The corresponding contour plots of the averaged strain are shown in Fig. 5.29. For  $\eta = 175$ , the wide band of larger strains, which is connected with the spread of microcracks, reshapes into one zone of localization understood as a "crack". For  $\eta = 350$  or 525, at the beginning of the computations a diffuse cracking character is obtained as previously, but two "cracks" can be distinguished and in further phases they dominate. For  $\eta = 700$  more dominant zones occur before divergence. Figure 5.30 shows more clearly that ductility also influences the final deformation. However, analogically to the beam without the reinforcement, in the theory both patterns are admissible, because one or two plastic hinges in the beam can be considered.

The material model with  $\eta = 350$  is accepted for further computations, so that they are numerically stable and possibly realistic. If  $l = 96$  mm is applied the fracture has a totally distributed character (cf. Fig. 5.31). The failure mode seems to strongly depend on the assumed length scale and the regularization looks excessive. The parameter  $l$  from the simulation in the previous subsection gives here only a guideline, but remains valid. In Fig. 5.28(b) the diagram for this case is confronted with the one for  $l = 16$  mm.

Figure 5.28(c) compares load-deflection paths for two different values compressive/tensile strength ratio  $k$ , cf. Eq. (2.15). If  $k = 50$  an extremely huge value of the compressive strength for concrete matrix is implied, so the damage function  $f^d$  is never violated in compression. The slight softening after peak point like for the basic ratio  $k = 10$  is not observed. Moreover, in the contour plot in Fig. 5.32(b) the damage zone does not reach the top edge directly under the force location.

Further, the case of gradient damage coupled to Huber-Mises-Hencky plasticity is considered. The coupling to plasticity does not cause significant changes in the obtained results. If the concrete compressive strength as the yield limit is assumed, the results of computations are identical to those without the coupling. It means that the coupling is not activated in the algorithm, because the yield strength is not reached. If the tensile strength as the yield limit is introduced, the coupling is activated. The effects, depicted in Fig. 5.28(d), are a smaller stiffness and divergence after the peak. The more ductile diagram is related to the contour plots in Fig. 5.33, where one dominant zone of localization is simulated.

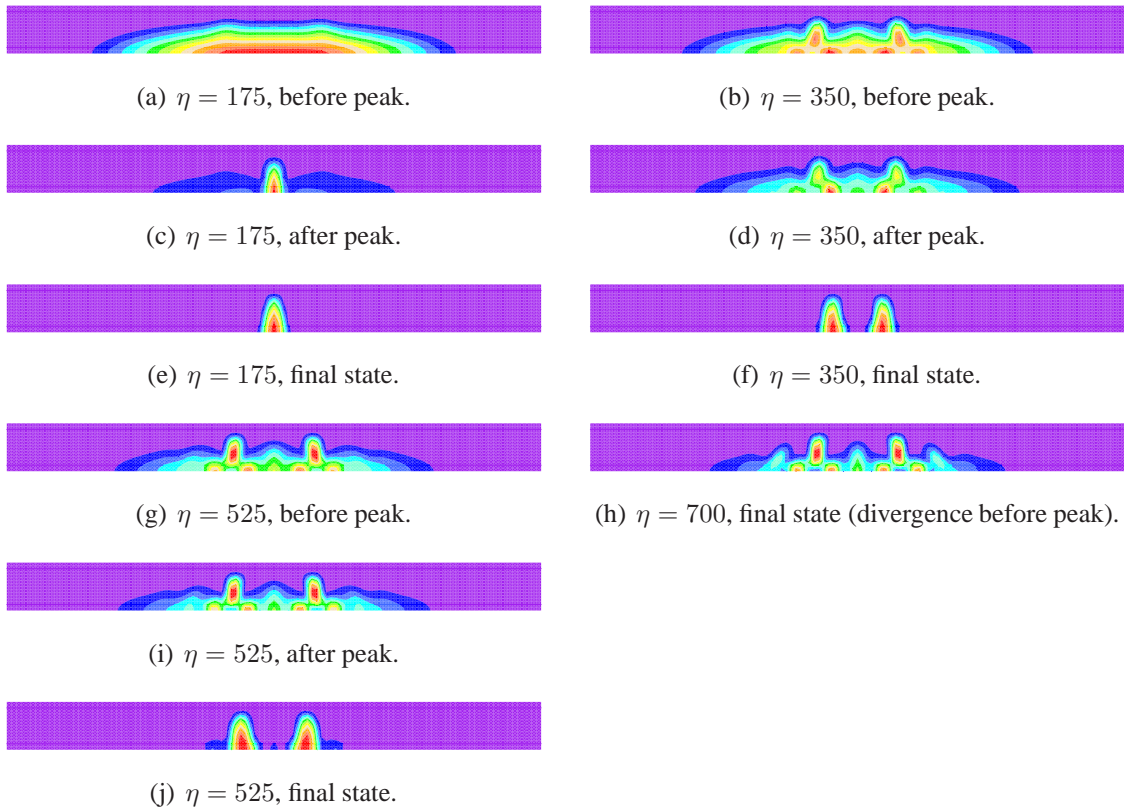


Figure 5.29: Averaged strain – comparison of results for different ductility parameter  $\eta$ .

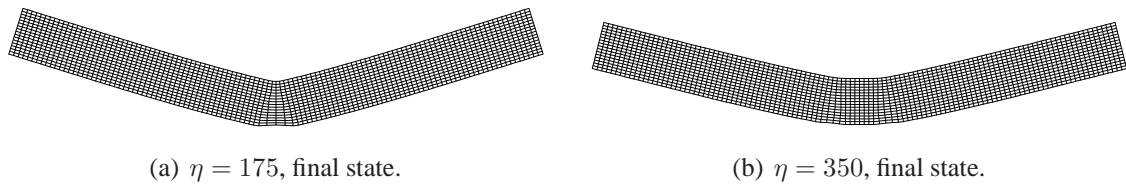


Figure 5.30: Deformation patterns for two values of  $\eta$ .

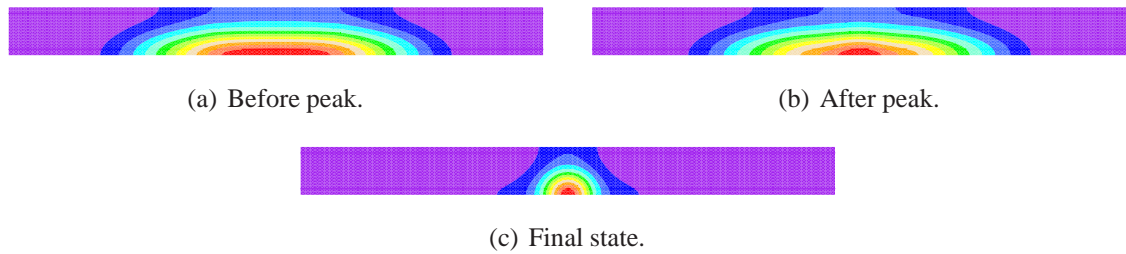


Figure 5.31: Averaged strain for larger  $l = 96$  mm.



Figure 5.32: Damage – influence of compressive strength to tensile strength ratio.



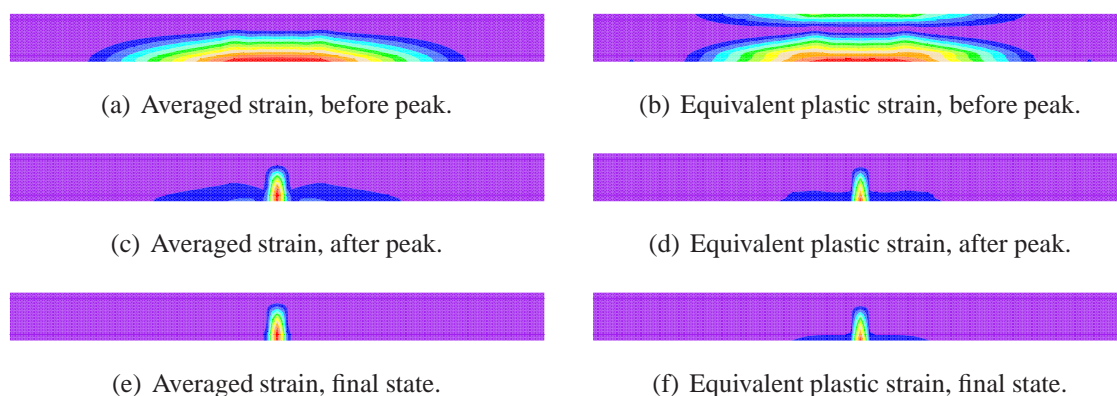


Figure 5.33: Averaged and equivalent plastic strain for damage coupled to plasticity with  $\sigma_y = f_t$ .

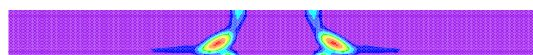


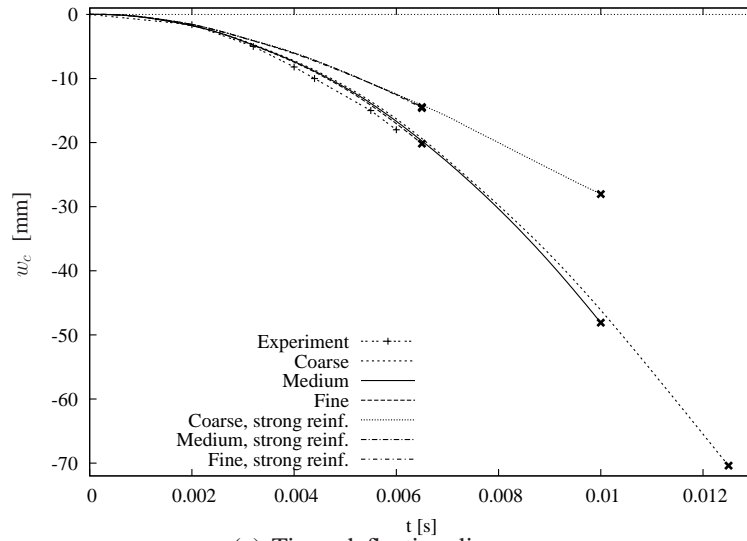
Figure 5.34: Averaged strain for reinforcement ratio multiplied by 4, final state.

The original reinforcement ratio is equal to 0.62%. For much stronger reinforcement, when the reinforcement ratio is equal to 2.64% (double diameters), the beam exhibits more pronounced softening, see Fig. 5.28(e). This is caused by a shear failure which starts before the beam can attain its load carrying capacity in bending (here the computed theoretical ultimate force in bending is about 149 kN). Figure 5.34 shows clearly the zones of shear failure from the top edge to the thin zones of damage along the bottom reinforcement.

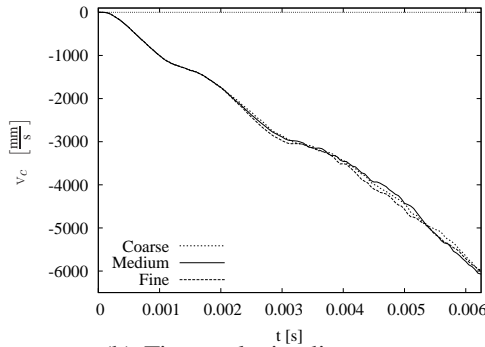
Numerical material modelling and similar analyses for a reinforced concrete beam under static loading have been performed by many authors, see for example [18, 66, 117].

### 5.3.3 DYNAMICS – REINFORCED CONCRETE, IMPACT LOADING

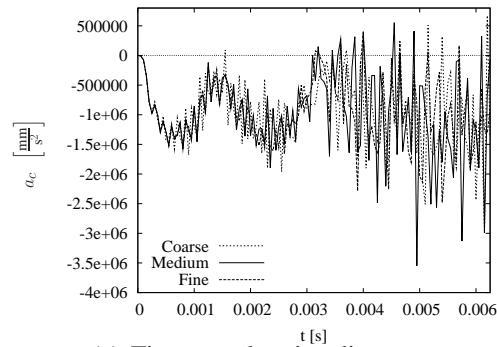
The displacement-time diagram obtained in the experiment is taken from [46]. Here, two aspects of numerical simulations are considered, namely the mesh dependence and the influence of the reinforcement ratio. For the original reinforcement all the computed deflection histories, shown in Fig. 5.35(a), exhibit a quite good agreement with the experimental response. Of course, for the stronger reinforcement a stiffer response is noticed. Cross marks denote the final points of the computations before the solution diverges. Figures 5.35(b) and 5.35(c) present the velocity and acceleration histories for the original reinforcement. It is seen that the time-velocity paths are almost independent of the assumed discretizations, whereas the accelerations plots in the time domain are much more sensitive to the used meshes. Such a phenomenon is typical for dynamic computations [67]. It is also noticed that the analyzed problem does not tend towards an equilibrium state, but, to the contrary, the values of velocity and acceleration increase continuously leading to a failure of the beam.



(a) Time-deflection diagrams.



(b) Time-velocity diagrams.



(c) Time-acceleration diagrams.

Figure 5.35: Deflection, velocity and acceleration history diagrams.

Figures 5.36 and 5.37 present the averaged strain measure and deformation at the same time instant  $t = 0.00625$  s for the original and stronger reinforcement, respectively. For the beam with the original reinforcement mesh-independent results are reproduced. For the coarse mesh the contour plot of averaged strain in Fig. 5.36(a) strongly depends on the size of the mesh, but for the medium and fine meshes the contour plots (Figs 5.36(c) and 5.36(e)) are almost the same. It is analogical behaviour like for results of the plain concrete beam under statical load. Apart from the fact that the final points of the time-deflection paths are different, the character and tendency of failure patterns are really well-reproduced for each mesh.

However, mesh dependence is observed for the strong reinforcement. Although the diagrams run almost identically, two times longer paths can be followed for the coarse mesh. It is confirmed if the averaged strain measure in Fig. 5.37 is compared. The time instant  $t = 0.00625$  s is just before computations diverge for the medium and fine meshes, while for the coarse mesh the averaged strain contour plot does not reach the state of clear cracks yet. The character of the final contour plots for averaged strain in the case of medium and fine meshes is also different.

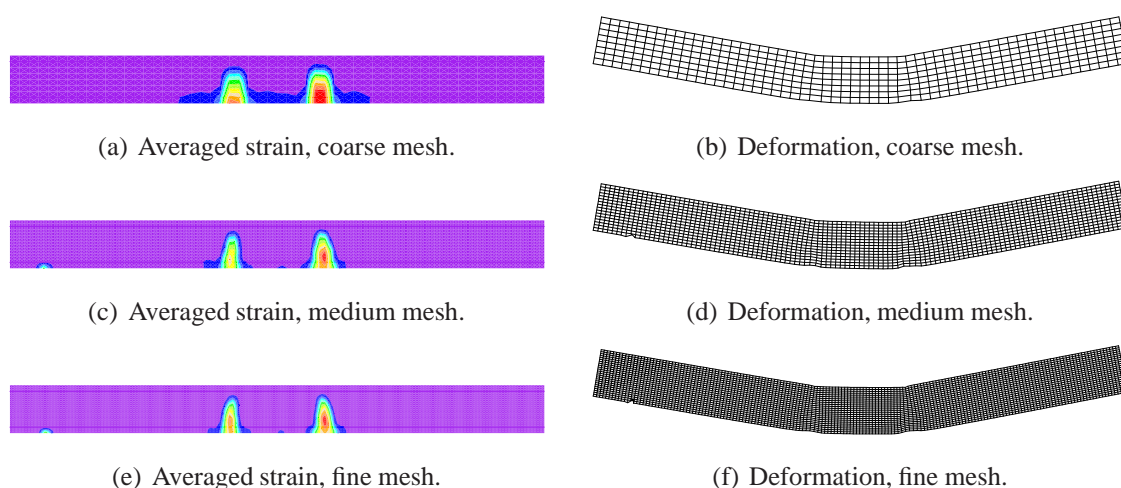


Figure 5.36: Averaged strain and deformation for three different meshes ( $t = 0.00625$  s, beam with original reinforcement).

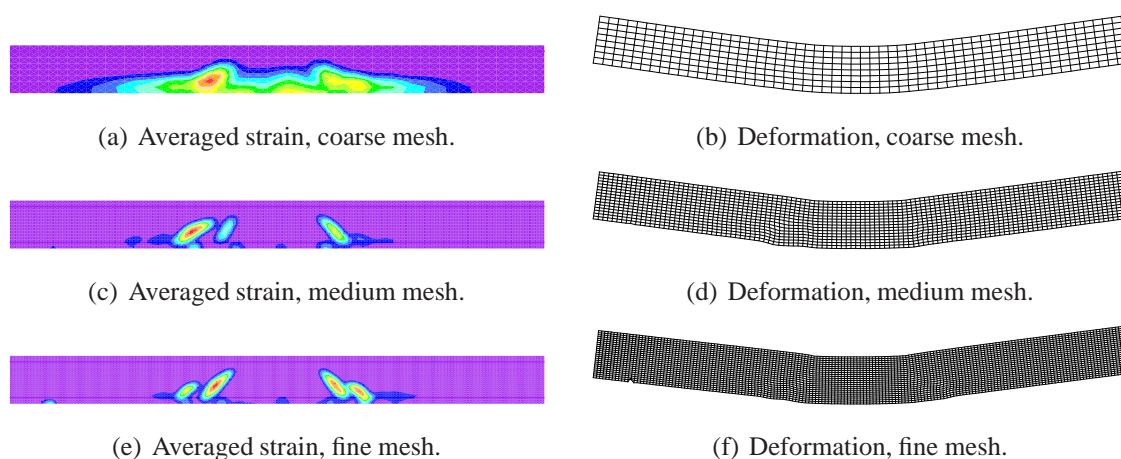


Figure 5.37: Averaged strain and deformation for three different meshes ( $t = 0.00625$  s, beam with stronger reinforcement).

Some other experimental tests, the description of material models and simple numerical benchmarks for a three-point bending RC beam under impact loading can be found in [11, 19].

## 5.4 DOWEL ACTION IN 3D

Many experiments of dowel action were performed with reinforcement pushed against concrete core (called strong mechanism, see for example [39]) or a concrete cover (weak mechanism) with (cf. [40]) or without embedded stirrups in concrete or fibre-concrete specimen like in [41]. The dowel action in reinforced concrete can simply be analyzed by means of the so-called dowel disk test in two-dimensional plane stress analysis (cf. [42, 50, 85]) or as a three-dimensional slice like in Appendix C (see also [85]). However, the weak mechanism of the loading in the dowel

disk test is slightly different from the dowel bar test. In the former one the rebar is pulled upwards on both the front and back sides, while in the latter one only on the front side. If dowelling against the concrete cover is simulated, localization directly below and above the reinforcement is firstly observed. Then shear transmission occurs, which leads to crack opening. A more realistic dowel action is reproduced when, after crack opening, spalling of the cover in the third dimension finally emerges, hence the dowel disc test is insufficient. For a better agreement with observations of structures (for instance: joints, slab foundations) and also experiments, the numerical analysis requires modelling in three dimensions. Here the dowel bar test is modelled and comparison of results with the experiment [41] is performed (see Fig. 5.38).

The following geometry data were adopted in the experiment: height – 200 mm, width – 300 mm and length – 400 mm. In the simulation only a symmetric half of the whole specimen is considered in order to reduce the computing time. The computations for the whole specimen, but with a coarse division in length direction were performed in [85]. Additionally, the computational domain is limited to the first half-length of the specimen, so that its dimensions in the numerical analysis are as follows: height – 200 mm, width – 150 mm and length – 200 mm. Boundary conditions, apart from the cutting rear plane, are depicted in Fig. 5.39(a). The horizontal normal displacements in the symmetry plane are blocked. The bottom wall is clamped.

Table 5.6: Material model data for dowel bar.

<p>CONCRETE: damaging            Young's modulus: <math>E_c = 35600</math> MPa            Poisson's ratio: <math>\nu = 0.2</math>            Tensile strength: <math>f_t = 3.64</math> MPa            Equivalent strain measure:            modified von Mises definition, <math>k = 10</math>            Damage growth function:            exponential softening  <math>\alpha = 0.98</math> <math>\eta = 550</math>            Fracture energy: <math>G_f = 0.0867</math>N/mm            Internal length scale:  <math>l = 2\sqrt{2}</math> mm, i.e. <math>c = 4.0</math>            Threshold: <math>\kappa_o = 10.225 \times 10^{-5}</math></p>	<p>INTERPHASE: damaging            Young's modulus: <math>E_c^* = 17800</math> MPa            Poisson's ratio: <math>\nu = 0.2</math>            Tensile strength: <math>f_t^* = 2.912</math> MPa            Equivalent strain measure:            modified von Mises definition, <math>k = 10</math>            Damage growth function:            exponential softening  <math>\alpha = 0.98</math> <math>\eta = 450</math>            Fracture energy: <math>G_f = 0.0867</math>N/mm            Internal length scale:  <math>l = 2\sqrt{2}</math> mm, i.e. <math>c = 4.0</math>            Threshold: <math>\kappa_o = 16.36 \times 10^{-5}</math></p>
<p>REINFORCEMENT (STEEL): elastic            Young's modulus: <math>E_s = 206000</math> MPa            Poisson's ratio: <math>\nu = 0.3</math></p>	

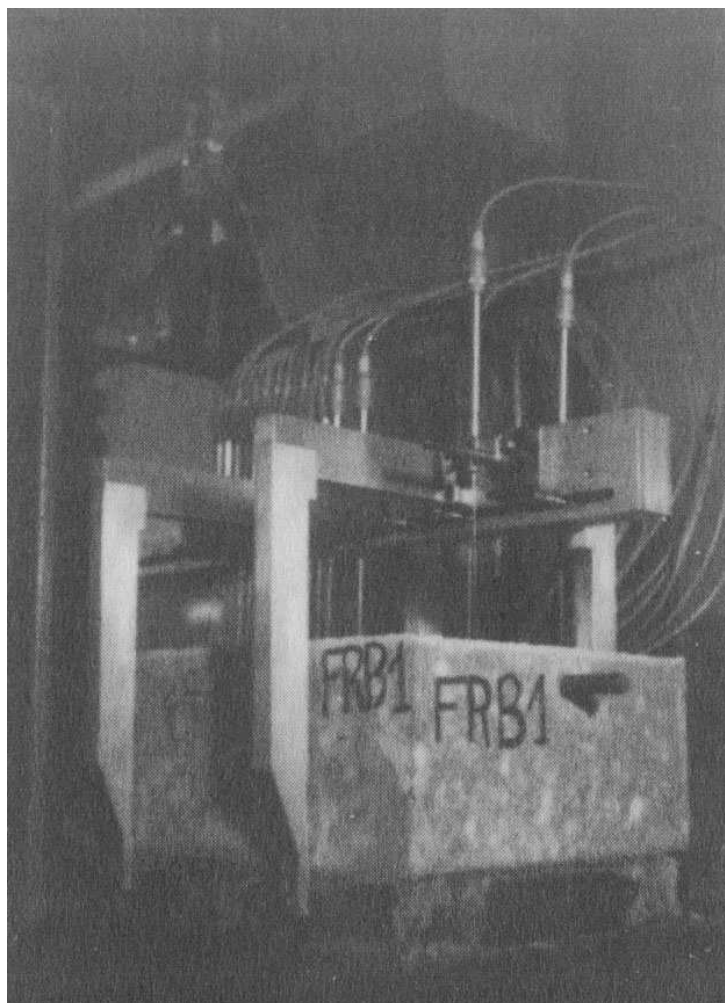
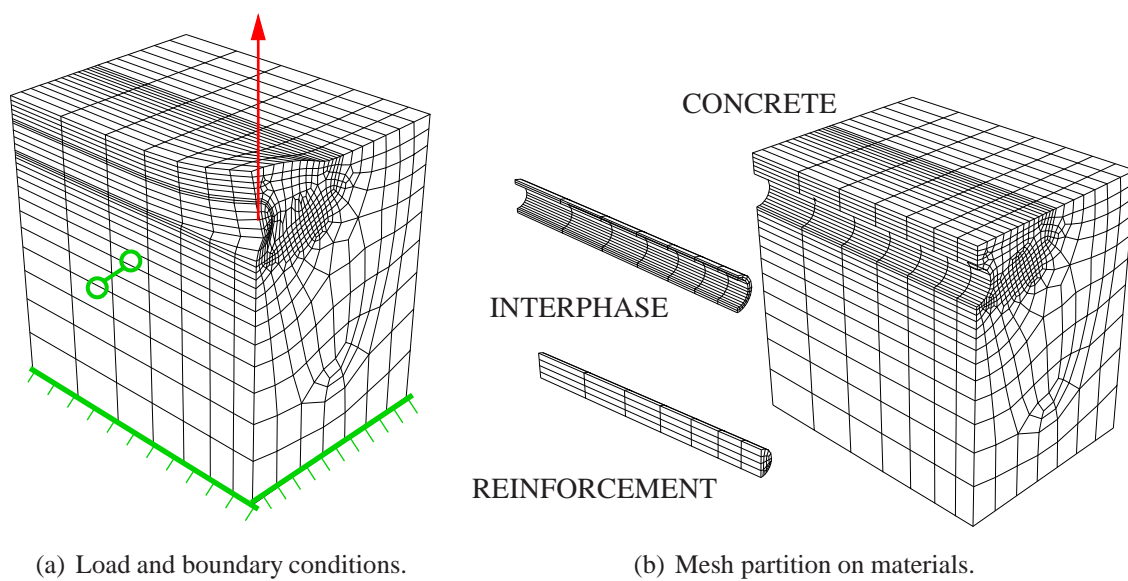


Figure 5.38: Dowel bar test – from experiment in [41].



(a) Load and boundary conditions.

(b) Mesh partition on materials.

Figure 5.39: Dowel bar test – numerical definition of problem.

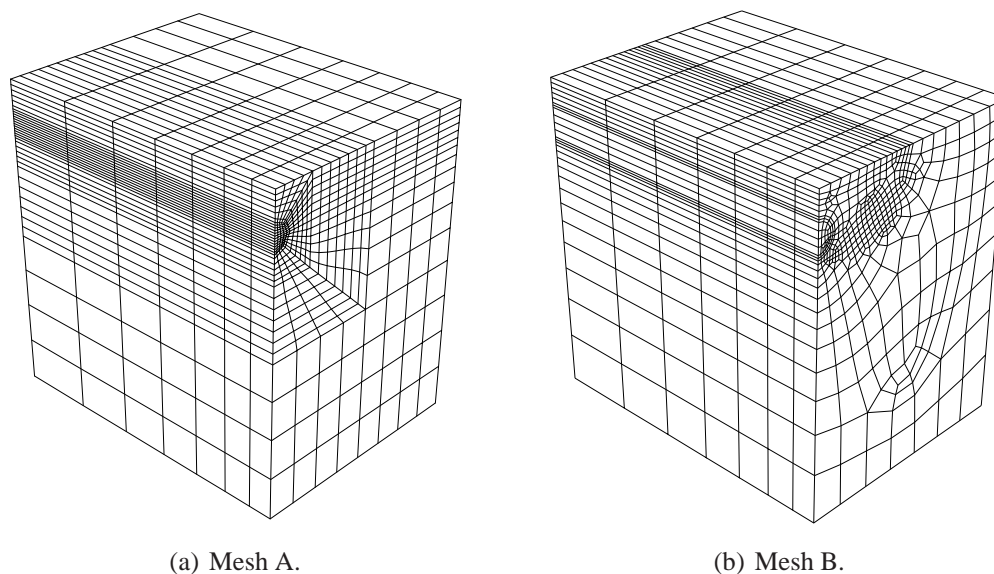


Figure 5.40: Dowel bar test – applied meshes.

Two kinds of supports at the cutting rear plane are analyzed:

- case 1 – the rear plane is not supported,
- case 2 – the horizontal displacement in the direction parallel to the reinforcing bar is equal to zero on the rear plane.

It is common knowledge, that the real situation is between these two cases. The load is applied upwards to the axis of the reinforcement at the front point under displacement control as shown in Fig. 5.39(a), so that the rebar is pushed against the concrete cover. The diameter of the rebar is equal to 18 mm and the concrete cover has the same thickness.

In the computational domain not only concrete and reinforcement are specified, but also an interface zone called an interphase, similarly to the numerical analysis of the dowel disk test in [42, 50]. The interphase joins the concrete matrix and the steel rebar and weaker concrete within it is assumed. The thickness of the interphase is assumed to equal 3 mm. On the basis of [41] the compression strength  $f_c = 45.56$  MPa (FRB1 concrete) is introduced and other parameters for concrete are calculated according to [51]. The material data are presented in detail in Table 5.6. Young's modulus ( $E_c^* = 0.5E_c$ ) and the tensile strength ( $f_t^* = 0.8f_t$ ) are reduced for the interphase. The connected quantities are recalculated.

Two different meshes (Fig. 5.40) have been prepared basing on a mesh-independence investigation: mesh A – semi-structural, mesh B – pseudo-adapted. Only linear brick B8/8 elements are employed and the pure gradient damage model is applied for concrete and the interphase. The partition of mesh B into materials is shown in Fig. 5.39(b). The stirrups and ducts inside the specimen are omitted.

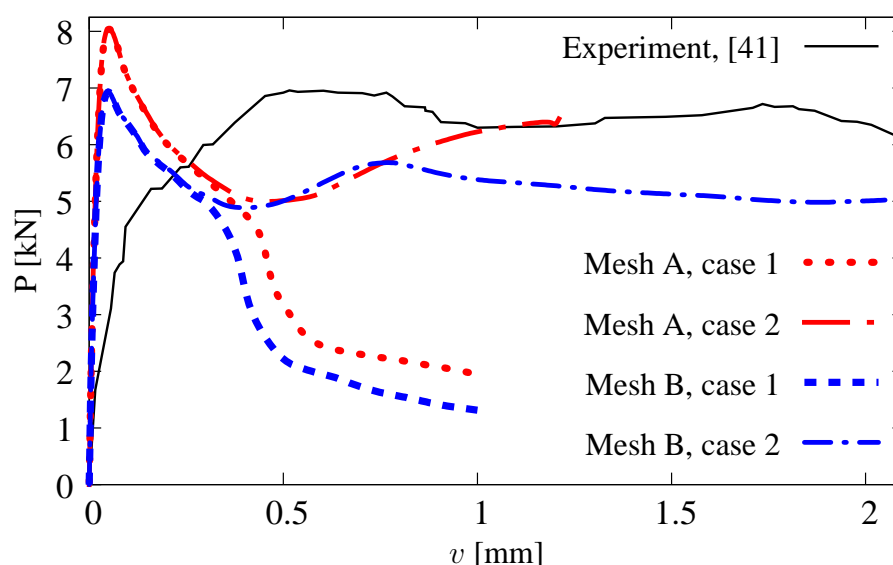
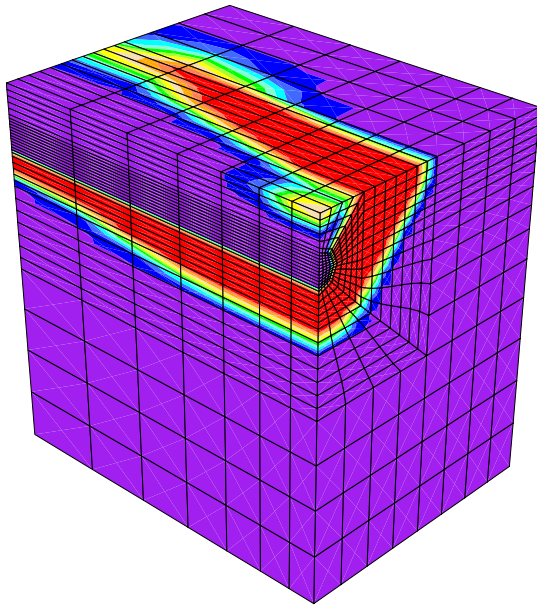
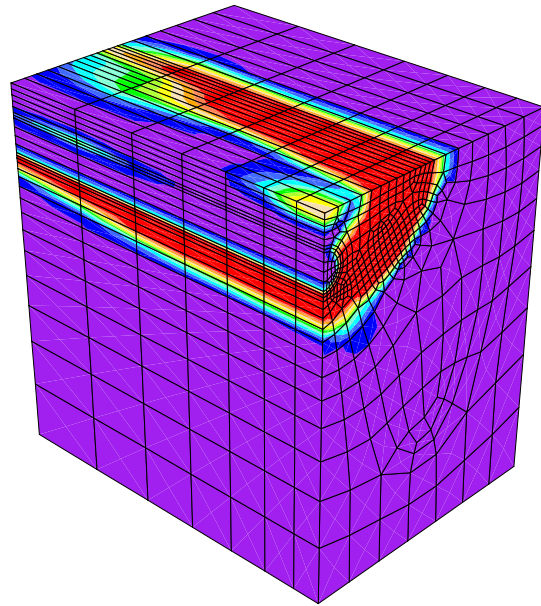
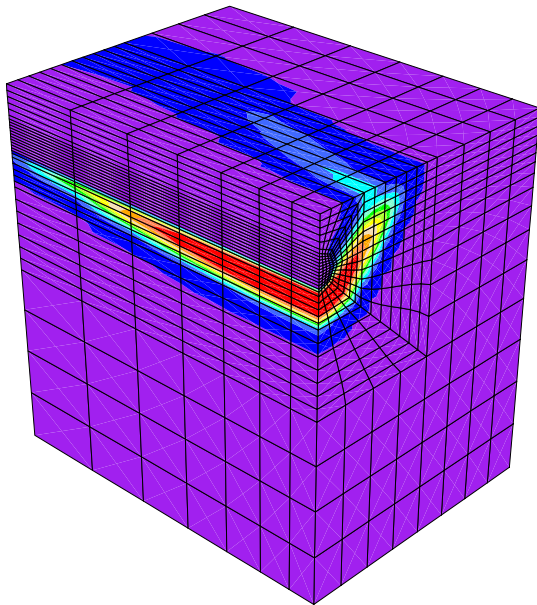
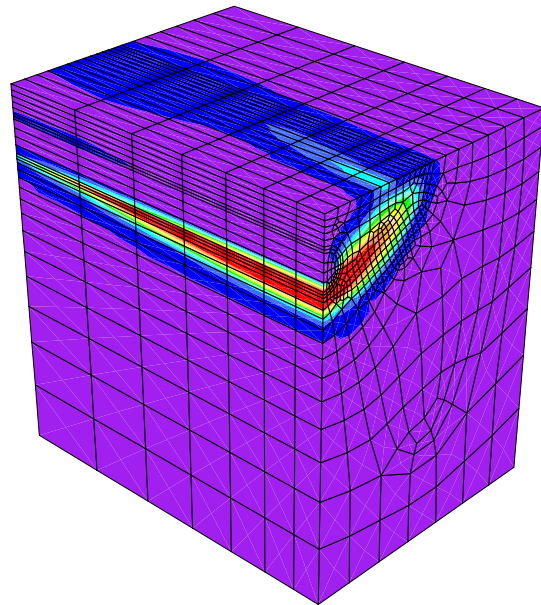


Figure 5.41: Dowel bar test – load-displacement diagrams.

The load-displacement diagrams in Fig. 5.41 show that the nearest diagram to the experimental path is in case 2 for mesh B. The level of the peak value is quite close, although all the simulations exhibit a much higher initial stiffness. For both meshes in case 1, when the cutting rear wall is not constrained, the softening curve occurs. It turns out that the localization zone reaches the rear boundary plane (cf. Fig. 5.42), so such a kind of support is not acceptable. After the peak in case 2 (see again Fig. 5.41) for mesh A and B stages of mild softening and hardening are observed. Despite the fact that the crack patterns presented in Fig. 5.43 correspond to the results in [41] (Fig. 5.44), the obtained diagrams approximate the experimental path rather coarsely. The inclination of the propagating crack (cf. also the experiment in [50]) and the domain of the spalled cover are similar to the ones observed in the experiment. If attention is focused only on the contour plots (Fig. 5.43) again it is noticed that the results are almost mesh-independent. It is possible that the mesh adapted in the third dimension and/or the analysis of the full-length symmetry domain could give even better results. In Fig. 5.45 the development of the damage parameter is shown. It is expected that fracture under and crushing over the rebar (Fig. 5.45(a)) are seen firstly. Next, a localization zone develops in the direction of the top surface and along the specimen (Figs 5.45(b) and 5.45(c)). The final failure stage, where the damage zone turns to the symmetry plane, was presented earlier in Fig. 5.43(b).

(a)  $\omega$ , mesh A.(b)  $\omega$ , mesh B.(c)  $\bar{\epsilon}$ , mesh A.(d)  $\bar{\epsilon}$ , mesh B.Figure 5.42: Dowel bar test. Final contour plots for case 1 ( $v = 1.0$  mm).



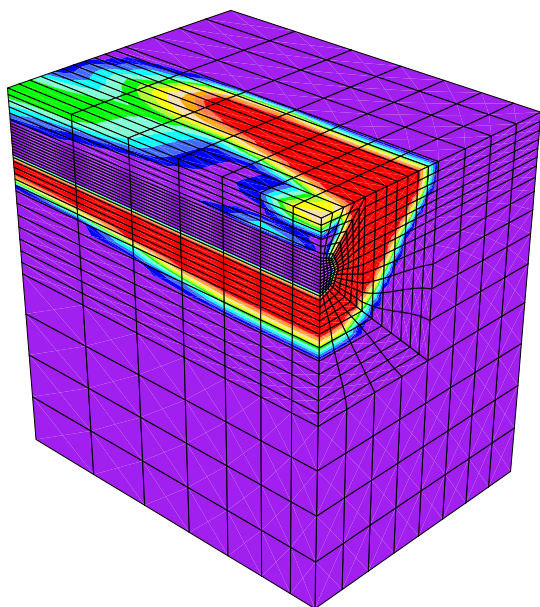
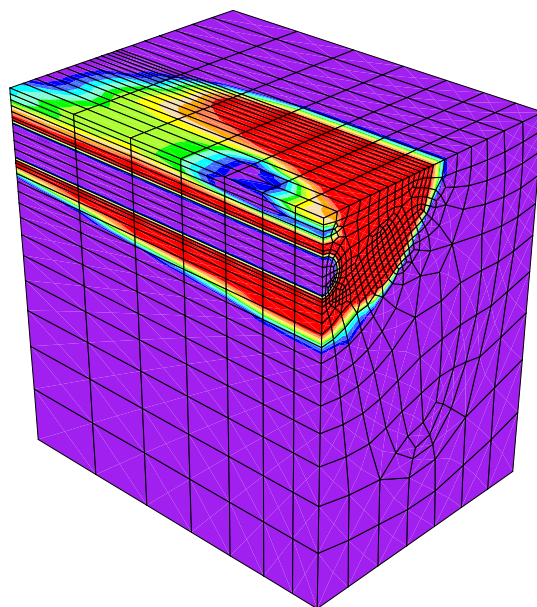
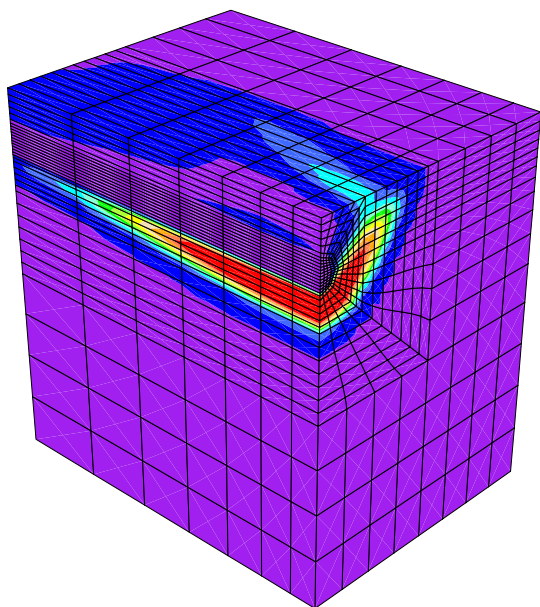
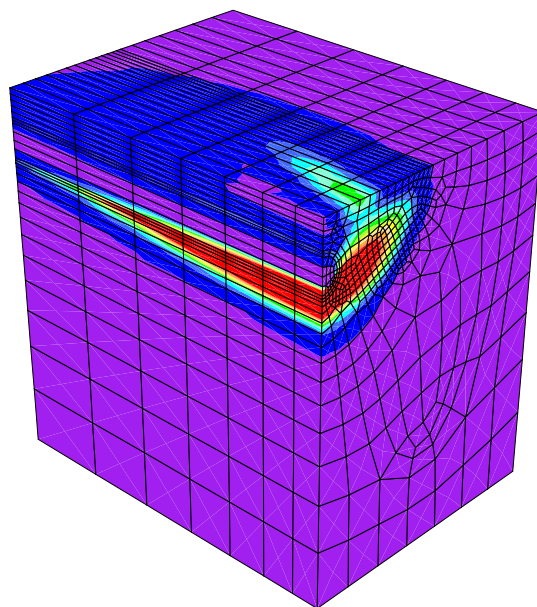
(a)  $\omega$ , mesh A ( $v = 1.21$  mm).(b)  $\omega$ , mesh B ( $v = 2.05$  mm).(c)  $\bar{\epsilon}$ , mesh A ( $v = 1.21$  mm).(d)  $\bar{\epsilon}$ , mesh B ( $v = 2.05$  mm).

Figure 5.43: Dowel bar test. Final contour plots for case 2.

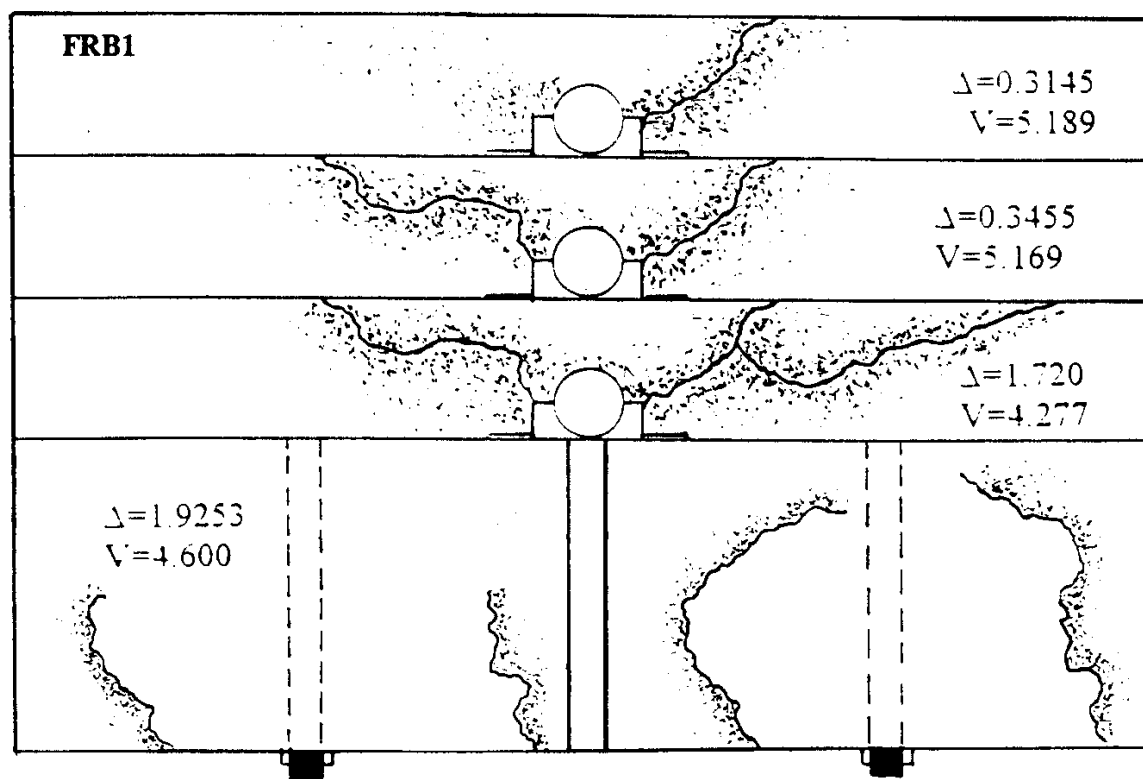


Figure 5.44: Dowel bar test. Crack pattern evolution for concrete FRB1 in experiment [41], front and top view.

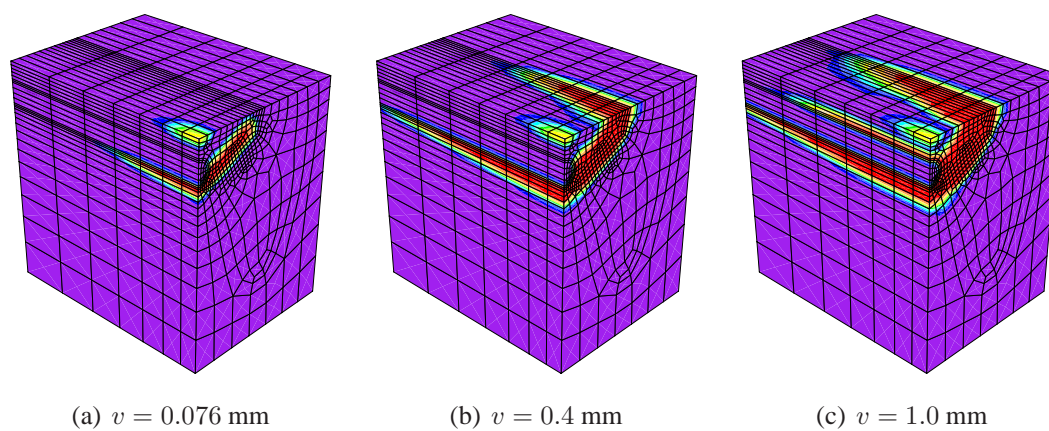


Figure 5.45: Dowel bar test. Development of damage parameter, mesh B, case 2.

## 5.5 RC SLAB-COLUMN CONNECTION<sup>†</sup>

### 5.5.1 PUNCHING SHEAR IN RC SLABS – PROBLEM DESCRIPTION AND EXPERIMENT [1]

In multi-storey buildings designers commonly apply flat slab-column structures instead of slab-girder-column combinations. Advantages of flat floors are well-known, they include the reduced height of buildings and more economical design and performance. However, the problem of punching shear failure occurs in flat slabs.

When a typical internal slab-column segment is considered, cracks usually form due to bending of the slab, on its surface under tensile stresses, in radial directions from the column. On the other hand, punching can be caused by a concentration of shear stresses in the vicinity of the column. In this case cracking along circular lines is observed directly around the column on the compressed surface of the slab and, at a certain distance around the column, on the surface under tension. The description of this phenomenon, some experimental results and analytical model can be found for instance in [104, 163].

Strengthening of reinforced concrete slabs against punching shear is then a necessity in many practical situations. Many well-known methods which help one to avoid the punching failure can be used during the construction of a building, e.g. thickening of slabs near column capitals or additional reinforcement (stirrups, bent bars, studs, etc.). A new technique for the retrofit of existing slabs near slab-column connections has recently been developed and experimentally tested at the University of Waterloo [1]. To increase the punching shear strength and ductility a number of shear bolts like in Fig. 5.46 are installed in the critical zone near the column. They are steel bars anchored at both ends at slab surfaces. The strengthening requires drilling of a small hole through the slab and anchoring the bolt. The bolts are not bonded to the slab and no prestressing is required. This simple method can effectively prevent the destruction due to punching shear failure in slabs.

The problem of punching shear is not trivial to be simulated, since the interaction between flexural and shear failure needs to be reproduced, while localized fracture zones evolve. Some numerical simulations of punching shear are presented in [93, 105, 111, 133, 166, 177]. Although the problem of proper simulation of localized failure seems to be less severe in reinforced structures, it has been decided to employ a regularized continuum description to minimize the effects of pathological mesh sensitivity and numerical instabilities. This section thus reports on the simulations of a laboratory test using the damage model which was first proposed in [125] and is developed also in this thesis. It includes a gradient localization limiter and linear kinematics. For comparison, the same configuration is computed with the classical cracking model using the DIANA FE package [43].

---

<sup>†</sup>Section partly based on [176]



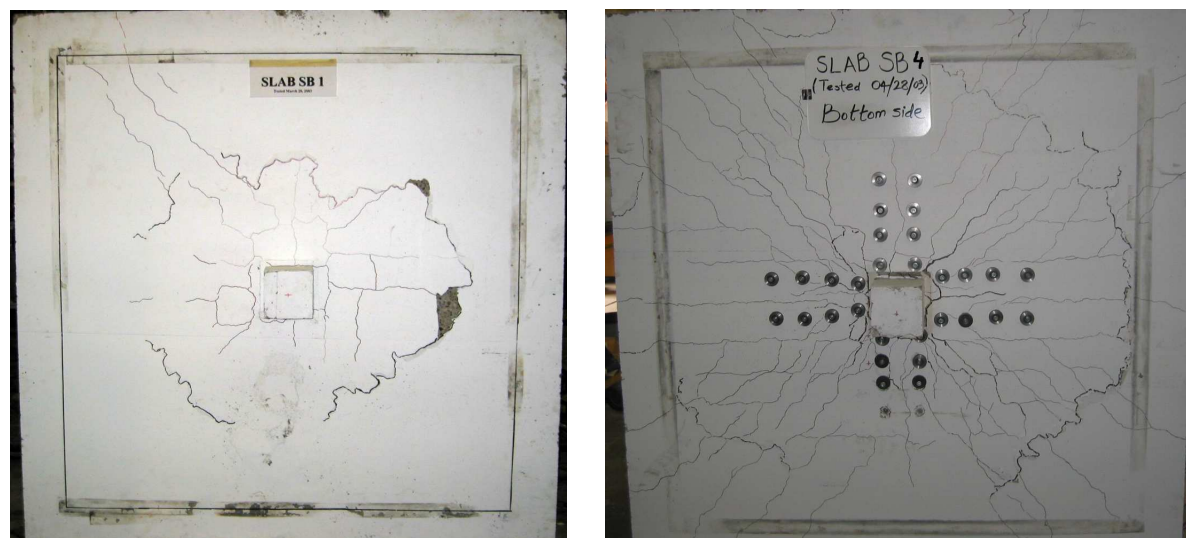
Figure 5.46: RC slab-column connection. Bolt installed to prevent punching shear failure in existing slabs. Photo quoted from [1].

Table 5.7: RC slab-column connection – experimental data [1].

Dimensions	mm	mm	mm	Reinforce- ment	Spacing	Cover	Section area	Yield strength
Slab	1800	1800	120					
Column	150	150			mm	mm	mm <sup>2</sup>	MPa
Supports	1500	1500						
Concrete				In slab:				
strength	MPa			Tensile	90/100	20	100	455
				Compressive	200	20	100	455
				In column:				
Tensile	2.13			Bars			300	455
Compressive	41			Ties			50	455
				Bolts:				
				First	45 ÷ 60		70.8	381
				Subsequent	75 ÷ 90		70.8	381

In the experimental research [1] full-scale models representing interior slab-column connections were tested. The dimensions of the slabs were  $1800 \times 1800 \times 120$  mm and the columns had square cross-section  $150 \times 150$  mm. Simple supports were introduced at the bottom plane of the slab 150 mm from its edges. Additionally, the corners of the slab were clamped at the top against lifting. The specimen was loaded downwards through the column until failure. Note that the experimental configuration was in an upside down position in comparison with the real structural case. The flexural reinforcement was formed by bars of cross-section area  $A_r = 100$  mm<sup>2</sup>. The bars in the tension mat had the spacing of 100 mm and 90 mm for the upper and lower bar families, respectively, in order to produce almost identical bending capacities in the two orthogonal directions. The reinforcement bars at the compression side formed a grid with two times larger spacing. The column segments were reinforced with 4 bars having  $A_r = 300$  mm<sup>2</sup>.

Some slabs had openings constructed near the column. One slab, called SB1, had no shear bolts installed and served as a control specimen. The other specimens were strengthened using an increasing number of symmetrically placed bolts with 9.5 mm diameter, at most four in each row, as in specimen SB4 shown in Fig. 5.47(b). The geometry and material properties from the experiment are gathered in Table 5.7.



(a) Crack pattern for SB1.

(b) Crack pattern for SB4.

Figure 5.47: RC slab-column connection. Final crack patterns for slabs SB1 and SB4, visible from the tension side. Photos quoted from [1].

The test results in terms of deflections, strains and crack widths were monitored. The experimental load-deflection diagrams for SB1 and SB4 are reproduced further in Fig. 5.49 together with numerical results. The final experimental crack patterns for the selected slabs SB1 and SB4, as seen from the tension side, are presented in Fig. 5.47. For all examined specimens, the flexural cracks initiated at column corners and propagated radially towards the slab edges. It was found that specimen SB1 failed due to punching shear, but specimen SB4 failed in a flexural mode. The application of shear bolts increased the shear strength of the connection and significantly improved its ductility.

### 5.5.2 SIMULATION – SIMPLIFICATIONS AND DATA

For the simulation a symmetric slab-column geometry and loading are selected, hence one quarter of the configuration is analyzed. The specimens with openings are not considered. The slab and column are discretized with B8/8 elements, i.e. a linear interpolation of the displacements and averaged strain is used with full integration (FI). A top view on the applied mesh is presented in Fig. 5.48(a). Elasto-plastic truss elements are employed as the reinforcement. Bond-slip between concrete and reinforcement is neglected. In the numerical simulations the configuration is limited by support lines, i.e. a slab segment with dimensions  $1500 \times 1500 \times 120$  mm is computed. Clamps are simulated by supporting three nodes near the corner of the slab. The distance between the tensile reinforcement truss elements is equal to 100 mm in both directions. The basic data for the computations are specified in Table 5.8. The location of the whole reinforcement including bolts is depicted in Fig. 5.48(b). Two cases are considered in

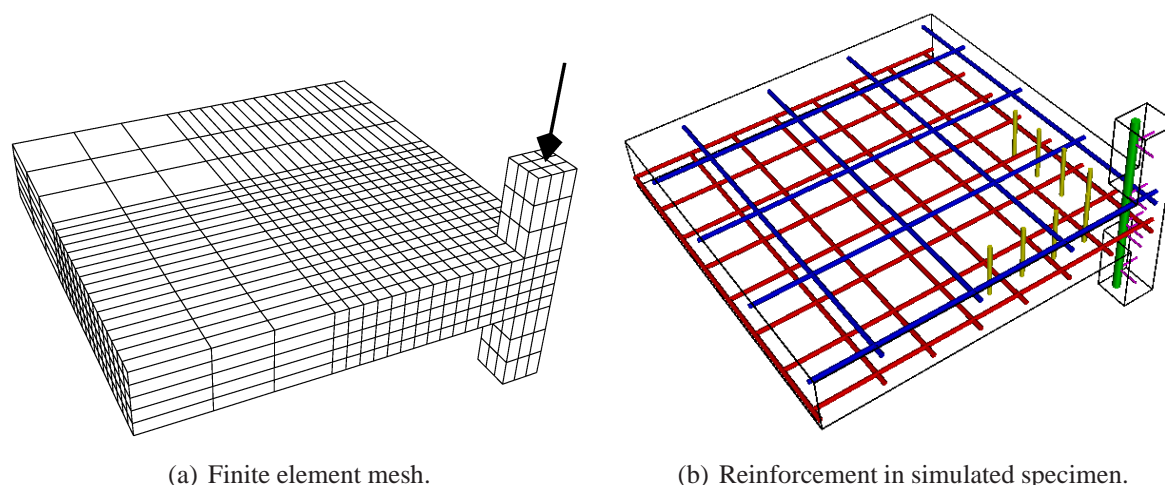


Figure 5.48: RC slab-column connection. Simulated specimen.

Table 5.8: RC slab-column connection – numerical simulation data.

Dimensions	mm	mm	mm	Reinforce- ment	Spacing mm	Cover (to axis) mm	Section area mm <sup>2</sup>	Yield strength MPa
Slab	1500	1500	120					
Column	150	150						
Supports	1500	1500						
Elastic constants				In slab:				
	Young's modulus	Poisson's ratio		Tensile	100	24	100	455
	GPa			Compress.	200	24	100	455
Concrete	34.4	0.2		In column:				
Steel	205	0.3		Bars		25	300	455
				Ties			50	455
				Bolts:				
				First	50		70.8	381
				Subseq.	75		70.8	381
Concrete strength		MPa						
	Tensile, $f_t$	2.13						
	Compressive, $f_c$	$k \times f_t$						

the simulations: the slab without bolts (SB1) and the slab with eight bolts at each side of the column (SB4), idealized using bar elements connected to the slab at its surfaces. Static loading shown in Fig. 5.48(a) is applied under displacement control, i.e. the vertical movement of the upper plane of the column segment is imposed monotonically.

The parameters for the gradient damage model are as follows: threshold  $\kappa_o = 6.2 \times 10^{-5}$ , exponential softening according to Eq. (2.21) with residual stress parameter  $\alpha = 0.94$  and ductility parameter  $\eta = 400$ . Modified von Mises definition (2.15) is employed and it is treated as the basic case, when the ratio  $k = f_c/f_t$  is equal to 20. This value of  $k$  approximates the

material data. In the simulation this model can be combined with the Burzyński-Drucker-Prager hardening plasticity by means of weak coupling, i.e. only the elastic strains induce damage. The parameters for the plastic part of the model are: yield strength  $\sigma_y = 2.13$  MPa, hardening modulus for cohesion  $h = 17.2$  GPa, friction and dilatancy coefficients  $\sin \varphi = \sin \psi = 0.5$ . Another possibility is to use the isotropic model with different damage growth for volumetric and deviatoric parts. There are analyzed cases with combinations of ductility parameters  $\eta_i$  ( $i = K, G$ ), similarly to the previously presented examples for the isotropic model (cf. Subsection 5.2.2). At the beginning the internal length scale was  $l = 20$  mm, but after the examination of the results this value has been changed. A detailed explanation is given in the next subsection. For  $l = 20$  mm the relation  $c = \frac{1}{2}l^2$  is assumed to be valid [4] and the width of the fracture band is estimated as  $w_f \approx 6l$ . In order to mitigate the effect that cracking in the slab induces damage in the column due to non-locality, which does not seem to have a physical background, the behaviour of concrete elements in the column is constrained to be elastic by introducing  $\kappa_o = 6.2 \times 10^{-3}$ .

Since the simulation results are not satisfactory for the model of the slab without bolts, the same configuration is computed with the classical smeared cracking model using the DIANA FE package [43], see also e.g. [140]. Here brick elements with selective integration of shear terms are used. The discrete elasto-plastic reinforcement bars are embedded in the continuum elements. In the cracking model in DIANA the fracture energy is  $G_f = 106.5$  N/m, the estimated numerical crack band width is  $w_f = 24$  mm (smallest element size) and the shear retention factor equals 0.2.

### 5.5.3 NUMERICAL RESULTS AND DISCUSSION

Figure 5.49 presents a comparison of experimental and computed diagrams. Initial responses of both numerical models, without and with coupling of damage to plasticity, are too stiff. It is also clearly seen that almost identical results are computed for the simulation without and with bolts (experimental case SB1 and SB4, respectively). Actually, instead of four different diagrams from numerical analyses, only two can be distinguished, the first one for pure damage and the second for the coupled model. This proves that the bolts are in fact hardly active in the numerical model, which is in contradiction with the experimental results. The modelling of bolts seems to be too crude, it does not include the anchorage bond like in [111]. Moreover, the peak for pure gradient damage occurs too early and the whole equilibrium path is not representative with reference to either of the experimental diagrams. The load carrying capacity is well-reproduced for the coupled model with bolts (experimental case SB4). However, this is not crucial: it is not too difficult to tune the parameters of the damage-plasticity model to achieve this. On the other hand, it is shown that the coupling to plasticity results in a largely increased ductility of the model. All branches are obtained for  $l = 20$  mm. This value of the internal length is quite large, the expected width of the fracture band is approximately  $w_f = 120$  mm which is equal to

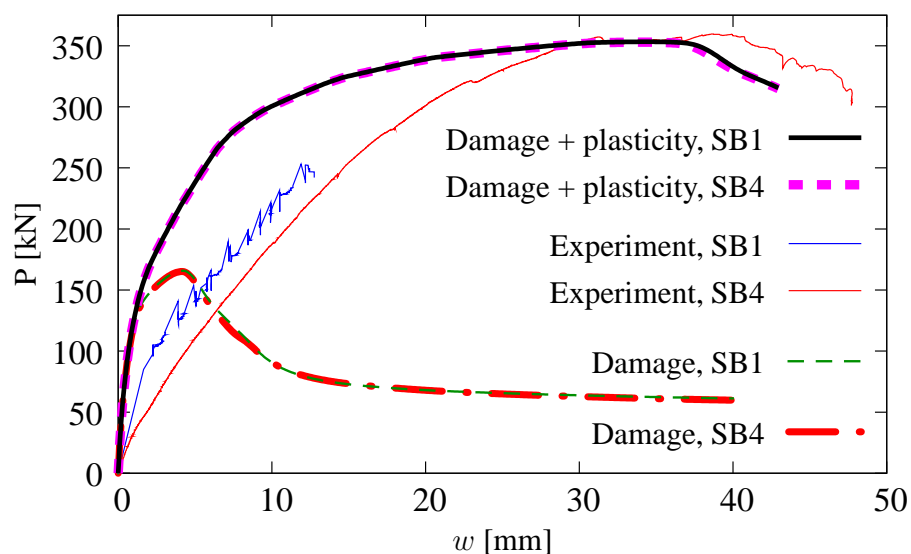


Figure 5.49: RC slab-column connection. Load-displacement diagrams, experiment versus simulation.

the slab depth. The averaging and smoothing effect is then quite strong, the dissipated fracture energy strongly exaggerated, and for larger deflections damage is predicted in a large part of the slab, which does not seem realistic.

Figure 5.50 presents the simulated averaged strain patterns for the case with the coupled damage-plasticity model and the simulated bolts taken into account (thus representing the experimental case SB4). The contour plots of the averaged strain measure are connected with the distributed cracking zones for three slab deflection values  $w \approx 3, 12, 41$  mm. The plots are drawn for the bottom face of the slab which exhibits tensile cracks (figures on the left) and for a cross section of the configuration with a vertical symmetry plane (on the right). A bending mode of failure is reproduced and the fracture first localizes in the direct vicinity of the column, then extending in zones following the symmetry planes of the configuration. As can be noticed in Fig. 5.50(e) and 5.50(f) the largest strains finally occur at the bottom slab-column connection line. These averaged strain patterns are similar for the case without bolts, which is unrealistic and means that the model fails in predicting the punching shear phenomenon. As shown in [176] the tendency that the slab is cut directly at the column is observed also for other values of parameter  $k = f_c/f_t$ .

The unsuccessful results induce the search for the punching shear failure mode similar to the experimental case SB1. Therefore, in next simulations attention is focused on the model without bolts and a parametric study aiming at the reproduction of the punching shear effect. In contradiction to the data assumed in the previous section, a quite small value of the internal length parameter  $l = 4$  mm is adopted. The related value  $w_f = 24$  mm equals the element size in the dense mesh part, so this seems to be the limit value for the regularization to be active. Additional computations with  $l = 8$  mm can be treated as an intermediate case. The second



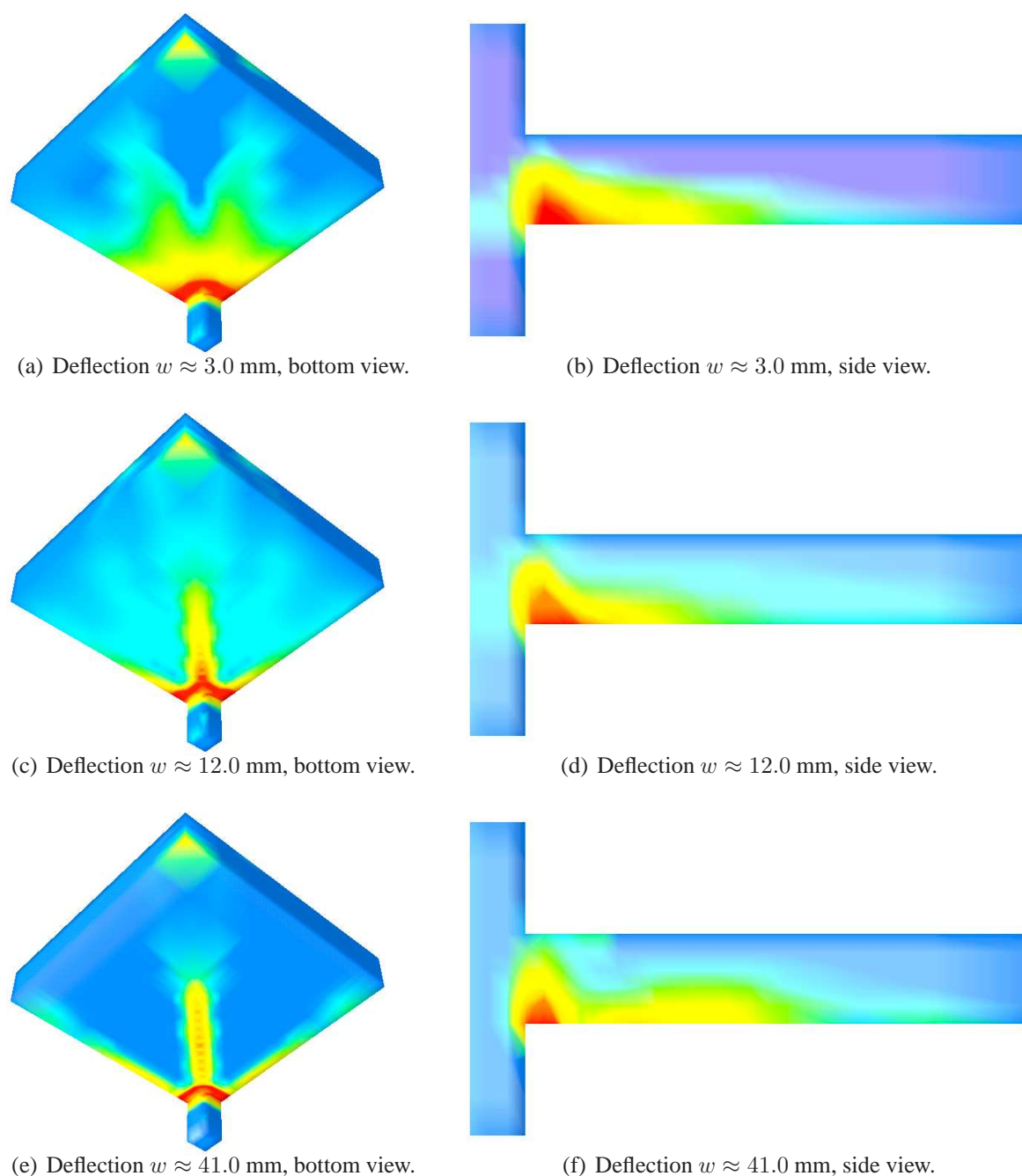


Figure 5.50: RC slab-column connection, SB4. Contour plots of averaged strain for gradient damage-plasticity,  $l = 20$  mm.

change is the introduction of an alternative denser mesh with a double number of elements along the height of the slab. The difference between basic and denser meshes is illustrated in Fig. 5.52. From now on the basic mesh will also be called the coarse mesh.

The previous computations have confirmed that the internal length parameter  $l = 20$  mm is too large. The non-locality region is so wide that the model is not able to analyze the formation of cracks in the slab beside the ones originating from the flexural failure mode. The load-

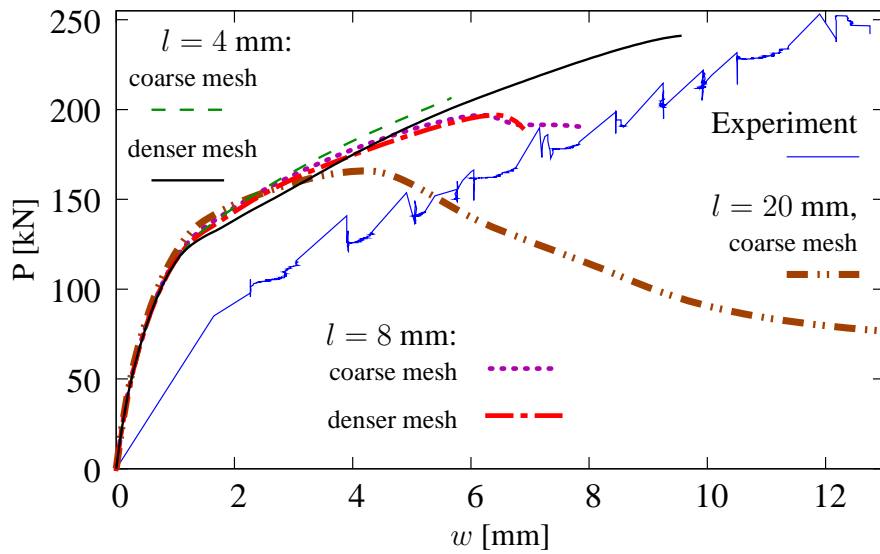


Figure 5.51: RC slab-column connection, SB1. Load-displacement diagrams, influence of internal length scale, gradient damage (without plasticity).

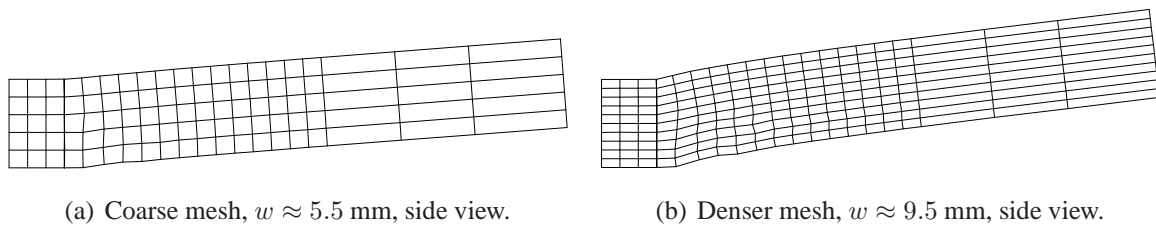


Figure 5.52: RC slab-column connection, SB1. Deformation (magnification factor is 10) of slab for two different meshes, gradient damage,  $l = 4$  mm.

deflection diagrams, where the influence of the internal length scale is verified, are depicted in Fig. 5.51. Here the pure gradient damage model is adopted. The equilibrium paths for the two considered meshes are plotted for the cases with smaller  $l$  ( $l = 4$  mm or 8 mm). Additionally the diagram for  $l = 20$  mm and the coarse mesh, which has been previously presented in Fig. 5.49, is included. The diagram for the case with  $l = 4$  mm and the denser mesh resembles the experimental path. After the initial elastic phase in the numerical diagram a change of its slope fits the general character of the diagram observed in the experiment. Furthermore, the computations diverge, when the load reaches about 250 kN similar to the experimental load carrying capacity. For the other cases computations diverge earlier. If  $l = 8$  mm is adopted, in the final stage a change of stiffness is noticed into small softening.

The punching shear failure is a sudden phenomenon. Usually the moment of this failure follows the yielding of the tensile reinforcement in the slab. However, if the main reinforcement ratio is large enough it is also possible that the punching shear effect appears before the yield condition is attained in the reinforcement, see [163]. In the case with  $l = 4$  mm and the denser mesh, which seems to be the most adequate from the view point of the experiment,

the maximum stress in the tensile reinforcement of the slab is approximately 414 MPa (smaller than the yield strength).

The deformation of the slab at the final stage is depicted in Fig. 5.52. It is visible for both meshes that the slab is not cut directly at the column, but on the other hand the deformed elements do not form a clear oblique shear crack as is seen in experiments and reality.

Figures 5.53 and 5.54 illustrate the simulated averaged strain patterns for the case  $l = 4$  mm and both meshes. Similarly to Fig. 5.50, the contour plots are made for the bottom face of the slab and for the cross section along the vertical symmetry plane. Side views of averaged strain distributions again show that the simulated slab is not cracked near the connection, although the shear cone is poorly reproduced. The patterns at the bottom face of the slab are different from the case with  $l = 20$  mm. Now, for the small value of the internal length parameter, many flexural cracks are initiated at column corners and propagate radially. The averaged strain distributions still do not simulate circular cracks at some distance from the column, hence

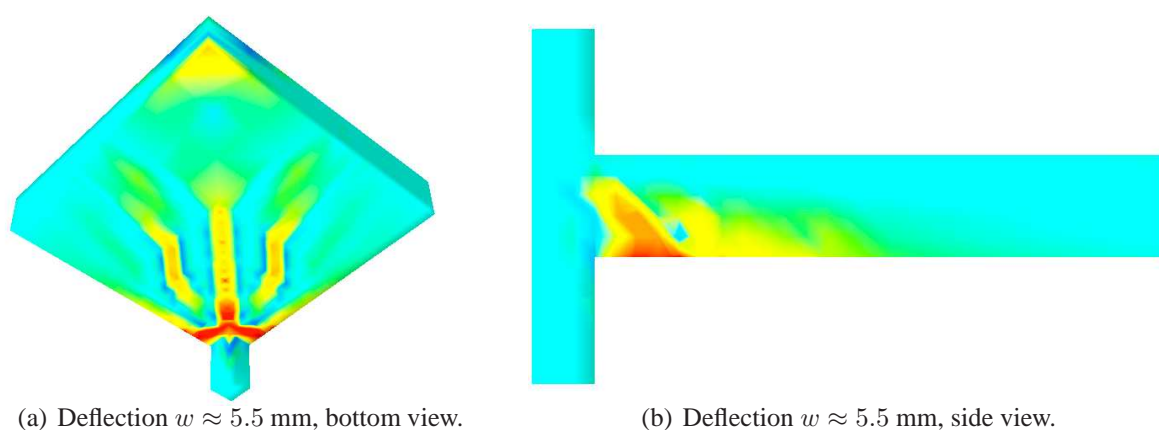


Figure 5.53: RC slab-column connection, SB1. Contour plots of averaged strain for coarse mesh, gradient damage,  $l = 4$  mm.

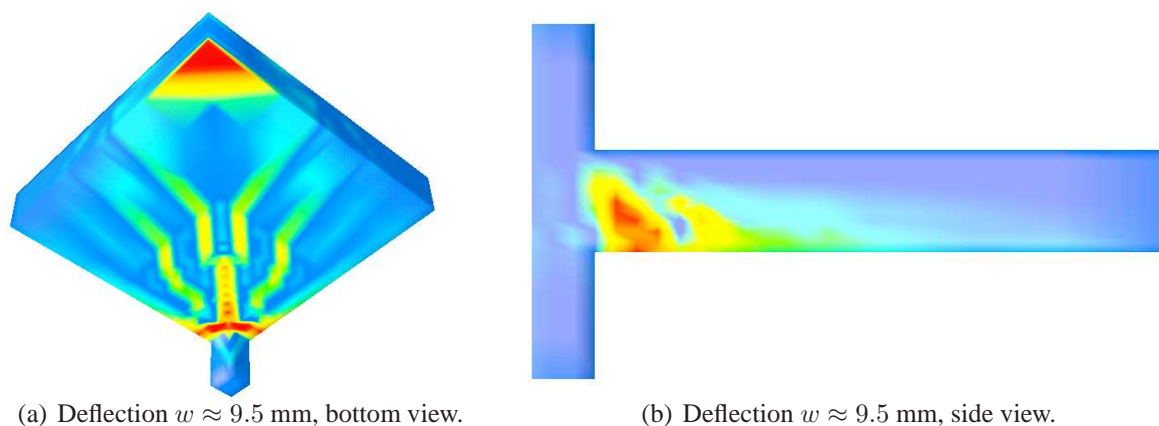


Figure 5.54: RC slab-column connection, SB1. Contour plots of averaged strain for denser mesh, gradient damage,  $l = 4$  mm.

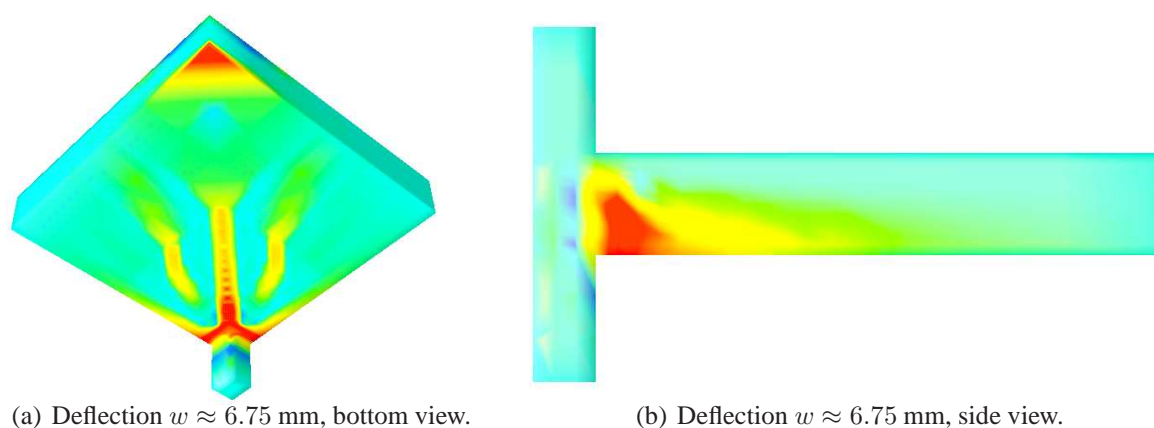


Figure 5.55: RC slab-column connection, SB1. Contour plots of averaged strain for denser mesh, gradient damage,  $l = 8$  mm.

the punching shear fracture along inclined cone-shaped surface is rather not observed. The results for  $l = 4$  mm look better than for  $l = 8$  mm also when averaged strain patterns are compared. Figure 5.55 presents the bottom and side views for  $l = 8$  mm. It was expected that the slightly more regularized model would make the results more correct and that circular cracks would be reproduced properly together with radial ones. It turns out that introducing a little larger non-locality, which corresponds to about two elements in the mesh, does not improve the results. Of course the localization zone is wider, but  $l = 8$  mm results in dominating averaged strains closer to the column than it is for  $l = 4$  mm.

The load-displacement diagrams depicted in Fig. 5.56 are drawn for computations with the denser mesh and two other options of the numerical model. As expected, the equilibrium path obtained for damage-plasticity is stiffer than for pure damage, but the solution diverges when the load is smaller than 200 kN. The results for the alternative loading function according to Mazars' definition (see Eq. (2.12) and Fig. 2.4), which seems to be promising for concrete in tension-compression regime, completely fail. It is reflected in the diagram in Fig. 5.56.

Next the numerical analysis is performed taking into account the isotropic damage model and the denser mesh. The internal length parameter  $l$  is equal to 4 mm. Table 5.9 summarizes all examined cases, where different ductility parameters for exponential softening law are adopted. Considering diagrams in Fig. 5.57 it can be concluded that the model with volumetric-deviatoric split (and as a consequence with two damage parameters) does not improve the results. A more intensive damage growth when  $\eta = 600$  induces more brittle response and computations diverge for the load equal to 170 kN. As expected, the diagrams for the cases where damage grows differently for volumetric and deviatoric parts run between the bounding cases *exp* and *exp, K & G*. The diagrams for cases *exp, G* and *exp, K & G* are very close to each other. It should be emphasized that in the case *exp, G* the damage growth function for the deviatoric part is the same as in the basic case *exp, K & G* ( $\eta = 400$ ).

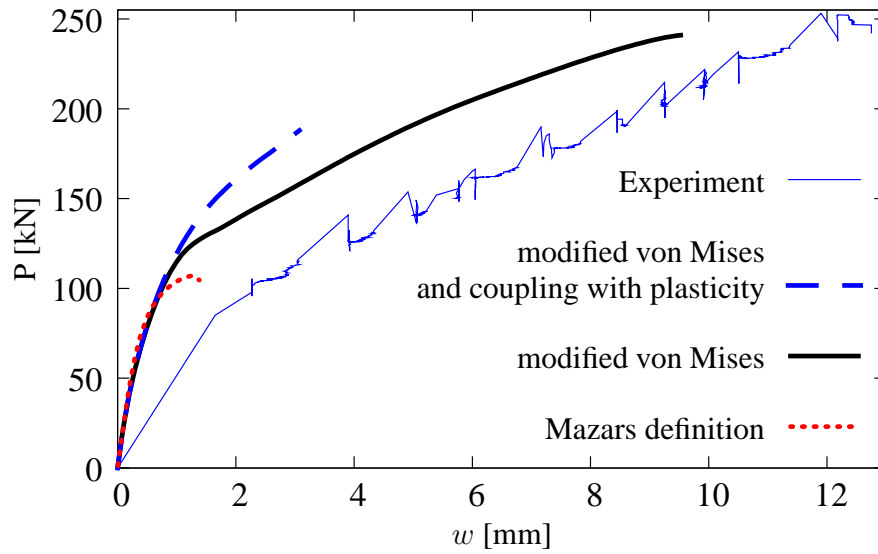


Figure 5.56: RC slab-column connection, SB1. Load-displacement diagrams, denser mesh,  $l = 4$  mm.

Table 5.9: RC slab-column connection, SB1 – cases for isotropic gradient damage.

Symbol of case	Parameters for exponential softening		Damage growth
	volumetric part	deviatoric part	
<i>exp</i> —	$\eta_K = 600$	$\eta_G = 600$	more intensive
<i>exp, K</i> - - -	$\eta_K = 400$	$\eta_G = 600$	$\omega_K < \omega_G$
<i>exp, G</i> - - -	$\eta_K = 600$	$\eta_G = 400$	$\omega_K > \omega_G$
<i>exp, K &amp; G</i> —	$\eta_K = 400$	$\eta_G = 400$	less intensive

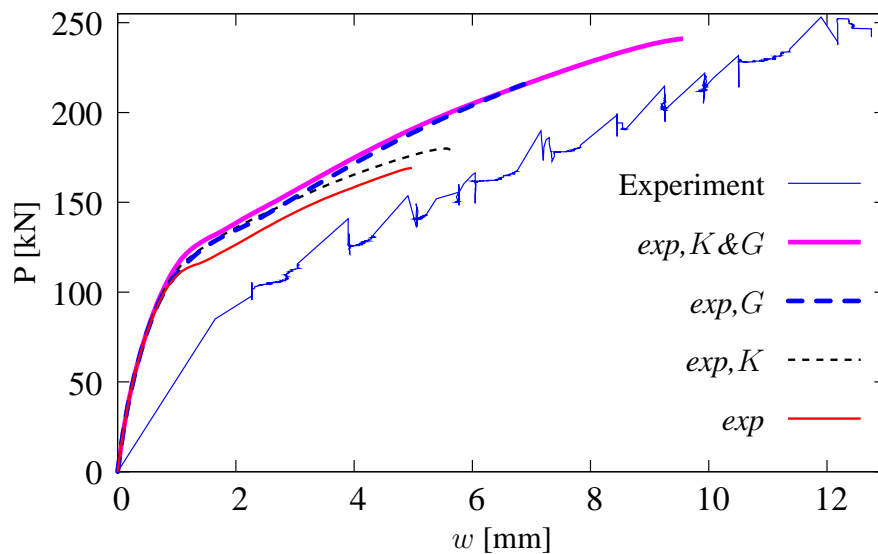


Figure 5.57: RC slab-column connection, SB1. Load-displacement diagrams obtained for isotropic model,  $l = 4$  mm.

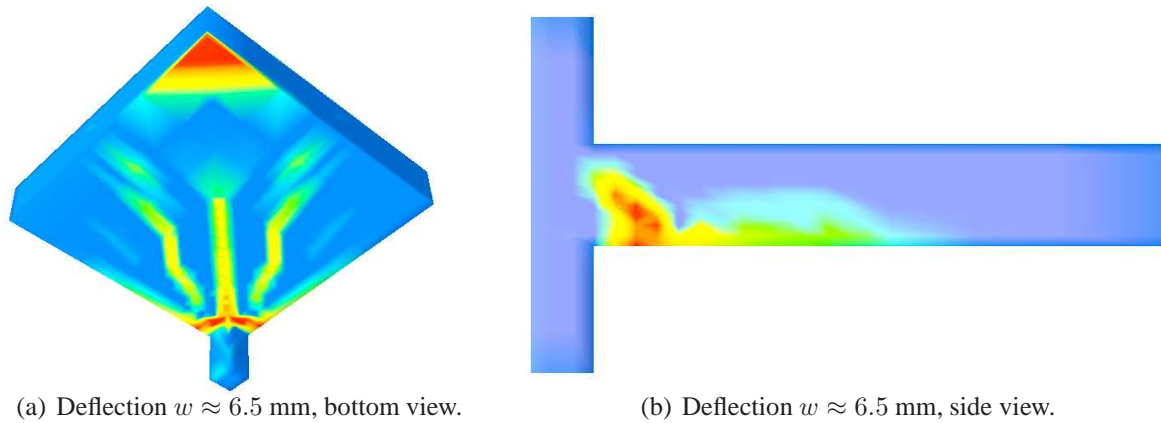


Figure 5.58: RC slab-column connection, SB1. Contour plots of averaged strain for isotropic gradient damage, case  $exp, G$ ,  $l = 4$  mm.

Figure 5.58 depicts contour plots of averaged strain for case  $exp, G$ . In fact, these results are similar to the ones obtained for the basic case  $exp, K \& G$  (cf. Fig. 5.54). The larger difference between the ductility parameters for volumetric and deviatoric damage can involve the problem with negative values of Poisson's ratio  $\nu_\omega$  (see Section 2.4). Generally, introducing the isotropic model does not cause the results to reproduce the punching shear phenomenon.

Since a possible reason for the above-described incorrect simulation results can be that the nonlocal smoothing prevents the formation of secondary inclined fracture surface related to shear, the analysis of the SB1 configuration (without bolts) is repeated once again with local smeared crack models in the DIANA FE package. Two types of the model are verified, namely

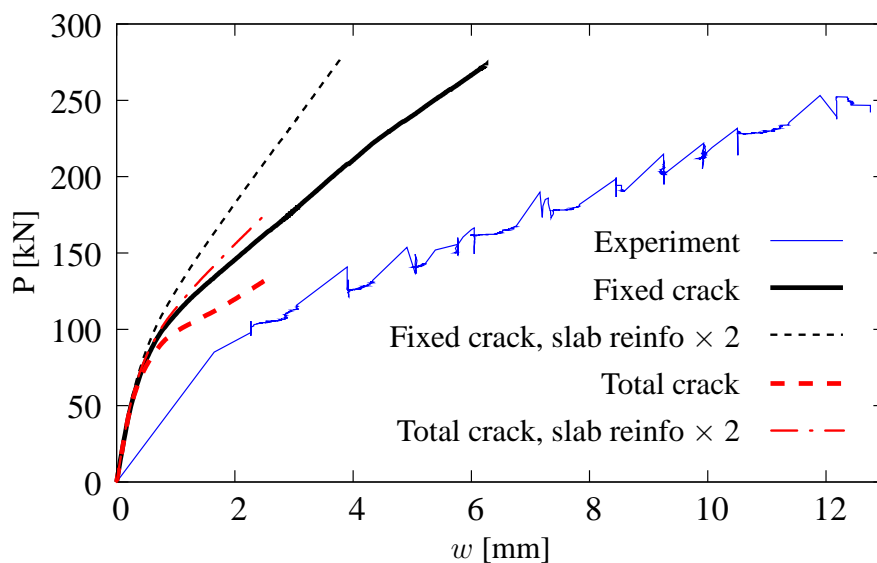


Figure 5.59: RC slab-column connection, SB1. Load-displacement diagrams obtained using DIANA package.

fixed and total crack models, [43]. The load-displacement diagrams in Fig. 5.59 are obtained for the two considered cases: the slab with the basic main reinforcement (cross-section area equals 100 mm<sup>2</sup>) and double cross-section of the main reinforcement (to increase the flexural stiffness of the slab). It is noticed that for the fixed crack model the failure of simulation for the two cases occurs at similar load values. On the other hand for the total crack model the computations end when similar values of the deflection are reached.

Figures 5.60 and 5.61 present the contour plots of the equivalent deviatoric strain measure  $J_2^{\epsilon}$  for the two respective models, performed right before the computations stop. Neither of the plots reproduces satisfactorily the punching shear failure mode. Secondary fracture zones

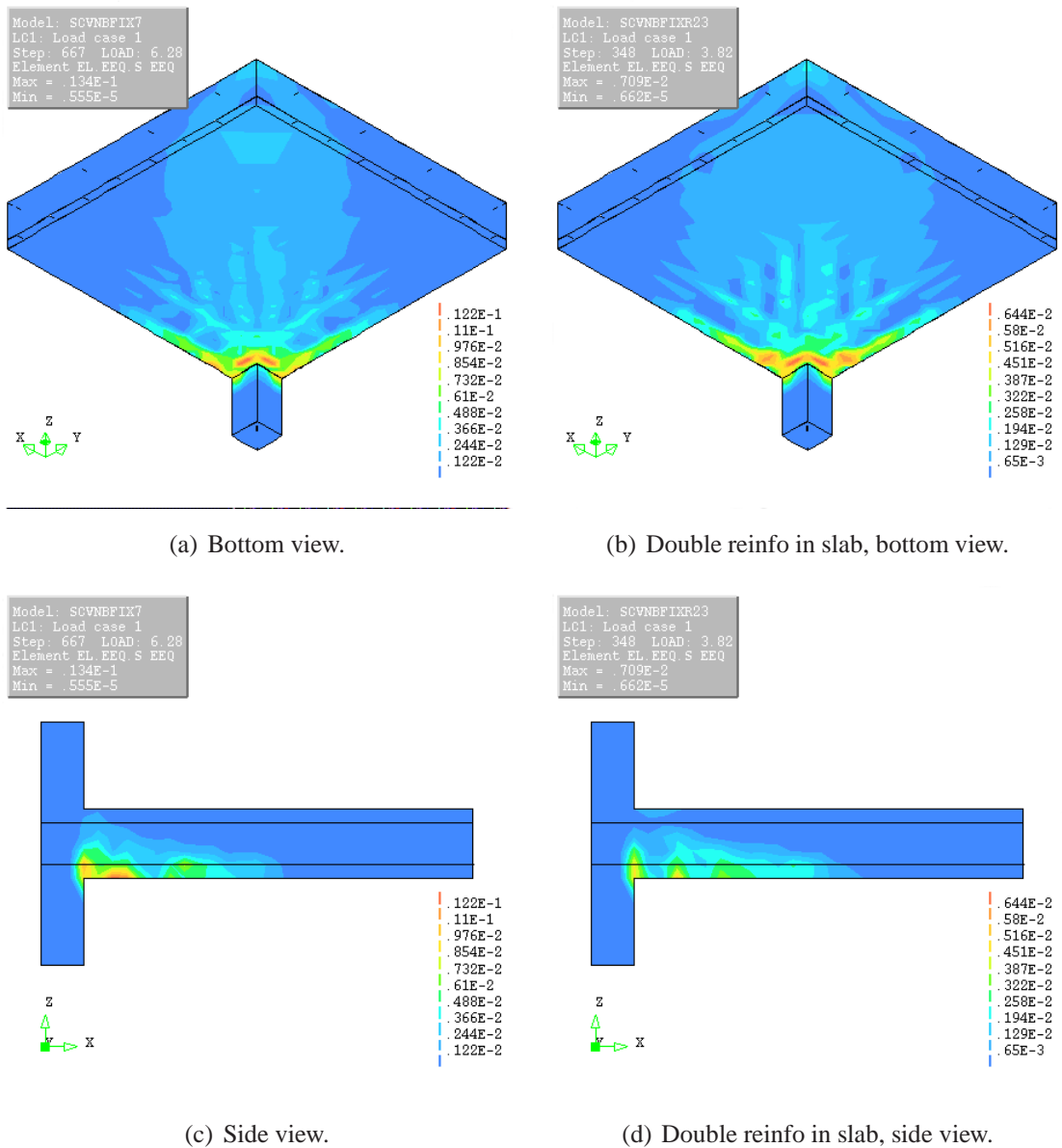


Figure 5.60: RC slab-column connection, SB1. Contour plots of equivalent strain for fixed crack model, final state.

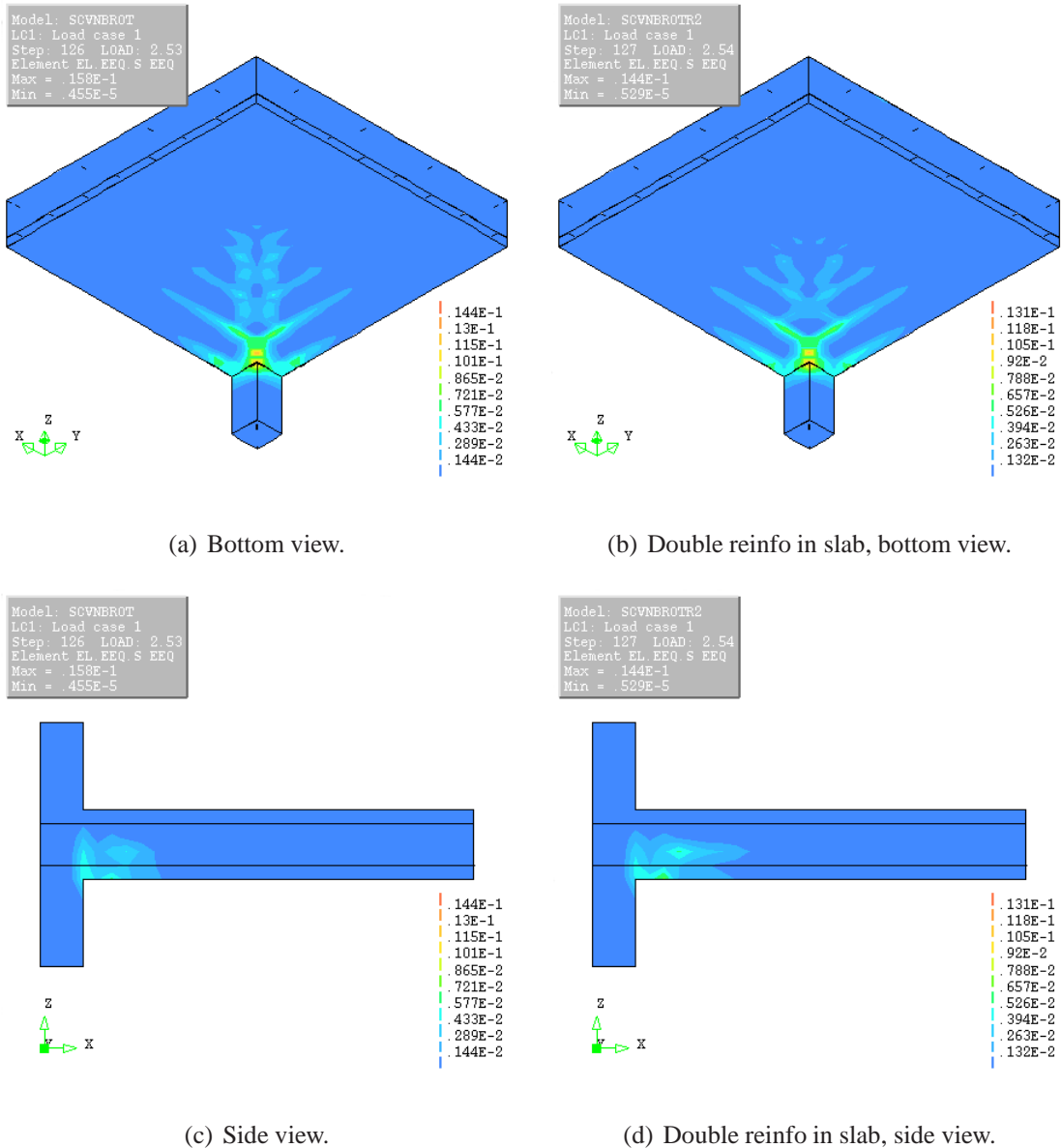


Figure 5.61: RC slab-column connection, SB1. Contour plots of equivalent strain for total crack model, final state.

emerging at some distance from the column are observed for the fixed crack model, which could initiate the shear cone similar to the experiments, but the iterative process fails. Moreover, the ductility of both types of the model is insufficient, see the diagrams in Fig. 5.59.

The numerical simulations of fracture in the experimental slab-column configuration taken from [1] do not predict the expected punching shear failure for the model without strengthening bolts. For the case with the denser mesh and the small value of the internal length parameter  $l = 4$  mm the solution is the closest to the experimental observations, but in fact it is unclear if the punching shear failure is reproduced. In fact, the results are neither satisfactory for different



versions of the gradient-enhanced model implemented in FEAP, nor for the classical crack models from DIANA. The inability of the gradient model in simulating the punching shear failure can have the following reasons:

- the employed meshes are too coarse,
- the nonlocal smoothing prevents the formation of secondary inclined fracture surface related to shear effect causing the bending mode to be dominant,
- the proposed loading functions are improper for the three-dimensional analysis of a configuration where shear (mixed mode) effects should be precisely computed,
- full bond between concrete and reinforcement seems to be a too rough modelling of the reinforcement structure (without and with bolts),
- since the gradient-enhanced isotropic model with two damage parameters does not improve the results, maybe an anisotropic damage description for concrete with a gradient or nonlocal integral enhancement of all strain tensor components could be a solution.

Summarizing, the implemented numerical model reproduces the bending-type failure, so phenomena where shear effects govern the final fracture should be analyzed using another (possibly fully anisotropic) version of the damage model, or another fracture model. It is a good subject for further research.



## CHAPTER 6

# CONCLUSIONS

Extensions of the gradient damage model coupled to the plasticity theory have been verified in this thesis. This model, proposed in [36, 117], is employed to reproduce properly the phenomena of localization and failure in (reinforced) concrete. The cracking process in quasi-brittle materials like concrete, which is unavoidable during the service time of structures, can be objectively simulated owing to the presence of the intrinsic length scale in the formulation. This is because the non-local approach like gradient damage guarantees that the spurious mesh sensitivity of results is avoided. Three-dimensional problems, dynamics without damping effects and the implementation of effective finite elements have been examined.

At the point level the scalar damage theory in the strain space has been reviewed. The coupled model has been adopted in order to incorporate irreversible strains, and as a consequence a better agreement with the real response. Hardening plasticity has been formulated in the stress space, so the coupling has been introduced according to [74, 145]. Moreover, the crack closure phenomenon, which is observed in structures subjected to load reversals, has been included. Although this seemingly complicated model can represent different physical components, there are only few model parameters to determine.

If isotropic damage is considered, it is possible to equip the damage model with two strain measures and/or two damage parameters. The simplest case with one equivalent strain measure and two different damage parameters has been implemented. In this case two different groups of parameters can be adopted for damage growth definitions. Since linear softening functions can provide unrealistic change of the Poisson's effect, exponential softening law is more adequate.

The so-called Willam's test has been performed to verify each option of the model. In this benchmark at the beginning a material point is loaded in uniaxial tension. After the tensile strength is reached, tension in two directions and additionally shear are enforced. Such loading process is observed during the analysis of real RC structures as mentioned in [171]. The results for all the options of the model show that the conditions to pass this test have been satisfied.

The initial boundary value problem (IBVP) has been regularized by means of the averaging Helmholtz equation identically to [125], so independent interpolations of displacements and averaged strain fields have been employed. The two-field formulation holds for scalar and

isotropic gradient damage, as long as one strain measure is applied. However, for the possible approach with two strain measures, separately for the volumetric and deviatoric parts, a discretization with three primary fields should be introduced.

For dynamics, the algorithm requires only a minor modification with respect to the static case proposed in [36], i.e. the equations of motion are implemented as an extension of the equilibrium equations. The finite elements (FEs) have been programmed in the FEAP package [158] using three variants of  $C^0$ -continuous interpolation.

The properties of the implemented elements have been examined by means of spectral analysis of a single FE including different types of interpolation and integration. In three-dimensional (3D) elements with full integration (FI) the computational cost for large scale problems can be too much and one-point Gaussian integration is a better solution. Before attacking 3D implementation in the future, the 2D four-noded element with reduced integration (RI) has been constructed. If RI is applied in the four-noded FE mesh then for effective computations a stabilization must be assured in the formulation. The possibility of stabilization in such finite elements has been proposed and verified in the spectral analysis. As demonstrated, the stabilization terms are needed in both variational equations, i.e. the motion equations and the averaging equation. Then a proper quality of FE and stable numerical results are obtained. In the discussed approach two different methods of stabilization for the given equations have been assumed, namely Galerkin least-square (GLS) method for the equations of motion according to [162, 178] and operator  $\gamma$  method for the averaging equation according to [13]. This is because the GLS method for the averaging equation does not work, as confirmed in Appendix B.

The simulation of uniaxial tension for a bar with imperfection is the most basic benchmark. The employed numerical model was verified previously in [36, 125], but some new results have been shown in this thesis. The differences between pure gradient damage and the coupled model have been brought up. Neither the presence of stabilization in the formulation, nor also the isotropic split in the model destroy the quadratic rate of convergence during the iterative process. It is noticed, that in large scale problems discretized with fine meshes of twenty-noded 3D FEs too much time can be consumed. Therefore the FE with linear interpolation has been chosen despite the fact that the solution can then produce less accurate results.

The differences in the dynamic response between plain and reinforced concrete have been examined by means of the 2D direct tension test. For the same load scaling factor for plain concrete the elongation tends to infinity due to fracture, while for reinforced concrete the axial displacement oscillates around a certain state. Nevertheless, for both responses a standing wave and strain localization have been observed.

A cantilever beam subjected to reversed loading has been analyzed in order to verify the correctness of the algorithm with crack closing. For the model with crack closure effect the original stiffness has been retrieved, but only for zero Poisson's ratio. If crack closing is activated and

$\nu \neq 0$ , the solution diverges. The reason is probably the discontinuity (Heaviside function) introduced in the formulation, while the crack closure phenomenon has the continuous character and the change of the stiffness does not involve any jumps. The experimental observation is that microdefects do not close suddenly but rather gradually, so it should be reflected in the numerical model, cf. e.g. [53].

The compressive loading in the so-called Brazilian test induces splitting inside the concrete specimen and the tensile strength can be established during the experiment. The gradient damage model, scalar or isotropic, is able to simulate this behaviour. A snapback response can follow in the wake of the splitting process. It has been observed that the modelling of the load transferring platen on the concrete specimen is insignificant, but the model parameters decide whether or not and how the splitting phenomenon appears. Moreover, if isotropic gradient damage is employed in the analysis, the deviatoric damage is more important in the stiffness degradation.

Four-point bending in a reinforced concrete (RC) beam had been analyzed experimentally under dynamic loading by Eibl et al. [46]. This benchmark has been examined to show similarities and differences between the responses of the static and dynamic loading. At first, the static response of the beam without reinforcement has been computed and the minimum value of the internal length parameter for mesh-independent results has been found. If FEs with stabilization are applied it can be concluded that the reduced integration results in a slightly less stiff response of the model. For the RC beam under static loading the computations with the coupled damage-plasticity model have been performed and the coupling to plasticity has not caused significant changes in the numerical response. The obtained contour plots correspond to the theory, because one or two plastic hinges in the beam can be considered. For dynamics, the displacement-time diagram exhibits a quite good agreement with the experimental response. For the RC beam under the dynamic loading mesh-independent results are obtained.

If dowelling of a reinforcement bar against the concrete cover in a RC specimen is observed in experiments, localization directly below and above the reinforcement is first visible. Further loading leads to crack opening. After that finally the spalling of concrete in the third dimension is exhibited. Therefore, for a better agreement with observations of structures, the numerical analysis requires modelling in three dimensions. Within the limits of continuum modelling, the numerical results are a reasonable representation of the experimental ones from [41].

In the numerical analysis of punching shear a symmetric slab-column configuration has been modelled based on the experiment presented in [1]. The gradient damage-plasticity description for concrete and embedded elastic-plastic reinforcement bars have been adopted. Two cases have been considered: the slab without bolts and the slab with eight bolts at each side of the column. In reality the bolts are installed to increase the punching shear strength and the ductility in the slab. The performed simulations have not predicted the expected punching shear failure for the model without strengthening bolts, although the case with the smallest internal length and denser mesh gave the results which resemble the experimental ones. The possible

reasons can be as follows: the finite-element mesh is too coarse, nonlocal smoothing causes that the bending failure is too strong and the formation of the shear fracture mode is prevented, the employed loading functions are improper for the three-dimensional analysis, when shear effects are dominant, the influence of bond-slip in the model is omitted.

Summarizing, the most important conclusions are listed below:

- The scalar description in the damage model is sufficient in the analysis where tension/compression and/or bending dominate.
- The introduction of two damage parameters into the model is simple. On the other hand, difficulties with the interpretation of the results can appear, for example negative Poisson's ratio can be obtained.
- Both the scalar and isotropic damage can be ineffective if shearing dominates. The coupling of scalar damage with plasticity does not remove this disadvantage.
- The implicit gradient enhancement guarantees mesh objectivity and well-posedness of the solution.
- For dynamics, the algorithm requires only a minor modification with respect to the static case and proper results of localization simulations are obtained.
- The presence of the reinforcement does not provide the regularization of the cracking problem.
- Stabilized elements with one-point reduced integration give more efficient algorithm.

Finally, the following topics can be considered in the future:

- The implementation of efficient three-dimensional elements with hourglass control according to the formulations derived in this thesis.
- The verification of isotropic description of damage with two different averaged strain measures and additionally combination with plasticity.
- The application of a bond slip-model in RC modelling, and in particular for slab-column connection. In this case the modelling of bolts should include the anchorage slip similar to [111].
- The incorporation of the projection operator with continuous function.
- The formulation, implementation and application of the continuous-discontinuous model similar to [146], but extended to three-dimensional problems.

Especially, the last issue seems a challenge in advanced numerical modelling of concrete.

## APPENDIX A

# LOCAL DAMAGE

### A.1 LOCAL DAMAGE – FORMULATION

The governing equations for the local damage theory at the material point level was summarized in Table 3.1 together with suitable boundary conditions. The weak form of motion equations (2.1) has the final form as in Eq. (3.21).

The interpolation of displacements  $\mathbf{u}$  is as follows:

$$\mathbf{u} = \mathbf{N} \mathbf{a} \quad (\text{A.1})$$

where  $\mathbf{N}$  contains suitable shape functions. Hence:

$$\boldsymbol{\epsilon} = \mathbf{B} \mathbf{a} \quad (\text{A.2})$$

where  $\mathbf{B} = \mathbf{L} \mathbf{N}$ . Therefore, the variations and time derivatives can be obtained:

$$\delta \mathbf{u} = \mathbf{N} \delta \mathbf{a} \quad \text{and} \quad \delta \boldsymbol{\epsilon} = \mathbf{B} \delta \mathbf{a} \quad (\text{A.3})$$

$$\dot{\boldsymbol{\epsilon}} = \mathbf{B} \dot{\mathbf{a}} \quad \text{and} \quad \ddot{\mathbf{u}} = \mathbf{N} \ddot{\mathbf{a}} \quad (\text{A.4})$$

If the above relations are introduced and assuming that the discretized equations of motion must hold for any admissible  $\delta \mathbf{a}$  the form like in Eq. (3.33) is obtained.

The increments of nodal displacements are considered from time  $t$  to time  $t + \Delta t$ :

$$\mathbf{a}^{t+\Delta t} = \mathbf{a}^t + \Delta \mathbf{a} \quad (\text{A.5})$$

Now, at the integration point the following relations are written:

$$\boldsymbol{\epsilon}^{t+\Delta t} = \boldsymbol{\epsilon}^t + \Delta \boldsymbol{\epsilon} \quad \tilde{\boldsymbol{\epsilon}}^{t+\Delta t} = \tilde{\boldsymbol{\epsilon}}^t + \Delta \tilde{\boldsymbol{\epsilon}} \quad \omega^{t+\Delta t} = \omega^t + \Delta \omega \quad (\text{A.6})$$

The stress update is:

$$\boldsymbol{\sigma}^{t+\Delta t} = \boldsymbol{\sigma}^t + \Delta \boldsymbol{\sigma} \quad (\text{A.7})$$

After that the equations of motion are represented like in Eq. (3.39). The constitutive equation in the incremental form can be derived:

$$\Delta \boldsymbol{\sigma} = (1 - \omega^t) \mathbf{E}^{\text{ep}} \Delta \boldsymbol{\epsilon} - \Delta \omega \hat{\boldsymbol{\sigma}}^t \quad (\text{A.8})$$

where:  $\hat{\boldsymbol{\sigma}}^t = \mathbf{E}^e (\boldsymbol{\epsilon}^e)^t$  and  $\Delta \omega = \left[ \frac{\partial \omega}{\partial \kappa^d} \right]^t \left[ \frac{\partial \kappa^d}{\partial \tilde{\epsilon}} \right]^t \Delta \tilde{\epsilon}$ . The following definitions are valid:

$$\Delta \boldsymbol{\epsilon} = \mathbf{B} \Delta \mathbf{a} \quad \text{and} \quad \Delta \tilde{\epsilon} = \left[ \frac{\partial \tilde{\epsilon}}{\partial \boldsymbol{\epsilon}} \right]^t \Delta \boldsymbol{\epsilon} \quad (\text{A.9})$$

If the notation from Eqs (2.48) and (2.49) is additionally adopted then the increment of damage can be written as:

$$\Delta \omega = \mathcal{L}^t [\mathbf{s}^T]^t \mathbf{B} \Delta \mathbf{a} \quad (\text{A.10})$$

and the increment of stresses as:

$$\Delta \boldsymbol{\sigma} = (1 - \omega^t) \mathbf{E}^{\text{ep}} \mathbf{B} \Delta \mathbf{a} - \mathcal{L}^t \mathbf{E}^e \boldsymbol{\epsilon}^t [\mathbf{s}^T]^t \mathbf{B} \Delta \mathbf{a} \quad (\text{A.11})$$

The discretized Eq. (3.33) in a matrix form reads:

$$\mathbf{K} \Delta \mathbf{a} + \mathbf{M} \ddot{\mathbf{a}}^{t+\Delta t} = \mathbf{f}_{\text{ext}}^{t+\Delta t} - \mathbf{f}_{\text{int}}^t \quad (\text{A.12})$$

The mass matrix  $\mathbf{M}$  is defined in a standard way, see Eq. (3.51). The force vectors are given in Eqs (3.49) and (3.50). The tangent operator is defined in the following way:

$$\mathbf{K} = \int_{\mathcal{B}} \mathbf{B}^T \left[ (1 - \omega^t) \mathbf{E}^{\text{ep}} - \mathcal{L}^t \mathbf{E}^e \boldsymbol{\epsilon}^t [\mathbf{s}^T]^t \right] \mathbf{B} dV \quad (\text{A.13})$$

## A.2 LOCALIZATION IN CANTILEVER BEAM

The aim of this example is a brief presentation of the test, for which results are spuriously mesh-sensitive. Now the cantilever beam considered previously in Section 5.1 is pulled upwards, so damage is expected at the bottom near the clamped edge. Two meshes are adopted, the coarse mesh as in Fig. A.2 (here deformation is also visible) and the fine mesh shown in Fig. 5.1. The data are identical to the ones used for the computations in Section 5.1, except Poisson's ratio  $\nu$  which equals now 0.2. The coupling with plasticity and the crack closure effect are omitted. For gradient damage the internal length parameter  $c$  is 4 mm<sup>2</sup>. The local damage theory is implemented according to the previous section, so here only the introduction of a material model subroutine for non-linear analysis is required in comparison to a standard FEM code.



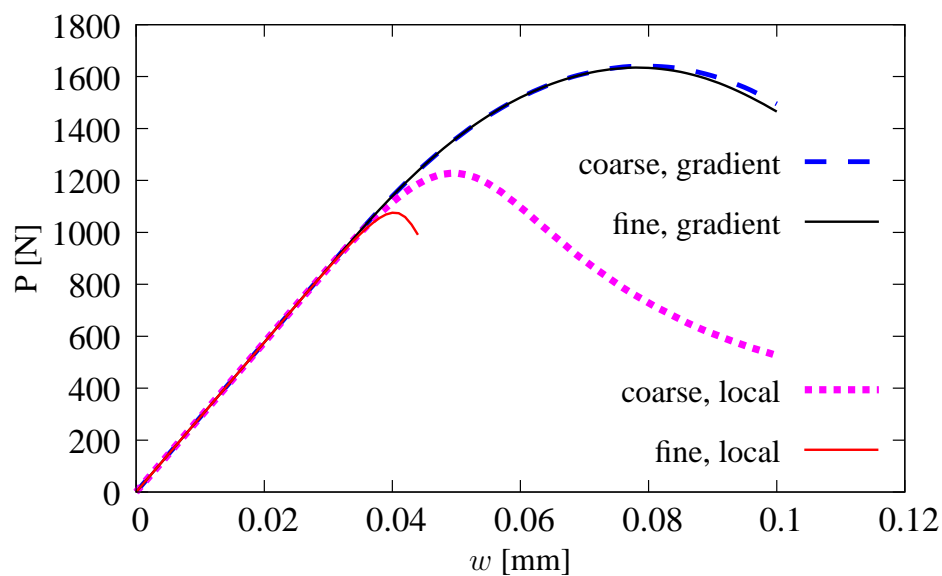


Figure A.1: Cantilever beam. Local vs gradient damage – load-displacement diagrams.

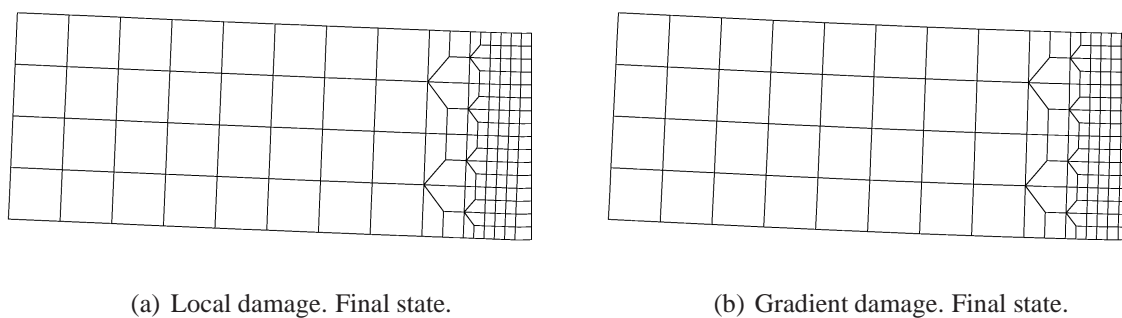
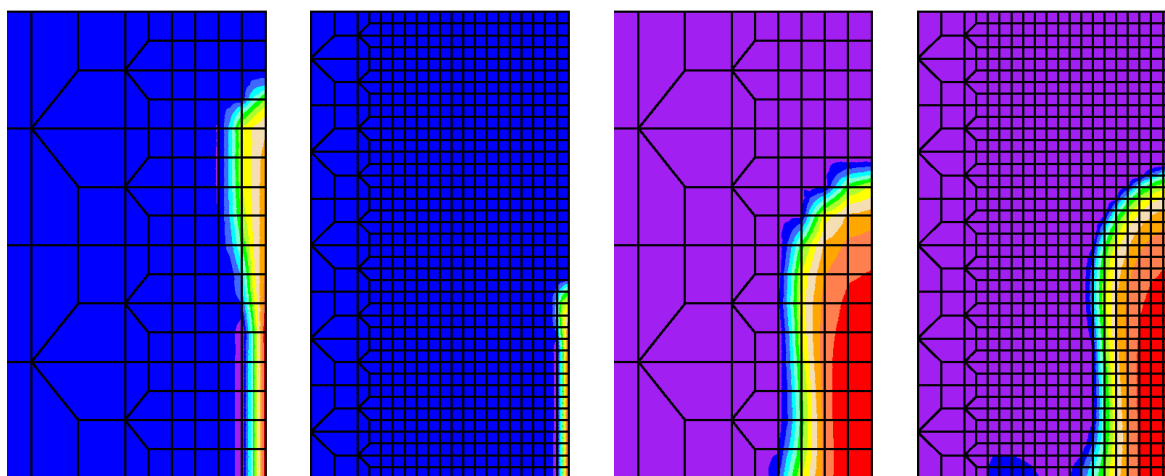


Figure A.2: Cantilever beam – deformation (100 times larger) for coarse mesh.



(a) Local damage, coarse. (b) Local damage, fine. (c) Gradient dam., coarse. (d) Gradient damage, fine.

Figure A.3: Part of cantilever near clamped edge. Contour plots for damage  $\omega$  in final state.

The results clearly illustrate the mesh-dependence for local damage and overcoming this problem by means of the gradient model. Indeed, in case of local damage the load-carrying capacity (see Fig. A.1) is different for both meshes and for the fine mesh the computations diverge just after the peak. Spurious mesh-sensitive results are also visible in the damage patterns in Figs A.3(a) and A.3(b).

## APPENDIX B

# PROPERTIES OF FOUR-NODED ELEMENT – SUPPLEMENT

### B.1 STABILIZATION OF AVERAGING EQUATION – DISCARDED PROPOSALS

#### B.1.1 GALERKIN LEAST-SQUARE (GLS) METHOD

The additional term  $R_2^{\text{stab}}$  for GLS method in the variational averaging equation has a general form as in Eq. (3.119).

The weighting part of  $R_2^{\text{stab}}$  in this method is:

$$\mathbf{P}_2(\delta\bar{\epsilon}) = \delta\bar{\epsilon} - c\nabla^2\delta\bar{\epsilon} \quad (\text{B.1})$$

Further,  $\mathbf{P}_2(\delta\bar{\epsilon})$  is changed into the discrete form:

$$\mathbf{P}_2(\delta e) = (\mathbf{h}^T - c\nabla^2\mathbf{h}^T) \delta e = \mathbf{G}_e^h \delta e \quad (\text{B.2})$$

The linearization of the residual part is introduced:

$$\mathbf{R}_{\bar{\epsilon},i+1} = \bar{\epsilon}_i + d\bar{\epsilon} - c\nabla^2(\bar{\epsilon}_i + d\bar{\epsilon}) - (\tilde{\epsilon}_i + d\tilde{\epsilon}) = \mathbf{R}_{\bar{\epsilon},i} + d\mathbf{R}_{\bar{\epsilon}} \quad (\text{B.3})$$

where  $\mathbf{R}_{\bar{\epsilon},i} = \bar{\epsilon}_i - c\nabla^2\bar{\epsilon}_i - \tilde{\epsilon}_i$ ,  $d\mathbf{R}_{\bar{\epsilon}} = d\bar{\epsilon} - c\nabla^2d\bar{\epsilon} - d\tilde{\epsilon}$ . The matrix  $\mathbf{G}_e^h$  can be applied after discretization. Additionally matrix  $\mathbf{G}_a^h = -[\mathbf{s}^T]^t \mathbf{B}$  is defined. Therefore:

$$d\mathbf{R}_{\bar{\epsilon}} = (\mathbf{h}^T - c\nabla^2\mathbf{h}^T) de - [\mathbf{s}^T]^t \mathbf{B} da = \mathbf{G}_e^h de + \mathbf{G}_a^h da \quad (\text{B.4})$$

and eventually the residual can be computed from the following relation:

$$\mathbf{R}_{\bar{\epsilon},i+1} = \mathbf{R}_{\bar{\epsilon},i} + \mathbf{G}_e^h de + \mathbf{G}_a^h da \quad (\text{B.5})$$

The stabilization term (3.119) is written using matrices:

$$R_2^{\text{stab}} = \sum_{e=1}^{n_{el}} \int_{\mathcal{B}^e} (\mathbf{G}_e^h \delta e)^T \chi_2 (\mathbf{R}_{\bar{\epsilon},i} + \mathbf{G}_a^h da + \mathbf{G}_e^h de) dV \quad (\text{B.6})$$

In addition to the matrices derived for the equilibrium equations, such new matrices should be defined for GLS method:

$$\bar{\mathbf{K}}_{ea} = \int_{\mathcal{B}^e} (\mathbf{G}_e^h)^T \chi_2 \mathbf{G}_a^h dV \quad (\text{B.7})$$

$$\bar{\mathbf{K}}_{ee} = \int_{\mathcal{B}^e} (\mathbf{G}_e^h)^T \chi_2 \mathbf{G}_e^h dV \quad (\text{B.8})$$

$$\bar{\mathbf{f}}_e = \int_{\mathcal{B}^e} (\mathbf{G}_e^e)^T \chi_2 (\mathbf{R}_{\bar{\epsilon},i}) dV \quad (\text{B.9})$$

Finally, the matrix equations are reformulated as:

$$\begin{bmatrix} \mathbf{K}_{aa} + \bar{\mathbf{K}}_{aa} & \mathbf{K}_{ae} + \bar{\mathbf{K}}_{ae} \\ \mathbf{K}_{ea} + \bar{\mathbf{K}}_{ea} & \mathbf{K}_{ee} + \bar{\mathbf{K}}_{ee} \end{bmatrix} \begin{bmatrix} d\mathbf{a} \\ d\mathbf{e} \end{bmatrix} = \begin{bmatrix} \mathbf{f}_{\text{ext}} - \mathbf{f}_{\text{int}} - \bar{\mathbf{f}} \\ \mathbf{f}_{\epsilon} - \mathbf{f}_e - \bar{\mathbf{f}}_e \end{bmatrix} \quad (\text{B.10})$$

### B.1.2 GRADIENT GALERKIN LEAST-SQUARE (GGLS) METHOD

Introducing gradients of continuous fields according to [63] the term  $R_2^{\text{stab}}$  is as in Eq. (3.121).

The weighting part of  $R_2^{\text{stab}}$  in GGLS method can be proposed as follows:

$$\mathbf{P}_2(\delta\bar{\epsilon}) = \nabla (\delta\bar{\epsilon} - c\nabla^2\delta\bar{\epsilon}) \quad (\text{B.11})$$

It is obvious that  $\nabla^3\bar{\epsilon}$  is equal to 0. Hence after discretization Eq. (B.11) is reduced to:

$$\mathbf{P}_2(\delta e) = \mathbf{g}^T \delta e \quad (\text{B.12})$$

The residual part of  $R_2^{\text{stab}}$  can be linearized starting from:

$$\mathbf{R}_{\bar{\epsilon},i+1} = \nabla\bar{\epsilon}_i + \nabla d\bar{\epsilon} - c\nabla^3(\bar{\epsilon}_i + d\bar{\epsilon}) - \nabla(\bar{\epsilon}_i + d\bar{\epsilon}) = \mathbf{R}_{\bar{\epsilon},i} + d\mathbf{R}_{\bar{\epsilon}} \quad (\text{B.13})$$

Next the following notation is applied:  $\mathbf{R}_{\bar{\epsilon},i} = \nabla\bar{\epsilon}_i - c\nabla^3\bar{\epsilon}_i - \nabla\bar{\epsilon}_i$ ,  $d\mathbf{R}_{\bar{\epsilon}} = \nabla d\bar{\epsilon} - c\nabla^3 d\bar{\epsilon} - \nabla d\bar{\epsilon}$ . As previously  $\nabla^3\bar{\epsilon}$  is equal to 0. Therefore, matrix  $\mathbf{G}_a^h$  is now determined by the relation:

$$\mathbf{G}_a^h = -[\nabla \mathbf{s}^T]^t \mathbf{B} \quad (\text{B.14})$$

Further,  $d\mathbf{R}_{\bar{\epsilon}}$  is:

$$d\mathbf{R}_{\bar{\epsilon}} = \mathbf{g}^T d\mathbf{e} - [\nabla \mathbf{s}^T]^t \mathbf{B} d\mathbf{a} = \mathbf{g}^T d\mathbf{e} + \mathbf{G}_a^h d\mathbf{a} \quad (\text{B.15})$$

The final form of the residual part is characterized as follows:

$$\mathbf{R}_{\bar{\epsilon},i+1} = \mathbf{R}_{\bar{\epsilon},i} + \mathbf{g}^T d\mathbf{e} + \mathbf{G}_a^h d\mathbf{a} \quad (\text{B.16})$$

The term (3.121) after discretization and linearization can be presented in this manner:

$$R_2^{\text{stab}} = \sum_{e=1}^{n_{el}} \int_{\mathcal{B}^e} (\mathbf{g}^T \delta e)^T \chi_2 (\mathbf{R}_{\bar{\epsilon},i} + \mathbf{G}_a^h d\mathbf{a} + \mathbf{g}^T d\mathbf{e}) dV \quad (\text{B.17})$$

Introducing the following definitions for this method:

$$\bar{\mathbf{K}}_{ea} = \int_{B^e} \mathbf{g} \chi_2 \mathbf{G}_a^h dV \quad (\text{B.18})$$

$$\bar{\mathbf{K}}_{ee} = \int_{B^e} \mathbf{g} \chi_2 \mathbf{g}^T dV \quad (\text{B.19})$$

$$\bar{\mathbf{f}}_e = \int_{B^e} \mathbf{g} \chi_2 (\mathbf{R}_{\bar{\epsilon},i}) dV \quad (\text{B.20})$$

the matrix formulation has the form:

$$\begin{bmatrix} \mathbf{K}_{aa} + \bar{\mathbf{K}}_{aa} & \mathbf{K}_{ae} + \bar{\mathbf{K}}_{ae} \\ \mathbf{K}_{ea} + \bar{\mathbf{K}}_{ea} & \mathbf{K}_{ee} + \bar{\mathbf{K}}_{ee} \end{bmatrix} \begin{bmatrix} d\mathbf{a} \\ d\mathbf{e} \end{bmatrix} = \begin{bmatrix} \mathbf{f}_{\text{ext}} - \mathbf{f}_{\text{int}} - \bar{\mathbf{f}} \\ \mathbf{f}_\epsilon - \mathbf{f}_e - \bar{\mathbf{f}}_e \end{bmatrix} \quad (\text{B.21})$$

## B.2 SPECTRAL ANALYSIS FOR STABILIZED ELEMENT

### – SUPPLEMENT

Both proposals derived in the previous section do not result in stabilization. The spectral analysis of a single FE confirms that hourglass control, for which GLS or GGLS method is applied in formulation of the averaging equation, does not behave properly. One spurious zero eigenvalue of submatrix  $\mathbf{K}_{ee}$  corresponds to a twisted eigenmode for the averaged strain field (see the figures below), apart from the damage phase in Fig. B.5, where four combinations of rigid motions of the element are observed instead of the correct three. The eigenforms are shown in specific manner, which is explained at the beginning of Section 3.4.

Table B.1: Eigenvalues for Q4/4, improper stabilization of averaging equation,  $\chi = 0.0001$ ,  $c = 1$ .

(a) RI and GLS stabilization, Eq. (B.10).							(b) RI and GGLS stabilization, Eq. (B.21).												
	Elasticity			Damage			Unloading				Elasticity			Damage			Unloading		
s. eigs	+	0	-	+	0	-	+	0	-	s. eigs	+	0	-	+	0	-	+	0	-
$\mathbf{K}_{aa} + \bar{\mathbf{K}}_{aa}$	5	3	0	5	3	0	5	3	0	$\mathbf{K}_{aa} + \bar{\mathbf{K}}_{aa}$	5	3	0	5	3	0	5	3	0
$\mathbf{K}_{ee} + \bar{\mathbf{K}}_{ee}$	3	1	0	3	1	0	3	1	0	$\mathbf{K}_{ee} + \bar{\mathbf{K}}_{ee}$	3	1	0	3	1	0	3	1	0
$\mathbf{K} + \bar{\mathbf{K}}$	8	4	0	7	4	1	8	4	0	$\mathbf{K} + \bar{\mathbf{K}}$	8	4	0	7	4	1	8	4	0

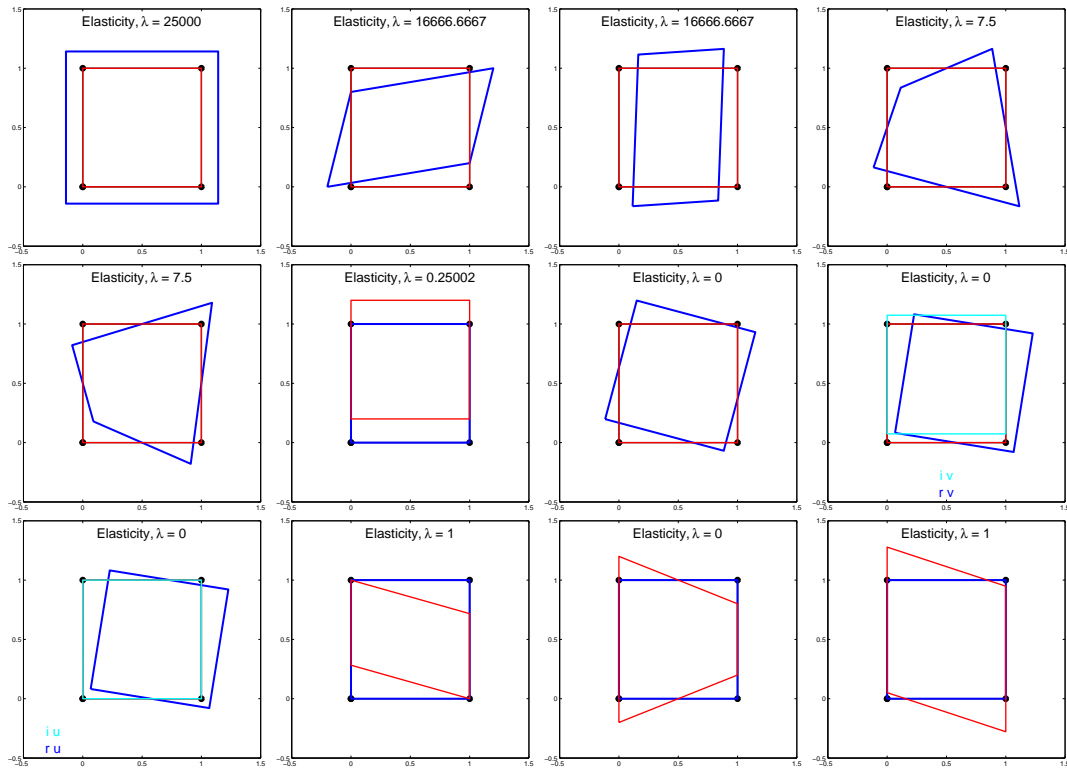


Figure B.1: Eigenforms for Q4/4, RI and GLS according to Eq. (B.10),  $\chi = 0.0001$ ,  $c = 1$ , elastic phase.

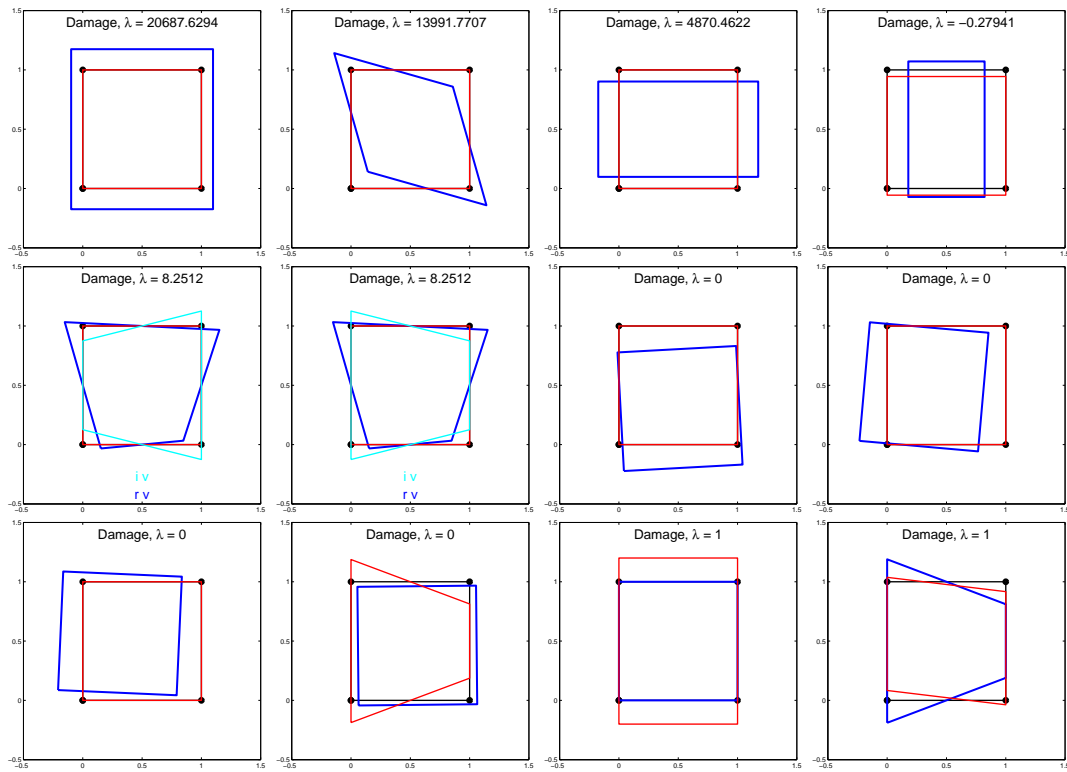


Figure B.2: Eigenforms for Q4/4, RI and GLS according to Eq. (B.10),  $\chi = 0.0001$ ,  $c = 1$ , damage phase.

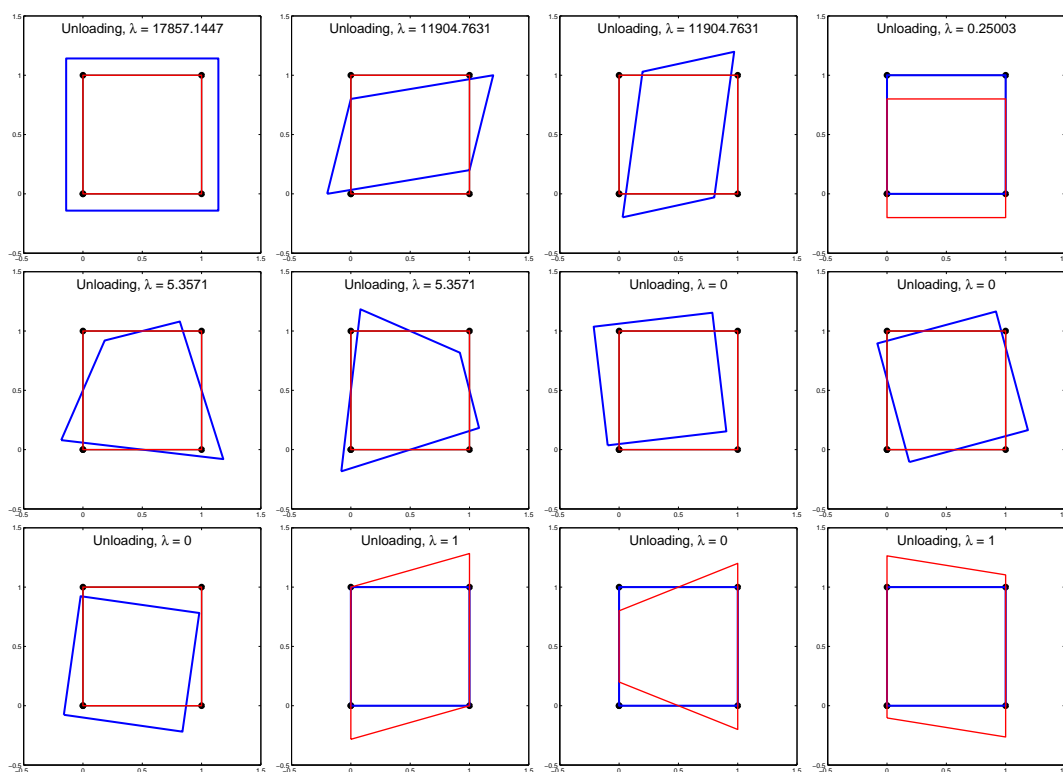


Figure B.3: Eigenforms for Q4/4, RI and GLS according to Eq. (B.10),  $\chi = 0.0001$ ,  $c = 1$ , unloading.

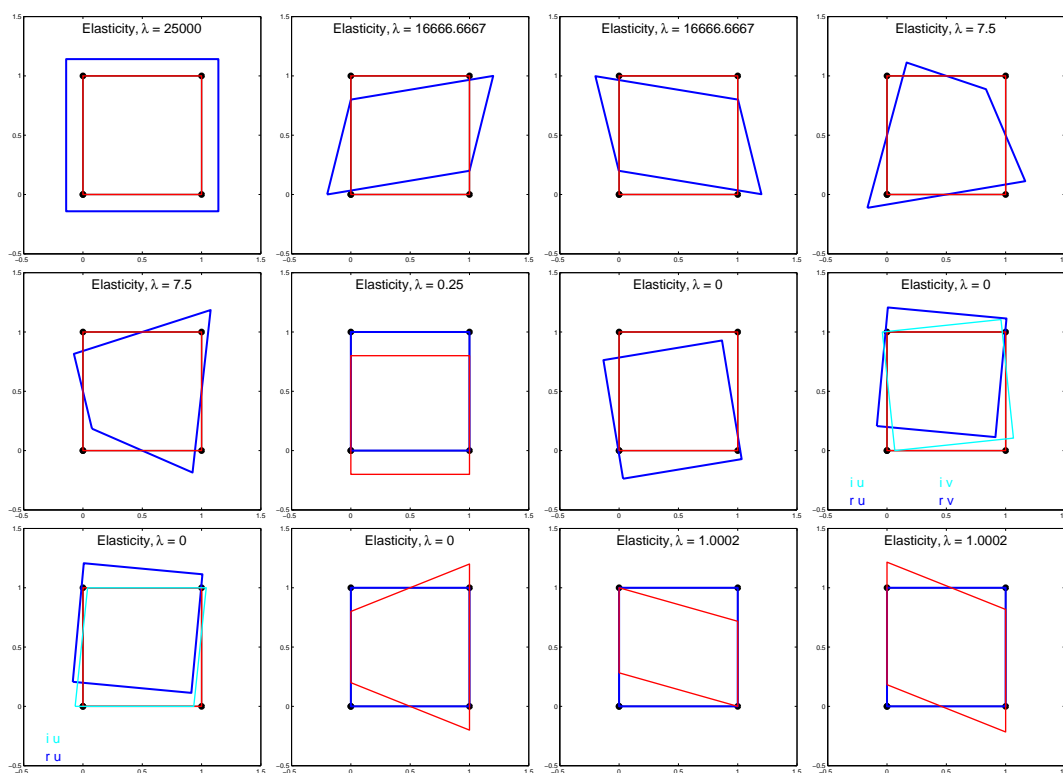


Figure B.4: Eigenforms for Q4/4, RI and GGLS according to Eq. (B.21),  $\chi = 0.0001$ ,  $c = 1$ , elastic phase.

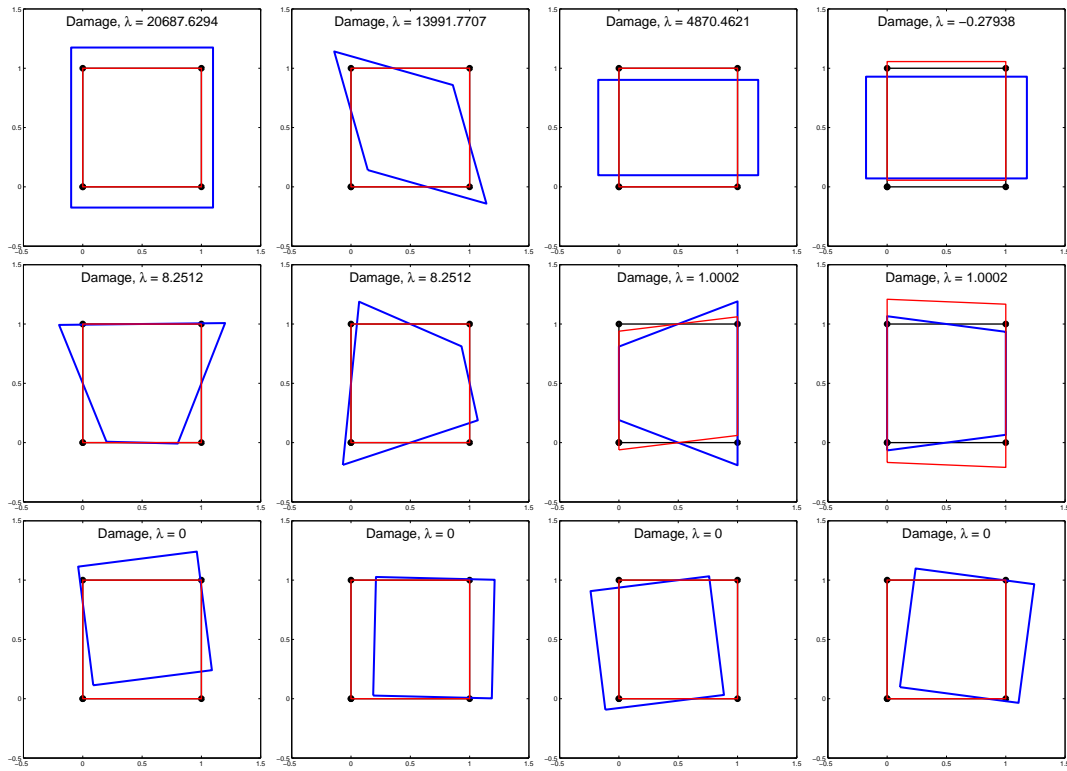


Figure B.5: Eigenforms for Q4/4, RI and GGLS according to Eq. (B.21),  $\chi = 0.0001$ ,  $c = 1$ , damage phase.

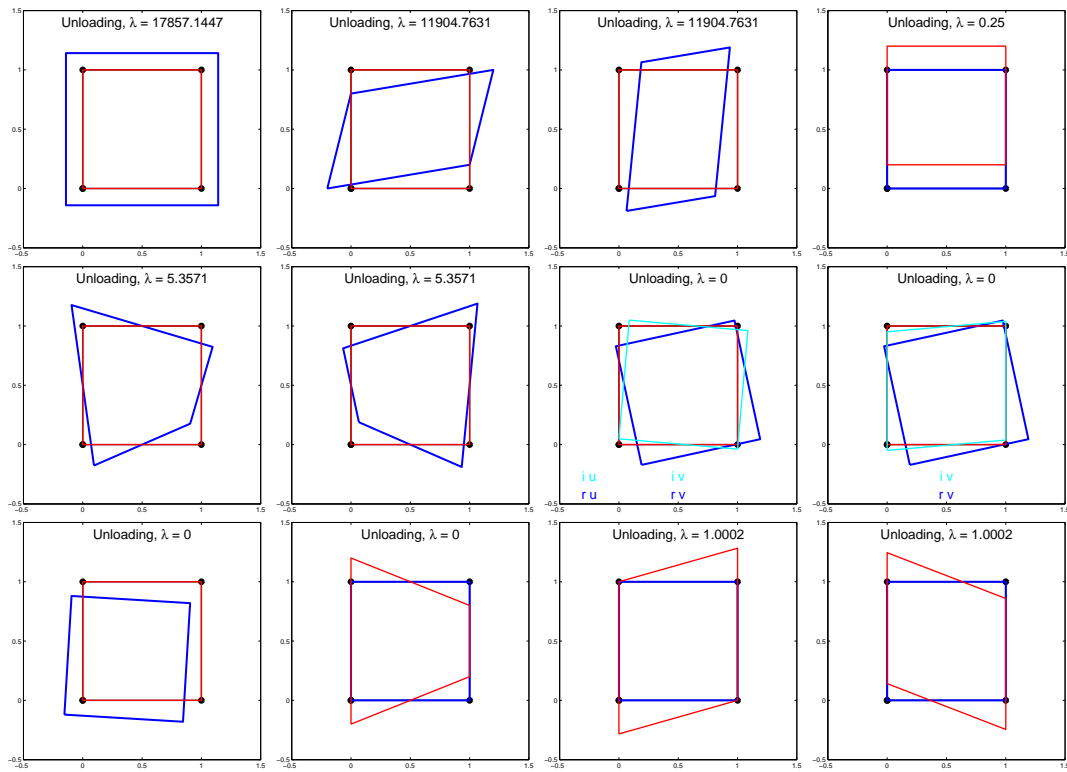


Figure B.6: Eigenforms for Q4/4, RI and GGLS according to Eq. (B.21),  $\chi = 0.0001$ ,  $c = 1$ , unloading.



## APPENDIX C

# DOWEL DISC TEST

The dowel disc test can be treated as an introduction into the full three-dimensional analysis of dowel action, which was presented in Section 5.4. Now meshes A and B are three-dimensional slices of finite elements and half of the specimen is considered. The structure of both meshes in plane is like for the dowel bar test. Boundary conditions are the following: the symmetry plane is assumed, at the bottom all horizontal and vertical displacements are zero, additionally at the corner on the right one displacement perpendicular to the front plane is restrained. The load acts upwards at the axis of the rebar. The deformation control is used. The cover thickness is equal to the diameter of the rebar, identically to the analysis in Section 5.4. Apart from the rebar, the concrete matrix and the interphase are distinguished in the material structure. The material data given in Table C.1 come from [50]. They are almost the same as for the dowel bar test, but now

Table C.1: Material model data for dowel disc.

<p>CONCRETE: damaging            Young's modulus: <math>E_c = 34000</math> MPa            Poisson's ratio: <math>\nu = 0.2</math>            Tensile strength: <math>f_t = 3.5</math> MPa            Equivalent strain measure:            modified von Mises definition, <math>k = 13.143</math>            Damage growth function:            exponential softening  <math>\alpha = 0.98</math> <math>\eta = 550</math>            Fracture energy: <math>G_f = 0.11</math>N/mm            Internal length scale:  <math>l = 2\sqrt{2}</math> mm, i.e. <math>c = 4.0</math>            Threshold: <math>\kappa_o = 10.225 \times 10^{-5}</math></p>	<p>INTERPHASE: damaging            Young's modulus: <math>E_c^* = 17000</math> MPa            Poisson's ratio: <math>\nu = 0.2</math>            Tensile strength: <math>f_t^* = 2.8</math> MPa            Equivalent strain measure:            modified von Mises definition, <math>k = 13.143</math>            Damage growth function:            exponential softening  <math>\alpha = 0.98</math> <math>\eta = 450</math>            Fracture energy: <math>G_f = 0.11</math>N/mm            Internal length scale:  <math>l = 2\sqrt{2}</math> mm, i.e. <math>c = 4.0</math>            Threshold: <math>\kappa_o = 16.471 \times 10^{-5}</math></p>
<p>REINFORCEMENT (STEEL): elastic            Young's modulus: <math>E_s = 206000</math> MPa      Poisson's ratio: <math>\nu = 0.3</math></p>	

three different cases are taken into account. The basic case is pure gradient damage with the modified von Mises definition (2.15) as the loading function. The first modification is only the change of the loading function to the Mazars definition, see Eq. (2.12). The model coupled with linear hardening plasticity is an alternative modification. If the weak coupling is activated, the following data for the BDP plasticity are assumed: hardening modulus  $h = E_c/2$ , friction and dilatancy coefficients  $\sin \varphi = \sin \psi = 0.5$  and two different yield strengths equal to  $f_t$  and  $f_t^*$  for the concrete matrix and for the interphase, respectively (cf. Table C.1).

The results are confronted with the experimental ones obtained in [50]. The load value at the center of the reinforcement is plotted against the vertical displacement at this point. Additionally damage and averaged strain contour plots for the final stage are depicted in each case.

It is difficult to say which computed case fits the experiment the best. The load-displacement diagrams in Fig. C.1 for the coupled model seem to be the closest, but the load peak is evidently different. On the other hand if pure damage with the modified von Mises definition is employed, the value of the peak load is about 5 kN like for the experiment, but the softening path is quite different. If the Mazars definition is adopted, the results are questionable. The load-displacement diagrams for both meshes exhibit a too high peak and further a too steep slope of the softening path is observed. It is confirmed also in Figs C.2(a) and C.3(a) for damage and in Figs C.4(a) and C.5(a) for averaged strain distributions. These crack patterns show that the spalled cover is too small and the angle of the crack front is too large in comparison to the experimental patterns presented in [50]. Hence this loading function is rather improper in this test. The distributions are closer to the experimental patterns if the modified von Mises definition is assumed. For both the pure and coupled models contour plots resemble the crack patterns presented in [50].

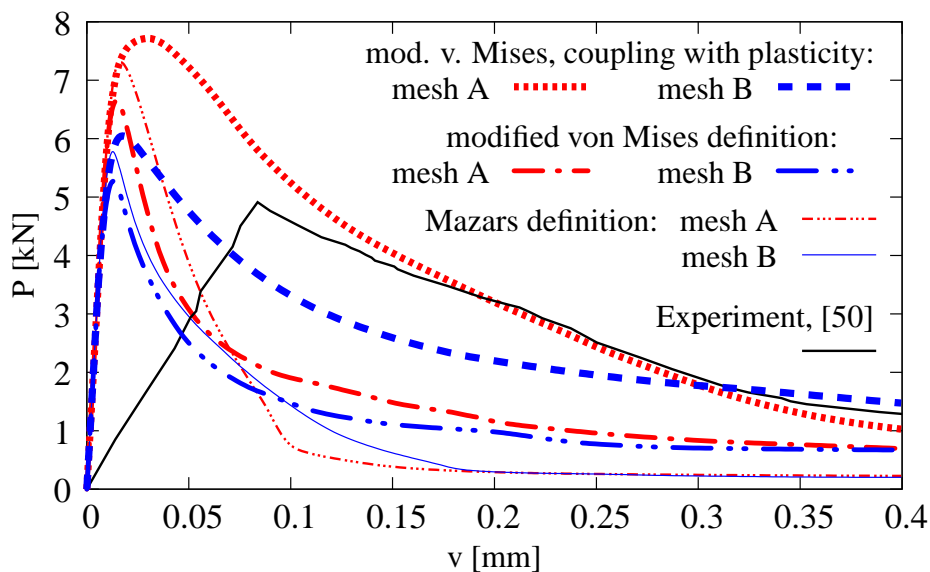


Figure C.1: Dowel disc test – load-displacement diagrams.

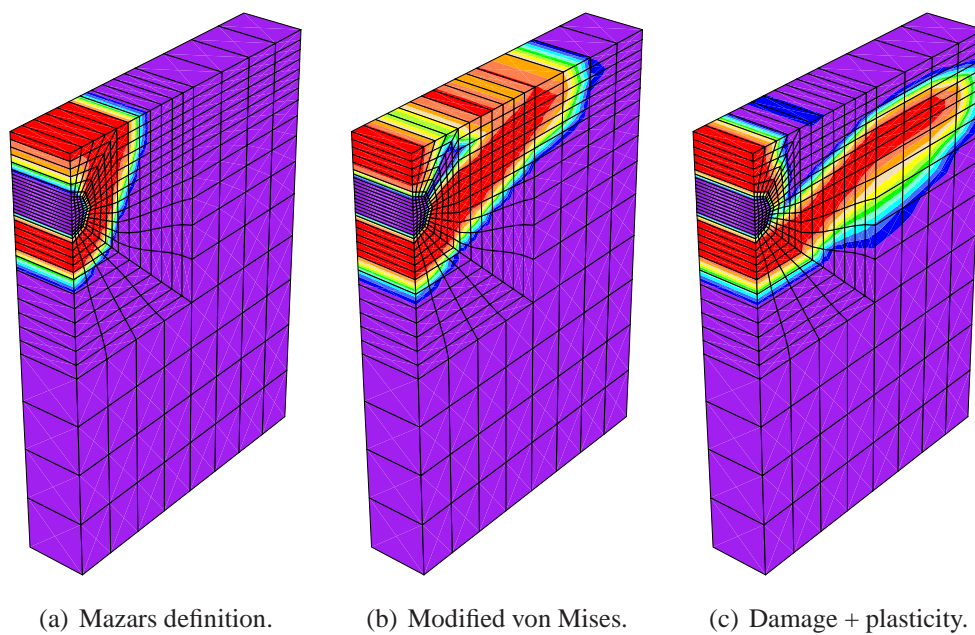


Figure C.2: Dowel disc test. Final damage distribution for mesh A ( $v = 0.4$  mm).

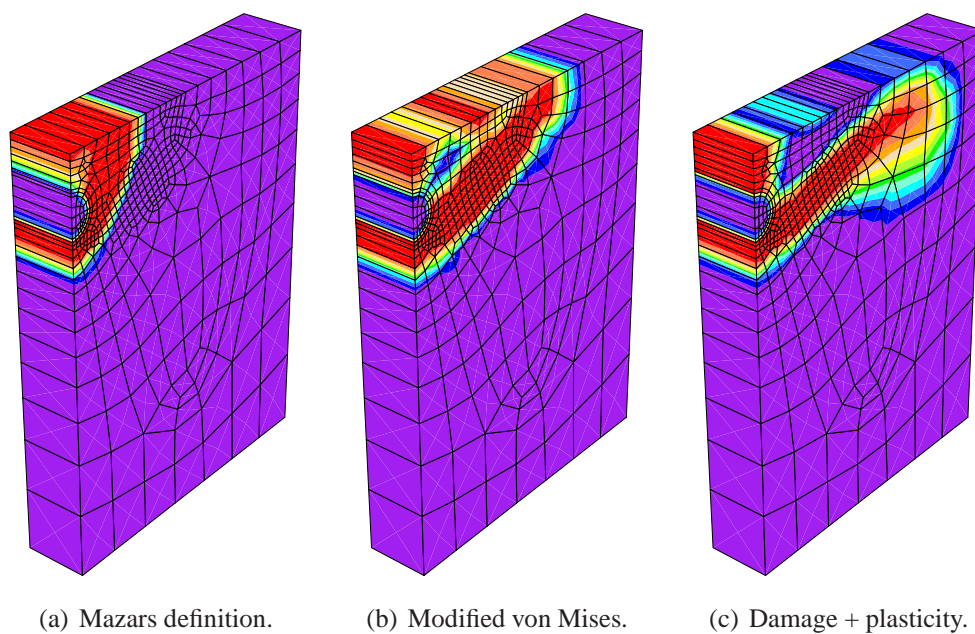


Figure C.3: Dowel disc test. Final damage distribution for mesh B ( $v = 0.4$  mm).

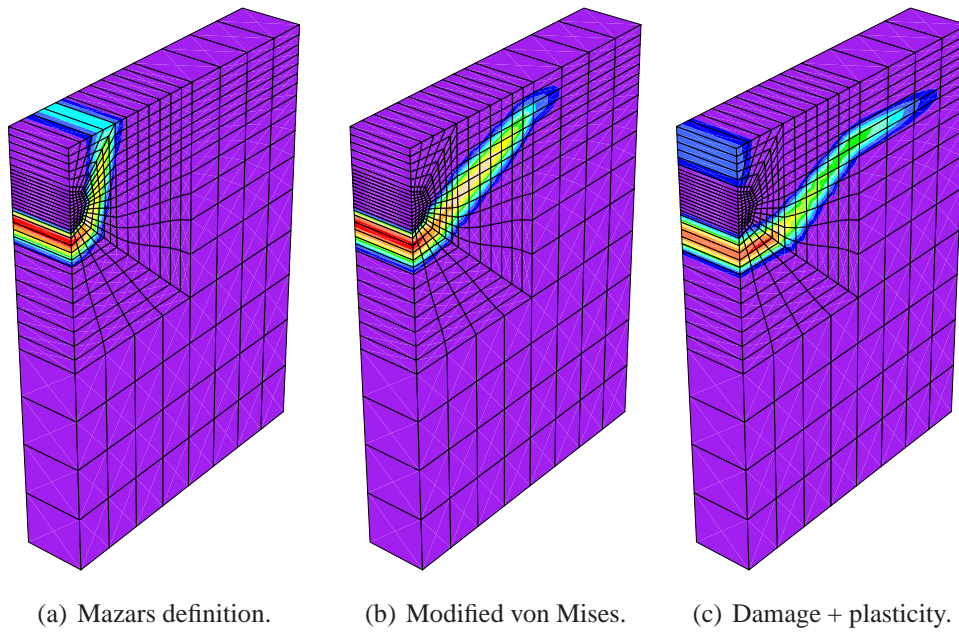


Figure C.4: Dowel disc test. Final averaged strain distribution for mesh A ( $v = 0.4$  mm).

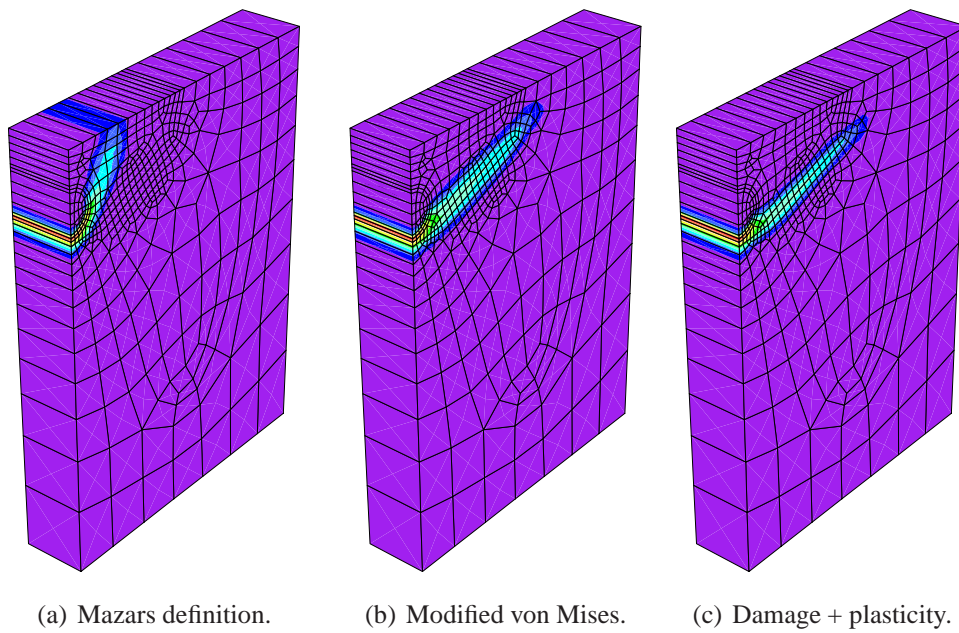


Figure C.5: Dowel disc test. Final averaged strain distribution for mesh B ( $v = 0.4$  mm).

# LIST OF FIGURES

1.1	Concept of damage. . . . .	2
1.2	Degradation process in quasi-brittle materials. Based on [56]. . . . .	3
1.3	Discontinuity surface (curve in 2D). Definition of unit vectors $\boldsymbol{\nu}$ and $\boldsymbol{\mu}$ . . . . .	5
1.4	Discontinuity – displacement and strain distribution in one dimension. . . . .	7
1.5	Fracture energy for discrete and smeared crack. . . . .	8
1.6	Classification of models mentioned in the review. . . . .	10
2.1	Idea of strain equivalence. . . . .	14
2.2	Scheme of scalar damage model. . . . .	14
2.3	EER definition of $\tilde{\epsilon}$ (2.11) in strain space. . . . .	16
2.4	Mazars definition of $\tilde{\epsilon}$ (2.12) in strain space. . . . .	17
2.5	Modified von Mises definition of $\tilde{\epsilon}$ (2.15) in strain space, 2D problems. . . . .	18
2.6	Modified von Mises definition (2.15) in strain space for 3D problems, $\tilde{\epsilon} = 1.0$ . . . . .	19
2.7	Loading functions in 2D strain space. . . . .	20
2.8	Damage growth functions. . . . .	21
2.9	Schemes for damage coupled to hardening plasticity. . . . .	25
2.10	Damage, plasticity and coupled models. . . . .	25
2.11	Stiffness change in crack closure phenomenon (without irreversible strains). . . . .	27
2.12	Incorporation of crack closing into scalar damage. . . . .	31
2.13	Incorporation of crack closing into coupled model. . . . .	32
2.14	Influence of ultimate $\kappa_u$ in linear softening for isotropic model. . . . .	36
2.15	Influence of ductility parameter $\eta_i$ ( $i = K, G$ ) in exponential softening for isotropic model. . . . .	37
2.16	Influence of predefining damage growth functions with different character. . . . .	37
2.17	Sensitivity of Poisson’s ratio $\nu_\omega$ to adopted damage growth functions. . . . .	38
2.18	Sensitivity of dilatation $\theta$ to adopted damage growth functions. . . . .	39
2.19	Willam’s test – prescribed displacements for the corresponding strain state. . . . .	41
2.20	Willam’s test – strain evolution. . . . .	42
2.21	Willam’s test – influence of assumed loading functions. . . . .	44
2.22	Willam’s test – comparison of stress components for different loading functions. . . . .	45
2.23	Willam’s test – evolution of principal stresses for different loading functions. . . . .	46

2.24	Willam's test – results for pure damage and coupled to plasticity. . . . .	47
2.25	Willam's test – comparison of stress components in coupled models. . . . .	48
2.26	Willam's test – evolution of principal stresses for different kinds of scalar model. . . . .	48
2.27	Willam's test – differences between pure and coupled models. . . . .	49
2.28	Willam's test – influence of ductility parameter $\eta_i$ ( $i = K, G$ ) in isotropic model. . . . .	51
2.29	Willam's test – comparison of stress components in isotropic model. . . . .	52
2.30	Willam's test – evolution of principal stresses for isotropic model, $\alpha = 1.0$ . . . . .	53
2.31	Willam's test – evolution of principal stresses for isotropic model, $\alpha = 0.97$ . . . . .	53
2.32	Willam's test – sensitivity of Poisson's ratio $\nu_\omega$ in isotropic model. . . . .	54
3.1	Two consequences of using higher-order gradients. Based on [5]. . . . .	58
3.2	Loading-unloading path used in spectral analysis. . . . .	72
3.3	Eigenforms for Q4/4, FI, $c = 1$ , elastic phase. . . . .	75
3.4	Eigenforms for Q4/4, FI, $c = 1$ , damage phase. . . . .	75
3.5	Eigenforms for Q4/4, FI, $c = 1$ , unloading. . . . .	76
3.6	Eigenforms for Q4/4, RI, $c = 1$ , elastic phase. . . . .	76
3.7	Eigenforms for Q4/4, RI, $c = 1$ , damage phase. . . . .	77
3.8	Eigenforms for Q4/4, RI, $c = 1$ , unloading. . . . .	77
3.9	Eigenforms for Q4/4, RI, $c = 0$ , elastic phase. . . . .	79
3.10	Eigenforms for Q4/4, RI, $c = 0$ , damage phase. . . . .	79
3.11	Eigenforms for Q4/4, RI, $c = 0$ , unloading. . . . .	80
3.12	Eigenforms for Q4/4, RI with stabilization according to Eq. (3.117), $c = 1$ , $\chi = 0.0001$ , elastic phase. . . . .	86
3.13	Eigenforms for Q4/4, RI with stabilization according to Eq. (3.117), $c = 1$ , $\chi = 0.0001$ , damage phase. . . . .	86
3.14	Eigenforms for Q4/4, RI with stabilization according to Eq. (3.117), $c = 1$ , $\chi = 0.0001$ , unloading. . . . .	87
3.15	Eigenforms for Q4/4, RI with stabilization according to Eq. (3.133), $c = 1$ , $\chi = 0.0001$ , elastic phase. . . . .	87
3.16	Eigenforms for Q4/4, RI with stabilization according to Eq. (3.133), $c = 1$ , $\chi = 0.0001$ , damage phase. . . . .	88
3.17	Eigenforms for Q4/4, RI with stabilization according to Eq. (3.133), $c = 1$ , $\chi = 0.0001$ , unloading. . . . .	88
4.1	Bar with imperfection for localization test in tension. . . . .	94
4.2	Tensile bar with imperfection in 1D. Stress-displacement diagrams for different numbers of elements. . . . .	95
4.3	Tensile bar with imperfection in 1D. Results for different numbers of elements – mesh-independence. . . . .	95

4.4	Tensile bar with imperfection in 1D. Stress-displacement diagrams for different values of internal length parameter. . . . .	96
4.5	Tensile bar with imperfection in 1D – internal length influence. . . . .	97
4.6	Tensile bar with imperfection in 1D – different damage growth. . . . .	98
4.7	Tensile bar with imperfection in 1D – stress-displacement diagrams for gradient damage and hardening plasticity. . . . .	99
4.8	Pure gradient damage – evolution of chosen variables. . . . .	99
4.9	Weak coupling of gradient damage and plasticity – evolution of chosen variables. . . . .	100
4.10	Strong coupling of gradient damage and plasticity – evolution of chosen variables. . . . .	100
4.11	Tensile bar with imperfection in 2D. Stress-displacement diagrams - different types of integration in FE Q4. . . . .	101
4.12	Results for bar with imperfection – elements Q4 with FI. . . . .	102
4.13	Results for bar with imperfection – elements Q4 with RI and stabilization according to Eq. (3.133), $\chi = 0.000001$ . . . . .	102
4.14	Tensile bar with imperfection (2D). Isotropic gradient damage. Load-displacement diagrams – different types of equivalent strain measure. . . . .	104
4.15	Tensile bar with imperfection (2D). Isotropic gradient damage. Damage distribution along the bar in final state. . . . .	106
4.16	Tensile bar with imperfection (2D). Isotropic gradient damage. Deformation and strain state. . . . .	106
4.17	Bar with imperfection (2D). Isotropic gradient damage. Poisson's ratio evolution. . . . .	107
4.18	Tensile bar with imperfection in 3D. Load-displacement diagrams. . . . .	108
4.19	Results for bar with imperfection. 3D elements, damage – final distribution. . . . .	109
4.20	Results for the bar under one-dimensional dynamic tension. . . . .	110
4.21	Dynamic direct tension test. . . . .	112
4.22	Elongation history for plain vs reinforced concrete. . . . .	112
4.23	Internal length influence for plain and reinforced concrete bar. . . . .	113
4.24	Sensitivity of results to load intensity and reinforcement ratio. . . . .	114
5.1	Cantilever beam under load reversals together with FE mesh. . . . .	115
5.2	Cantilever beam under load reversals – load-displacement diagrams. . . . .	116
5.3	Cantilever beam under load reversals – evolution of stress $\sigma_{11}$ along line A-A. . . . .	118
5.4	Cantilever beam, load reversals – evolution of stress $\sigma_{11}$ , line A-A (continued). . . . .	119
5.5	Part of cantilever near clamped edge. Damage coupled to plasticity and crack closing – contour plots for maximum upward displacement $w$ . . . . .	120
5.6	Part of cantilever near clamped edge. Damage coupled to plasticity and crack closing – contour plots for maximum downward displacement $w$ . . . . .	120
5.7	Idea of Brazilian split test. Subfigures (b), (c) and (d) quoted from [137]. . . . .	121
5.8	Exemplary meshes for Brazilian test. . . . .	121

5.9	Load-displacement diagrams for used meshes in Brazilian test – summary. . . . .	123
5.10	Load-displacement diagrams for coarse, medium and fine meshes in Brazilian test. . . . .	124
5.11	Brazilian test. Contour plots for mesh C12. . . . .	124
5.12	Brazilian test. Contour plots for mesh M20. . . . .	125
5.13	Brazilian test. Contour plots for mesh F24. . . . .	125
5.14	Brazilian test. Influence of internal length scale – diagrams. . . . .	126
5.15	Brazilian test. Influence of internal length scale – contour plots. . . . .	126
5.16	Brazilian test. Influence of platen definition – diagrams. . . . .	127
5.17	Brazilian test. Influence of platen – contour plots (M20/M20wp). . . . .	127
5.18	Brazilian test. Influence of ductility parameter $\eta_i$ ( $i = K, G$ ) in isotropic model – load-displacement diagrams. . . . .	129
5.19	Brazilian test. Contour plots of averaged strain $\bar{\epsilon}$ for isotropic model. . . . .	129
5.20	Contour plots of strain invariants for isotropic model in Brazilian test. . . . .	130
5.21	Damage patterns for isotropic model in Brazilian test. . . . .	131
5.22	Change of Poisson’s ratio $\nu_w$ for isotropic model in Brazilian test. . . . .	131
5.23	RC beam in four point bending. . . . .	133
5.24	Diagrams for plain concrete beam. . . . .	134
5.25	Load-deflection diagrams – influence of meshes and integration types. . . . .	134
5.26	Averaged strain distribution for plain concrete beam. . . . .	135
5.27	Deformation for plain concrete beam. . . . .	135
5.28	Comparison of load–deflection diagrams for RC beam. . . . .	136
5.29	Averaged strain – comparison of results for different ductility parameter $\eta$ . . . . .	138
5.30	Deformation patterns for two values of $\eta$ . . . . .	138
5.31	Averaged strain for larger $l = 96$ mm. . . . .	138
5.32	Damage – influence of compressive strength to tensile strength ratio. . . . .	138
5.33	Averaged and equivalent plastic strain for damage coupled to plasticity with $\sigma_y = f_t$ . . . . .	139
5.34	Averaged strain for reinforcement ratio multiplied by 4, final state. . . . .	139
5.35	Deflection, velocity and acceleration history diagrams. . . . .	140
5.36	Averaged strain and deformation for three different meshes ( $t = 0.00625$ s, beam with original reinforcement). . . . .	141
5.37	Averaged strain and deformation for three different meshes ( $t = 0.00625$ s, beam with stronger reinforcement). . . . .	141
5.38	Dowel bar test – from experiment in [41]. . . . .	143
5.39	Dowel bar test – numerical definition of problem. . . . .	143
5.40	Dowel bar test – applied meshes. . . . .	144
5.41	Dowel bar test – load-displacement diagrams. . . . .	145
5.42	Dowel bar test. Final contour plots for case 1 ( $v = 1.0$ mm). . . . .	146



5.43	Dowel bar test. Final contour plots for case 2. . . . .	147
5.44	Dowel bar test. Crack pattern evolution for concrete FRB1 in experiment [41], front and top view. . . . .	148
5.45	Dowel bar test. Development of damage parameter, mesh B, case 2. . . . .	148
5.46	RC slab-column connection. Bolt installed to prevent punching shear failure in existing slabs. Photo quoted from [1]. . . . .	150
5.47	RC slab-column connection. Final crack patterns for slabs SB1 and SB4, visible from the tension side. Photos quoted from [1]. . . . .	151
5.48	RC slab-column connection. Simulated specimen. . . . .	152
5.49	RC slab-column connection. Load-displacement diagrams, experiment versus simulation. . . . .	154
5.50	RC slab-column connection, SB4. Contour plots of averaged strain for gradient damage-plasticity, $l = 20$ mm. . . . .	155
5.51	RC slab-column connection, SB1. Load-displacement diagrams, influence of internal length scale, gradient damage (without plasticity). . . . .	156
5.52	RC slab-column connection, SB1. Deformation (magnification factor is 10) of slab for two different meshes, gradient damage, $l = 4$ mm. . . . .	156
5.53	RC slab-column connection, SB1. Contour plots of averaged strain for coarse mesh, gradient damage, $l = 4$ mm. . . . .	157
5.54	RC slab-column connection, SB1. Contour plots of averaged strain for denser mesh, gradient damage, $l = 4$ mm. . . . .	157
5.55	RC slab-column connection, SB1. Contour plots of averaged strain for denser mesh, gradient damage, $l = 8$ mm. . . . .	158
5.56	RC slab-column connection, SB1. Load-displacement diagrams, denser mesh, $l = 4$ mm. . . . .	159
5.57	RC slab-column connection, SB1. Load-displacement diagrams obtained for isotropic model, $l = 4$ mm. . . . .	159
5.58	RC slab-column connection, SB1. Contour plots of averaged strain for isotropic gradient damage, case <i>exp,G</i> , $l = 4$ mm. . . . .	160
5.59	RC slab-column connection, SB1. Load-displacement diagrams obtained using DIANA package. . . . .	160
5.60	RC slab-column connection, SB1. Contour plots of equivalent strain for fixed crack model, final state. . . . .	161
5.61	RC slab-column connection, SB1. Contour plots of equivalent strain for total crack model, final state. . . . .	162
A.1	Cantilever beam. Local vs gradient damage – load-displacement diagrams. . . .	171
A.2	Cantilever beam – deformation (100 times larger) for coarse mesh. . . . .	171
A.3	Part of cantilever near clamped edge. Contour plots for damage $\omega$ in final state. . . .	171

B.1	Eigenforms for Q4/4, RI and GLS according to Eq. (B.10), $\chi = 0.0001$ , $c = 1$ , elastic phase. . . . .	176
B.2	Eigenforms for Q4/4, RI and GLS according to Eq. (B.10), $\chi = 0.0001$ , $c = 1$ , damage phase. . . . .	176
B.3	Eigenforms for Q4/4, RI and GLS according to Eq. (B.10), $\chi = 0.0001$ , $c = 1$ , unloading. . . . .	177
B.4	Eigenforms for Q4/4, RI and GGLS according to Eq. (B.21), $\chi = 0.0001$ , $c = 1$ , elastic phase. . . . .	177
B.5	Eigenforms for Q4/4, RI and GGLS according to Eq. (B.21), $\chi = 0.0001$ , $c = 1$ , damage phase. . . . .	178
B.6	Eigenforms for Q4/4, RI and GGLS according to Eq. (B.21), $\chi = 0.0001$ , $c = 1$ , unloading. . . . .	178
C.1	Dowel disc test – load-displacement diagrams. . . . .	180
C.2	Dowel disc test. Final damage distribution for mesh A ( $v = 0.4$ mm). . . . .	181
C.3	Dowel disc test. Final damage distribution for mesh B ( $v = 0.4$ mm). . . . .	181
C.4	Dowel disc test. Final averaged strain distribution for mesh A ( $v = 0.4$ mm). . . . .	182
C.5	Dowel disc test. Final averaged strain distribution for mesh B ( $v = 0.4$ mm). . . . .	182

# LIST OF TABLES

2.1	Tension in one direction – all cases computed by means of isotropic damage. . . . .	35
3.1	Set of initial boundary value problem (IBVP) equations. . . . .	62
3.2	The algorithm of Newmark method for gradient damage model. . . . .	70
3.3	Available elements for gradient damage model. . . . .	71
3.4	Eigenvalues for Q4/4, $c = 1$ . . . . .	73
3.5	Eigenvalues for Q4/4, $c = 0$ . . . . .	73
3.6	Eigenvalues for stabilized Q4/4, $c = 1$ , $\chi = 0.0001$ . . . . .	85
3.7	Eigenvalues for other 2D elements, $c = 1$ . . . . .	90
3.8	Eigenvalues for 3D elements, $c = 1$ . . . . .	91
4.1	General problem data. . . . .	94
4.2	Basic data for gradient damage model (also with plasticity). . . . .	94
4.3	Convergence study – bar with imperfection. Two types of integration. . . . .	103
4.4	Bar with imperfection – cases computed by means of isotropic gradient damage. . . . .	104
4.5	Convergence study – bar with imperfection. Scalar vs isotropic models. . . . .	105
4.6	Bar with imperfection – different 3D discretizations. . . . .	108
5.1	Brazilian test – discretizations used in simulations. . . . .	122
5.2	Brazilian test – material model data. . . . .	122
5.3	Brazilian test – cases computed by means of isotropic gradient damage. . . . .	128
5.4	Four point bending – geometry data for beam. . . . .	133
5.5	General material data in four point bending test. . . . .	133
5.6	Material model data for dowel bar. . . . .	142
5.7	RC slab-column connection – experimental data [1]. . . . .	150
5.8	RC slab-column connection – numerical simulation data. . . . .	152
5.9	RC slab-column connection, SB1 – cases for isotropic gradient damage. . . . .	159
B.1	Eigenvalues for Q4/4, improper stabilization of averaging equation, $\chi = 0.0001$ , $c = 1$ . . . . .	175
C.1	Material model data for dowel disc. . . . .	179



# BIBLIOGRAPHY

- [1] ADETIFA, B., AND POLAK, M. A. Retrofit of interior slab-column connections for punching using shear bolts. *ACI Structural Journal* 102, 2 (2005), 268–274.
- [2] AIFANTIS, E. C. On the microstructural origin of certain inelastic models. *J. Eng. Mater. Technol.* 106 (1984), 326–330.
- [3] ASKES, H. *Advanced spatial discretization strategies for localized failure - mesh adaptivity and meshless methods*. Ph.D. dissertation, Delft University of Technology, Delft, 2000.
- [4] ASKES, H., PAMIN, J., AND DE BORST, R. Dispersion analysis and element-free Galerkin solutions of second- and fourth-order gradient-enhanced damage models. *Int. J. Numer. Meth. Engng* 49 (2000), 811–832.
- [5] ASKES, H., SUIKER, A. S. J., AND SLUYS, L. J. A classification of higher-order strain-gradient models - linear analysis. *Archive of Applied Mechanics* 72, 2-3 (2002), 171–188.
- [6] BABUŠKA, I., AND MELENK, J. M. The Partition of Unity Method. *Int. J. Numer. Meth. Engng* 40, 4 (1997), 727–758.
- [7] BAŽANT, Z. P. Imbricate continuum and its variational derivation. *ASCE J. Eng. Mech.* 110 (1984), 1693–1712.
- [8] BAŽANT, Z. P., AND BELYTSCHKO, T. Wave propagation in a strain-softening bar: exact solution. *ASCE J. Eng. Mech.* 111(3) (1985), 381–389.
- [9] BAŽANT, Z. P., AND OH, B. Crack band theory for fracture of concrete. *RILEM Materials and Structures* 16 (1983), 155–177.
- [10] BAŽANT, Z. P., AND PIJAUDIER-CABOT, G. Nonlocal continuum damage, localization instability and convergence. *ASME J. Appl. Mech.* 55 (1988), 287–293.
- [11] BĄK, G., AND STOLARSKI, A. Nonlinear analysis of reinforced concrete bar structures loaded impulsively. Tech. Rep. 30, Civil Engng. Com. Polish Acad. Sci., Warsaw, 1990, (in Polish).

- [12] BELYTSCHKO, T., AND LASRY, D. A study of localization limiters for strain-softening in statics and dynamics. *Comput. & Struct.* 33 (1989), 707–715.
- [13] BELYTSCHKO, T., ONG, J. S.-J., LIU, W. K., AND KENNEDY, J. M. Hourglass control in linear and nonlinear problems. *Comput. Methods Appl. Mech. Engrg.* 43 (1984), 251–276.
- [14] BETTEN, J. Damage tensors in continuum mechanics. *J. Méc. Théor. Appl.* 2, 1 (1983), 13–32.
- [15] BETTEN, J. Applications of tensor functions in damage mechanics of anisotropic materials. In *Proc. Int. Symp. Anisotropic Behaviour of Damaged Materials* (Cracow, 2002), J. Skrzypek and A. Ganczarski, Eds., Cracow University of Technology. Published on 24 pages.
- [16] BIĆANIĆ, N., PEARCE, C. J., AND OWEN, D. R. J. Failure predictions of concrete like materials using softening Hoffman plasticity model. In Mang et al. [100], pp. 185–198.
- [17] BOBIŃSKI, J. *Implementation and application examples of nonlinear concrete models with nonlocal softening*. Ph.D. dissertation, Gdansk University of Technology, Gdańsk, 2006, (in Polish).
- [18] BOBIŃSKI, J., AND TEJCHMAN, J. Simulations of size effects in concrete within a non-local both softening plasticity and damage mechanics. In Garstecki et al. [54]. published on CDROM (6 pages).
- [19] BRANDES, K. Strain rate effects appearing in the mechanical behaviour of reinforced concrete structures under impact load. In *Proc. Int. Symp. Mechanics of Inelastic Media and Structures* (Warsaw, 1978), O. Mahrenholtz and A. Sawczuk, Eds., Inst. of Fundamental Technological Research PAS, pp. 73–85.
- [20] CAROL, I., RIZZI, E., AND WILLAM, K. On the formulation of anisotropic elastic degradation.: II. Generalized pseudo-rankine model for tensile damage. *Int. J. Solids Struct.* 38, 4 (2001), 519–546.
- [21] CAROL, I., RIZZI, E., AND WILLAM, K. An ‘extended’ volumetric/deviatoric formulation of anisotropic damage based on a pseudo-log rate. *Eur. J. Mech. A/Solids* 21, 5 (2002), 747–772.
- [22] CHABOCHE, J.-L. Continuous damage mechanics: a tool to describe phenomena before crack initiation. *Nuclear Engng. and Design* 64, 2 (1981), 233–247.
- [23] CHABOCHE, J.-L. Damage induced anisotropy: on the difficulties associated with the active/passive unilateral condition. *Int. J. Damage Mechanics* 1, 2 (1992), 148–171.

- [24] CHEN, W. F., AND CHANG, T. Y. P. Plasticity solutions for concrete splitting tests. *ASCE J. Eng. Mech. Div. 104*, EM3 (1978), 691–704.
- [25] CHRZANOWSKI, M. Use of the damage concept in describing creep-fatigue interaction under prescribed stress. *Int. J. Mech. Sci. 18* (1976), 69–73.
- [26] COMI, C. Computational modelling of gradient-enhanced damage in quasi-brittle materials. *Mech. Cohes.-frict. Mater. 4*, 1 (1999), 17–36.
- [27] COMI, C. A non-local model with tension and compression damage mechanisms. *Eur. J. Mech. A/Solids 20*, 1 (2001), 1–22.
- [28] COMI, C., AND PEREGO, U. Numerical aspects of nonlocal damage analyses. *Revue européenne des éléments finis 10*, 2-3-4 (2001), 227–242.
- [29] COMMEND, S., TRUTY, A., AND ZIMMERMANN, T. Stabilized finite elements applied to elastoplasticity: I. Mixed displacement–pressure formulation. *Comput. Methods Appl. Mech. Engrg. 193* (2004), 3559–3586.
- [30] CORDEBOIS, J. L., AND SIDOROFF, F. Damage induced elastic anisotropy. In *Mechanical behaviour of Anisotropic Solids* (Hague, the Netherlands, 1982), J. Boehler, Ed., Martinus Nijhoff, pp. 761–774.
- [31] DAVIDSON, L., AND STEVENS, A. L. Thermodynamical constitution of spalling elastic bodies. *J. Appl. Phys. 44* (1973), 667–674.
- [32] DE BORST, R. Simulation of strain localisation: A reappraisal of the Cosserat continuum. *Eng. Comput. 8* (1991), 317–332.
- [33] DE BORST, R., ET AL., Eds. *Proc. EURO-C 1998 Int. Conf. Computational Modelling of Concrete Structures* (Rotterdam/Brookfield, 1998), A. A. Balkema.
- [34] DE BORST, R., GEERS, M. G. D., KUHL, E., AND PEERLINGS, R. H. J. Enhanced damage models for concrete fracture. In de Borst et al. [33], pp. 231–248.
- [35] DE BORST, R., AND MÜHLHAUS, H.-B. Gradient-dependent plasticity: Formulation and algorithmic aspects. *Int. J. Numer. Meth. Engng 35* (1992), 521–539.
- [36] DE BORST, R., PAMIN, J., AND GEERS, M. G. D. On coupled gradient-dependent plasticity and damage theories with a view to localization analysis. *Eur. J. Mech. A/Solids 18*, 6 (1999), 939–962.
- [37] DE BORST, R., SLUYS, L. J., MÜHLHAUS, H.-B., AND PAMIN, J. Fundamental issues in finite element analyses of localization of deformation. *Eng. Comput. 10* (1993), 99–121.

- [38] DE VREE, J. H. P., BREKELMANS, W. A. M., AND VAN GILS, M. A. J. Comparison of nonlocal approaches in continuum damage mechanics. *Comput. & Struct.* 55, 4 (1995), 581–588.
- [39] DEI POLI, S., DI PRISCO, M., AND GAMBAROVA, P. G. Shear response, deformations, and subgrade stiffness of a dowel bar embedded in concrete. *ACI Structural Journal* 89 (1992), 665–675.
- [40] DEI POLI, S., DI PRISCO, M., AND GAMBAROVA, P. G. Cover and stirrup effects on the shear response of dowel bar embedded in concrete. *ACI Structural Journal* 90 (1993), 441–450.
- [41] DI PRISCO, M., CARUSO, M. L., AND PIATTI, S. On fiber role in dowel action. *Studi e Ricerche* 15 (1994), 151–194.
- [42] DI PRISCO, M., FERRARA, L., MEFTAH, F., PAMIN, J., DE BORST, R., MAZARS, J., AND REYNOUARD, J. M. Mixed mode fracture in plain and reinforced concrete: some results on benchmark tests. *Int. J. Fracture* 103 (2000), 127–148.
- [43] DIANA. DIANA Finite Element Analysis - User's manual, release 7.2. Tech. rep., TNO Building and Construction Research, Delft, 1999.
- [44] DRAGON, A. Plasticity and ductile fracture damage: Study of void growth in metals. *Eng. Fract. Mech.* 21, 4 (1983), 875–885.
- [45] DUBÉ, J.-F., PIJAUDIER-CABOT, G., AND BORDERIE, C. L. Rate dependent damage model for concrete in dynamics. *J. of Engng. Mech.* 122, 10 (1996), 939–947.
- [46] EIBL, J., BISCHOFF, P. H., AND LOHRMANN, G. Failure mechanics of fibre-reinforced concrete and pre-damaged structures: dynamic loading conditions. Tech. Rep. BRITE/EURAM P-89-3275, Univ. of Karlsruhe, Karlsruhe, Germany, 1994.
- [47] ENGELEN, R. A. B. *Plasticity-induced damage in metals. Nonlocal modelling at finite strains*. Ph.D. dissertation, Eindhoven University of Technology, Eindhoven, 2005.
- [48] ERINGEN, A. C. *Mechanics of Continua*. J. Wiley & Sons, New York, 1967.
- [49] FEENSTRA, P. H. *Computational aspects of biaxial stress in plain and reinforced concrete*. Ph.D. dissertation, Delft University of Technology, Delft, 1993.
- [50] FERRARA, L. *A contribution to the modelling of mixed mode fracture and shear transfer in plain and reinforced concrete*. Ph.D. dissertation, Politecnico di Milano, Milan, 1998.
- [51] FIB, Ed. *Structural Concrete. The Textbook on Behaviour, Design and Performance. Updated knowledge of the CEB/FIP Model Code 1990*, vol. 1, Bulletin No 1. fib, 1999.



- [52] GANCZARSKI, A. *Problems of acquired anisotropy and coupled thermo-mechanical fields of CDM*. Monograph 25, Cracow University of Technology, Cracow, 2001, (in Polish).
- [53] GANCZARSKI, A., AND BARWACZ, L. Low cycle fatigue based on unilateral damage evolution. *Int. J. Damage Mechanics* 16 (2007), 159–177.
- [54] GARSTECKI, A., MOCHNACKI, B., AND SCZYGIOL, N., Eds. *Proc. CEACM Conf. on Computational Mechanics and 16th Int. Conf. Computer Methods in Mechanics CMM-2005* (Częstochowa, 2005), Czestochowa University of Technology, Publishing House of Czestochowa University of Technology.
- [55] GEERS, M. G. D. *Experimental analysis and computational modelling of damage and fracture*. Ph.D. dissertation, Eindhoven University of Technology, Eindhoven, 1997.
- [56] GEERS, M. G. D. Continuum damage mechanics. Fundamentals, higher-order theories and computational aspects. Lecture notes PRO 1526-TUE, Eindhoven University of Technology, Eindhoven, 1998.
- [57] GEORGIN, J. F., SLUYS, L. J., AND REYNOUARD, J. M. A coupled damage-viscoplasticity model for the analysis of localisation and size effects. *Computers & Concrete* 1, 2 (2004), 169–188.
- [58] GERMAIN, N., BESSON, J., AND FEYEL, F. Composite layered materials: Anisotropic nonlocal damage models. *Comput. Methods Appl. Mech. Engrg.* 196 (2007), 4272–4282.
- [59] GLEMA, A. *Analysis of wave nature in plastic strain localization in solids*. Monograph 379, Poznań University of Technology, Poznań, 2004, (in Polish).
- [60] GRABACKI, J. *Mechanics of materials with internal structure*. Monograph 131, Cracow University of Technology, Cracow, 1992, (in Polish).
- [61] GRASSL, P., AND JIRÁSEK, M. Plastic model with non-local damage applied to concrete. *Int. J. Num. Anal. Meth. Geomech.* 30 (2006), 71–90.
- [62] HANSEN, N. R. *Theories of elastoplasticity coupled with continuum damage mechanics*. Ph.D. dissertation, Sandia National Laboratories, Albuquerque, New Mexico, 1993.
- [63] HARARI, I., FREY, S., AND FRANCA, L. P. A note on a recent study of stabilized finite element computations for heat conduction. *Computational Mechanics* 28 (2002), 63–65.
- [64] HASHAGEN, F. *Numerical analysis of failure mechanisms in fibre metal laminates*. Ph.D. dissertation, Delft University of Technology, Delft, 1998.

- [65] HILL, R. A general theory of uniqueness and stability in elastic-plastic solids. *J. Mech. Phys. Solids* 6 (1958), 236–249.
- [66] HORDIJK, D. A. *Local approach to fatigue of concrete*. Ph.D. dissertation, Delft University of Technology, Delft, 1991.
- [67] HUGHES, T. J. R. *The Finite Element Method. Linear Static and Dynamic Analysis*. Prentice-Hall, New Jersey, 1987.
- [68] JIRÁSEK, M. Nonlocal models for damage and fracture: Comparison of approaches. *Int. J. Solids Struct.* 35, 31-32 (1998), 4133–4145.
- [69] JIRÁSEK, M. Modeling of localized inelastic deformation. Lecture notes, Czech Technical University in Prague, Prague, 2006.
- [70] JIRÁSEK, M., AND MARFIA, S. Nonlocal damage model based on displacement averaging. *Int. J. Numer. Meth. Engng* 63 (2005), 77–102.
- [71] JIRÁSEK, M., AND PATZÁK, B. Consistent tangent stiffness for nonlocal damage models. *Comput. & Struct.* 80 (2002), 1279–1293.
- [72] JIRÁSEK, M., ROLSHOVEN, S., AND GRASSL, P. Size effect on fracture energy induced by non-locality. *Int. J. Num. Anal. Meth. Geomech.* 28 (2004), 653–670.
- [73] JIRÁSEK, M., AND ZIMMERMANN, T. Embedded crack model: I. Basic formulation. II: Combination with smeared cracks. *Int. J. Numer. Meth. Engng* 50, 6 (2001), 1269–1305.
- [74] JU, J. W. On energy-based coupled elastoplastic damage theories: constitutive modeling and computational aspects. *Int. J. Solids Struct.* 25, 7 (1989), 803–833.
- [75] JU, J. W. Isotropic and anisotropic damage variables in continuum damage mechanics. *ASCE J. Eng. Mech.* 116, 12 (1990), 2764–2770.
- [76] KACHANOV, L. M. Time of rupture process under creep conditions. *Izd. Akad. Nauk SSSR, Otd. Tekh. Nauk* 8 (1958), 26–31, (in Russian).
- [77] KACZMARCZYK, Ł. *Numerical analysis of multiscale problems in mechanics of inhomogeneous media*. Ph.D. dissertation, Cracow University of Technology, Cracow, 2006, (in Polish).
- [78] KLISIŃSKI, M., AND MRÓZ, Z. *Description of inelastic deformations and damage of concrete*. Monograph 193. Poznań University of Technology, Poznań, 1988, (in Polish).
- [79] KOZICKI, J. *Application of discrete models to describe the fracture process in brittle materials*. Ph.D. dissertation, Gdansk University of Technology, Gdańsk, 2007.

- [80] KRAJCI NOVIC, D. Damage mechanics. *Mechanics of Materials* 8, 2-3 (1989), 117–197.
- [81] KRAJCI NOVIC, D., AND FONSEKA, G. U. Continuous damage theory of brittle materials. *ASME J. Appl. Mech.* 48, 4 (1981), 809–824.
- [82] K UHL, D., BANGERT, F., AND MESCHKE, G. Coupled chemo-mechanical deterioration of cementitious materials. part I: Modeling. part II: Numerical methods and simulations. *Int. J. Solids Struct.* 41, 1 (2004), 15–67.
- [83] K UHL, E. *Numerische Modelle für kohäsive Reibungsmaterialien*. Ph.D. dissertation, University of Stuttgart, Stuttgart, 2000.
- [84] K UHL, E., RAMM, E., AND DE BORST, R. An anisotropic gradient damage model for quasi-brittle materials. *Comput. Methods Appl. Mech. Engrg.* 183, 1-2 (2000), 87–103.
- [85] KUKLA, K. *Numerical analysis of selected concrete mechanics problems using a gradient damage model*. Diploma thesis, Cracow University of Technology, Cracow, 2003.
- [86] KUNA-CISKAŁ, H. AND SKRZYPEK, J. J. CDM based modelling of damage and fracture mechanics in concrete under tension and compression. *Eng. Fract. Mech.* 74, (2004), 681-698.
- [87] KUPFER, H. *Das Verhalten des Betons unter mehrachsiger Kurzzeitbelastung unter besonderer Berücksichtigung der zweiachsigen Beanspruchung*. No. 229. Deutscher Ausschuss für Stahlbeton, Berlin, 1973.
- [88] KUPFER, H., HILSDORF, H. K., AND RUSCH, H. Behavior of concrete under biaxial stresses. *Am. Concrete Inst.-J.* 66, 8 (1969), 655–666.
- [89] LABORDERIE, C. *Phénomènes unilatéraux dans un matériel endommageable*. Ph.D. dissertation, Université Paris 6, Paris, 1991.
- [90] LEMAITRE, J. Evaluation of dissipation and damage in metals. In *Proc. I.C.M.* (Kyoto, Japan, 1971), vol. 1.
- [91] LEMAITRE, J. How to use damage mechanics. *Nucl. Engng Des.* 80 (1984), 233–245.
- [92] LEMAITRE, J., AND CHABOCHE, J.-L. *Mechanics of Solid Materials*. Cambridge University Press, Cambridge, 1990.
- [93] LEWIŃSKI, P. M., AND WIĘCH, P. P. FEM analysis of punching failure of RC slabs versus results of experimental research. *Theoretical Foundations of Civil Eng.* XV (2007), 433–440. (in Polish).

- [94] LIEBE, T., STEINMANN, P., AND BENALLAL, A. Theoretical and computational aspects of a thermodynamically consistent framework for geometrically linear gradient damage. *Comput. Methods Appl. Mech. Engrg.* 190 (2001), 6555–6576.
- [95] LITEWKA, A. Effective material constants for orthotropically damaged elastic solid. *Arch. Mech.* 37, 6 (1985), 631–642.
- [96] ŁODYGOWSKI, T. *Theoretical and numerical aspects of plastic strain localization*. Monograph 312, Poznań University of Technology, Poznań, 1996.
- [97] LOURENÇO, P. B. *Computational strategies for masonry structures*. Ph.D. dissertation, Delft University of Technology, Delft, 1996.
- [98] LUBLINER, J., OLIVER, J., OLLER, S., AND OÑATE, E. A plastic-damage model for concrete. *Int. J. Solids Struct.* 25, 3 (1989), 299–326.
- [99] MAIER, G., AND HUECKEL, T. Nonassociated and coupled flow rules of elastoplasticity for rock-like materials. *Int. J. Rock Mech. Min. Sci. & Geomech. Abstr.* 16 (1979), 77–92.
- [100] MANG, H., ET AL., Eds. *Proc. EURO-C 1994 Int. Conf. Computer Modelling of Concrete Structures* (Swansea, 1994), Pineridge Press.
- [101] MAUGIN, G. A. Nonlocal theories or gradient-type theories: a matter of convenience? *Arch. Mech.* 31, 1 (1979), 15–26.
- [102] MAZARS, J. *Application de la mécanique de l'edommagement au comportement non linéaire et à la rupture du béton de structure*. Ph.D. dissertation, Université Paris 6, Paris, 1984.
- [103] MAZARS, J., AND PIJAUDIER-CABOT, G. Continuum damage theory - application to concrete. *ASCE J. Eng. Mech.* 115 (1989), 345–365.
- [104] MENÉTREY, P. Synthesis of punching failure in reinforced concrete. *Cement & Concrete Composites* 24 (2002), 497–507.
- [105] MENÉTREY, P., AND WILLAM, K. J. Punching shear in reinforced concrete: Localized process. In de Borst et al. [33], pp. 867–876.
- [106] MESCHKE, G., MACHT, J., AND LACKNER, R. A damage-plasticity model for concrete accounting for fracture-induced anisotropy. In de Borst et al. [33], pp. 3–12.
- [107] MOËS, N., DOLBOW, J., AND BELYTSCHKO, T. A finite element method for crack growth without remeshing. *Int. J. Numer. Meth. Engng* 46, 1 (1999), 131–150.
- [108] MÜHLHAUS, H.-B., AND VARDOULAKIS, I. The thickness of shear bands in granular materials. *Geotechnique* 37 (1987), 271–283.

- [109] MURAKAMI, S., AND OHNO, N. A continuum theory of creep and creep damage. In *IUTAM Symp., Creep in Structures* (Berlin, 1981), A. R. S. Ponter and D. R. Hayhurst, Eds., Springer, pp. 422–444.
- [110] NEEDLEMAN, A. Material rate dependence and mesh sensitivity in localization problems. *Comput. Methods Appl. Mech. Engrg.* 67 (1988), 69–86.
- [111] NEGELE, A., ELIGEHAUSEN, R., OŽBOLT, J., AND POLAK, M. A. Finite-element simulations on punching tests of shear-retrofitted slab-column connections. In *Fracture Mechanics of Concrete and Concrete Structures* (Catania/Leiden, 2007), A. Carpinteri and P. Gambarova, Eds., FRAMCOS 6, A. A. Balkema, pp. 911–918.
- [112] NOORU-MOHAMED, M. B. *Mixed-mode fracture of concrete: an experimental approach*. Ph.D. dissertation, Delft University of Technology, Delft, 1992.
- [113] OLIVER, J., CERVERA, M., OLLER, S., AND LUBLINER, J. Isotropic damage models and smeared crack analysis of concrete. In *Proc. Second Int. Conf. Computer Aided Analysis and Design of Concrete Structures* (Swansea, 1990), N. Bićanić et al., Eds., Pineridge Press, pp. 945–957.
- [114] OLIVER, J., LINERO, D. L., HUESPE, A. E., AND MANZOLI, O. L. Two-dimensional modeling of material failure in reinforced concrete by means of a continuum strong discontinuity approach. *Comput. Methods Appl. Mech. Engrg.* 197, 5 (2008), 332–348.
- [115] ORTIZ, M. A constitutive theory for the inelastic behaviour of concrete. *Mechanics of Materials* 4 (1985), 67–93.
- [116] PAMIN, J. *Gradient-dependent plasticity in numerical simulation of localization phenomena*. Ph.D. dissertation, Delft University of Technology, Delft, 1994.
- [117] PAMIN, J. *Gradient-enhanced continuum models: formulation, discretization and applications*. Series Civil Engineering, Monograph 301, Cracow University of Technology, Cracow, 2004.
- [118] PAMIN, J. Gradient plasticity and damage models: a short comparison. *Computational Materials Science* 32 (2005), 472–479.
- [119] PAMIN, J., AND DE BORST, R. Stiffness degradation in gradient-dependent coupled damage-plasticity. *Arch. Mech.* 51, 3-4 (1999), 407–433.
- [120] PAMIN, J., MATUSZAK, A., STANKIEWICZ, A., AND WINNICKI, A. Further developments in project no. 7 T07A 036 12. Tech. Rep. L-5/B-77/99, Institute of Computer Methods in Civil Engineering, Cracow University of Technology, Cracow, 1999.

- [121] PAMIN, J., AND WINNICKI, A. Gradient enhanced modelling of crack band width and crack spacing in reinforced concrete. In *Proc. 3rd Int. Conf. Analytical Models and New Concepts in Mechanics of Concrete Structures* (Wrocław, 1999), Wrocław University of Technology, pp. 217–222.
- [122] PAMIN, J., WOSATKO, A., AND WINNICKI, A. Two- and three-dimensional gradient damage-plasticity simulations of cracking in concrete. In *Proc. EURO-C 2003 Int. Conf. Computational Modelling of Concrete Structures* (Rotterdam/Brookfield, 2003), N. Bićanić et al., Eds., A. A. Balkema, pp. 325–334.
- [123] PEARCE, C. J., NIELSEN, C. V., AND BIĆANIĆ, N. Gradient enhanced thermo-mechanical damage model for concrete at high temperatures including transient thermal creep. *Int. J. Num. Anal. Meth. Geomech.* 28, 7-8 (2004), 715–735.
- [124] PEERLINGS, R. H. J. *Enhanced damage modelling for fracture and fatigue*. Ph.D. dissertation, Eindhoven University of Technology, Eindhoven, 1999.
- [125] PEERLINGS, R. H. J., DE BORST, R., BREKELMANS, W. A. M., AND DE VREE, J. H. P. Gradient-enhanced damage for quasi-brittle materials. *Int. J. Numer. Meth. Engng* 39 (1996), 3391–3403.
- [126] PEERLINGS, R. H. J., DE BORST, R., BREKELMANS, W. A. M., AND GEERS, M. G. D. Gradient-enhanced damage modelling of concrete fracture. *Mech. Cohes.-frict. Mater.* 3 (1998), 323–342.
- [127] PEERLINGS, R. H. J., GEERS, M. G. D., DE BORST, R., AND BREKELMANS, W. A. M. A critical comparison of nonlocal and gradient-enhanced softening continua. *Int. J. Solids Struct.* 38, 44-45 (2001), 7723–7746.
- [128] PIETRUSZCZAK, S., AND MRÓZ, Z. Finite element analysis of deformation of strain-softening materials. *Int. J. Numer. Meth. Engng* 17 (1981), 327–334.
- [129] PIJAUDIER-CABOT, G., AND BAŽANT, Z. P. Nonlocal damage theory. *ASCE J. Eng. Mech.* 113 (1987), 1512–1533.
- [130] PIJAUDIER-CABOT, G., LA BORDERIE, C., AND FICHANT, S. Damage mechanics for concrete modelling: Applications and comparisons with plasticity and fracture mechanics. In Mang et al. [100], pp. 17–36.
- [131] PIVONKA, P., OŽBOLT, J., LACKNER, R., AND MANG, H. A. Comparative studies of 3d-constitutive models for concrete: application to mixed-mode fracture. *Int. J. Numer. Meth. Engng* 60 (2004), 549–570.

- [132] PODLEŚ, K. *Nonlocal, elasto-plastic constitutive concrete model for analysis of ultimate and serviceability limits states of massive hydraulic structures*. Ph.D. dissertation, Cracow University of Technology, Cracow, 2004, (in Polish).
- [133] POLAK, M. A. Modelling punching shear of reinforce concrete slabs using layered finite elements. *ACI Structural Journal* 95, 1 (1998), 71–80.
- [134] RABOTNOV, Y. N. Creep rupture. In *Proc. 12th International Congress of Applied Mechanics* (Standford, Calif., 1968), pp. 342–349.
- [135] READ, H. E., AND HEGEMIER, G. A. Strain softening of rock, soil and concrete - a review article. *Mech. Mater.* 3 (1984), 271–294.
- [136] RICE, J. R. The localization of plastic deformation. In *Proc. 14th Int. Cong. Theoretical and Applied Mechanics* (Amsterdam, 1976), W. Koiter, Ed., North-Holland Publishing Company, pp. 207–220.
- [137] ROCCO, C., GUINEA, G. V., PLANAS, J., AND ELICES, M. Mechanisms of rupture in splitting tests. *ACI Materials Journal* 96 (1999), 52–60.
- [138] RODRIGUEZ-FERRAN, A., AND HUERTA, A. Failure and post-failure modelling of the Brazilian test. In *Conf. on Trends in Computational Structural Mechanics* (Barcelona, 2001), K.-U. Bletzinger, K. Schweizerhof, and W. Wall, Eds., CIMNE, pp. 189–197.
- [139] ROMANOWSKI, P. *Numerical analysis of concrete structures durability under chemo-mechanical loading*. Ph.D. dissertation, Cracow University of Technology, Cracow, 2005, (in Polish).
- [140] ROTS, J. G. *Computational modeling of concrete fracture*. Ph.D. dissertation, Delft University of Technology, Delft, 1988.
- [141] RUDNICKI, J. W., AND RICE, J. R. Conditions for the localization of deformation in pressure-sensitive dilatant materials. *J. Mech. Phys. Solids* 23 (1975), 371–394.
- [142] RUIZ, G., ORTIZ, M., AND PANDOLFI, A. Three-dimensional finite-element simulation of the dynamic Brazilian tests on concrete cylinders. *Int. J. Numer. Meth. Engng* 48 (2000), 963–994.
- [143] SCHELLEKENS, J. C. J. *Computational strategies for composite structures*. Ph.D. dissertation, Delft University of Technology, Delft, 1992.
- [144] SCHLANGEN, E. *Experimental and numerical analysis of fracture processes in concrete*. Ph.D. dissertation, Delft University of Technology, Delft, 1993.

- [145] SIMO, J. C., AND JU, J. W. Strain- and stress-based continuum damage models - I. Formulation, II. Computational aspects. *Int. J. Solids Struct.* 23, 7 (1987), 821–869.
- [146] SIMONE, A. *Continuous-discontinuous modelling of failure*. Ph.D. dissertation, Delft University of Technology, Delft, 2003.
- [147] SIMONE, A., ASKES, H., PEERLINGS, R. H. J., AND SLUYS, L. J. Interpolation requirements for implicit gradient-enhanced continuum damage models. *Communications in Numerical Methods in Engineering* 19 (2003), 563–572. (see also [148]).
- [148] SIMONE, A., ASKES, H., PEERLINGS, R. H. J., AND SLUYS, L. J. Corrigendum 'Interpolation requirements for implicit gradient-enhanced continuum damage models'. *Communications in Numerical Methods in Engineering* 20 (2004), 163–165.
- [149] SKRZYPEK, J. J., AND GANCZARSKI, A. *Modelling of Material Damage and Failure of Structures: Theory and Applications*. Springer, Berlin, New York, 1999.
- [150] SLUYS, L. J. *Wave propagation, localization and dispersion in softening solids*. Ph.D. dissertation, Delft University of Technology, Delft, 1992.
- [151] SLUYS, L. J. Dynamic failure in reinforced concrete structures. In *DIANA Computational Mechanics '94* (Dordrecht, 1994), G. Kusters and M. Hendriks, Eds., Kluwer Academic Publishers, pp. 193–203.
- [152] SLUYS, L. J. Gradient theory: Discretization principles and application. In Mang et al. [100], pp. 403–412.
- [153] SLUYS, L. J., AND DE BORST, R. Failure in plain and reinforced concrete - an analysis of crack width and crack spacing. *Int. J. Solids Struct.* 33 (1996), 3257–3276.
- [154] STEINMANN, P. Formulation and computation of geometrically non-linear gradient damage. *Int. J. Numer. Meth. Engng* 46, 5 (1999), 757–779.
- [155] SVEDBERG, T. *On the modelling and numerics of gradient-regularized plasticity coupled to damage*. Ph.D. dissertation, Chalmers University of Technology, Gothenburg, 1999.
- [156] SZARLIŃSKI, J., WINNICKI, A., AND PODLEŚ, K. *Concrete structures in plane states. Computer-aided analysis and design*. Cracow University of Technology, Cracow, 2002, (in Polish).
- [157] TAYLOR, R. L. FEAP - A Finite Element Analysis Program, Version 7.4, Theory manual. Tech. rep., University of California at Berkeley, Berkeley, 2001.



- [158] TAYLOR, R. L. FEAP - A Finite Element Analysis Program, Version 7.4, User manual. Tech. rep., University of California at Berkeley, Berkeley, 2001.
- [159] TEJCHMAN, J., AND WU, W. Numerical study on patterning of shear bands in a Cosserat continuum. *Acta Mechanica* 99, 1-4 (1993), 61–74.
- [160] TIJSSENS, M. G. A. *On the cohesive surface methodology for fracture of brittle heterogeneous solids*. Ph.D. dissertation, Delft University of Technology, Delft, 2000.
- [161] TRĄPCZYŃSKI, W. A., HAYHURST, D. R., AND LECKIE, F. A. Creep rupture of copper and aluminium under non-proportional loading. *J. Mech. Phys. Solids* 29, 5-6 (1981), 353–374.
- [162] TRUTY, A. *On certain class of mixed and stabilized mixed finite element formulations for single and two-phase geomaterials*. Monograph 48, Cracow University of Technology, Cracow, 2002.
- [163] URBAN, T. S. *Punching in concrete. Selected problems*. Monograph 959, Łódź Technical University, Łódź, 2005, (in Polish).
- [164] VAKULENKO, A. A., AND KACHANOV, L. M. Continuum theory of medium with cracks. *Izd. Akad. Nauk SSSR, Mech. Tver. Tela* 4 (1971), 159–166, (in Russian).
- [165] VAN MIER, J. G. M. *Strain-softening of concrete under multiaxial loading conditions*. Ph.D. dissertation, Eindhoven University of Technology, Eindhoven, 1984.
- [166] WANDZIK, G., AND MAJEWSKI, S. Analysis of 3D stress state in reinforced concrete slab-column connection. In *European Conf. on Computational Mechanics ECCM-2001* (Cracow, 2001), Z. Waszczyszyn and J. Pamin, Eds., Cracow University of Technology, pp. 1098–1099, 13 pages on CDROM.
- [167] WANG, K., JANSEN, D. C., AND SHAH, S. P. Permeability study of cracked concrete. *Cement and Concrete Research* 27 (1997), 381–393.
- [168] WELLS, G. N. *Discontinuous modelling of strain localisation and failure*. Ph.D. dissertation, Delft University of Technology, Delft, 2001.
- [169] WILLAM, K., PRAMONO, E., AND STURE, S. Fundamental issues of smeared crack models. In *Proc. SEM-RILEM Int. Conf. on Fracture of Concrete and Rock* (Bethel, Connecticut, 1987), S. Shah and S. Swartz, Eds., Society of Engineering Mechanics, pp. 192–207.
- [170] WINNICKI, A. Crack closing effect in damage mechanics. In *Proc. XII Conf. Computer Methods in Design and Analysis of Hydrostructures* (Cracow, 2000), W. Biliński, Ed., Cracow University of Technology, pp. 155–164.

- [171] WINNICKI, A., AND CICHÓN, C. Numerical analysis of the plain concrete model prediction for nonproportional loading paths. In *Advances in Finite Element Technology* (Edinburgh, 1996), B. Topping, Ed., Civil-Comp Press, pp. 331–339.
- [172] WINNICKI, A., PEARCE, C. J., AND BIĆANIĆ, N. Viscoplastic Hoffman consistency model for concrete. *Comput. & Struct.* 79 (2001), 7–19.
- [173] WOSATKO, A., AND PAMIN, J. Dynamic localization in gradient damage-plasticity. In Garstecki et al. [54]. Paper on CDROM (9 pages).
- [174] WOSATKO, A., AND PAMIN, J. Stabilized four-noded finite element for gradient damage. In *Proc. I Congress of Polish Mechanics* (Warsaw, 2007), J. Kubik, W. Kurnik, and W. Nowacki, Eds., Warsaw University of Technology, Publishing House of Warsaw University of Technology, Abstract p. 169. Paper on CDROM (10 pages), (in Polish).
- [175] WOSATKO, A., PAMIN, J., AND WINNICKI, A. Gradient damage in simulations of behaviour of RC bars and beams under static and impact loading. *Archives of Civil Engineering* 52, 1 (2006), 455–477.
- [176] WOSATKO, A., PAMIN, J., WINNICKI, A., PUTANOWICZ, R., AND POLAK, M. A. Numerical simulation of damage in reinforced concrete slab-column connection. In *Proc. EURO-C 2006 Int. Conf. Computational Modelling of Concrete Structures* (London/Leiden, 2006), G. Meschke et al., Eds., Taylor and Francis, pp. 881–889.
- [177] XIAO, R. Y., AND O’FLAHERTY, T. Finite-element analysis of tested concrete connections. *Comput. & Struct.* 78 (2000), 247–255.
- [178] ZIENKIEWICZ, O. C., TAYLOR, R. L., AND ZHU, J. Z. *The Finite Element Method: Its Basis and Fundamentals*, sixth ed. Elsevier Butterworth-Heinemann, 2005.

# SUMMARY

## FINITE-ELEMENT ANALYSIS OF CRACKING IN CONCRETE USING GRADIENT DAMAGE-PLASTICITY

The thesis concerns the numerical analysis of the behaviour in plain and reinforced concrete during static and dynamic loading processes. The application of a proper numerical model is the fundamental issue in the simulations of cracking phenomenon, which is observed in quasi-brittle materials, in particular in concrete. A gradient enhancement of the damage theory coupled to plasticity ensures mesh-objective results.

The model presented previously in the paper by de Borst et al (1999) is further developed in this dissertation. Three-dimensional problems, dynamics without damping effects and the implementation of effective finite elements are dealt with. Next the model is verified in different applications together with parameter studies.

At the beginning of Chapter 1 the damage concept is briefly explained. Different aspects of numerical analysis for (reinforced) concrete are discussed. The localization problem, mesh dependence of results and different approaches to overcoming this difficulty are reviewed. The main simplifying assumptions and limitations are listed in Section 1.3.

In Chapter 2 the model is considered at the point level. The scalar damage theory is first used and the strain equivalence is postulated. The damage loading and damage growth functions are proposed. The coupling with the plasticity theory is included in order to incorporate the physically observed irreversible strains. Additionally the crack closure phenomenon can be taken into account as shown in Section 2.3. Another approach is to split the damage constitutive relation into volumetric and deviatoric parts to obtain isotropic damage with two parameters. The model is verified performing uniaxial tension and Willam's tests.

Chapter 3 contains a compact description of gradient enhancement proposals for the damage models. The formulation and implementation of the initial boundary value problem (IBVP) are discussed. It should be emphasized that the averaging equation is enclosed in the system of equations, so two primary fields must be discretized: the displacements and the averaged

strain measure. The algorithm for dynamics without damping is shown. The properties of finite elements (FEs) for two- and three-dimensional (2D and 3D) problems are specified using spectral analysis. The stabilization of underintegrated gradient damage equations is derived for four-noded quadrilateral element in order to obtain an efficient hourglass control.

The standard test of a bar with an imperfection is analyzed in Chapter 4 under static and dynamic loading and the implemented FEs together with various parameters are examined. The response of plain and reinforced concrete are compared in the dynamic direct tension test.

Chapter 5 describes the applications of the numerical model. Two-dimensional configurations are computed first. The crack closing option is employed for the cantilever beam under load reversals. The Brazilian test is simulated in order to present the splitting effect inside the specimen which is subjected to compression. The scalar model, where one damage parameter is considered, is confronted with the isotropic model using two damage parameters. The last two-dimensional benchmark is the four-point bending test, where plain and reinforced concrete are first considered for statics. Next the reinforced concrete beam under impact loading is calculated. Further, the dowel action of reinforcement in concrete is examined. The three-dimensional numerical simulation of the dowel bar experiment is performed, because after crack opening spalling of the concrete cover is noticed in the third dimension. Finally, the punching shear in the RC slab-column connection is considered. Different models and their parameters are employed, but the results of this benchmark are not completely satisfactory. The reasons are briefly discussed.

Chapter 6 concludes the performed analysis. At the end the research perspectives are also proposed.

Three appendices are attached after the conclusions. The local approach for damage theory is criticized with reference to the gradient one, cf. Appendix A. Next, Appendix B includes the derivations and spectral analysis for ineffective hourglass control. The results for the dowel disc test in Appendix C can be treated as an introduction to Section 5.4.

# STRESZCZENIE

## NUMERYCZNA ANALIZA ZARYSOWANIA BETONU PRZY UŻYCIU GRADIENTOWEGO MODELU SPRZĘŻONEJ MECHANIKI USZKODZEŃ I PLASTYCZNOŚCI

### ROZDZIAŁ 1: WPROWADZENIE

1.1. PODSTAWY TEORII USZKODZENIA: Jako pierwszy pojęcie uszkodzenia wprowadził Kaczanow [76] w odniesieniu do pęczania metali pod obciążeniem jednoosiowym. Definicja jest jednak na tyle uniwersalna, że może być uogólniona nawet do anizotropii. Rysunek 1.1 ilustruje koncepcję tego pojęcia. Pewne ciało  $\mathcal{B}$  zostało myślowo przecięte. Z płaszczyzny przecięcia, która ma kierunek normalny  $\vec{n}$ , wybrano nieskończenie małą powierzchnię  $dS_{\vec{n}}$ . Powierzchnia ta składa się z części uszkodzonej  $dS_{\vec{n}}^d$  i nieuszkodzonej  $dS_{\vec{n}}^u$ . Warto podkreślić, że część uszkodzoną stanowią wszelkie mikrodefekty struktury materiału, natomiast część nieuszkodzoną jego szkielet. Definicja (1.2) wprowadza pojęcie uszkodzenia jako pewną miarę części uszkodzonej tej powierzchni. Dla materiału bez defektów uszkodzenie  $\omega_{\vec{n}} = 0$ , natomiast  $\omega_{\vec{n}}$  w materiale całkowicie uszkodzonym wynosi 1. Jeśli uszkodzenie jest różne w przekrojach o różnych normalnych  $\vec{n}$ , wówczas model jest anizotropowy. Gdy nie zachodzi konieczność wyróżnienia kierunków to model staje się izotropowy. Wprowadzona teoria nosi nazwę kontynualnej mechaniki uszkodzeń (KMU, skrót ang. *CDM*).

1.2. NUMERYCZNE MODELOWANIE BETONU (I ŻELBETU): Ogólna klasyfikacja materiałów może skupiać się na rodzaju degradacji ich wewnętrznej struktury (por. np. [69, 168]). Pierwszą grupę stanowią materiały silnie kruche, np. szkło, dla których odpowiednie jest stosowanie mechaniki pękania. Po drugiej stronie można wyróżnić materiały ciągliwe, np. niektóre metale, gdzie można stosować teorię plastyczności. Natomiast pomiędzy nimi znajdują się materiały quasi-kruche, takie jak beton. W tych materiałach obserwuje się dwa poziomy zniszczenia. Najpierw powstają mikrorysy i następuje lokalizacja odkształceń w jednej lub wielu strefach

ośrodka, a następnie w stanie zaawansowanej destrukcji widoczne są skoki przemieszczeń i pojawiają się makrorysy. Rysunek 1.2 przedstawia rozwój degradacji materiału quasi-kruhogo. Beton jest materiałem niejednorodnym (por. [78, 156]), który jako kompozyt może być modelowany przy pomocy teorii mieszanin jak np. w [115]. Upraszczając można przejść do skali makro, uwzględniając w modelu pewne efekty związane z niższym poziomem obserwacji. Obserwowana jest lokalizacja i osłabienie materiału, które nie jest rzeczywistą cechą materiału, ale wynikiem niejednorodnej deformacji z powodu tworzenia się makrorys, por. [135]. Zatem osłabienie materiału nie powinno być zawarte bezpośrednio w klasycznych związkach fizycznych ośrodka ciągłego. Pojawia się problem modelowania lokalizacji odkształceń.

Z podstaw matematycznych problemu lokalizacji wynika, że najpierw następuje lokalna utrata stateczności materiału, a w jej konsekwencji może nastąpić utrata stateczności jego całej struktury. Wówczas występuje tzw. nieciągłość odkształceń (zachowana jest ciągłość przemieszczeń) czyli lokalizacja. Zjawisku temu towarzyszy złe postawienie problemu początkowo-brzegowego. W statyce eliptyczny charakter równań zmienia się na hiperboliczny, a w dynamice hiperboliczny – na eliptyczny. Ponadto w dynamice prędkość fali staje się urojona, pojawia się tzw. fala stojąca. Problem jest źle postawiony i wówczas w analizie numerycznej pojawia się zależność szerokości strefy lokalizacji od dyskretyzacji, np. siatki elementów skończonych.

W numerycznym modelowaniu betonu wyróżnia się modele dyskretne i ciągłe. Do podejść dyskretnych można zaliczyć np. model beleczkowy (zob. [79, 144]), gdzie wzajemnie powiązane beleczki imitują strukturę materiału. W modelowaniu ciągłym osobną grupę stanowi tzw. model rys rozmazanych. W pracy [140] rozpatrywano różne warianty tego modelu. Symulacja zarysowania w betonie może być prowadzona przy pomocy dyskretyzacji standardowymi elementami skończonymi wraz z dodatkowymi elementami interfejsowymi w siatce, jak np. w pracach [140, 160]. Elementy interfejsowe są także przydatne przy uwzględnianiu poślizgu pomiędzy matrycą betonową a stalowym zbrojeniem [121, 140, 153]. Wyżej wymienione modele nie zawierają tzw. wewnętrznej skali długości.

Modele zregularyzowane „radzą sobie” w określony sposób z problemem lokalizacji. O rozwiązaniu nie decyduje wówczas zagęszczenie siatki, ale odrębny parametr zwany wewnętrznym parametrem długości. Najwcześniejsze prace [9, 128, 140] uwzględniają wpływ rozmiaru elementu skończonego na model konstytutywny poprzez energię pęknięcia  $G_f$ . Kolejną grupę stanowią modele zależne od prędkości deformacji, gdzie w równaniach fizycznych uwzględnia się człon wiskotyczny [59, 96, 110, 150, 172]. Modele wyższego rzędu można podzielić następująco: modele mikropolarne, modele nielocalne (całkowe) i modele gradientowe. W modelach mikropolarnych [32, 108, 159] regularyzacja działa pod warunkiem, że rozważa się lokalizację wywołaną poślizgiem. W odniesieniu do mechaniki uszkodzeń modele nielocalne (całkowe) były zaproponowane w pracach [7, 10, 129]. Użycie podejścia całkowego dla sprzężonej teorii mechaniki uszkodzeń i plastyczności można znaleźć w pracach [17, 61].

Modele gradientowe zostały zapoczątkowane dla teorii plastyczności [2, 12, 35, 37, 116], natomiast gradienty dla skalarnej mechaniki uszkodzeń pojawiły się w równaniu uśredniającym począwszy od pracy [125] i były dalej rozwijane w [55, 124, 126]. Użycie modelu gradientowego do mechaniki uszkodzeń i sprzężenie z plastycznością ze wzmocnieniem zaproponowano w [36, 117], a jego rozwinięcie i weryfikacja są przedmiotem niniejszej pracy.

Najbardziej zaawansowane są modele, które uwzględniają w analizie numerycznej jednocześnie regularyzację i nieciągłość przemieszczeń (idea podziału jedności) wewnątrz elementu skończonego, por. [73, 146, 168].

Ogólna klasyfikacja wyżej wymienionych modeli jest przedstawiona na Rys. 1.6.

1.3. CEL I ZAKRES: Celem pracy jest rozwinięcie i weryfikacja gradientowego modelu skalarnej mechaniki uszkodzeń w odniesieniu do różnego rodzaju symulacji zarysowania w betonie. Uogólnienie modelu dla problemów trójwymiarowych, uzupełnienie sformułowania o dynamikę (bez tłumienia) oraz implementacja efektywnych elementów skończonych umożliwiają poszerzenie zastosowań modelu. Analiza numeryczna zawiera szeroki zakres testów, jednak poczynione są pewne założenia upraszczające:

- do symulacji zarysowania stosuje się kontynuálną mechanikę uszkodzeń (KMU),
- beton jest traktowany jako materiał jednorodny,
- pomija się efekty reologiczne,
- obowiązują liniowe związki kinematyczne,
- zbrojenie jest modelowane za pomocą sprężysto-plastycznych elementów kratowych,
- nie uwzględnia się poślizgu pomiędzy matrycą betonową a stalowym zbrojeniem.

Praca obejmuje sześć rozdziałów. Rozdział 2 dotyczy rozważań na poziomie punktu materialnego. Oprócz rozpatrywanych komponentów modelu, na końcu opisany jest tzw. test Willama z charakterystycznym dla betonu procesem obciążania. Rozdział 3 dotyczy sformułowania i implementacji. Badane są również własności pojedynczego elementu skończonego na podstawie analizy spektralnej. Zaproponowana jest także implementacja czterowęzłowych elementów skończonych ze zredukowanym całkowaniem i stabilizacją. Rozdział 4 odnosi się do statycznych i dynamicznych testów elementów skończonych. Zastosowania modelu w mechanice betonu są zawarte w Rozdziale 5, gdzie kolejno są symulowane: wspornik pod obciążeniem znakozmiennym, test brazylijski rozłupywania próbki, czteropunktowe zginanie belki, kołkowe działanie zbrojenia i na końcu przebicie w połączeniu płyta-słup. Wnioski zawiera Rozdział 6.

## ROZDZIAŁ 2: SPRĘŻENIE MECHANIKI USZKODZEŃ I PLASTYCZNOŚCI

2.1. OPIS SKALARNY MECHANIKI USZKODZEŃ: Układ równań na poziomie punktu materialnego zawiera: równania ruchu (2.1), równania kinematyczne (2.2) oraz odpowiednie równania fizyczne. Na podstawie Podrozdziału 1.1 można wprowadzić pojęcie skalarnej miary

uszkodzenia nazywanej dalej krótko uszkodzeniem. W tej pracy uszkodzenie opiera się na postulacie równoważności odkształceń [90], zilustrowanym na Rys. 2.1. Fikcyjna konfiguracja z efektywnym tensorem naprężenia  $\hat{\sigma}$  reprezentuje nieuszkodzony szkielet. Pomiędzy rzeczywistym a efektywnym tensorem naprężenia zachodzi relacja (2.4). Powyższy postulat wiąże się z założeniem funkcji obciążenia (2.8), dla mechaniki uszkodzeń definiowanej w przestrzeni odkształceń. O rozwoju uszkodzenia  $\omega$  w czasie  $t$  decyduje parametr historii  $\kappa^d$ . Definicja funkcji obciążenia jest równoważna definicji równoważnej miary odkształcenia  $\tilde{\epsilon}$ .

W pracy wymienia się trzy definicje tej miary: unormowana miara energii sprężystej (skrót ang. *EER*) wg wzoru (2.11), definicja Mazarsa (2.12) oraz zmodyfikowane kryterium HMH (ang. *modified von Mises*). Ta ostatnia miara (2.15) została zaproponowana w [38] i jest obliczana na podstawie niezmienników tensora odkształcenia oraz współczynnika  $k$  zależnego od ilorazu wytrzymałości na ściskanie  $f_c$  do wytrzymałości na rozciąganie  $f_t$ . Na Rys. 2.3–2.7 przedstawiono powierzchnie uszkodzenia (funkcje obciążenia) według wyżej wymienionych definicji.

Obok funkcji obciążenia należy sprecyzować funkcję wzrostu uszkodzenia. Najprostsza jest definicja (2.19) zgodna z liniowym osłabieniem. Najczęściej stosowana jest natomiast definicja (2.21) związana z osłabieniem eksponencjalnym. Różnice są zilustrowane w przykładzie, gdzie na Rys. 2.8 pokazane są wykresy  $\epsilon_{11}$ - $\sigma_{11}$  dla tych definicji oraz tzw. zmodyfikowanego prawa potęgowego (2.20).

**2.2. SPRĘŻENIE Z PLASTYCZNOŚCIĄ:** Sprężenie skalarne modelu mechaniki uszkodzeń i teorii plastyczności ma na celu uwzględnienie nieodwracalnych odkształceń obserwowanych w rzeczywistości. Teoria uszkodzenia jest formułowana w przestrzeni odkształceń, natomiast teoria plastyczności – w przestrzeni naprężeń [74, 145]. Związek konstytutywny dla modelu sprężonego, który jest zapisany w prędkościach, przedstawia wzór (2.50). Sprężenie jest widoczne w użyciu klasycznego tensora sprężysto-plastycznego  $\mathbf{E}^{ep}$ , który jest skonstruowany według zależności (2.35). Istotną jest też kwestia czy odkształcenie równoważne  $\tilde{\epsilon}$  zależy od całego tensora odkształcenia czy też od jego części sprężystej. Jeśli jedynie odkształcenia sprężyste wpływają na definicję miary  $\tilde{\epsilon}(\epsilon^e)$ , to można mówić o słabym sprężeniu. Ten rodzaj sprężenia jest zazwyczaj stosowany w odniesieniu do betonu. Jeśli występuje pełne sprężenie, wówczas również odkształcenia plastyczne indukują odkształcenie równoważne, ponieważ istnieje zależność  $\tilde{\epsilon}(\epsilon)$ . Wpływ sprężenia ilustrują: schemat na Rys. 2.9 oraz przykład, którego wyniki znajdują się na Rys. 2.10.

**2.3. ZAMYKANIE SIĘ RYS:** W modelu na poziomie punktu materialnego dodatkowo można uwzględnić efekt zamykania rys, który po zadaniu obciążenia wywołującego rozciąganie i odciążeniu pojawia się wraz z wywołaniem ściskania. Idea tego zjawiska jest pokazana na wykresie na Rys. 2.11. Teoria bazuje na pracach [62, 102, 145] i była szerzej przedstawiana w [117, 122, 170]. Uwzględnienie zamykania rys wymaga odpowiedniej definicji tzw. operatora pro-



jekcji  $P^+$ , który odpowiada za wydzielenie dodatniej części ze sprężystego tensora odkształcenia, zgodnie ze wzorem (2.52). Operator tworzy iloczyn macierzy według równania (2.57), gdzie  $T$  jest macierzą transformacji do kierunków głównych, a  $H$  jest macierzą wybierającą. Można wyróżnić dwie propozycje definicji tej macierzy, a mianowicie Ortiza (2.65) oraz alternatywnie Simo, Ju i Hansena (2.69). Związek konstytutywny, gdzie efekt zamykania rys jest uwzględniony, stanowi relacja (2.85). Wpływ tego efektu widać w definicji operatora stycznego  $E_{\text{tan}}$  (2.83) oraz w dodatniej części efektywnego tensora naprężenia  $\hat{\sigma}^+$  (2.79). Przykłady na końcu podrozdziału pokazują wpływ uwzględnienia zamykania rys na poziomie punktu materialnego (pojedynczego elementu skończonego).

**2.4. MODEL IZOTROPOWY MECHANIKI USZKODZEŃ:** Opis skalarny jest najprostszym w teorii mechaniki uszkodzeń. Pozostając przy opisie izotropowym można jednak wyróżnić dwie miary odkształcenia i/lub dwa parametry uszkodzenia. Dekompozycja, która rozróżnia inny rozwój uszkodzenia pod wpływem rozciągania i ściskania została przedstawiona w pracach [27, 103, 130]. Możliwy jest również podział na część związaną ze zmianą objętości i postaci, jak np. w [98]. Taki aksjatorowo-dewiatorowy model został zaproponowany również w niniejszej pracy, zob. wzór (2.86). Rozpatruje się zatem dwa parametry uszkodzenia –  $\omega_K$  odpowiadające za redukcję modułu ściśliwości  $K$  i  $\omega_G$  redukujący moduł ścinania  $G$ . Zmiana tych parametrów w najprostszym sposobie może zależeć od jednej równoważnej miary odkształcenia. Alternatywnie można rozpatrywać dwie równoważne miary odkształcenia, odpowiadające za zmianę objętości i postaci. W pracy zaimplementowane jest podejście łatwiejsze.

Przykład jednokierunkowego rozciągania pojedynczego elementu skończonego pokazany w tym podrozdziale analizuje możliwość zadawania różnych funkcji wzrostu uszkodzenia dla części aksjatorowej i dewiatorowej. Zastosowanie prawa osłabienia liniowego (2.19) z różnymi wartościami końcowymi  $\kappa_u$  dla odkształcenia objętościowego i postaciowego przy wzroście jednego parametru historii  $\kappa^d$  powoduje silnie nieliniową odpowiedź w zakresie osłabienia. Co więcej, zmiana współczynnika Poissona  $\nu_\omega$  zdefiniowanego wzorem (2.97) może doprowadzić do takiego obniżenia jego wartości, która nie posiada odzwierciedlenia w obserwacjach materiału takiego jak beton. W trakcie procesu rozciągania efekt Poissona w betonie może zanikać (por. [75]), ale wartość  $\nu_\omega$  nie powinna zmierzać do granicy  $-1$ . Wprowadzenie prawa osłabienia eksponencjalnego (2.21) z odpowiednimi parametrami dla obu funkcji wzrostu uszkodzenia  $\omega_K(\kappa^d)$  i  $\omega_G(\kappa^d)$  łagodzi niepożądane tendencje, por. Rys. 2.17.

**2.5. TEST WILLAMA:** Numeryczny test rozciągania ze ścinaniem został pierwszy raz wykonany w [169] i jak wspomniano w [171] jest on charakterystyczny dla zachowania się konstrukcji żelbetowych. Niemniej jednak w literaturze nie można spotykać wyników eksperymentalnych, prawdopodobnie z powodu trudności w przeprowadzeniu takiego testu. Test dobrze weryfikuje dany model na poziomie punktu materialnego. Istnieją dwa warunki, które sprawdzają poprawność modelu: maksymalne naprężenie główne musi być co najwyżej równe

wytrzymałości na rozciąganie  $f_t$  oraz wszystkie składowe tensora naprężenia powinny zmierzać do zera w końcowym stadium procesu obciążenia. Test Willama można podzielić na dwie fazy. Pierwsza stanowi jednokierunkowe poziome rozciąganie, gdzie zależności pomiędzy przyrostami składowych odkształceń  $\Delta\epsilon_{11} : \Delta\epsilon_{22} : \Delta\gamma_{12} = 1 : -\nu : 0$  obowiązują do momentu osiągnięcia granicy wytrzymałości betonu na rozciąganie. Po przekroczeniu tej wartości konfiguracja zmienia się tak, że wymuszane jest rozciąganie w dwóch kierunkach wraz ze ściśnięciem:  $\Delta\epsilon_{11} : \Delta\epsilon_{22} : \Delta\gamma_{12} = 0.5 : 0.75 : 1$ . Rysunek 2.19 przedstawia deformację narzucaną w obu fazach.

Otrzymane wyniki pokazują, że są spełnione wymagania testu Willama dla modeli: czystej mechaniki uszkodzeń, sprzężonego z plastycznością oraz izotropowego z dwoma parametrami uszkodzenia. W przypadku modelu mechaniki uszkodzeń zachodzi współosiowość odkształceń i naprężeń głównych. Jeśli rozpatruje się sprzężenie modelu z plastycznością wówczas ta współosiowość nie jest zachowana i zmiana kierunków głównych dla naprężeń jest szybsza, zob. Rys. 2.27(a). Wyniki dla modelu izotropowego ponownie pokazują, że można tak dobrać parametry dla funkcji wzrostu uszkodzenia, że problem ujemnej wartości współczynnika Poissona  $\nu_w$  może być zniwelowany, zob. Rys 2.32.

## ROZDZIAŁ 3: ELEMENTY SKOŃCZONE

### DLA GRADIENTOWEGO MODELU MECHANIKI USZKODZEŃ

3.1. MOŻLIWOŚCI GRADIENTOWEGO WZBOGACENIA MODELU MECHANIKI USZKODZEŃ: Teoria prezentowana w Rozdziale 2 jest lokalna, co oznacza, że przy osłabieniu materiału sztywność styczna zmienia się na ujemną, a sformułowanie traci eliptyczność i dopuszczalna jest nieskończona liczba rozwiązań. Lokalizacja towarzysząca osłabieniu i obserwowana w materiałach ogranicza się do linii lub powierzchni (w trzech wymiarach), co przy analizie numerycznej oznacza, że o szerokości strefy lokalizacji decyduje gęstość dyskretyzacji, np. w MES jest to pasmo elementów skończonych o najmniejszej możliwej szerokości. Z tego powodu wprowadza się teorię nielokalną, aby zregulować problem.

W modelach gradientowych o strefie lokalizacji decyduje wówczas wewnętrzna skala długości  $l$ . Warto jednak podkreślić, że wprowadzenie gradientów danego pola może mieć dwojaki skutek – wygładza niejednorodność lub ją wprowadza, por. Rys 3.1 i [5]. Do gradientowego modelu mechaniki uszkodzeń obok standardowego kompletu równań wprowadza się dodatkowe równanie uśredniające (3.7), które powoduje uśrednianie równoważnej miary odkształcenia  $\tilde{\epsilon}$ . Równanie to nazywa się również równaniem dyfuzyjnym lub równaniem Helmholtza. Wielkość  $\bar{\epsilon}$  oznacza uśrednioną miarę odkształceń, a parametr  $c$  jest związany z wewnętrzną skalą długości  $l$  w następujący sposób  $c = \frac{1}{2}l^2$ . Ta relacja została wyprowadzona np. w [4]. Znane są podobne podejścia, gdzie równanie uśredniające odnosi się do innych wielkości. Szereg takich propozycji zostało opisanych w [34].

3.2. GRADIENTOWY MODEL MECHANIKI USZKODZEŃ Z JEDNYM LUB DWOMA PARAMETRAMI: Niniejszy podrozdział zawiera kompletne wyprowadzenie od sformułowania przez dyskretyzację, aż do otrzymania równania macierzowego dla gradientowego modelu mechaniki uszkodzeń w opisie skalarnym (jeden parametr uszkodzenia) i izotropowym (dwa parametry uszkodzenia). Do funkcji aktywacji uszkodzenia (3.18) wprowadza się zatem uśrednioną miarę odkształceń  $\bar{\epsilon}$ . Punktem startowym jest równanie ruchu (2.1) i równanie uśredniające (3.7), które po wprowadzeniu formy słabej i przestrzennej dyskretyzacji mają postać (3.33) i (3.34). Wprowadzona została zatem niezależna interpolacja (3.25) dla pola przemieszczeń jak w standardowym MES oraz dodatkowo dla pola uśrednionych odkształceń. Zatem w takim dwupolowym modelu poszukiwane będą węzłowe przemieszczenia  $\mathbf{a}$  i węzłowe wartości uśrednionej miary odkształcenia  $e$ . Po wprowadzeniu linearyzacji otrzymuje się macierzowy układ równań (3.58) dla modelu z jednym parametrem uszkodzenia lub (3.72) dla modelu z dwoma parametrami uszkodzenia. Model z dwoma parametrami jest nadal dwupolowy i oparty jest na założeniu, że zmiana tych parametrów zależy od jednej i tej samej miary odkształcenia. Gdyby te parametry zależały odpowiednio od pewnej uśrednionej miary odkształcenia objętościowego i postaciowego, to sformułowanie byłoby trójpolowe.

3.3. IMPLEMENTACJA DWUPOLOWYCH ELEMENTÓW SKOŃCZONYCH: Węzłowe przemieszczenia  $\mathbf{a}$  i węzłowe wartości uśrednionej miary odkształcenia  $e$  są poszukiwane na poziomie każdego kroku przyrostowego. Jeśli rozwiązywany jest test, gdzie obecne są również siły bezwładności, to oprócz standardowej iteracyjnej metody Newtona-Raphsona poszukiwania równowagi wewnątrz danego kroku przyrostowego (czasowego) do procedury rozwiązania włączony jest algorytm Newmarka z niejawnym całkowaniem po czasie. Rozwiązywane jest zatem równanie (3.78), gdzie wektor  $\mathbf{q}$  składa się ze wszystkich stopni swobody dla obu pól. Cały algorytm zawiera Tabela 3.2. Elementy skończone zaprezentowane w Tabeli 3.3 oprogramowano w pakiecie FEAP [158]. Jak wspomniano w [147], problem analizowany przy użyciu gradientowego modelu mechaniki uszkodzeń jest raczej sprzężony niż mieszany, zatem dopuszczalna jest interpolacja obu pól takimi samymi funkcjami kształtu, np. liniowymi.

3.4. WŁASNOŚCI ELEMENTÓW SKOŃCZONYCH I KONTROLA FORM PASOŻYTNICZYCH: Charakterystykę elementów skończonych można określić m.in. poprzez analizę problemu własnego. W przypadku gradientowego modelu mechaniki uszkodzeń sprzężonego z plastycznością operator styczny jest analizowany w trzech fazach: sprężystej, z aktywnym uszkodzeniem i w fazie odciążenia. Rysunek 3.2 przedstawia ścieżkę równowagi z zaznaczonymi punktami, kiedy analiza spektralna operatora stycznego została wykonana, odpowiednio dla każdej fazy.

Na początku analiza skupia się wyłącznie na czterowęzłowym elemencie skończonym. Rozpatrywane są przypadki z pełnym i zredukowanym całkowaniem oraz przy założeniu zerowej i niezerowej wartości parametru wewnętrznego długości  $c$ . Tabele 3.4 i 3.5 podają dodatnie, zerowe i ujemne wartości własne dla całego operatora stycznego  $\mathbf{K}$  oraz dla podmacierzy  $\mathbf{K}_{aa}$

i  $K_{ee}$  związanych odpowiednio z równaniami równowagi i z równaniem uśredniającym.

Rysunki 3.3–3.11 przedstawiają formy własne dla czterowęzłowego elementu skończonego w zależności od danego przypadku i poszczególnych faz. Na rysunkach od punktów węzłowych odłożone są składowe wektorów własnych dla odpowiadających im wartości własnych. Kolorem niebieskim zaznaczona jest ta część wektora, która odpowiada przemieszczeniowym stopniom swobody. Może być zatem interpretowana jako postać deformacji elementu skończonego. Forma zaznaczona kolorem czerwonym została skonstruowana w ten sposób, że wartości węzłowe uśrednionej miary odkształcenia są odłożone pionowo. Ponieważ cały operator  $K$  może być niesymetryczny, to dopuszczalne są zespolone składowe. Wówczas część urojona jest reprezentowana jako forma własna odłożona kolorem jasno niebieskim i/lub różowym, odpowiednio dla stopni swobody przemieszczeniowych i uśrednionej miary odkształcenia. Z tabel i rysunków wynika przede wszystkim, że w przypadku stosowania zredukowanego całkowania (z jednym punktem Gaussa) należy dokonać stabilizacji obu pól w celu wyeliminowania zerowych nadliczbowych wartości własnych czyli kontroli form pasożytniczych.

Do wariacyjnego równania równowagi z wprowadzoną interpolacją pola przemieszczeń dodaje się składnik tak, aby dokonać stabilizacji sformułowania Galerkinia przez metodę najmniejszych kwadratów (MNK, skrót ang. *GLS*) [162, 178]. W składniku tym występuje macierz skalująca  $\chi_1$  zależna od wymiaru charakterystycznego elementu skończonego, modułu ścinania  $G$  oraz współczynnika liczbowego  $\chi$ . Ostatecznie po stabilizacji wprowadzonej do równania równowagi układ równań w zapisie macierzowym ma postać (3.117). Pozornie łatwa do wykonania w słabej formie równania uśredniającego analogiczna procedura stabilizacji za pomocą MNK lub gradientowej MNK nie wprowadza kontroli form pasożytniczych. Skuteczną okazuje się konstrukcja składnika stabilizującego za pomocą operatora  $\gamma$ , podobnie jak w analizie równania Laplace'a przedstawionej w [13]. Operator ten zależy wyłącznie od geometrii elementu i nie ma wpływu na pola liniowe. W składniku stabilizującym  $\chi_2$  podobnie jak poprzednio występuje współczynnik skalujący  $\chi$ . Ostatecznie zapis równania macierzowego ze stabilizacją wprowadzoną do obu równań (równowagi i uśredniającego) przyjmuje postać (3.133).

Zgodnie z oczekiwaniami analiza spektralna elementu czterowęzłowego ze zredukowanym całkowaniem i wprowadzoną kontrolą form pasożytniczych według równania (3.133) pokazuje, że dopiero stabilizacja obu pól zapewnia poprawne spektrum wartości własnych i formy własne, zob. Tabela 3.6 i Rys. 3.12–3.17.

Tabele 3.7–3.8 na końcu Podrozdziału 3.4 pokazują liczby dodatnich, zerowych i ujemnych wartości własnych dla pozostałych dwu- i trójwymiarowych elementów skończonych.

## ROZDZIAŁ 4: TESTOWANIE ELEMENTÓW SKOŃCZONYCH

4.1. STATYCZNE ROZCIĄGANIE PRĘTA Z IMPERFEKCJĄ: Numeryczna analiza statycznego rozciągania pręta z imperfekcją jest podstawowym testem służącym do obserwacji i porównań modeli dla zagadnień fizycznie nieliniowych. W środku pręta wprowadza się imperfekcję, np.

niecو słabszy materiał, mniejszy przekrój, itd. W odpowiedzi można otrzymać lokalizację odkształceń w strefie imperfekcji oraz różne rezultaty, zależne np. od analizy parametrycznej danego modelu. W niniejszej pracy zawarto wyniki, które uzupełniają obliczenia zawarte w [36, 119, 125]. Weryfikowane są elementy jedno-, dwu- i trójwymiarowe.

Rysunek 4.2 pokazuje wykresy naprężenie-wydłużenie dla analizy jednowymiarowej. Oprócz dyskretyzacji 20 elementami, gdzie zadana wewnętrzna skala długości jest mniejsza od wymiaru pojedynczego elementu skończonego ( $2.83 \text{ mm} < 5 \text{ mm}$ ), wyniki są niezależne od dyskretyzacji. Widać to wyraźnie na Rys. 4.3, gdzie rozkłady parametru uszkodzenia i uśrednionej miary odkształcenia mają nieomal identyczne wartości. Rysunki 4.4 i 4.5 przedstawiają wpływ wewnętrznego parametru długości  $c$  na rozwiązanie. Oscylacje w rozkładach uszkodzenia i uśrednionego odkształcenia, widoczne dla przypadku  $c = 0$ , świadczą o braku regularyzacji.

Rysunek 4.6 ilustruje wpływ wyboru funkcji wzrostu uszkodzenia. Warto dodać, że parametry modelu zostały tutaj tak dobrane, aby wartość energii pęknięcia była podobna. Można zatem otrzymać zupełnie inną odpowiedź, por. wykresy naprężenie-wydłużenie oraz rozkłady uszkodzenia, pomimo, że wzrost uśrednionego odkształcenia będzie miał podobny charakter. Kolejna analiza porównawcza dotyczy obecności sprzężenia z plastycznością w modelu, zob. Rys. 4.7–4.10. Wartość modułu wzmocnienia  $h$  może wydawać się nierealistycznie wysoka, ale jak potwierdzono w [119] im większa wartość  $h$  tym większe zbliżanie się do rozwiązania jak dla czystego gradientowego modelu mechaniki uszkodzeń. Wynika to z faktu, że moduł wzmocnienia odnosi się do szkieletu materiału. Jeśli rozpatruje się słabe sprzężenie modeli, tzn.  $\tilde{\epsilon} = \epsilon^e$ , to rozwój uszkodzenia dla modelu sprzężonego i bez sprzężenia jest taki sam.

Kolejnym etapem analizy są symulacje dwuwymiarowe. Rysunki 4.11–4.13 dotyczą porównania wyników dla elementu czterowęzłowego w zależności od typu całkowania. Niecو mniej sztywną odpowiedź uzyskuje się dla całkowania z jednym punktem Gaussa i stabilizacją, choć rozkład wartości dla uśrednionej miary odkształcenia i parametru uszkodzenia nie różni się. Tabela 4.3 potwierdza fakt, że przy całkowaniu zredukowanym ze stabilizacją kwadratowa zbieżność iteracji w kroku przyrostowym zostaje zachowana.

Innym aspektem analizy dwuwymiarowej jest weryfikacja modelu izotropowego. W Tabeli 4.4 zostały zestawione przypadki, dodatkowo rozróżniając definicję funkcji obciążenia: miarę energii sprężystej ( $EER$ ) i zmodyfikowane kryterium HMH (*modified von Mises*). Okazuje się, że odpowiedź jest zależna od definicji tych funkcji, co widać na Rys. 4.14. Dalsze obliczenia skupiają się na zastosowaniu jedynie zmodyfikowanego kryterium HMH. Z Tabeli 4.5 wynika, że proces zbieżności przy stosowaniu modelu izotropowego nie pogarsza się w stosunku do standardowo używanego modelu skalarnego. Rysunki 4.15–4.17 ilustrują kolejne porównania dla używanego modelu izotropowego. W zależności od wzajemnej relacji zadanych parametrów ciągliwości  $\eta$  dla części aksjatorowej i dewiatorowej uzyskuje się inny rozwój degradacji materiału w osłabionej strefie. Najbardziej widoczna różnica jest dla zmiennego współczynnika Poissona  $\nu_\omega$ , którego wartość wrasta lub maleje w zależności od rozważanego przypadku.

Krótkie porównanie wyników obliczeń wykonanych przy pomocy elementów trójwymiarowych dotyczy przede wszystkim pomierzonych czasów obliczeń, zob. Tabela 4.6. Oczywiście najkrótszy czas jest dla przypadku, gdzie stosuje się elementy trójwymiarowe z ośmioma węzłami. Mimo wprowadzonej do nich interpolacji liniowej obu pól i w efekcie możliwych niedokładności wyników, ten element jest wybrany do dalszych obliczeń problemów trójwymiarowych.

4.2. DWA TESTY DLA DYNAMIKI: Kontynuując poprzedni podrozdział można przetestować model na przykładzie pręta pod działaniem obciążenia uderzeniowego. Znane jest rozwiązanie analityczne (por. np. [8, 150]) dla pręta jednostronnie zamocowanego, które wyjaśnia mechanizm propagacji fal przed i po odbiciu się od brzegu. W chwili kiedy następuje wyjście poza zakres sprężysty wraz z osłabieniem przy zamocowaniu pojawia się fala stojąca (z urojoną prędkością). Ostatecznie prowadzi to do lokalizacji i zniszczenia przy zamocowanym brzegu. W celu uniknięcia zależności rozwiązania numerycznego od siatki należy zastosować model z regularyzacją, tak aby nie nastąpiła lokalizacja wyłącznie w elemencie najbliższym zamocowania. Rysunki 4.20(a)–4.20(c) pokazują ewolucję uśrednionego odkształcenia, naprężenia osiowego i uszkodzenia. Widoczne jest powstanie fali stojącej i odbijanie się fali sprężystej. Rysunek 4.20(d) przedstawia ostateczny rozkład parametru uszkodzenia w pręcie.

Drugi test dotyczy jednokierunkowego dynamicznego rozciągania obszaru dwuwymiarowego, jak na Rys. 4.21. Wzdłuż poziomej osi opcjonalnie umieszcza się zbrojenie. Różnica pomiędzy konfiguracją bez zbrojenia (beton) i ze zbrojeniem (żelbet) jest widoczna na Rys. 4.22 i 4.23. Dla betonu otrzymuje się wyraźną lokalizację i wzrost wydłużenia do nieskończoności. Natomiast dla żelbetu pomimo lokalizacji widoczna jest obecność fali sprężystej i oscylacje wydłużenia wokół pewnego stanu. Rysunek 4.24 przedstawia zależność wyników od intensywności obciążenia i stopnia zbrojenia.

## ROZDZIAŁ 5: ZASTOSOWANIA MODELU NUMERYCZNEGO

5.1. WSPORNIK POD OBCIĄŻENIEM ZNAKOZMIENNYM: Test wspornika pod obciążeniem znakozmiennym ma na celu demonstrację zastosowania gradientowego modelu z opcją zamykania rys. Siatka elementów skończonych wraz z warunkami brzegowymi jest przedstawiona na Rys. 5.1. Test był analizowany w [117, 122], ale nie dotyczył on modelu sprzężonego z plastycznością i z opcją zamykania rys. Wykresy na Rys. 5.2 pokazują, że bez opcji zamykania rys nie jest przywracana początkowa sztywność przy zmianie znaku obciążenia. Dla modelu z plastycznością widoczna jest dodatkowo obecność trwałych odkształceń. Rysunki 5.3 i 5.4 pokazują ewolucję naprężenia  $\sigma_{11}$ . Można zauważyć, że wytrzymałość betonu na rozciąganie  $f_t$  nie zostaje przekroczona, a zamykanie rys pojawia się pomiędzy punktem 5 i 6, co odpowiada zmianie znaku naprężenia w dolnej strefie, Rys. 5.3(g). Rys. 5.5 i 5.6 obrazują (zaczynając od lewej) rozkłady uśrednionego odkształcenia, odkształcenia plastycznego i parametru

uszkodzenia. Warto zwrócić uwagę, że uszkodzenie jest wielkością niemalejącą i pomimo zmiany znaku obciążenia jest ono zachowywane.

**5.2. BRAZYLIJSKI TEST ROZŁUPYWANIA PRÓBKII:** Test rozłupywania próbki, zwany też testem brazylijskim ma na celu wyznaczenie wytrzymałości betonu na rozciąganie. Pod wpływem ściskania próbki w kształcie walca, jak to jest pokazane na Rys. 5.7, tworzą się rysy pierwotne i wtórne, ewentualnie klin, a następnie rozłupanie. Do obliczeń zastosowano model gradientowy samej mechaniki uszkodzeń (bez sprzężenia) dla 9 przypadków z różnym typem interpolacji i gęstością siatki. Dane są zestawione w Tabelach 5.1 i 5.2. Rysunki 5.9–5.13 przedstawiają wyniki dla wszystkich przypadków. Na Rys. 5.9 da się zauważyć podział wykresów na dwie grupy, ale generalnie wyniki są niezależne od wyboru siatki. Jest to widoczne przy porównaniu rysunków warstwicznych wybranych wielkości. Dalsze obliczenia dotyczą średniej siatki i elementów z mieszaną interpolacją. Na Rys. 5.14 i 5.15 można zauważyć wpływ wartości wewnętrznej skali długości  $l$  na wyniki obliczeń i na kwestię, czy efekt rozłupania zostanie odtworzony. Z drugiej strony różna definicja przekładki (Rys. 5.16 i 5.17) nie ma większego wpływu i zachowanie próbki walcowej jest zgodne z procesem obserwowanym w eksperymentach.

W drugiej części obliczeń weryfikowano model izotropowy i stosowanie dwóch parametrów uszkodzenia. Ponownie została użyta siatka średnia i elementy z mieszaną interpolacją. Dane dla rozważanych przypadków są zestawione w Tabeli 5.9. Z wyników obserwowanych na Rys. 5.18–5.22 można wywnioskować, że zadawana wartość parametru ciągliwości  $\eta$  może mieć wpływ na zachowanie się symulowanego procesu rozłupania próbki, co więcej bardziej istotna jest tutaj wartość tego parametru dla części dewiatorowej. Rysunek 5.22(b), na którym przedstawiona jest zmiana wartości współczynnika Poissona, ilustruje fakt, że ekstremalne ujemne wartości  $\nu_\omega$  pojawiają się w końcowej fazie testu na froncie strefy uszkodzenia.

**5.3. CZTEROPUNKTOWE ZGINANIE BELKI:** Analiza tego testu bazuje na doświadczeniu wykonanym przez Eibla i współpracowników [46]. Uzyskane wyniki eksperymentalne porównano wcześniej z wynikami symulacji numerycznych [45, 151, 152]. Belka została obciążona dynamicznie. Dane geometryczne i materiałowe oraz historia obciążenia są zestawione na Rys. 5.23 i w Tabelach 5.4–5.5. Obliczenia opisane w tym podrozdziale są podzielone na kilka etapów.

Pierwszy etap stanowi analiza belki betonowej (bez zbrojenia) pod obciążeniem statycznym w celu wyznaczenia granicznej wartości wewnętrzznego parametru długości, tak aby otrzymane wyniki były niezależne od gęstości siatek (rzadkiej –  $56 \times 8$ , średniej –  $112 \times 16$  i gęstej –  $168 \times 24$ ). Okazuje się, że graniczna wartość  $l$  wynosi 16 mm. Dodatkowo zweryfikowano przy pomocy tego przykładu możliwość całkowania z jednym punktem Gaussa i stabilizacją. Podobnie jak w teście jednoosiowym, generalna tendencja, iż uzyskuje się nieco mniej sztywną odpowiedź w porównaniu do obliczeń przy użyciu pełnego całkowania, nadal jest zachowana.

Rysunek 5.25 przedstawia odpowiednie wykresy, natomiast na Rys. 5.26 i 5.27 znajdują się mapy warstwiczne dla uśrednionego odkształcenia oraz deformacje dla wszystkich przypadków obliczeń.

Kolejny etap stanowią obliczenia statyczne belki żelbetowej (zbrojonej). Wykonano tutaj szereg porównań dotyczących parametrów modelu. Rysunek 5.28 przedstawia wykresy w zależności od wartości: parametru ciągliwości  $\eta$ , wewnętrznego parametru długości, współczynnika  $k$  będącego stosunkiem wytrzymałości na ściskanie  $f_c$  do wytrzymałości na rozciąganie  $f_t$ . Analizowany jest także wpływ sprężenia z plastycznością i zależność od stopnia zbrojenia. Natomiast Rys. 5.29–5.34 ilustrują te porównania na mapach warstwicznych.

Ostatni etap obliczeń dotyczy konfrontacji z eksperymentem. Wykresy na Rys. 5.35 pokazują zgodność symulacji belki żelbetowej pod obciążeniem dynamicznym i przeprowadzonego eksperymentu. Dodatkowo na Rys. 5.36 i 5.37 przedstawiono rozkłady uśrednionych odkształceń i deformacje dla belki zbrojonej zgodnie z danymi oraz z powiększonym zbrojeniem.

**5.4. EFEKT KOŁKOWANIA ZBROJENIA W TRZECH WYMIARACH:** Działanie kołkowe zbrojenia wywołujące odrywanie otuliny betonowej może być analizowane jako problem dwuwymiarowy lub trójwymiarowy przy ograniczeniu, że pręt zbrojeniowy przemieszcza się jednakowo wzdłuż osi (ang. *dowel disk test*). Bardziej rzeczywista jest jednak symulacja, gdzie zbrojenie jest odrywane na jednym końcu. Wówczas konieczna jest analiza zagadnienia w trzech wymiarach (ang. *dowel bar test*). Test numeryczny został wykonany w dowiązaniu do eksperymentu [41], ale wprowadzone zostały następujące ograniczenia: rozpatrywano połowę próbki ze względu na symetrię, pomiędzy zbrojeniem a matrycą betonową umieszczono tzw. interfaś. Dla zmniejszenia modelu obliczeniowego odrzucono tylną część próbki przy założeniu braku jakiegokolwiek podparcia tylnej ściany lub przy poziomym podparciu tej ściany równoległe do osi pręta (2 przypadki). Dane, warunki brzegowe, siatki przyjęte do obliczeń są zilustrowane na początku podrozdziału w Tabeli 5.6 i na Rys. 5.39–5.40. Wykresy siła-przemieszczenie znajdują się na Rys. 5.41. Rezultat najbliższy eksperymentalnemu uzyskano dla przypadku siatki nieregularnej i z poziomym podparciem tylnej ścianki próbki. Rysunki 5.42 i 5.43 przedstawiają końcowe rozkłady uszkodzenia i uśrednionego odkształcenia dla wszystkich obliczonych przypadków.

**5.5. ŻELBETOWE POŁĄCZENIE PŁYTA-SŁUP:** Bezpośrednie połączenie płyta-słup jest obecnie powszechnie stosowanym rozwiązaniem konstrukcyjnym. Temu rozwiązaniu towarzyszy niebezpieczeństwo przebiccia płyty, związane z działaniem ścinania ukośnie do powierzchni styku słupa z płytą. Tworzy się tzw. stożek przebiccia. Szczegółowy opis można znaleźć m.in. w [104,163]. Dlatego płyta w trakcie budowy wzmocniana jest na ścinanie strzemionami, itp. W istniejących konstrukcjach można stosować specjalne śruby, np. takie, które zostały eksperymentalnie zweryfikowane w pracy [1]. Doświadczenia opisane w [1] pokazują, że obecność takich śrub wzmocnia płytę i zapobiega zjawisku przebiccia. Zadaniem opisanym w niniejszym



podrozdziale jest odtworzenie tego eksperymentu.

Po wprowadzeniu założeń upraszczających zdecydowano, że test będzie analizowany przy użyciu gradientowego modelu bez sprzężenia (sama mechanika uszkodzeń), ale także sprzężonego z plastycznością. Dane obliczeniowe są zawarte w Tabeli 5.8. Na Rys. 5.48 przedstawiono siatkę MES oraz wizualizację zbrojenia (łącznie ze śrubami).

Porównanie wykresów siła-ugięcie uzyskanych z przeprowadzonego eksperymentu [1] oraz z rozwiązania numerycznego zostało umieszczone na Rys. 5.49. Nie ma różnicy pomiędzy wynikami obliczeń dla modelu ze śrubami i bez śrub. Stąd wniosek, że w trakcie symulacji nie potrafią się one uaktywnić, być może z powodu mało precyzyjnego ich modelowania, które nie uwzględnia efektu zakotwienia w płycie, jak np. w [111]. Wykresy otrzymane dla modelu mechaniki uszkodzeń bez sprzężenia nie są reprezentatywne w porównaniu z wykresami z doświadczeń, natomiast wykresy dla modelu sprzężonego są częściowo zgodne z eksperymentalnym przypadkiem, gdzie uwzględniono śruby. Jednakże nie jest trudno tak dostosować parametry modelu, aby osiągnąć zgodność krzywych. Mapy warstwiczne uśrednionego odkształcenia dla różnych etapów deformacji konfiguracji ze śrubami zamieszczono na Rys. 5.50. Jak widać największe odkształcenia występują na linii połączenia płyty ze słupem po stronie rozciągania, co oznacza, że nie tylko nie uzyskano różnic widocznych w eksperymencie, ale również nie jest symulowane samo zjawisko przebicia.

Powyższe wyniki skłoniły do poszukiwania takiego modelu, który byłby w stanie poprawnie odtworzyć zjawisko przebicia. Po wprowadzeniu małej wartości wewnętrznego parametru długości  $l = 4$  mm i jednokrotnym zagęszczeniu siatki po grubości płyty otrzymano wyniki bardziej zbliżone do eksperymentalnych. Jak pokazują Rys. 5.51–5.53 nie tylko obliczona krzywa przypomina kształtem uzyskaną z doświadczenia, ale także płyta nie zarysowuje się tuż przy połączeniu ze słupem. Warto jednak podkreślić, że maksymalna wartość naprężenia w zbrojeniu głównym (na rozciąganie przy zginaniu) nie przekroczyła granicy plastyczności, a zatem wciąż nie można powiedzieć, że zjawisko przebicia zostało poprawnie odtworzone. Pozostałe przypadki, włączając wyniki dla modelu izotropowego z dwoma parametrami oraz obliczone za pomocą pakietu DIANA standardowymi modelami dla mechaniki betonu, nie poprawiły jakości rozwiązania.

Można wymienić następujące prawdopodobne przyczyny niepoprawnej symulacji zjawiska przebicia dla połączenia płyta-słup:

- zbyt rzadkie siatki elementów skończonych,
- wprowadzenie modelu nielokalnego zapobiega tworzeniu się rys związanych ze ścinaniem, jednocześnie powodując, że występuje dominacja zginania,
- zastosowane nieodpowiedniej dla trójwymiarowego testu funkcji obciążenia (powierzchni uszkodzenia),
- pełna przyczepność (brak poślizgu) pomiędzy zbrojeniem i betonem.

Ponieważ model izotropowy nie podnosi jakości rozwiązania, więc być może należałoby zastosować model anizotropowy mechaniki uszkodzenia.

## ROZDZIAŁ 6: WNIOSKI

Po omówieniu szczegółowych wniosków z pracy na końcu tego rozdziału podano następujące najważniejsze uwagi:

- Skalarny opis uszkodzenia jest wystarczający do analizy numerycznej, jeśli występuje dominacja rozciągania/ściskania i/lub zginania.
- Wprowadzenie dwóch parametrów uszkodzenia do modelu jest proste. Z drugiej strony, taka wersja modelu nastęcza trudności z interpretacją wyników, np. pojawiają się ujemne wartości współczynnika Poissona.
- Opis izotropowy uszkodzenia z jednym lub dwoma parametrami nie wystarcza gdy dominuje ścinanie. Zastosowanie skalarnego modelu sprzężonego nie usuwa tej niedogodności.
- Model gradientowy zapewnia niezależność wyników od siatki.
- Algorytm dla dynamiki wymaga tylko niewielkiej modyfikacji w odniesieniu do algorytmu dla statyki, a lokalizacja jest symulowana poprawnie.
- Obecność zbrojenia nie gwarantuje regularyzacji rozwiązania.
- Elementy stabilizowane z jednym punktem całkowania dają efektywny algorytm obliczeń.

## DODATKI

Dodatek A przedstawia porównanie lokalnego i gradientowego modelu mechaniki uszkodzeń. Pokazana jest zależność rozwiązania od siatki dla modelu lokalnego.

Dodatek B dotyczy wyprowadzenia sformułowania ze stabilizacją przy pomocy MNK dla równania uśredniającego. Analiza spektralna potwierdza, że element zaprogramowany na bazie tego sformułowania nie usuwa pasożytniczych zerowych wartości własnych i odpowiadających im nieoczekiwanych form własnych.

Dodatek C pokazuje wyniki uzyskane dla testu kołkowego działania zbrojenia obliczanego przy pomocy jednej warstwy trójwymiarowych elementów (ang. *dowel disk test*).